Plasma Physics Reports, Vol. 27, No. 12, 2001, pp. 1001–1010. Translated from Fizika Plazmy, Vol. 27, No. 12, 2001, pp. 1059–1069.

TOKAMAKS

Effect of the Radial Electric Field on Lower Hybrid Plasma Heating in the FT-2 Tokamak

S. I. Lashkul*, V. N. Budnikov*, E. O. Vekshina, V. V. D'yachenko*, V. B. Ermolaev*, L. A. Esipov*, E. R. Its*, M. Yu. Kantor*, D. V. Kuprienko*, A. Yu. Popov*, and S. V. Shatalin****

**Ioffe Physicotechnical Institute, Russian Academy of Sciences, Politekhnicheskaya ul. 26, St. Petersburg, 194021 Russia*

***St. Petersburg State Technical University, Politekhnicheskaya ul. 29, St. Petersburg, 195251 Russia*

Received June 28, 2001; in final form, July 10, 2001

Abstract—Conditions for efficient ion heating in the interaction of lower hybrid waves with plasma are experimentally determined. Experiments show that efficient lower hybrid heating stimulates a transition to the improved confinement mode. The formation of internal and external transport barriers is associated with strong central ion heating, which results in a change of the radial electric field E_r and an increase in the shear of the poloidal plasma velocity. The improved confinement mode in the central region of the discharge is attained under the combined action of lower hybrid heating and an additional rapid increase in the plasma current. A new mechanism for the generation of an additional field E_r is proposed to explain the formation of a transport barrier. © *2001 MAIK "Nauka/Interperiodica".*

1. INTRODUCTION

The interaction of lower hybrid (LH) waves with plasma and the possibility of efficient RF plasma heating in this frequency range are being studied in the FT-2 tokamak [1]. FT-2 is a relatively small tokamak (R = 0.55 m, a = 0.08 m, B_t = 2.2 T, and I_{pl} = 22 kA) with initial electron and ion temperatures of an ohmically heated (OH) plasma equal to $T_i(0)$ = 100 eV and $T_e(0)$ = 300–500 eV, respectively. The central plasma density in experiments, $N_e(0) = (3 \pm 0.2) \times 10^{13}$ cm^{-3}, was chosen such that it corresponded to the LH resonance frequency. It was shown experimentally that the plasma is efficiently heated if the LH wave reaches the axis of the plasma column without being affected by parametric decay and is absorbed in the resonance region. To avoid absorption at the plasma edge due to parametric decay, the initial electron temperature should be sufficiently high, $T_e(0) \geq 350$ eV [2]. Under these conditions, the efficient heating of the ion component (from 100 to 350 eV) at P_{RF} = 100–150 kW was demonstrated for the first time in [3]. It turned out that such strong heating significantly affects transport processes in plasma. In experiments with efficient LH heating, a transition to the improved confinement mode was observed [4].

Experiments in large tokamaks (ASDEX-U, JET, D-IIID, JT-60, etc.) have demonstrated the possibility of achieving L–H transitions with various methods of auxiliary heating, such as neutral injection and ion cyclotron and electron cyclotron resonance heating [5]. Success was also achieved in plasma heating with Bernstein waves. In the literature, mechanisms for the formation of external and internal transport barriers has been considered (see, e.g., [6]). One of the effects hindering the achievement of high thermonuclear plasma parameters in a tokamak is known to be abnormally high (as compared to the neoclassical theory) heat and particle losses caused by microscale oscillations in plasma. Fortunately, there are mechanisms for suppressing turbulent transport. These mechanisms are related to a decrease in the correlation length of the oscillations responsible for abnormally high transport. In experiments, this is done by increasing the shear of the poloidal (toroidal) velocity of the plasma rotation caused by the change in the radial electric field E_r [7].

In this paper, we present the experimental data illustrating the effect of improved confinement during LH heating in the FT-2 tokamak and analyze the effect of the radial electric field on the formation of transport barriers both inside and at the edge of the plasma column. It is shown that the profile of the radial electric field can be significantly affected by the combined action of LH heating and an additional rapid increase in the plasma current.

2. LH HEATING EXPERIMENTS

In experiments on LH heating, RF energy (920 MHz, 100 kW) was launched from the low field side through a two-waveguide grill with a phase shift $\Delta\varphi = \pi$ between the waveguides. The duration of the ohmic discharge was 50 ms, and the duration of the RF pulse was 5 ms. The initial plasma density, $N_e(0) = (3 \pm 0.2) \times 10^{13}$ cm^{-3}, corresponded to the condition of ion heating,

1063-780X/01/2712-1001$21.00 © 2001 MAIK "Nauka/Interperiodica"

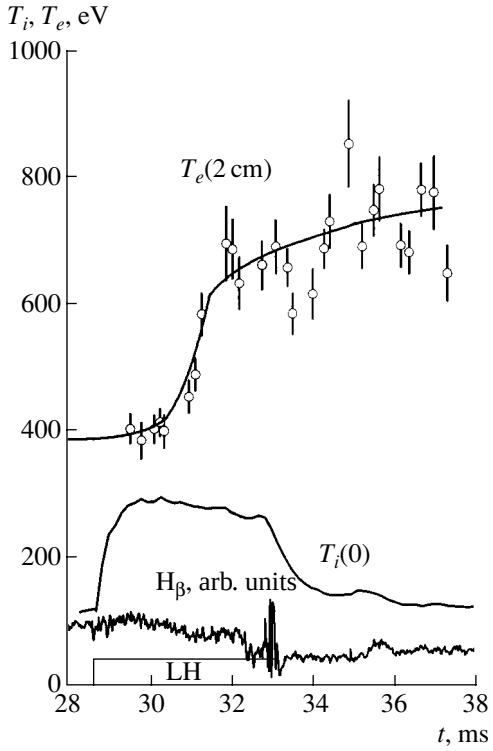

Fig. 1. Time evolution of the plasma parameters T_i ($r = 0$), T_e ($r \simeq 2$ cm), and the intensity of H_β line emission during on-axis LH heating.

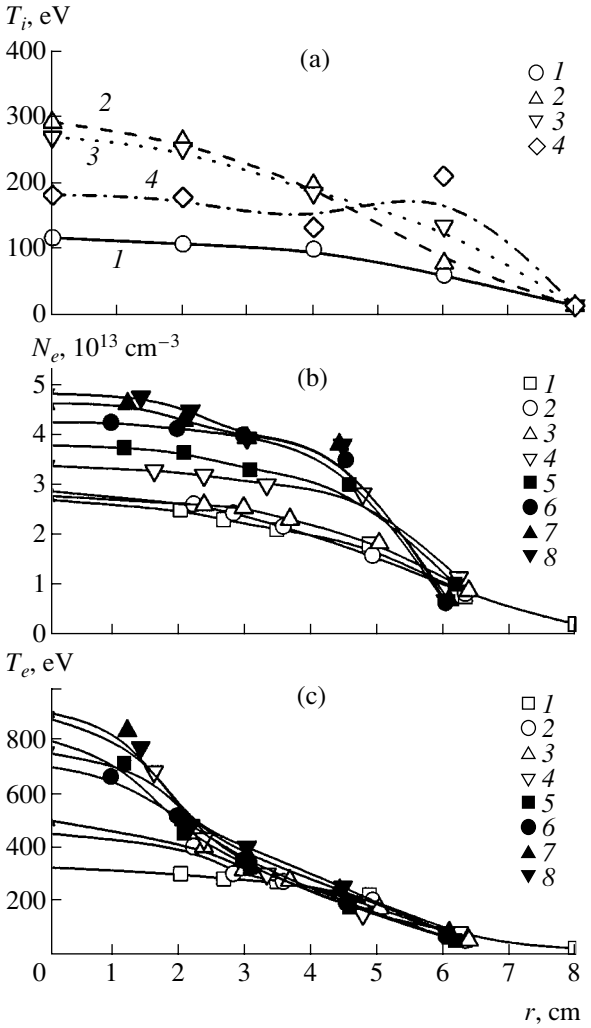

Fig. 2. Profiles of the plasma parameters (a) $T_i(r)$ at (*1*) 28.7 ms (OH mode), (*2*) 30 ms (LH heating), (*3*) 33 ms (LH heating), and (*4*) 35 ms and (b) $N_e(r)$ and (c) $T_e(r)$ at (*1*) 28, (*2*) 29, (*3*) 30, (*4*) 32, (*5*) 33, (*6*) 34, (*7*) 35, and (*8*) 37 ms for the case of on-axis heating; r is the radius of the magnetic surface.

and a sufficiently high electron temperature ensured the efficient absorption of RF energy. Two characteristic cases of (a) on-axis and (b) off-axis absorption of RF energy under auxiliary LH heating were examined.

The main experimental data for these two cases are presented in Figs. 1–4. Figures 1 and 2 show the evolution of the plasma parameters during on-axis heating. A 5-ms RF pulse is switched on 28 ms after the beginning of the discharge. It can be seen in Fig. 1 that the switching-on of the RF power is accompanied by a sharp increase in the ion temperature $T_i(0)$ from 100 to 320 eV, whereas the electron temperature T_e increases only slightly, which corresponds to the conditions of LH wave absorption at $n_e^{\mathrm{OH}}(0) = 2.7 \times 10^{13}$ cm^{-3}. However, at 31 ms, a sharp increase in T_e ($r = 2$ cm) from 350 to 650 eV is observed; simultaneously, the plasma density increases and the intensity of the H_β line emission decreases. We note that, during auxiliary heating, the plasma column is somewhat displaced outward, so that the above change in the temperature represents the averaged value for $r = 2$ cm and reflects the effects of both heating and displacement. Figure 2 shows the radial profile of the electron temperature in the magnetic surface coordinates. It can be seen that the profile $T_e(r)$ is peaked at 31 ms and its slope is maximum at $r = 3$–4 cm. The density profile is characterized by a flat top and a sharp gradient at $r = 6$–8 cm, where a transport barrier for the density is formed. After the end of the RF pulse, a slow decrease in the intensity of H_β line emission is followed by a more rapid drop, indicating the L–H transition. Upon cooling, the formation of a pedestal in the profile of the ion temperature (as well as in the density profile) is observed at $r = 6$–7 cm. We emphasize that the electron temperature in the post-heating phase does not decrease and even increases to 800–900 eV.

In experiments, the electron temperature and plasma density were measured with a high-accuracy multipulse Thomson scattering diagnostics [8]. The ion temperature was measured with a five-channel charge-exchange neutral-particle analyzer. We also used a 2-mm microwave interferometer, a spectrometer, a bolometer, and Langmuir and MHD probes. The

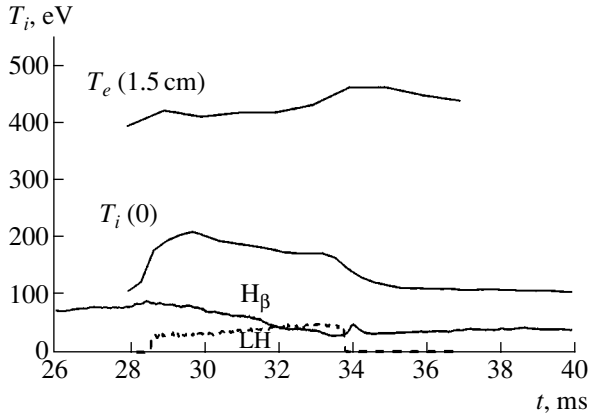

Fig. 3. Time evolution of the plasma parameters T_i (r = 0), T_e ($r \simeq 1.5$ cm), and the intensity of H_β line emission during off-axis LH heating.

increase in the electron temperature and density, as well as the increase in the energy confinement time from 1 to 3.5 ms, is attributed to the improved confinement at the center due to the formation of a transport barrier for the ion density and temperature at the radius r = 6–8 cm [9].

Figures 3 and 4 present similar data for an experiment with off-axis ion heating, which was provided by a somewhat higher initial central density, $n_e^{OH}(0) = 3 \times 10^{13}$ cm^{-3}. In Fig. 5, the calculated profiles of the RF power absorbed by the ion component are compared for on-axis and off-axis heating; the profiles are computed by the modeling of heat balance in the plasma with allowance for the variations in all the measured plasma parameters ($n_e(r)$, $T_i(r)$, $T_e(r)$, and Z_{eff}) and the relative decrease in the content of neutral hydrogen in the course of L–H transition. In both cases, the absorbed power was 16–20 kW. It is seen that additional ion heating also occurs during off-axis heating, but, in this case, the $T_i(r)$ profile is more flattened and the central temperature $T_i(0)$ increases from 100 to 200 eV. As in the previous experiment, an internal transport barrier (ITR) for the density (starting from 32 ms) and ion temperature is formed at the radius r = 6–7 cm. It is seen that, as in the case of on-axis heating, a slow decrease in the intensity of H_β line emission is followed by a more rapid drop by the end of the RF pulse (32 ms). Note that radiation losses begin to drop sharply starting from this time (Fig. 6). One of the main distinctions from on-axis heating is that, in this experiment, the additional electron heating is substantially weaker (Figs. 3, 4). After the end of the RF pulse, the value of $T_e(0)$ relaxes to the initial temperature with a time constant of ~2 ms, indicating that no appreciable improvement of confinement at the axis of the plasma column occurs in this case.

The modeling by the ASTRA code with allowance for the experimental data shows that, during on-axis heating, electrons are heated substantially due to the

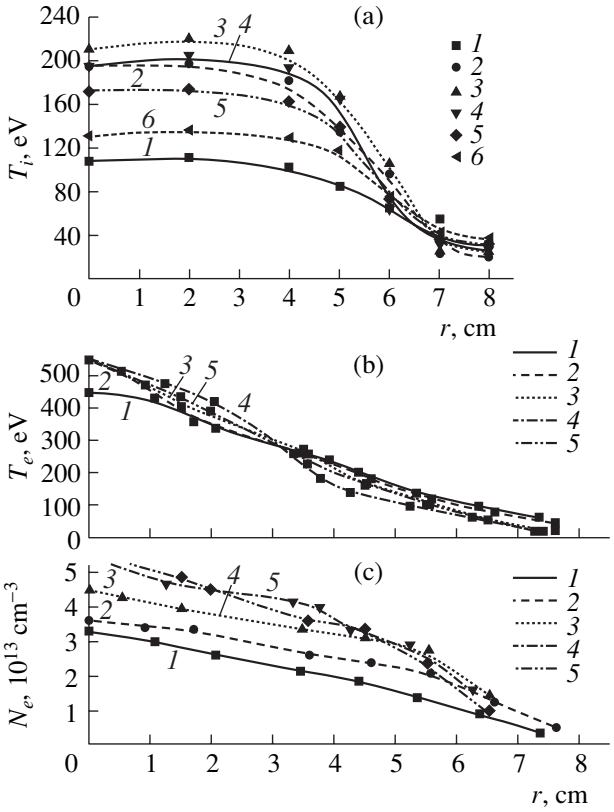

Fig. 4. Profiles of the plasma parameters (a) $T_i(r)$ at (*1*) 28, (*2*) 29.1, (*3*) 30, (*4*) 31.5, (*5*) 33, and (*6*) 36 ms and (b) $T_e(r)$ and (c) $N_e(r)$ at (*1*) 28, (*2*) 30, (*3*) 32, (*4*) 34, and (*5*) 36 ms in the case of off-axis heating; r is the radius of the magnetic surface.

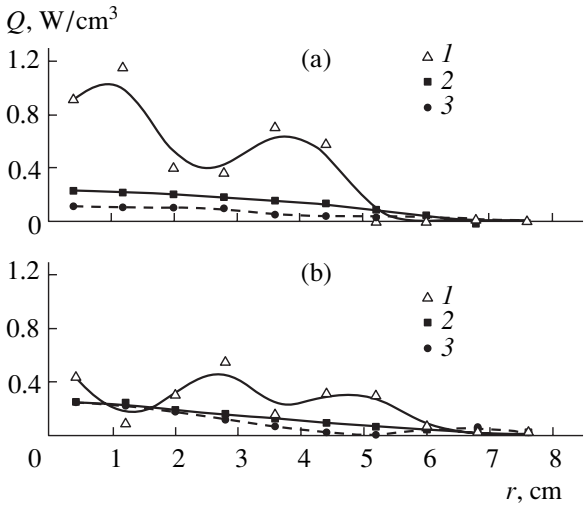

Fig. 5. Profiles of the RF power density Q_h absorbed in the ion component at 2 ms during LH heating (curves *1*) and the power density transferred from electrons to ions in the OH mode (curves *2*) and at 2 ms during LH heating (curves *3*) for the cases of (a) on-axis and (b) off-axis LH heating. The profiles are computed by the modeling of heat balance in the plasma.

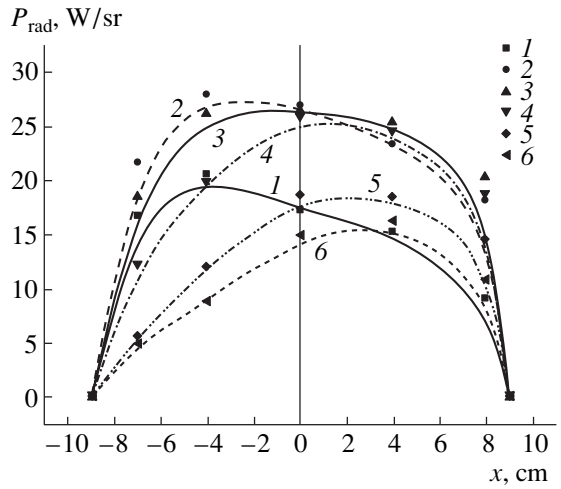

Fig. 6. Chord profiles of the radiation loss power P_{rad} at (*1*) 285, (*2*) 30.5, (*3*) 31.5, (*4*) 33.5, (*5*) 35.5, and (*6*) 38.5 ms for the case of off-axis LH heating.

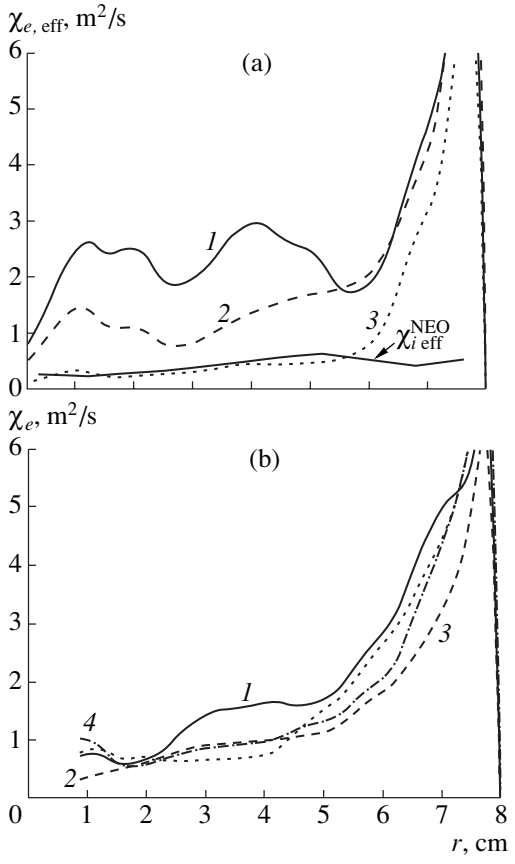

Fig. 7. Profiles of the effective thermal diffusivity $\chi_{e,\,\mathrm{eff}}$ for the cases of (a) on-axis heating at (*1*) 28, (*2*) 30, and (*3*) 34 ms and (b) off-axis heating at (*1*) 28, (*2*) 32, (*3*) 34, and (*4*) 35 ms and the profile of the neoclassical value of $\chi_{i,\,\mathrm{eff}}^{\mathrm{NEO}}$ calculated for the post-heating phase at t = 34 ms (plot a).

rapid decrease in the effective thermal diffusivity $\chi_{e,\,\mathrm{eff}}$ [9]. It is seen in Fig. 7 that, in the case of on-axis heating, $\chi_{e,\,\mathrm{eff}}$ decreases by almost one order of magnitude and remains at a level close to the neoclassical value $\chi_{i,\,\mathrm{eff}}^{\mathrm{NEO}}$ in the post-heating phase. For off-axis heating, this effect does not take place, although the transport barrier for the density and ion temperature at the periphery of the discharge is formed. The energy confinement time increases by a factor of ~3 for on-axis heating and a factor of ~2 for off-axis heating.

Experiments carried out in many tokamaks [5] showed that the improvement of confinement and the formation of transport barriers are associated with the suppression of microscale turbulence by the shear of the poloidal $\mathbf{E}\times\mathbf{B}$ drift velocity $\omega_s = \omega_{\mathbf{E}\times\mathbf{B}}$, where

$$\omega_{\mathbf{E}\times\mathbf{B}} = \frac{B_\theta R}{2\pi B_\phi}\frac{d}{dr}\left(\frac{E_r}{B_\theta R}\right).$$

According to [10], microscale turbulence is completely suppressed when $\omega_{\mathbf{E}\times\mathbf{B}} > \gamma_{\mathrm{lin}}^{\max}$, where $\gamma_{\mathrm{lin}}^{\max}$ is the maximum linear growth rate of the dominant instability in the case of $\omega_{\mathbf{E}\times\mathbf{B}} = 0$.

Let us consider in this context the formation of the radial electric field profile for the cases of on-axis and off-axis LH plasma heating.

3. MODELING OF THE RADIAL ELECTRIC FIELD

Direct measurement of the profile of the radial electric field is a rather laborious experimental task. We usually calculated this profile based on the measured plasma parameters. According to the standard neoclassical theory, the radial electric field is equal to [11]

$$E_e^{\mathrm{STAND}} = \frac{T_i}{e}\left[\frac{d}{dr}(\ln n) - (1-k)\frac{d}{dr}(\ln T_i)\right] + B_\theta v_\phi, \quad (1)$$

where k is a numerical factor depending on the collision frequency, B_θ is the poloidal magnetic field, and v_ϕ is the average poloidal velocity. This expression was obtained from the condition that the ion and electron viscosities averaged over the magnetic surface are equal to zero. In our experiments with an additional rapid increase in the plasma current [12, 13], attention was drawn to the role of the toroidal electric field E_ϕ in the formation of the E_r profile. According to theoretical predictions (see, e.g., [14]), the ion and electron viscosities begin to play an important role in the presence of E_ϕ. Taking into account the electron viscosity and the associated drift (the so-called Ware drift) substantially changes the calculated profile of the radial electric field, particularly during transition processes, such as gas puffing and an increase in the plasma current. To analyze our experimental data (at $\nu_e^* < \nu_i^*$), we used

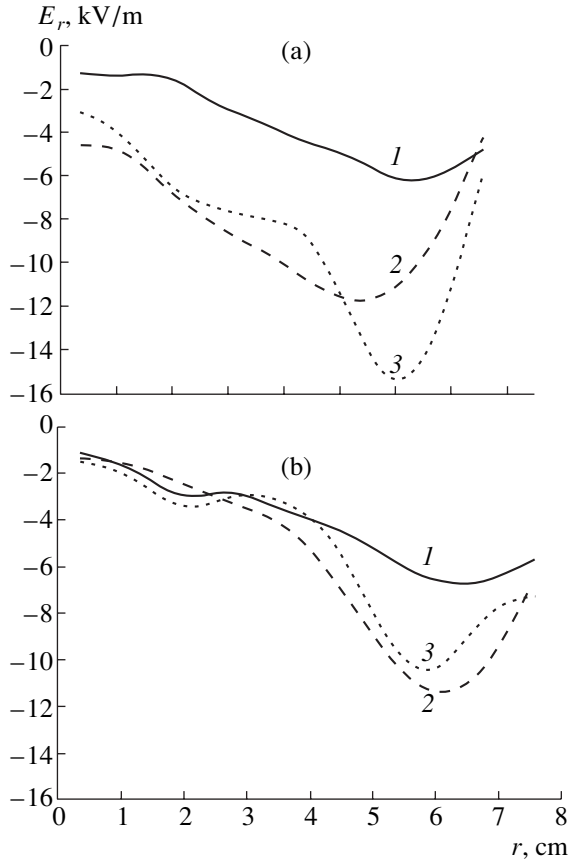

Fig. 8. Calculated profiles of the radial electric field for the cases of (a) on-axis heating at (*1*) 28, (*2*) 30, and (*3*) 33 ms and (b) off-axis heating at (*1*) 28, (*2*) 30, and (*3*) 34 ms; the curves calculated for 28 ms correspond to the OH mode.

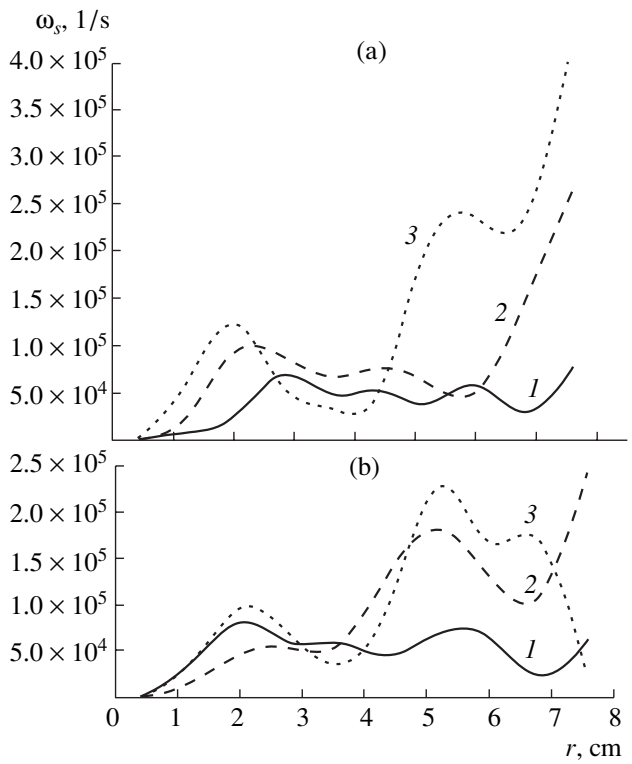

Fig. 9. Profiles of the shear ω_s of the radial electric field for the cases of (a) on-axis LH heating at (*1*) 28, (*2*) 30, and (*3*) 33 ms and off-axis LH heating at (*1*) 28, (*2*) 30, and (*3*) 32 ms. In plot (a), an increase in ω_s at r = 2 cm and r = 5–6 cm is observed at 30 ms. In plot (b), the shear decreases at the axis and increases at 4–6 cm.

the following refined expression for E_r based on the results of [14, 15]:

$$E_r = E^{\mathrm{STAND}} - \frac{2.3enE_\phi}{\sigma_\perp B_\theta}\frac{\sqrt{\varepsilon}}{(1+\nu_e^*\varepsilon^{3/2})(1+\nu_e^{*1/3}+\nu_e^*)}, \quad (2)$$

where

$$\Theta = \frac{B_\theta}{B}, \quad \sigma_\perp = \frac{\sigma_\perp^b}{1+\nu_i^*}, \quad \sigma_\perp^b = \frac{3}{2}\frac{\sqrt{\varepsilon}m_i n\nu_i}{B_\theta^2},$$

$$\nu_{i,e}^* = \frac{qR\nu_{i,e}}{\sqrt{2T_{i,e}/m_{i,e}}\varepsilon^{3/2}}.$$

This expression is derived from the condition that the sum of radial currents caused by the ion and electron viscosities is zero [15]. It is applicable in all collisional regimes. In experiments with auxiliary heating, when a fraction of high-energy toroidally trapped particles δn_b is fairly large (e.g., during LH heating or neutral injection), the relation between E_r and E_ϕ can be even more complicated. In this case, taking into account the longitudinal electron viscosity makes it necessary to also take into account the dependence of the radial electric field not only on the toroidal electric field, but also on the time and radial derivatives of this field. According to [14], expression (2) acquires an additional term on the order of

$$-\frac{e\delta n_b\sqrt{2}m_i rR}{\sigma_\perp 6\Theta^2 T_i B_\theta}\left[\frac{\partial^2 E_\phi}{\partial t^2}+\frac{E_\phi}{B_\theta}\frac{\partial}{\partial r}\left(\frac{E_\phi}{B_\theta}\frac{\partial E_\phi}{\partial r}\right)\right]. \quad (3)$$

Since variations in E_ϕ during LH heating are small, it is clear that variations in the ion temperature and density should significantly affect the results of calculations of E_r and its variations in both experimental situations under consideration (Figs. 1–4). Below, when considering an experiment with the combined LH heating and rapid increase in the plasma current, it will be shown that the contribution from E_ϕ can play a decisive role.

Figure 8 shows the calculated values of the radial electric fields for experiments with on-axis and off-axis LH heating. The time evolution of the shear of the radial electric field during auxiliary LH heating is shown in Fig. 9. We emphasize that, in the case of strong central ion heating, the values of E_r and shear

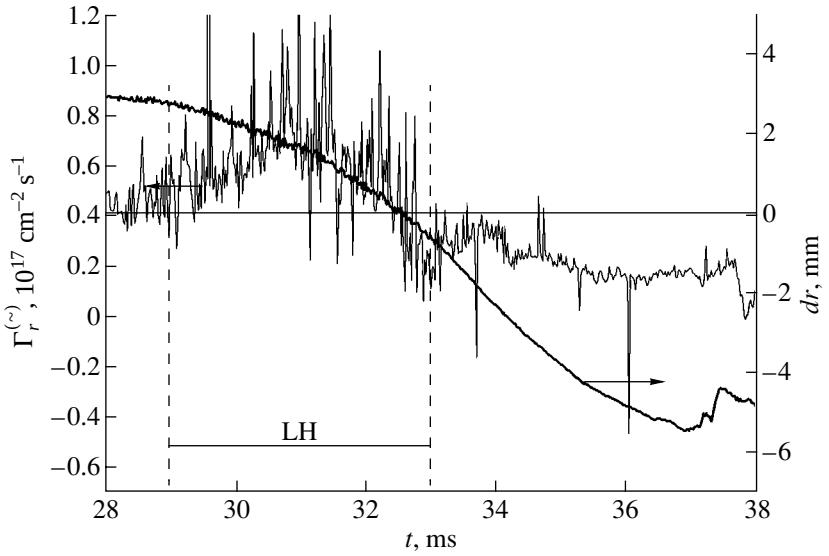

Fig. 10. Integral radial fluctuating drift flux $\Gamma_r^{(\sim)}$ calculated from the results of Langmuir probe measurements near the LCMS and the displacement of the plasma column dr in the course of auxiliary LH heating measured with the help of magnetic probes.

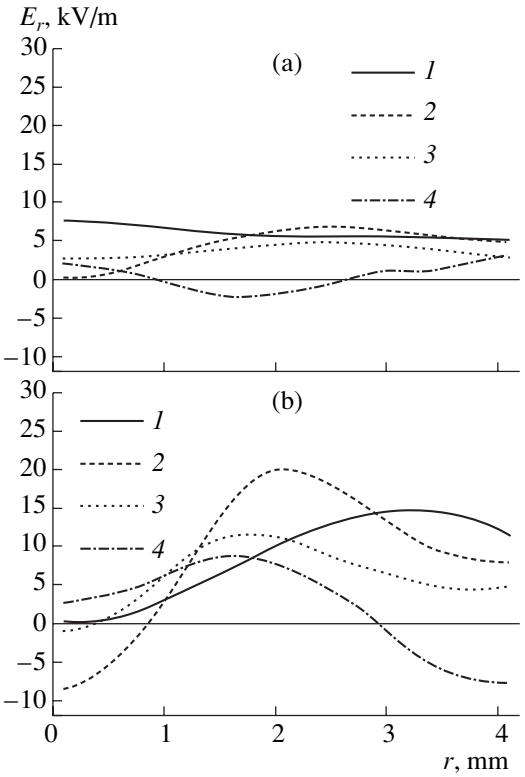

Fig. 11. Profiles of the radial electric field measured with Langmuir probes in the SOL and near the LCMS (r = 75–80 mm) (a) during the OH phase and (b) at the end of the RF pulse for different poloidal angles of the outer perimeter of the torus: θ = (*1*) 0°, (*2*) 10°, (*3*) 20°, and (*4*) –10°. The angle θ is counted from the equatorial plane in the counter-clockwise direction. The radial coordinate is counted from the limiter edge (r = 77 mm) toward the chamber wall.

$\omega_{\mathbf{E}\times\mathbf{B}}$ increase both at the axis and at the periphery of the discharge already during the first milliseconds of the RF pulse. During off-axis heating, both the radial field and the shear increase mainly at the periphery. In [16], it was shown that microscale oscillations are strongly suppressed when $\omega_{\mathbf{E}\times\mathbf{B}}$ is on the order of 10^5 s^{-1}. In view of the condition $\omega_{\mathbf{E}\times\mathbf{B}} > \gamma_{\text{lin}}^{\max}$ (where $\gamma_{\text{lin}}^{\max}$ is the maximum linear growth rate of the dominant instability; $\gamma_{\text{lin}}^{\max} \sim 10^5$ s^{-1} [5, 10]), we consider the increase in the shear of the radial electric field (or the poloidal rotation velocity) to be the main mechanism for suppressing anomalous heat transport in the plasma column.

The possibility of suppressing transport via the above mechanism during strong central ion heating was demonstrated with the help of a BATRAK self-consistent transport code [17]. In this code (unlike conventional codes), the transport coefficients are functions of the shear of the poloidal $\mathbf{E}\times\mathbf{B}$ drift. In our experiments, according to expressions (1) and (2), additional central ion heating leads to a substantial increase in $|E_r|$. The shear $\omega_{\mathbf{E}\times\mathbf{B}}$ at the axis increases and becomes higher than the critical value, and the transport coefficients drop sharply. This results in an increase in the electron temperature and density, which agrees with the experiment (Figs. 1, 2). Apparently, a similar process also occurs at the periphery of the discharge. Here, a sharp increase in $\omega_{\mathbf{E}\times\mathbf{B}}$ is also caused by the growth of ΔT_i and Δn during auxiliary LH heating.

4. OBSERVATION OF THE SUPPRESSION OF MICROSCALE TURBULENCE

At present, we do not have direct evidence of the suppression of microscale turbulence in the central region of the plasma column. However, at the periphery of the discharge (r = 6–8 cm), the suppression of microscale plasma oscillations in the frequency band 10–500 kHz was observed during LH heating and during the transition to the improved confinement mode. These data were obtained with an enhanced-scattering diagnostics and reflectometry [18, 19] and are related to the region of the plasma column where the shear of the poloidal drift velocity $\omega_{\mathbf{E}\times\mathbf{B}}$ increases and a transport barrier is formed in both of the LH heating modes under consideration. Microscale oscillations are suppressed most strongly in the post-heating phase, after the RF pulse is switched off. This phase is characterized by a sharp decrease in the intensity of H_β emission. In some cases, bursts of ELM-activity were observed [19]. These and other data indicate that an external transport barrier (ETB) is formed in the post-heating phase.

Characteristic variations in the density, temperature, radial electric field, and fluctuating fluxes near the last closed magnetic surface (LCMS) were observed with the help of multielectrode Langmuir probes [20, 21]. Measurements were carried out using three movable five-electrode Langmuir probes located in the same cross section of the chamber. With these probes, it was possible to obtain data on the plasma parameters in the scrape-off layer (SOL) of an annular poloidal limiter. This diagnostics allowed us to trace the time evolution of the local values of the electron temperature, density, and plasma potential; to measure the fluctuations of these parameters in the frequency band up to 500 kHz; and to determine the local densities of quasi-steady and fluctuating drift fluxes. The local densities of fluctuating drift fluxes were measured with a step of 20°–30° in the poloidal angle and a step of 1 mm in the minor radius r. Based on these measurements, we calculated the integral radial flux $\Gamma_{fl}(t) = \frac{c}{B^2}[\langle n^{(\sim)}(t)\mathbf{E}^{(\sim)}(t)\rangle, \mathbf{B}]$ $\Gamma_r^{(\sim)}$ through the surface r = 8 cm (Fig. 10). It is seen in the figure that the transition to the improved confinement mode after switching off auxiliary heating is accompanied by a decrease in this flux by nearly one-half as compared to the OH phase. Diamagnetic measurements confirm a nearly two-fold increase in the energy confinement time after the L–H transition as compared to the initial OH mode [4]. This correlates with the suppression of microscale plasma oscillations and the associated fluctuating fluxes measured at the periphery, in particular, near the LCMS.

In these experiments, we could trace the correlation between the plasma parameters and the radial electric field and its variations in the SOL and LCMS regions. Figure 11 shows the profiles of the radial electric field at the plasma edge, under the shadow of the limiter (r =

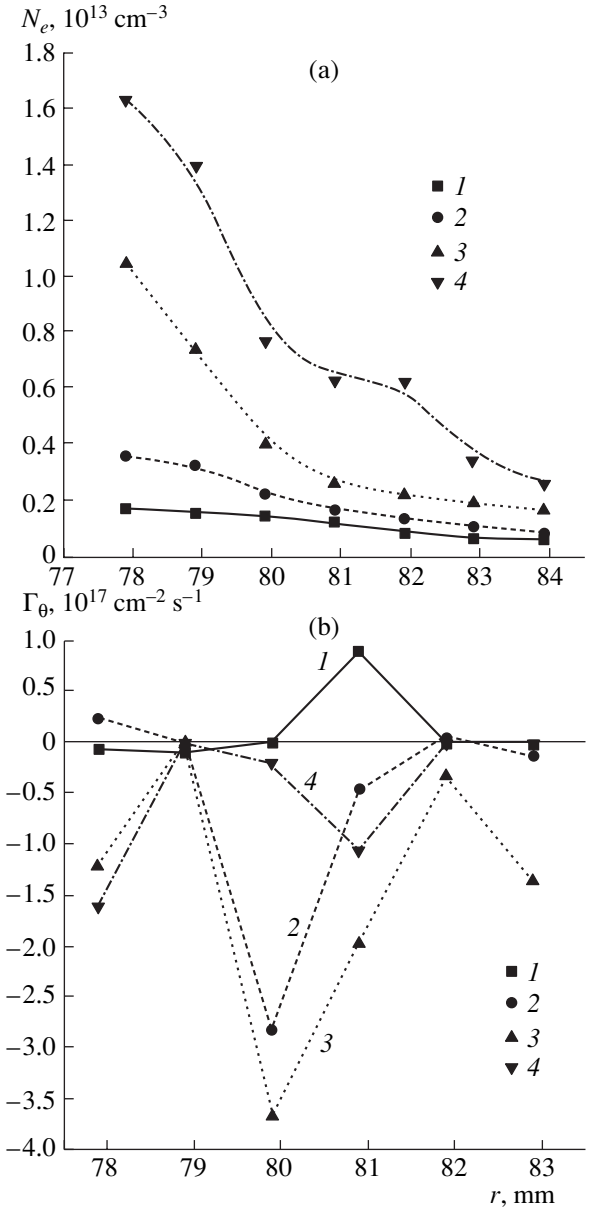

Fig. 12. Density profiles measured with Langmuir probes in the SOL and near the LCMS (r = 77–80 mm) for the poloidal angle of θ = 30° of the outer perimeter of the torus at (*1*) 28, (*2*) 34, (*3*) 36, and (*4*) 38 ms and (b) the poloidal particle flux at (*1*) 30, (*2*) 34, (*3*) 36, and (*4*) 38 ms for P_{RF} (32–36 ms) = 100 kW.

75–80 mm) for different poloidal angles of the outer perimeter of the torus. The value of E_r was deduced from probe measurements of the plasma floating potential with allowance for the local gradient of T_e [21]. The measurement accuracy was 15–20%. The transition to an ETB is accompanied by the appearance of a pronounced inhomogeneity of E_r (with respect to both the poloidal angle and the radius). The inhomogeneity of E_r leads to the stochastic behavior of the drift particle fluxes and the formation of a transport barrier. It is

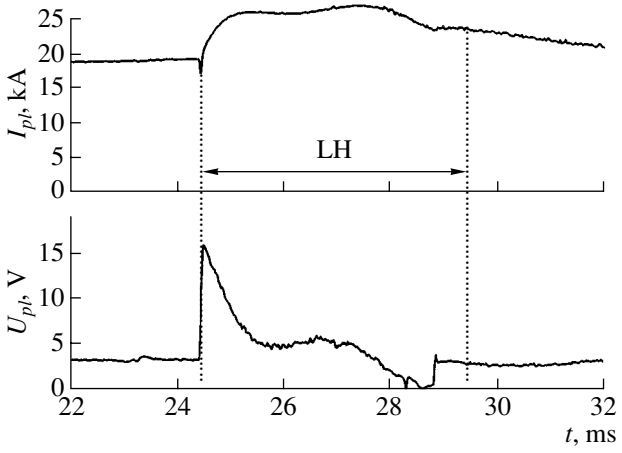

Fig. 13. Plasma current I_{pl} and the loop voltage U_{pl} in the experiment with LH heating and an additional rapid increase in the plasma current.

interesting to note that the decrease in the radial turbulent transport in the post-heating phase is accompanied by an increase in the poloidal component of the fluctuating particle flux. This is illustrated in Fig. 12, which demonstrates that the sharp increase in the density gradient is accompanied by an increase in the poloidal particle flux near the LCMS. The data are presented for a fixed probe position corresponding to 30° at the outer perimeter of the torus.

5. EXPERIMENTS WITH COMBINED LH HEATING AND A RAPID INCREASE IN THE CURRENT

According to the third scenario, the transition to the improved confinement mode is provided by the combined action of LH heating and a rapid (in 0.5 ms) increase in the plasma current I_{pl} from 22 to 30 kA. Figure 13 shows a typical behavior of I_{pl} and the loop voltage U_{pl} when the LH heating pulse and an additional current are switched on simultaneously. Figures 14 and 15 show the corresponding variations in the profiles of the density and the electron and ion temperatures. We emphasize that pedestals in the density and ion temperature profiles form more rapidly as compared to the first and second scenarios. During such a combined heating, the $T_e(r)$ rapidly (over about 1 ms) grows and becomes peaked. Rapid electron heating is also observed in experiments without LH heating (with only a rapid additional increase in the plasma current) [22]. This is explained by the nonlocal character of the process. We note that, in experiments without LH heating, neither the density nor the ion temperature vary during the current rise.

The values of E_r calculated by formulas (2) and (3) for the OH mode and under the combined LH heating and increase in the plasma current are compared in

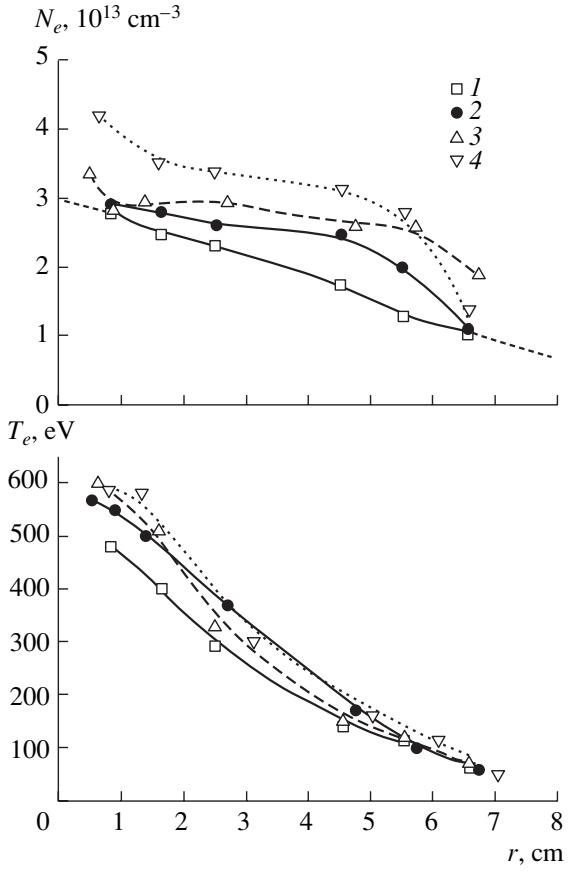

Fig. 14. Density and electron temperature profiles at (*1*) 24, (*2*) 26, (*3*) 28, and (*4*) 30 ms in the experiment with LH heating and an additional rapid increase in the plasma current.

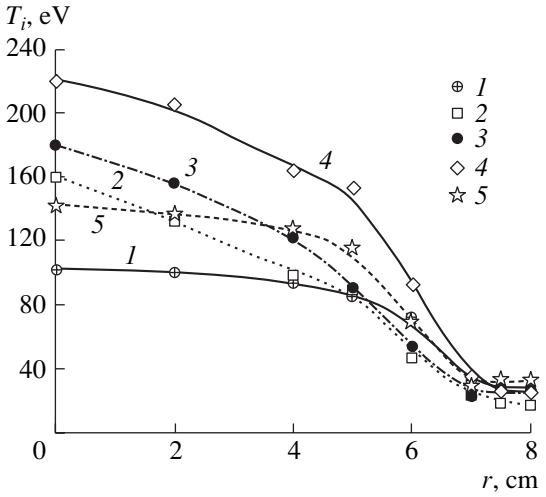

Fig. 15. Ion temperature profiles at (*1*) 31.15, (*2*) 32.2, (*3*) 33.6, (*4*) 37.1, and (*5*) 41.3 ms in the experiment with LH heating and an additional rapid increase in the plasma current. The temperature is determined with the help of a charge-exchange neutral analyzer and from spectroscopic measurements of the HeII line emission; $T_{i,\,\mathrm{opt}}$ stands for the experimental points obtained from spectroscopic measurements at the radii r = 7, 7.5, and 8 cm.

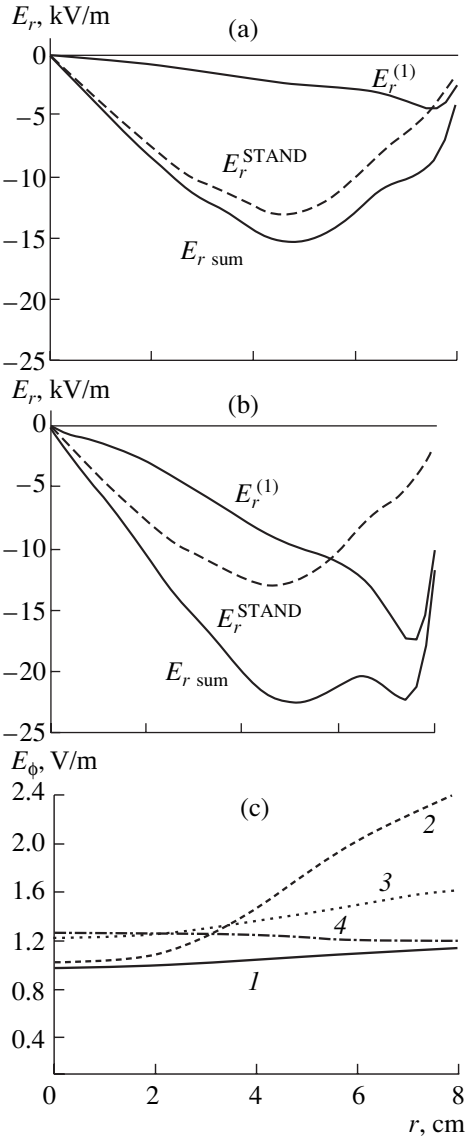

Fig. 16. Calculated values of the radial electric field E_r (a) in the OH mode at t = 24 ms and (b) during the plasma current rise at t = 24.6 ms and (c) the profiles of the toroidal electric field E_ϕ (used to calculate E_r) obtained with the ASTRA code at (*1*) 24, (*2*) 24.5, (*3*) 26, and (*4*) 28 ms.

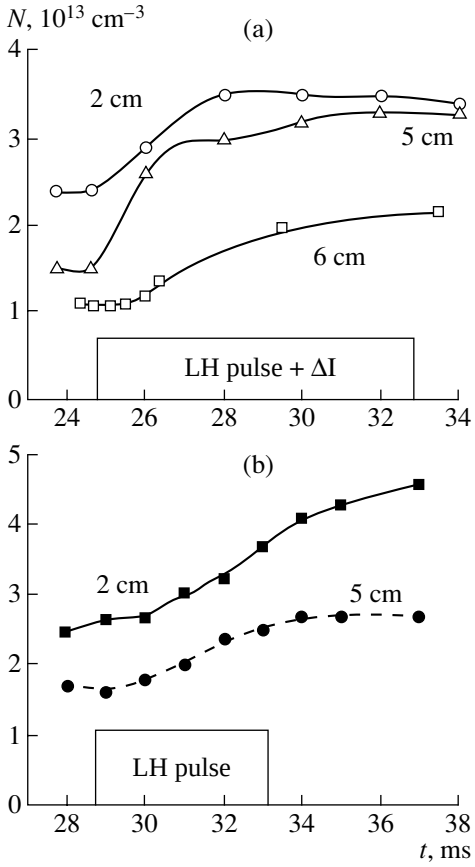

Fig. 17. Time evolution of the plasma density on different magnetic surfaces for (a) the combined LH heating and increase in the plasma current and (b) LH heating only.

Fig. 16. The figure shows the component of E_r related to the density and temperature profiles (E_r^{STAND}) and the component related to the toroidal electric field ($E_r^{(1)}$). It is the increase in E_ϕ during the plasma current rise that leads to a rapid initial growth of E_r and the shear of the poloidal $\mathbf{E}_r \times \mathbf{B}$ rotation velocity. A transport barrier is formed at a radius of 4.5–6 cm immediately after the beginning of the current rise. Figure 17 compares the time evolution of the density at different radii for the first and third scenarios. Furthermore, after the current rise, the poloidal magnetic field diffuses into the plasma column, so that the toroidal electric field decreases at the periphery. However, the radial electric field inside the transport barrier remains large due to the contribution from E_r^{STAND} [15]. High-resolution spectral measurements confirmed these characteristic features of the formation of a transport barrier at the periphery of the plasma column under the combined action of LH heating and a rapid increase in the plasma current [23]. To visualize the processes in the region r = 5–8 cm, we used an additional gas (helium) puffing. In experiments, in addition to the density growth (Fig. 17), we also observed a rapid growth of ΔT_i (r = 6 cm). The change in the poloidal rotation of the HeII ions indicates that E_r is negative and increases substantially in magnitude. This fact can be regarded as direct evidence in favor of the mechanism for the generation of an additional radial electric field.

6. CONCLUSION

The experimental results indicate that efficient LH heating acts to stimulate a transition to an improved confinement mode. The mechanism for improved confinement can be attributed to a change in the radial electric field due to substantial heating of the ion compo-

nent and, as a result, an increase in the shear of the poloidal $\mathbf{E}_r \times \mathbf{B}$ plasma rotation velocity. The radial field E_r is calculated with allowance for the longitudinal electron and ion viscosities. In this case, E_r is determined not only by the value of E_r^{STAND} calculated by the standard neoclassical theory, but also by the longitudinal electric field E_ϕ. Several experimental scenarios are analyzed. In the first scenario (on-axis ion heating), $T_i(0)$ increases from 100 to 300 eV; in the second scenario (off-axis ion heating), $T_i(0)$ increases from 100 to 200 eV and the ion profile is broader; and, in the third experimental scenario, a transition to the improved confinement mode occurs under the combined action of LH heating and a rapid increase in the plasma current.

In the first two scenarios, a transition to the improved confinement mode in the course of LH heating occurs spontaneously. The electron heating from 400 to 900 eV in the first scenario is explained by the fact that anomalous heat transport is substantially suppressed in the central region of the plasma column. During both on-axis and off-axis heating, an internal transport barrier for the density and ion temperature is formed at $r = 4.5$–6 cm. In the post-heating phase, an L–H transition occurs and an additional external transport barrier is formed.

In the third experimental scenario, a transition to the improved confinement mode occurs under the combined action of LH heating and a rapid (in 0.5 ms) increase in the plasma current from 22 to 30 kA. It is the increase in E_ϕ during the plasma current rise that leads to the fast initial growth of E_r. A transport barrier at a radius of 4.5–6 cm is formed almost immediately after the beginning of the current rise. In this case, a key factor is the increase in both the radial electric field and the shear of the $\mathbf{E}_r \times \mathbf{B}$ poloidal rotation velocity. New experimental data confirming the proposed mechanism for the generation of an additional radial electric field E_r have been obtained.

The model describing the suppression of heat transport implies that the condition $\omega_{\mathbf{E}\times\mathbf{B}} > \gamma_{\mathrm{lin}}^{\max}$ is satisfied, where the maximum linear instability growth rate is assumed to be $\gamma_{\mathrm{lin}}^{\max} \sim 10^5\ \mathrm{s}^{-1}$. This value of $\gamma_{\mathrm{lin}}^{\max}$ is consistent with the estimates for the growth rate of the ion gradient mode [24]. In the present paper, we did not analyze the type of dominant microscale oscillation mode that is responsible for anomalous heat transport. This problem is the subject of our further studies.

ACKNOWLEDGMENTS

This study was supported in part by the Russian Foundation for Basic Research (project nos. 98-02-18346, 00-02-16927, and 00-15-96762) and by the Ministry of Education of the Russian Federation (grant no. TOO-7.4-2797).

REFERENCES

1. V. N. Budnikov and M. A. Irzak, Plasma Phys. Controlled Fusion **38**, A135 (1996).
2. S. I. Lashkul, V. N. Budnikov, V. V. Dyachenko, *et al.*, in *Proceedings of the 2nd EPS Conference on RF Heating and CD in Fusion Devices, Brussels, 1998*, p. 165.
3. S. P. Hirshman and D. J. Sigmar, Nucl. Fusion **21**, 1079 (1981).
4. V. N. Budnikov, V. V. D'yachenko, L. A. Esipov, *et al.*, Pis'ma Zh. Éksp. Teor. Fiz. **59**, 651 (1994) [JETP Lett. **59**, 685 (1994)].
5. Y. Kamada, Plasma Phys. Controlled Fusion **42**, A65 (1999).
6. E. J. Synakowsky, Plasma Phys. Controlled Fusion **40**, 581 (1998).
7. T. Stringer, Nucl. Fusion **33**, 1249 (1993).
8. M. Yu. Kantor and D. V. Kuprienko, Rev. Sci. Instrum. **70**, 780 (1999).
9. S. I. Lashkul, V. N. Budnikov, V. V. Dyachenko, *et al.*, in *Proceedings of the 26th EPS Conference on Controlled Fusion and Plasma Physics, Maastricht, 1999*, p. 1729.
10. R. E. Waltz, G. D. Kerbel, and J. Milovich, Phys. Plasmas **1**, 2229 (1994).
11. S. P. Hirshman and D. J. Sigmar, Nucl. Fusion **21**, 1079 (1981).
12. S. I. Lashkul, V. N. Budnikov, V. V. Dyachenko, *et al.*, Plasma Phys. Controlled Fusion **42**, A169 (2000).
13. S. I. Lashkul, V. N. Budnikov, V. V. Bulanin, *et al.*, in *Proceedings of the 2nd EPS Conference on RF Heating and CD in Fusion Devices, Brussels, 1998*, p. 161.
14. V. Rozhansky, Czech. J. Phys. **48** (3), 72 (1998).
15. V. A. Rozhansky, S. P. Voskoboĭnikov, and A. Yu. Popov, Fiz. Plazmy **27**, 219 (2001) [Plasma Phys. Rep. **27**, 205 (2001)].
16. H. Biglari, P. H. Diamond, and P. H. Terry, Phys. Fluids B **2**, 1 (1990).
17. S. P. Voskoboĭnikov, S. I. Lashkul, A. Yu. Popov, and V. A. Rozhansky, Pis'ma Zh. Tekh. Fiz. **26** (19), 39 (2000) [Tech. Phys. Lett. **26**, 867 (2000)].
18. V. N. Budnikov, V. V. D'yachenko, L. A. Esipov, *et al.*, Fiz. Plazmy **21**, 865 (1995) [Plasma Phys. Rep. **21**, 817 (1995)].
19. V. N. Budnikov, V. V. D'yachenko, L. A. Esipov, *et al.*, Pis'ma Zh. Tekh. Fiz. **23** (1), 52 (1997) [Tech. Phys. Lett. **23**, 32 (1997)].
20. E. O. Vekshina, P. R. Goncharov, S. V. Shatalin, *et al.*, Pis'ma Zh. Tekh. Fiz. **26** (19), 52 (2000) [Tech. Phys. Lett. **26**, 873 (2000)].
21. S. V. Shatalin, L. A. Esipov, P. R. Goncharov, *et al.*, in *Proceedings of the 27th EPS Conference on Controlled Fusion and Plasma Physics, Budapest, 2000*, p. 740.
22. V. N. Budnikov, V. V. Bulanin, L. A. Esipov, *et al.*, Fiz. Plazmy **25**, 1053 (1999) [Plasma Phys. Rep. **25**, 969 (1999)].
23. S. I. Lashkul, V. N. Budnikov, A. A. Borevich, *et al.*, in *Proceedings of the 27th EPS Conference on Controlled Fusion and Plasma Physics, Budapest, 2000*, p. 508.
24. K. Lackner, S. Gunter, F. Genko, and R. Wolf, Plasma Phys. Controlled Fusion **42**, B37 (2000).

Translated by N. F. Larionova

Plasma Physics Reports, Vol. 27, No. 12, 2001, pp. 1011–1016. Translated from Fizika Plazmy, Vol. 27, No. 12, 2001, pp. 1070–1075.

STELLARATORS

One Possible Way to Affect the Impurity Influx into the Plasma of a Stellarator with Poloidal Slits in the Vacuum Wall

D. L. Grekov

Kharkov Institute for Physics and Technology, National Science Center, Akademicheskaya ul. 1, Kharkov, 61108 Ukraine
e-mail: grekov@ipp.kharkov.ua

Received March 28, 2001; in final form, July 17, 2001

Abstract—A possible way to affect the influxes of heavy impurities into the plasma of a stellarator with poloidal slits in the vacuum wall (e.g., the W7-AS stellarator) by RF heating of the impurities is discussed. It is shown that the influxes can be reversed in direction by applying a relatively low RF power. The design features of the W7-AS stellarator are such that there is no need to place additional antennas inside the vacuum chamber.

1. INTRODUCTION

The influxes of heavy impurities during discharges in tokamaks and stellarators contaminate the plasma, increase radiation losses, and degrade confinement. Impurity influxes can be avoided by conditioning the discharge chamber and by coating RF antennas and the design elements of the chamber with special materials. The divertor configuration of the confining magnetic field makes it possible to ignite high-density and high-temperature discharges. On the other hand, as early as 1976–1977, Burrell [1] theoretically showed that, by using asymmetric particle sources and/or asymmetric sources for heating the bulk plasma, it is possible to reverse the direction of impurity influxes. For a toroidal plasma column, a proper choice of the source configuration makes it possible to achieve this effect in the edge region, where the particle transport occurs in the strongly collisional regime (the Pfirsch–Schlüter regime). In [2], it was shown that, if the impurity ions are affected by a weak thermal force, then their influxes can be stopped by heating them asymmetrically. In this case, the power required to reverse the direction of impurity influxes turns out to be significantly lower than that expended on heating the bulk ions. In the present paper, a possible way to affect heavy impurity influxes into the discharge plasma by an asymmetric heating of impurity ions is studied using the Wendelstein 7AS (W7-AS) stellarator as an example of a facility with poloidal slits in the vacuum chamber.

2. MODEL FOR THE W7-AS MAGNETIC SYSTEM

The W7-AS stellarator, which was put into operation in the late 1980s at the Max-Planck-Institut für Plasmaphysik (Garching, Germany), is one of the largest stellarators in the world. The "advanced stellarator" (AS) concept implies that the confining magnetic field should be created in such a way as to bring the particle orbits closer to the magnetic surfaces than is possible in a "classical" stellarator [3]. In the W7-AS stellarator, the confining magnetic field has five periods along the torus ($m = 5$) and is created by a periodic system of particularly curved coils. The coordinate dependence of the W7-AS magnetic field can be described by the following model expressions:

$$\begin{aligned}
B_\varphi \approx B &= B_0[1 - \varepsilon_t x\cos\vartheta + \varepsilon_1 x\cos(\vartheta + m\varphi) \\
&+ \varepsilon_1 x\cos(\vartheta - m\varphi) + \varepsilon_{21}x^2\cos(2\vartheta - m\varphi) \\
&+ \varepsilon_{22}x^2\cos(2\vartheta - 2m\varphi) + \varepsilon_{32}x^3\cos(3\vartheta - 2m\varphi) \\
&- \varepsilon_m\cos m\varphi], \\
B_\vartheta \approx B_0\frac{R_0}{ma}&\Big[\varepsilon_1\cos(\vartheta + m\varphi) - \varepsilon_1\cos(\vartheta - m\varphi) \\
&- 2\varepsilon_{21}x\cos(2\vartheta - m\varphi) - \varepsilon_{22}x\cos(2\vartheta - 2m\varphi) \\
&- \frac{3}{2}\varepsilon_{32}x^2\cos(3\vartheta - 2m\varphi)\Big], \\
B_r \approx B_0\frac{R_0}{ma}&\Big[\varepsilon_1\sin(\vartheta + m\varphi) - \varepsilon_1\sin(\vartheta - m\varphi) \\
&- 2\varepsilon_{21}x\sin(2\vartheta - m\varphi) - \varepsilon_{22}x\sin(2\vartheta - 2m\varphi) \\
&- \frac{3}{2}\varepsilon_{32}x^2\sin(3\vartheta - 2m\varphi)\Big].
\end{aligned} \tag{1}$$

Here, B_0 is the toroidal magnetic field at the geometrical axis of the torus; R is the distance from the geometrical axis; r is the radial coordinate in the minor cross

1063-780X/01/2712-1011$21.00

section of the torus; a is the average minor radius of the vacuum chamber; ϑ and φ are the poloidal and toroidal angles of the quasitoroidal coordinate system, respectively; m is the number of magnetic field periods along the torus; $\varepsilon_t = a/R \ll 1$; ε_b, ε_m, ε_{21}, ε_{22}, and ε_{32} are constants; $\varepsilon_1 = \varepsilon_b\varepsilon_t/2$; and $x = r/a$. In further calculations, we assume $\varepsilon_b = 1.2$, $\varepsilon_t = 0.2$, $\varepsilon_{21} = -0.04$, $\varepsilon_m = 0.05$, $\varepsilon_{22} = 0.12$, and $\varepsilon_{32} = -0.04$. This model harmonic content of the magnetic field reflects the main features of the spatial behavior of the magnetic field strength and magnetic surfaces. With allowance for the relationships $\varepsilon_\alpha = \varepsilon_t, \varepsilon_{21}, \varepsilon_m, \varepsilon_{22}, \varepsilon_{32} \ll 1$, the magnetic flux function $\Psi(x, \vartheta, \varphi)$ was obtained from the equation $\mathbf{B}\cdot\nabla\Psi = 0$ to first order in ε_α:

$$\Psi(x,\vartheta,\varphi) = \frac{x^2}{2} + \left(\frac{R_0}{ma}\right)^2\Big[\varepsilon_1 x\cos(\vartheta + m\varphi) + \varepsilon_1 x\cos(\vartheta - m\varphi) + 2\varepsilon_{21}x^2\cos(2\vartheta - m\varphi) + \frac{1}{2}\varepsilon_{22}x^2\cos(2\vartheta - 2m\varphi) + \frac{3}{4}\varepsilon_{32}x^3\cos(3\vartheta - 2m\varphi)\Big]. \quad (2)$$

3. HEAVY IMPURITY INFLUX IN W7-AS IN THE PRESENCE OF HEAT SOURCES

At the periphery of the plasma column in W7-AS, the following two conditions are satisfied: $\lambda_I \ll L$ and $\lambda_i \leq L$, where λ_I and λ_i are the mean free paths of impurity and bulk ions, respectively; $L = \pi R/\iota$ is the connection length; and ι is the rotational transform. Consequently, the particle transport occurs in the strongly collisional regime (the Pfirsch–Schlüter regime). It is well known (see, e.g., [4]) that, because of the toroidal nonuniformity of the confining magnetic field, the radial transport in tokamaks is enhanced by a factor of $1/\iota^2$ above the classical transport. In such a field, oppositely charged particles drift in opposite directions, thereby giving rise to a poloidal electric field at the magnetic surfaces. If there were no friction, this poloidal electric field, which has a nonzero component along the magnetic field lines, would be short-circuited by the particles moving along these lines. Because of collisions, the poloidal electric field remains nonzero. Averaging the radial particle drift in crossed fields (a poloidal electric field and a toroidal magnetic field) over the magnetic surface leads to the familiar expressions for the radial particle fluxes. Rutherford [5] showed that, in a system consisting of ions and heavy impurities, diffusion can be described in essentially the same way as in an electron–ion system. This approach yields the following expression for the radial flux Γ_I of impurity ions in the Pfirsch–Schlüter regime in a tokamak [1, 5]:

$$\Gamma_I = -\Gamma_i/Z_I = \frac{n_i q^2 \rho_i^2}{Z_I\tau_{iI}T_I} \times\left[\left(C_1 + \frac{C_2^2}{C_3}\right)\left(\frac{1}{n_i}\frac{\partial p_i}{\partial r} - \frac{1}{Z_I n_I}\frac{\partial p_I}{\partial r}\right) - \frac{5C_2}{2C_3}\frac{\partial T_i}{\partial r}\right]. \quad (3)$$

Here, $q = rB_t/RB_p = 1/\iota$, B_t and B_p are the toroidal and poloidal components of the tokamak magnetic field; ρ_i is the Larmor radius of the bulk ions; p_α, n_α, $Z_\alpha e$, m_α, and T_α are, respectively, the pressure, density, charge, mass, and temperature of the ions of species α ($\alpha = i, I$); τ_{iI} is the scattering time of the bulk ions by the impurity ions; and C_k are constants. From expression (3), we can see that the term $\frac{1}{n_i}\frac{\partial p_i}{\partial r}$ is responsible for the fact that the impurity flux Γ_I is directed toward the plasma center.

For stellarators, the impurity ion flux should be calculated for the magnetic field, which is more complicated in structure than the tokamak field. Thus, the expression for Γ_I should be supplemented with the terms that account for the helical nonuniformity of the confining magnetic field [6]. However, these terms are, as a rule, small in comparison to those in expression (3).

Now, we assume that, in the plasma, there is a heat source that affects the impurity ions and has the components

$$Q_I = Q_I^t\sin\vartheta + Q_I^\pm\sin(\vartheta \pm m\varphi) + Q_I^{21}\sin(2\vartheta - m\varphi) + Q_I^{22}\sin(2\vartheta - 2m\varphi) + Q_I^{32}\sin(3\vartheta - 2m\varphi). \quad (4)$$

Note that the remaining components of the Fourier series expansion of the function $Q_I(r, \vartheta, \varphi)$ in angular variables do not contribute to the radial impurity flux, provided that the magnetic field is chosen in the form (1). The heat source acts to change the heat impurity flux $\mathbf{q}_{I\|}$ along the magnetic field lines in accordance with the equation $\nabla\cdot(\mathbf{q}_{I\|} + \mathbf{q}_{I\wedge}) = Q_I$, where $\mathbf{q}_{I\wedge} = \frac{5}{2}\frac{n_I T_I}{Z_I e B^2}\mathbf{B}\times\nabla T_I$ is an oblique heat flux. Setting $\mathbf{q}_{I\|} = \mathbf{B}L_I$ yields the following equation for L_I:

$$\frac{1}{R_0}\frac{\partial L_I}{\partial\varphi} \approx \frac{Q_I}{B_0} + \frac{5p_I}{Z_I e B_0^3}\frac{\partial\Psi}{\partial r}\frac{1}{r}\frac{\partial B}{\partial\vartheta}.$$

We integrate this equation along the magnetic field line $\vartheta_0 = \vartheta - \iota\varphi$ to obtain

$$L_I = \frac{R_0}{B_0}\Big[\frac{-1}{\iota}Q_I^t\cos\vartheta - \frac{Q_I^\pm}{\iota \pm m}\cos(\vartheta \pm m\varphi) - \frac{Q_I^{21}}{2\iota - m}\cos(2\vartheta - m\varphi) - \frac{Q_I^{22}}{2\iota - 2m}\cos(2\vartheta - 2m\varphi)$$

$$-\frac{Q_I^{32}}{3\iota-2m}\cos(3\vartheta-2m\varphi)\Big]$$
$$+\frac{5p_IR_0}{Z_IeB_0^2a^2}\frac{\partial T_I}{\partial\Psi}\Big[-\frac{\varepsilon_t}{\iota}\cos\vartheta \tag{5}$$
$$+\frac{\varepsilon_1}{\iota\pm m}\cos(\vartheta\pm m\varphi)+\frac{2\varepsilon_{21}x}{2\iota-m}\cos(2\vartheta-m\varphi)$$
$$+\frac{\varepsilon_{22}x}{\iota-m}\cos(2\vartheta-2m\varphi)+\frac{3\varepsilon_{32}x^2}{3\iota-2m}\cos(3\vartheta-2m\varphi)\Big].$$

Since $\mathbf{q}_{\|I}=-C_3'\frac{n_IT_I}{m_I}\frac{\tau_{II}\tau_{Ii}}{\tau_{II}+\tau_{Ii}}\nabla_\|T_I$, the heat source contributes additively to the temperature gradient of the impurities along the magnetic field lines. In turn, the change in the temperature gradient causes a change in the thermal force $\mathbf{R}_{I\|}^T=-C_2'n_I\frac{\tau_{II}}{\tau_{Ii}+\tau_{II}}\nabla_\|T_I$ acting on impurity ions and, as a consequence, a change in the electric field that gives rise to the radial impurity flux. The MHD equation for impurity ions has the form [5]

$$\nabla p_I = n_IZ_Ie(\mathbf{E}+\mathbf{v}_I\times\mathbf{B})+\mathbf{R}_I, \tag{6}$$

where $\mathbf{v}_I$ is the velocity of impurity ions and $\mathbf{R}_I$ is the frictional force experienced by them. Taking the scalar product of Eq. (6) with $\mathbf{B}$ gives $\mathbf{B}\cdot\mathbf{E}=-\mathbf{B}\cdot\mathbf{R}_I/Z_Ien_I$. Then, we take into account the potential character of the electric field ($\mathbf{E}=-\nabla\phi$) in order to determine how the thermal force acting on impurity ions contributes to the field: $\mathbf{B}\cdot\nabla\phi^T=-\frac{C_2'}{C_3'}\frac{4}{3\sqrt{\pi}}\frac{m_in_i}{\tau_{iI}}\frac{B_0^2}{Z_Ien_I^2T_I}L_I$. In what follows, we will be interested only in the contribution ϕ_Q^T of the heat sources to the electric field:

$$\phi_Q^T = \frac{C_2'}{C_3'}\frac{4}{3\sqrt{\pi}}\frac{m_in_i}{\tau_{iI}}\frac{R_0^2}{Z_Ien_I^2T_I}\Big[\frac{Q_I^t}{\iota^2}\sin\vartheta$$
$$+\frac{Q_I^\pm}{(\iota\pm m)^2}\sin(\vartheta\pm m\varphi)+\frac{Q_I^{21}}{(2\iota-m)^2}\sin(2\vartheta-m\varphi)$$
$$+\frac{Q_I^{22}}{(2\iota+2m)^2}\sin(2\vartheta-2m\varphi)$$
$$+\frac{Q_I^{32}}{(3\iota-2m)^2}\sin(3\vartheta-2m\varphi)\Big].$$

We take the vector product of Eq. (6) with $\mathbf{B}$ to obtain the impurity flux across the magnetic surfaces:

$$\Gamma_I = \frac{\mathbf{B}\times\nabla\Psi}{Z_IeB^2|\nabla\Psi|}(Z_Ien_I\mathbf{E}+\mathbf{R}_I).$$

The contribution of the heat sources is equal to $\Gamma_I^T\approx\frac{n_I}{B^2}\frac{B_\varphi\nabla_r\Psi E_\vartheta^T}{|\nabla\Psi|}\approx\frac{n_I}{B}\nabla_\vartheta\phi_I^T$. We average this contribution over the magnetic surface whose shape is determined by the equation $\Psi(x,\vartheta,\varphi)=\text{const}$. As a result, to first order in ε_α, we obtain

$$\Gamma_I^T = \frac{4}{3\sqrt{\pi}}\frac{C_2'}{C_3'}\frac{m_in_i}{\tau_{iI}}\frac{B_tR_0}{B_0^2Z_Ie}\frac{G}{n_IT_I},$$
$$G = \frac{Q_I^\pm}{(\iota\pm m)^2}\frac{\varepsilon_1}{2\varepsilon_t}\Big[1+\frac{1}{\bar{x}}\Big(\frac{R_0}{ma}\Big)^2\Big]$$
$$+\frac{Q_I^{21}}{(2\iota-m)^2}\frac{\varepsilon_{21}\bar{x}}{\varepsilon_t}\Big[1+\frac{2}{\bar{x}}\Big(\frac{R_0}{ma}\Big)^2\Big] \tag{7}$$
$$+\frac{Q_I^{22}}{(2\iota-2m)^2}\frac{\varepsilon_{22}\bar{x}}{\varepsilon_t}\Big[1+\frac{2}{2\bar{x}}\Big(\frac{R_0}{ma}\Big)^2\Big]$$
$$+\frac{Q_I^{32}}{(3\iota-2m)^2}\frac{3\varepsilon_{32}\bar{x}^2}{2\varepsilon_t}\Big(1+\frac{3}{4\bar{x}}\Big(\frac{R_0}{ma}\Big)^2\Big)-\frac{Q_I^t}{\iota^2},$$

where $\bar{x}=\bar{r}/a$ and $\bar{r}$ is the mean radius of the magnetic surface. Consequently, if the magnitudes and signs of the components $B_tQ_I^\pm$, $B_tQ_I^{21}$, $B_tQ_I^{22}$, $B_tQ_I^{32}$, and $B_tQ_I^t$ of the heat source are chosen so that G is positive, then the impurity influx into the plasma can be stopped by compensating for its driving force, i.e., by canceling the term that describes the impurity influx in expression (3).

4. RF SOURCE FOR HEATING IMPURITIES

In this section, we consider how the source for heating impurity ions should be designed in order to have an appropriate content of the poloidal and toroidal harmonics. For this purpose, it is proposed here to heat impurity ions by an RF source. In order that the impurity ions absorb RF energy, we choose the oscillator frequency to be $\omega\approx\omega_{cI}$, where $\omega_{cI}=Z_IeB/m_Ic$ is the cyclotron frequency of the impurity ions. The possibility of launching RF energy into the plasma column should be analyzed by taking into account the fact that the vacuum chamber in the W7-AS stellarator consists of five metal sections connected by dielectric inserts. These poloidal inserts can serve as slit antennas through which RF energy can be launched into the W7-AS plasma [7].

The parameters of the W7-AS stellarator are as follows. The major radius is $R_0=200$ cm, the mean minor radius of the vacuum chamber is $a_c=40$ cm, the mean minor radius of the plasma column is about $a_p\approx20$ cm, and the magnetic field at the chamber axis is $B_0=2.5$ T.

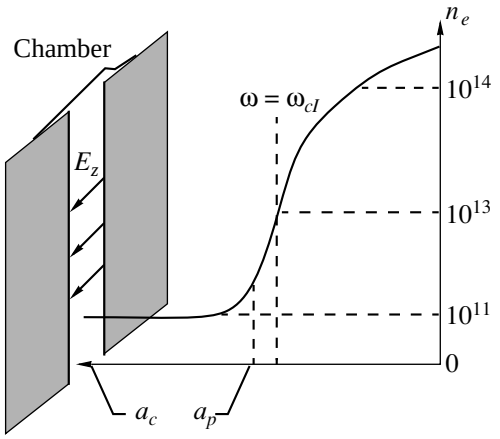

Fig. 1. Plasma density profile $n_e(r)$ and position of the region of cyclotron resonance for impurity ions. The RF field E_z is applied to the ends of the chamber sections that are separated by the poloidal dielectric inserts.

Note that the radial and poloidal components of the W7-AS magnetic field are much weaker (by a factor of about $\sim\varepsilon_\alpha$) than the toroidal component. The mean plasma density is $\bar{n}_i = 10^{14}$ cm^{-3}, the plasma density at the periphery is about $n_i(a_p) \approx 10^{13}$ cm^{-3}, and the ion temperature at the periphery is about $T_i(a_p) \approx 50$ eV [8]. The region between the plasma column and the chamber wall is filled with a cold low-density plasma, $n_i \sim 10^{11}$ cm^{-3} (Fig. 1). In what follows, Ti_{48} atoms are considered to be a heavy impurity, because, at such an edge temperature, they can be stripped of up to eight electrons [9]. Note that, at a temperature of 50 eV, other impurity ions can also be stripped to the ionization states with the appropriate values of Z_I/m_I, specifically, Cr_{52}^{8}, Mn_{55}^{9}, Fe_{56}^{9}, Ni_{59}^{9}, and Cu_{63}^{10} ions [9]. We assume that impurity ions are in a layer with a thickness of about 4 cm at the plasma periphery.

We consider an external RF source connected to the ends of the chamber sections that are separated by the poloidal dielectric inserts. In this case, the waves that are excited most efficiently are those whose component $E_\parallel = \mathbf{E}\cdot\mathbf{B}/B$ (which is nearly purely toroidal) is much larger than the component $E_\perp$ (which is nearly purely poloidal at the plasma boundary). Such waves are usually called "slow" waves. Since the thickness of the insert is $d \ll c/\omega$, the electric field within the slit can be assumed to be potential, $\mathbf{E}(a_c, \vartheta, \varphi) = -\nabla\phi$, in which case the potential difference between the slit ends has the form

$$U = R\int_{-\Phi/2}^{\Phi/2} E_\varphi(a_c, \vartheta, \varphi)\,d\varphi, \qquad (8)$$

where $R\Phi = d$. Taking into account the fact that the electric field at the chamber wall is periodic in the φ direction, we seek a solution to the Maxwell equations for $E_\parallel$ in the form of a series:

$$E_\parallel(r, \vartheta, \varphi) = \sum_{l=0}^{\infty} E_{\parallel l}(r, \vartheta)\cos(l\varphi).$$

We assume that the chamber wall is perfectly conducting, $\sigma \longrightarrow \infty$. In this case, the field $E_\parallel$ at the wall surface is nonzero only at the poloidal inserts. If the amplitude of the RF field and its phase do not differ between the slits, then we have $E_{\parallel l} = 0$ for $l \neq mn$ (where $m = 5$ and n is an integer). Since, for every integer $n \ll 1/(m\Phi)$, $\cos(l\varphi) \approx 1$ holds in the interval $-\Phi/2 < \varphi < \Phi/2$, we obtain

$$E_{\parallel n}(a_c, \vartheta) = 2E_{\parallel 0}(a_c, \vartheta) = \frac{mU}{\pi R}.$$

Note that, by appropriately choosing the amplitudes and phases of the potential difference U across the slits, it is also possible to achieve $E_{\parallel l} \neq 0$ for $l \neq mn$. Since $1/(m\Phi) \gg 1$, the spectrum of the expressed waves is broad.

Far from the Alfvén resonance region ($\varepsilon_1 = N_\parallel^2$), slow waves are described by the dispersion relation

$$D = N_\perp^2 + \frac{\varepsilon_3}{\varepsilon_1}(\varepsilon_1 - N_\parallel^2) = 0. \qquad (9)$$

Here, $\varepsilon_3 \approx 1 - \dfrac{\omega_{pe}^2}{\omega^2}$, $\omega_{p\beta} = (4\pi n_\beta Z_\beta^2 e^2/m_\beta)^{1/2}$ and $\omega_{c\beta} = Z_\beta eB/(m_\beta c)$ are the plasma and cyclotron frequencies of the particles of species β ($\beta = i, I, e$), $\varepsilon_1 = 1 + \sum_\beta \delta\varepsilon_\beta$ outside the regions where $\omega \approx \omega_{c\beta}$, $\delta\varepsilon_\beta = \dfrac{\omega_{p\beta}^2}{\omega_{c\beta}^2 - \omega^2}$, $N_\parallel = \mathbf{N}\cdot\mathbf{B}/B$, $\mathbf{N} = \mathbf{k}c/\omega$, $\mathbf{k}$ is the wave vector, and $N_\perp^2 = N^2 - N_\parallel^2$. Under the condition $\dfrac{N_\parallel^2}{N_\parallel^2 - \varepsilon_1}\dfrac{\delta\varepsilon_I}{\varepsilon_1} \ll 1$, the impurities have little impact on the dispersion of the slow wave. Far from the region of cyclotron resonance for impurity ions, this condition yields a weak restriction $N_\parallel^2 - \varepsilon_1 \sim N_\parallel^2$, provided that $\dfrac{n_I}{n_i} \ll \dfrac{m_i}{m_I}$.

For all $l \neq 0$, the low-density plasma region is transparent to the slow wave because, in this region, we have $\varepsilon_1 \approx 1 + N_A^2 \ll N_\parallel^2$ and $\varepsilon_3 < 0$ and, accordingly, $N_\perp^2 \approx N_r^2 + N_\vartheta^2 > 0$. The group velocity $\mathbf{v}_g = -\dfrac{\partial D}{\partial \mathbf{k}}\Big/\dfrac{\partial D}{\partial \omega}$ of the

wave is directed preferentially along the magnetic field lines:

$$v_{gr} \approx v_{g\perp} = -\sqrt{\frac{m_e}{m_i}}\frac{\omega}{\omega_{ci}}|v_{g\parallel}|.$$

Consequently, in the low-density plasma region, the slow wave propagates mainly along the magnetic field lines $\vartheta = \vartheta_0 + \iota\varphi$, experiencing a slight radial displacement toward the center of the vacuum chamber. In this region, the wave remains long enough to complete several revolutions along the torus before reaching the periphery of the plasma column. Then, the wave propagates in the peripheral layer, which contains impurity ions. When propagating along the magnetic field lines in the edge plasma, the wave passes through zones in which $\omega - \omega_{cI} < \sqrt{2}\,k_\parallel v_{TI}$. In these zones, we have $\delta\varepsilon_I \approx j\sqrt{\frac{\pi}{8}}\frac{\omega_{pI}^2}{\omega k_\parallel v_{TI}}\exp\left[-\left(\frac{\omega-\omega_{cI}}{\sqrt{2}k_\parallel v_{TI}}\right)^2\right]$ (see, e.g., [10]). Under the condition $\frac{n_I}{n_i} \ll \frac{m_i}{m_I}k_\parallel\rho_{LI}$, the impurities have no effect on the wave dispersion. The rate at which the slow wave is damped due to the cyclotron absorption by impurity ions can be determined from Eq. (9) by the perturbation technique, the small parameter being $\mathrm{Im}\delta\varepsilon_I/\varepsilon_1$. We assume that $\mathrm{Im}k_\parallel \ll |k_\parallel|$ and equate the imaginary part of Eq. (9) to zero to obtain $\mathrm{Im}k_\parallel = \frac{1}{4}\sqrt{\frac{\pi}{2}}\frac{n_I}{n_i}\frac{m_I}{m_i}\frac{1}{\rho_{LI}}$. Note that $\mathrm{Im}k_\parallel$ is independent of $N_\parallel$. Nevertheless, the wave damping rate depends on $N_\parallel$, because the wave is damped along the portions of the path where the condition $\omega - \omega_{cI} \le \sqrt{2}\,k_\parallel v_{TI}$ holds. Since the dependence of B on r, ϑ, and φ is rather complicated, the damping rate of the wave along its path can be estimated only numerically. Figure 2 shows how the fraction of RF power that is absorbed by impurity ions along the wave path depends on the poloidal angle at which the wave is launched into the plasma. We can see that, for $l = 5$, the impurities absorb about 80% of the input RF energy and, for $l = 10$, the fraction of the absorbed energy is larger than 90%. Moreover, the power of the waves launched from the inner side of the torus is absorbed most efficiently. As for the other mechanisms for RF energy absorption, note that the collisional damping mechanism can be neglected, because $\nu_{\mathrm{eff}}/\omega \sim 10^{-3}$. On the other hand, since $z_e = \omega/\sqrt{2}\,k_\parallel v_{Te} \approx 20/l = 20/(mn)$, the main mechanism by which the waves with $n \ge 3$ are damped is electron Cherenkov absorption.

In treating the problems related to RF plasma heating, the electrodynamic properties of the exciting antennas are characterized by such quantities as the input conductance (for details about slot antennas, see, e.g., [7]) or the input impedance. In the problem under discussion here, the fundamental questions are as follows:

(i) Is it possible to excite waves in the plasma in such a way that the source for heating impurities has the desired harmonic content?

(ii) What is the power level required to stop the impurity influx into the plasma?

The value of the quantity G required to reverse the direction of the impurity influx can be estimated from expressions (3) and (7). For the above parameters of the W7-AS stellarator and for $n_I/n_i \approx 10^{-5}$, we obtain $G \approx 7.5 \times 10^{-6}$ W/cm^3. Figure 3 shows the dependence of G on the poloidal angle at which RF energy is launched into the plasma. We can see that, in order for the input RF energy to be absorbed most efficiently, the slits should be powered in the following two ranges of poloidal angles: 80°–180° and 290°–340°, in which case the total contribution of all of the wave paths to G is

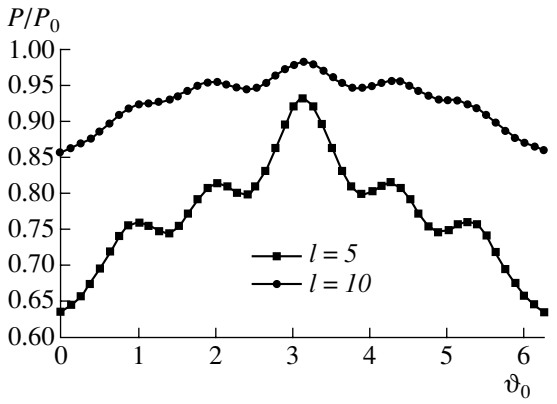

Fig. 2. Dependence of the fraction P/P_0 of the RF power absorbed by impurities on the poloidal angle ϑ_0 at which RF energy is launched into the plasma for toroidal modes with $l = 5$ and 10. Higher toroidal modes are absorbed by the electrons.

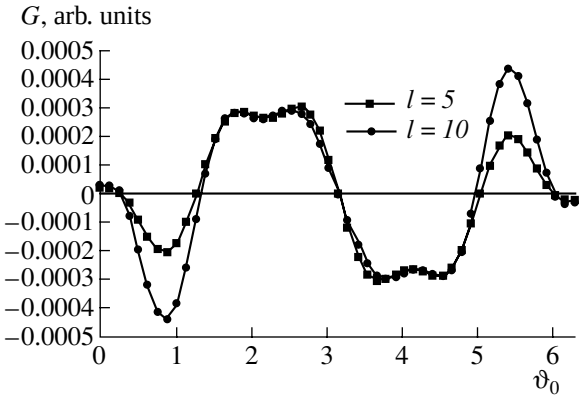

Fig. 3. Dependence of the factor G, determining the efficiency with which RF heating affects the heavy impurity influx, on the poloidal angle ϑ_0 at which RF energy is launched into the plasma for toroidal modes with $l = 5$ and 10.

approximately equal to $\sim 10^{-2}$. We also take into account the fact that, if the slits are used as antennas, they excite a broad toroidal mode number spectrum in which the contribution of the desired modes with $l = 5$ and 10 amounts to about $\sim 10^{-2}$. As a result, the RF energy density in the volume occupied by impurities should be about $\sim 7.5 \times 10^{-2}$ W/cm^3. Integrating the RF energy density over this volume, we find that the required total RF power is about 50 kW.

5. CONCLUSION

In conclusion, note that the results obtained are qualitative rather than quantitative. In order to implement the method proposed here, it is necessary to carry out additional calculations for the actual (rather than model) stellarator magnetic configuration. As a result, the optimum ranges of the poloidal angles for launching RF energy into the plasma may turn out to differ from those calculated using the above model expressions. The estimated RF power level required to reverse the direction of impurity influxes can also be somewhat refined through calculations for a realistic magnetic configuration (the magnetic field and magnetic surfaces), whose harmonic content is far richer than the model one.

Hence, we have shown that the design features of the W7-AS stellarator provide the possibility of reversing the direction of heavy impurity influxes into the plasma by RF heating of impurities, in which case the required RF power level is relatively low. The proposed concept can be implemented without installing special antennas for launching RF energy into the plasma.

ACKNOWLEDGMENTS

I am grateful to K.N. Stepanov for discussing this work and for valuable remarks.

REFERENCES

1. T. K. Burrell, Phys. Fluids **19**, 401 (1976); **20**, 342 (1977).
2. D. L. Grekov, Vestn. Khar'k. Gos. Univ., Ser. Fiz.: Yadra, Chastitsy, Polya, No. 421, 73 (1998).
3. H. Wobig, Z. Naturforsch. A **37**, 906 (1982).
4. B. B. Kadomtsev, *Collective Phenomena in Plasma* (Nauka, Moscow, 1976).
5. P. H. Rutherford, Phys. Fluids **17**, 1782 (1974).
6. A. V. Zolotukhin and A. A. Shishkin, Preprint No. 88-15 (Kharkov Inst. for Physics and Technology, Kharkov, 1988).
7. A. V. Longinov, Zh. Tekh. Fiz. **42**, 1591 (1972) [Sov. Phys. Tech. Phys. **17**, 1273 (1972)].
8. K. McCormick, P. Grigull, J. Baldzuhn, *et al.*, Plasma Phys. Controlled Fusion **41**, B285 (1999).
9. D. E. Post, R. V. Jensen, C. B. Tarter, *et al.*, At. Data Nucl. Data Tables **20**, 397 (1977).
10. *Plasma Electrodynamics*, Ed. by A. I. Akhiezer (Nauka, Moscow, 1974; Pergamon, Oxford, 1975).

Translated by I. A. Kalabalyk

Plasma Physics Reports, Vol. 27, No. 12, 2001, pp. 1017–1020. Translated from Fizika Plazmy, Vol. 27, No. 12, 2001, pp. 1076–1080.

INERTIAL CONFINEMENT FUSION

Fast Ignitor Concept with Light Ions

V. Yu. Bychenkov[1,2], W. Rozmus[2], A. Maksimchuk[3], D. Umstadter[3], and C. E. Capjack[4]

[1]*Lebedev Institute of Physics, Russian Academy of Sciences, Leninskiĭ pr. 53, Moscow, 119991 Russia*

[2]*Theoretical Physics Institute, Department of Physics, University of Alberta, Edmonton T6G 2J1, Alberta, Canada*

[3]*Center for Ultrafast Optical Science, University of Michigan, Ann Arbor, MI 48109-2099, USA*

[4]*Department of Computer and Electrical Engineering, University of Alberta, Edmonton, Alberta, T6G 2J1, Canada*

Received June 25, 2001

Abstract—A short-laser-pulse driven ion flux is examined as a fast ignitor candidate for inertial confinement fusion. Ion ranges in a hot precompressed fuel are studied. The ion energy and the corresponding intensity of a short laser pulse are estimated for the optimum ion range and ion energy density flux. It is shown that a light-ion beam triggered by a few-hundreds-kJ laser at intensities of $\gtrsim 10^{21}$ W/cm^2 is relevant to the fast ignitor scenario. *© 2001 MAIK "Nauka/Interperiodica".*

In the fast ignitor scenario [1], which is a milestone of the concept of inertial confinement fusion (ICF), a relativistic electron beam is considered to be the most suitable source for igniting a hot spot much smaller than the dense compressed DT core. Studies of the feasibility of fast ignition with relativistic electrons are now being carried out at many laboratories [2–5]. In addition, a 15-GeV bismuth ion beam from an external source instead of an electron beam generated directly in the target corona was also examined [6].

Over the past year, there have been several observations of multi-MeV ion beams generated by high-intensity ultrashort laser pulses in the interaction with solid targets [5, 7–9]. In this context, the present paper aims to provide insight into the feasibility of the fast ignition concept with high energy beams of light ions generated in laser–plasma interaction. Apart from the standard studies about the electron fast ignitor concept for ICF, our main concern is to prove that a light-ion beam is capable of igniting a hot spot on a reasonable laser energy scale. In contrast to relativistic electron beams, ions are much less influenced by collective plasma phenomena and have straight-line trajectories. Light ions, similar to electrons, can be generated due to laser–plasma interaction in a target, while a heavy ion beam must be produced by an external driver and transported to the target. Ion transport is not inhibited so much by the self-consistent electric field because the ions accelerated by the charge separation field at a near-critical density are much heavier and propagate inertially inside the target together with the electrons as a charge-compensated neutral beam. Below, the optimum parameters of an ion beam and laser pulse that are suitable for an ignition spark in a hot precompressed DT fuel are estimated as a rough guide.

The mechanism for ion acceleration is charge separation in a plasma due to high-energy electrons driven by the laser inside the target [9] and/or an inductive electric field as a result of the self-generated magnetic field [10]. These electrons can be accelerated up to multi-MeV energies due to several processes, such as stimulated Raman scattering [11], resonant absorption [12], laser wakefield [13], ponderomotive acceleration by standing [14] and propagating [15] laser pulses, "vacuum heating" due to the $\mathbf{V} \times \mathbf{B}$ Lorentz force [16] or Brunel effect [17], and betatron resonance provided by laser pulse channeling [18].

It is unlikely that the ponderomotive mechanism [14] at laser intensities higher than 10^{18} W/cm^2 can produce ions with the observed energies (see [9]). The maximum proton energy in experiments with foils at a high-contrast intensity ratio was explained by acceleration in the charge-separation field arising due to "vacuum heating" [9]. However, for the fast ignitor scheme, this mechanism is inapplicable because of the extended plasma corona at the front of the dense target. Recent experiments carried out at the Center for Ultrafast Optical Science [19] demonstrated a significant increase in the ion energy (as compared to [9]) if the laser intensity contrast ratio decreases. Thus, one may identify a preformed plasma as a source of enhanced electron generation and, hence, enhanced electrostatic field that efficiently accelerates the ions. We believe that the Raman scattering mechanism for electron forward acceleration [11] together with the laser channeling effects [18] are the most likely processes at the corona of an ICF target which produce a strong sheath electrostatic field and are responsible for ion beam generation by short laser pulses at laser intensities of $>10^{18}$ W/cm^2.

Hot electrons, accelerated in an underdense plasma (with a density n_e comparable to the critical density n_c) up to the energy ϵ_e, penetrate into the target at a distance on the order of the Debye length $\lambda_{De} \propto \sqrt{\epsilon_e/n_e}$ and create a strong sheath electrostatic field, which accelerates ions forward. Acceleration gradients of sev-

1063-780X/01/2712-1017$21.00

eral tens of GeV/cm are expected for MeV electrons. As electrons are decelerated, their kinetic energy transforms into the electrostatic field energy and the electric potential should be expected to be at the level of the hot electron energy ϵ_e. Correspondingly, the magnitude of the electric potential determines the ion energy $\epsilon \sim Ze\phi \sim Z\epsilon_e$, where e and Ze are the electron and ion charges. Most of the measurements suggest that protons and deuterons are the major species of laser triggered particle emission, although heavy ions have recently been identified [20]. Their energy is proportional the charge number Z, which is consistent with the electrostatic process of ion acceleration. Clearly, an evaluation of the feasibility of fast ignition with energetic ions must be based on the conversion efficiency of the laser light into ion beam energy and scaling of the beam parameters versus laser characteristics. A systematic investigation of both of these issues has only begun. However, the data on the ~6% conversion efficiency into ions of several MeV energy [8] and the square root dependence of the proton energy on the laser intensity inferred from the latest experiments are very promising.

The general approach to fast ignition involves a powerful external unspecified source and aims to define the ignition parameters for a beam and a core. The first study of fast ignitor parameters was presented by Tabak *et al.* [1]. As was pointed out in [21], the original fast ignitor concept [1] dealt with a nearly isobaric fuel configuration and underestimated the energy required for ignition, which is more relevant to a nearly isochoric process and is somewhat larger than first proposed. The results of [21] roughly agree with those presented in [6] and predict a larger ignition energy than that given by the analytical model of Piriz and Sanchez [22]. According to [21], the optimum particle range is $R = 0.6$ g/cm^2, while the model [22] predicts $R = 0.25$ g/cm^2. Regardless of the differences between [21] and [22], we consider a wide enough domain of the particle ranges to include both of these estimations.

Similar to [23], where the physics of the electron fast ignitor was discussed, our key issue includes an estimation of the ion penetration depth into the dense compressed DT core with a density of ~300 g/cm^3 and temperature of ~10 keV. For ions with energies higher than one-hundred keV, the penetration depth is determined by their collisions with electrons; i.e., fast ions heat electrons of the core and lose energy in accordance with the equation [24]

$$-\frac{d\epsilon}{dx} = \frac{2\pi e^4 Z^2 n_e}{uT_e}\Lambda F(u), \qquad F(u) = \psi(u) - (m_e/m_i)\psi'(u), \tag{1}$$

where ϵ is the ion energy, T_e is the electron temperature, $m_{e(i)}$ is the mass of an electron (ion), Λ is the Coulomb logarithm, $u = m_e\epsilon/m_iT_e$, and

$$\psi(u) = \frac{2}{\sqrt{\pi}}\int_0^u dt\sqrt{t}e^{-t}. \tag{2}$$

The Coulomb logarithm in Eq. (1),

$$\Lambda \simeq 33 - \ln[Z\sqrt{n_e(1 + ZT_e/\epsilon)}/T_e^{3/2}(1 + u)],$$

where the electron density and temperature are in cm^{-3} and keV, respectively, depends only slightly on the ion energy for the parameters of particular interest ($Zm_e/m_i \lesssim u \lesssim 1$) and typically is 6–8.

We define the ion range R (in g/cm^2) as where a particle loses its energy up to the double thermal plasma energy ($3T_e$):

$$R = 0.06\frac{AT_e^2}{Z^2}\int_{u_0}^u \frac{udu}{\Lambda F}, \qquad \Lambda = \frac{1}{2}\left[13 - \ln\left(\frac{\rho(Z^2 + 5.5\times 10^{-4}Z^3/Au)}{(1+u)^2T_e^3}\right)\right], \tag{3}$$

where A is the atomic number of a projectile and $u_0 = 3m_e/m_i$. In Eq. (3) and below, ϵ is in MeV, T_e is in keV, ρ is in g/cm^3, and R is in g/cm^2. For moderately energetic ions ($0.01ZT_e \ll \epsilon \ll AT_e$), one can estimate range (3) and present R in a simple form

$$R = \frac{0.08}{\Lambda Z^2}\sqrt{AT_e^3\epsilon}, \tag{4}$$

where $\Lambda \simeq 6.5 - \ln(Z\sqrt{\rho}/T_e^{3/2})$. In Fig. 1, range (3) for H, D, and Be ions is shown versus the energy ϵ in a core with the temperature $T_e = 5$, 10, and 15 keV and density $\rho = 300$ g/cm^3. The domain between the dashed lines in Fig. 1 corresponds to the region $0.15 < R < 1.2$ g/cm^2, where, according to [21], the ignition parameters were found to depend very little on R. We assume below that this domain of parameters is required for the ignition of a hot spot. Note that Eq. (4) qualitatively describes the dependence of the particle range on the ion energy and plasma parameters and, for the examples given in Fig. 1, estimates R with an accuracy of ~50%, somewhat underestimating the particle range. Figure 1 shows that a significantly higher energy is required for Be ions as compared to protons and deuterons.

In accordance with [21, 22], the minimum intensity of the pulse of fast particles I_p required for ignition is slightly less than 10^{20} W/cm^2. We accept as a rough guide I_p as given in [21] ($I_p \simeq 6.5\times 10^{19}$ W/cm^2) to examine whether the required ion energy is consistent with the ignition window for R shown in Fig. 1. We estimate the typical ion density n_i from the quasineutrality condition $n_i \approx n_e/Z$, choosing a hot electron density n_e equal to approximately the quarter critical value $n_c/4$,

typical of the Raman instability, which efficiently accelerates electrons in the forward direction. The critical density reads as $n_c \simeq 0.85 \times 10^{21} \lambda^{-1} \sqrt{I/10^{18}}$ cm^{-3}, where the laser wavelength λ and intensity I are in μm and W/cm^2, respectively, and the plasma relativistic transparency is taken into account.

Apparently, no theory exists that describes the ion energy dependence on the laser intensity. However, some recent experiments [8, 9, 20] have shed light on this issue. Figure 2 shows that, at the intensities $5 \times 10^{18} \le I \le 3 \times 10^{20}$ W/cm^2 of 1-μm laser light, the maximum proton energy ϵ_{max} is well approximated by a square root dependence $\epsilon_{max} \simeq 3.6\sqrt{I/10^{18}}$ MeV. However, the more relevant average energy of protons in the beam is several times smaller. We estimate it as $\epsilon_{max}/7$ in accordance with the results of [9], where the effective temperature and maximum energy of the protons was 230 keV and 1.5 MeV, respectively. Such an estimate also agrees with the results of [8]. Therefore, the scaling

$$\epsilon \approx 0.5 Z \lambda \sqrt{I/10^{18}} \text{ MeV} \qquad (5)$$

can be inferred from recent experiments on high energy ion generation. Note that the Z-proportionality in Eq. (5) corresponds to the electrostatic mechanism for ion acceleration. However, Eq. (5) may overestimate the ion energy with a specific charge number Z in a multispecies plasma that contains lighter ions (with charge numbers smaller than Z). Heavier ions have little chance to be significantly accelerated because of their lower mobility. They follow behind the light-ion bunch and, therefore, experience a significantly lower accelerating electric field. Consequently, their energy should be significantly lower than the energy of light ions. This is why high-energy protons were mostly observed in the current experiments.

Using Eq. (5) for the estimation of the ion energy flux $I_i \simeq n_i (2/m_i)^{1/2} \epsilon^{3/2}$, one can obtain

$$I_i \approx 1.7 \times 10^{-2} \left(\frac{I}{10^{18}}\right)^{5/4} \sqrt{\frac{Z\lambda}{A}} \frac{\text{W}}{\text{cm}^2}, \qquad (6)$$

where we assume that ions are nonrelativistic. Equation (6) predicts that a conversion efficiency of laser energy into energetic ions scales with an intensity of $I^{1/4}$ and, for $Z = 1$, $\lambda = 1$ μm, and $I = 3 \times 10^{20}$ W/cm^2, gives 7% for the conversion coefficient, which agrees well with the experiment [8].

From the condition $I_i = I_p$, we obtain the threshold intensity for a 1-μm laser, which is found to be practically the same for proton (1.2×10^{21} W/cm^2), deuteron (1.5×10^{21} W/cm^2), and beryllium (1.6×10^{21} W/cm^2) beams with typical ion energies of 6.8, 7.7, and 32 MeV, respectively. It is likely that the core temperature should be $T_e \gtrsim 10$ keV (rather than $T_e < 10$ keV), which basically excludes deuterons as a possible ignitor

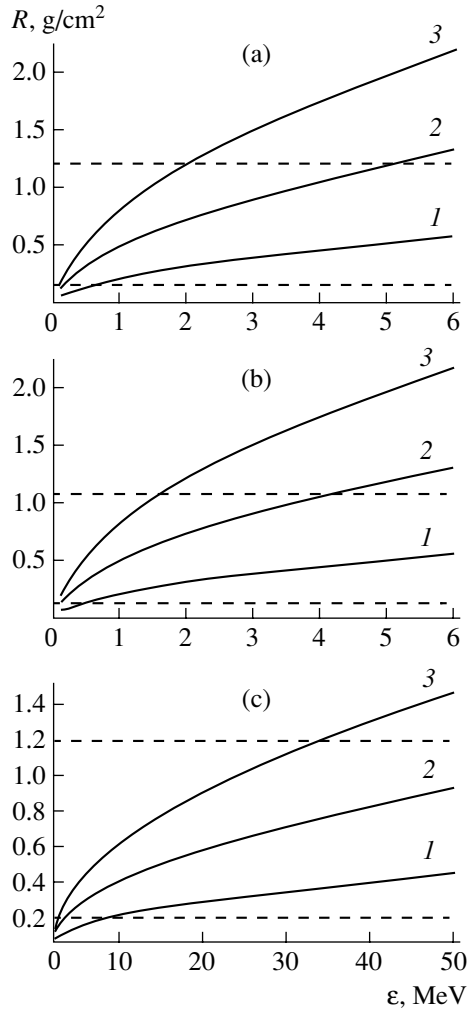

Fig. 1. The $R(\epsilon)$ dependence for (a) H, (b) D, and (c) Be ions for the core temperatures (*1*) 5, (*2*) 10, and (*3*) 15 keV.

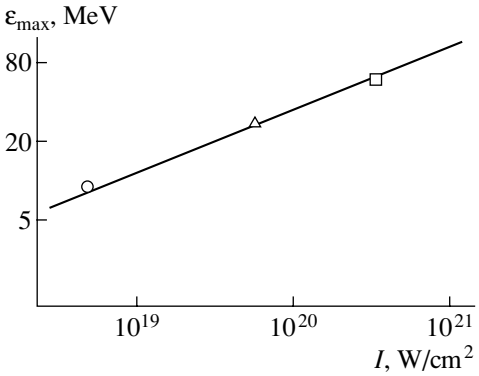

Fig. 2. Maximum proton energy vs. the laser intensity. The square, circle, and triangle mark the results of [8, 9, 20], respectively. The solid line is the fit $\epsilon_{max} \simeq 3.6\sqrt{I/10^{18}}$ MeV, where I is in W/cm^2.

because its range is too long (Fig. 1b) for this temperature. Such a situation is somewhat similar to that with a proton beam. However, it has a chance to be used as an ignitor at the upper boundary of the range ignition window, $R \simeq 1.2$ g/cm^2 (Fig. 1a). The energy $\epsilon \simeq 32$ MeV of a beryllium ion beam for a core temperature of $T_e \sim 10$ keV agrees well with $R \approx 0.6$ g/cm^2, which was interpreted in [21] as the optimum for ignition. We note that deuterons were discarded because of their long range, as compared to $R = 1.2$ g/cm^2 found in [21] as an upper limit for fast ignition. The latter should be reconsidered if a new optimum regime for ignition is found for longer ion ranges. In addition, deuterons with energies of several MeV propagating in a dense DT plasma may participate in thermonuclear reactions. However, our estimates show that all the possible nuclear channels of energy release cannot provide more than several percent of the additional energy, which does not affect our conclusion.

As a final remark, we note that one of the key issues of fast ignition is the self-heating of a hot spot. This cannot be achieved in a hot spot that is too small, so the penetration depth cannot be shorter than the hot-spot diameter and, consequently, the ignition energy should be large enough. However, analytical model [22] and numerical hydrodynamic simulations [21] give different estimates for the hot-spot size. The latter predicted a much higher energy threshold for the triggering of spark ignition, which is $\simeq$17 kJ for the optimum set of parameters. Accepting this more pessimistic estimate, we conclude that ignition with a light-ion beam might be expected at a $\gtrsim$200-kJ laser energy.

In summary, we have examined the feasibility of light-ion triggered spark ignition for ICF using the computation of the ion range in a hot core and recent experimental results on high-energy ion generation in laser–plasma interactions. The estimated requirements for short laser pulses correspond to an intensity of $\gtrsim 10^{21}$ W/cm^2 and energy $\gtrsim$200 kJ. The weak dependence of the required laser intensity on the ion atomic number has been found from a comparison of proton, deuteron, and beryllium ion beams. This may have practical importance, making fast ignition quite insensitive to the ion species.

Originally, this work was prepared for the journal Comments on Plasma Physics and Controlled Fusion, where it was accepted in autumn 2000 for publication in the first issue for 2001. Because of the change of the owner and his wish to stop the publishing of Comments on Plasma Physics and Controlled Fusion, the manuscript was resubmitted for Plasma Physics Reports. At that time, we were aware of the publication of paper [25] devoted to fast ignition with a proton beam.

ACKNOWLEDGMENTS

This work was supported in part by the Russian Foundation for Basic Research (project no. 00-02-16063), the Natural Sciences and Engineering Research Council of Canada, and the National Science Foundation of USA.

REFERENCES

1. M. Tabak, I. Hammer, E. M. Glinsky, *et al.*, Phys. Plasmas **1**, 1626 (1994).
2. M. H. Key, M. D. Cable, T. E. Cowan, *et al.*, Phys. Plasmas **5**, 1966 (1998).
3. T. A. Hall, S. Ellwi, D. Batani, *et al.*, Phys. Rev. Lett. **81**, 1003 (1998).
4. L. Gremillet, F. Amiranoff, S. D. Baton, *et al.*, Phys. Rev. Lett. **83**, 5015 (1999).
5. K. A. Tanaka, R. Kodama, H. Fujita, *et al.*, Phys. Plasmas **7**, 2014 (2000).
6. A. Caruso and V. A. Pais, Nucl. Fusion **36**, 745 (1996); Phys. Lett. A **243**, 319 (1998).
7. E. L. Clark, K. Krushelnick, J. R. Davies, *et al.*, Phys. Rev. Lett. **84**, 670 (2000).
8. S. P. Hatchett, C. G. Brown, T. E. Cowan, *et al.*, Phys. Plasmas **7**, 2076 (2000).
9. A. Maksimchuk, S. Gu, K. Flippo, *et al.*, Phys. Rev. Lett. **84**, 4108 (2000).
10. T. Zh. Esirkepov, Y. Sentoku, K. Mima, *et al.*, Pis'ma Zh. Éksp. Teor. Fiz. **70**, 80 (1999) [JETP Lett. **70**, 82 (1999)].
11. C. D. Decker, W. B. Mori, and T. Katsouleas, Phys. Rev. E **50**, 3338 (1994).
12. S. C. Wilks and W. L. Kruer, IEEE J. Quantum Electron. **33**, 1954 (1997).
13. T. Tajima and J. M. Dawson, Phys. Rev. Lett. **43**, 267 (1979).
14. S. C. Wilks, W. L. Kruer, M. Tabak, and A. B. Langdon, Phys. Rev. Lett. **69**, 1383 (1992).
15. W. Yu, V. Bychenkov, Y. Sentoku, *et al.*, Phys. Rev. Lett. **85**, 570 (2000).
16. W. L. Kruer and K. Estabrook, Phys. Fluids **28**, 430 (1985).
17. F. Brunel, Phys. Rev. Lett. **59**, 52 (1987).
18. A. Pukhov, Z.-M. Sheng, and J. Meyer-ter-Vehn, Phys. Plasmas **6**, 2847 (1999).
19. K. Nemoto, S. Banerjee, K. Flippo, *et al.*, Appl. Phys. Lett. **78**, 595 (2001).
20. K. Krushelnick, E. L. Clark, M. Zepf, *et al.*, Phys. Plasmas **7**, 2055 (2000).
21. S. Atzeni, Jpn. J. Appl. Phys. **34**, 1980 (1995); Phys. Plasmas **6**, 3316 (1999).
22. A. R. Piriz and M. M. Sanchez, Phys. Plasmas **5**, 2721 (1998); **5**, 4373 (1998).
23. C. Deutsch, H. Furukawa, K. Mima, *et al.*, Phys. Rev. Lett. **77**, 2483 (1996).
24. B. A. Trubnikov, in *Reviews of Plasma Physics*, Ed. by M. A. Leontovich (Gosatomizdat, Moscow, 1963; Consultants Bureau, New York, 1963), Vol. 1.
25. M. Roth, T. E. Cowan, M. H. Key, *et al.*, Phys. Rev. Lett. **86**, 436 (2001).

Translated by the authors

Plasma Physics Reports, Vol. 27, No. 12, 2001, pp. 1021–1024. Translated from Fizika Plazmy, Vol. 27, No. 12, 2001, pp. 1081–1084.

NONIDEAL PLASMA

Mechanism for the Disappearance of Spectral Lines in a Nonideal Plasma

V. K. Gryaznov*, O. B. Denisov, M. I. Kulish*, V. B. Mintsev*, N. Yu. Orlov**, and V. E. Fortov****

**Institute of Chemical Physics, Russian Academy of Sciences, Chernogolovka, Moscow oblast, 142432 Russia*

***Institute for High Energy Densities, Associated Institute for High Temperatures, Russian Academy of Sciences, Izhorskaya ul. 13/19, Moscow, 127412 Russia*

Received June 14, 2001; in final form, June 25, 2001

Abstract—The mechanism for the "disappearance" of spectral lines in a nonideal plasma is explained theoretically. A comparison of the calculated results with the experimental data from measurements of the emission spectra from a shocked xenon plasma makes it possible to draw the conclusion that this mechanism is attributed to the Stark broadening of the spectral lines. Quantum-mechanical calculations of the state of an ensemble of plasma atoms and ions were carried out on the basis of the ion plasma model. The parameters of the Stark broadening were calculated using the method developed by N.N. Kalitkin and I.O. Golosnoĭ. © *2001 MAIK "Nauka/Interperiodica".*

1. INTRODUCTION

In recent years, intense investigations of the optical and thermophysical properties of a strongly nonideal plasma have led to substantial progress in this area of research [1]. In experiments aimed at measuring the optical parameters of strongly nonideal plasmas, a number of new physical phenomena were observed [2]. Thus, it was found that some spectral lines are deformed so substantially that, at a sufficiently high plasma density, they may turn out to be practically unresolvable. This phenomenon is the subject of our paper.

Note that recent developments in experimental methods and techniques were accompanied by theoretical studies of the optical properties of a strongly nonideal plasma. An important result of current theoretical work is the elaboration of new analytical and numerical methods aimed at incorporating the Stark effect [3]. Another important result is the construction of a theoretical plasma model known as the ion model [4, 5], in which the full statistical ensemble of plasma atoms and ions is described by the solution to the set of equations for a self-consistent field. This approach provides reliable calculations of the quantum-mechanical parameters of the plasma in a broad range of plasma temperatures and densities, including those of a shocked plasma [6]. In the present paper, we apply the calculation method based on a combination of the ion model and the method for taking the Stark effect into account [3].

Since experiments [2] were carried out at relatively low temperatures (about 3 eV), in which case the multiplet structure of the terms becomes important, we had to apply an approximate approach. Specifically, we calculated the parameters of an ensemble of plasma atoms and ions (in particular, their densities) in the ion model by using the basic wave functions obtained by solving the Schrödinger equations in which the exchange interaction was taken into account only approximately. When solving the Hartree–Fock equations, we took into account the multiplet structure of the terms [7] that determine the parameters of the spectral line studied in experiments. Here, we give only a brief description of the ion model, because it was described in detail in [4–6].

2. ION PLASMA MODEL

We consider an ensemble of interacting plasma atoms and ions in the ground and excited states. As subsystems for Gibbs statistics, we can adopt spherical atomic cells of radius r_0 (with a nucleus of charge Z at the center). The radius of the cell can be defined as

$$r_0 = \left(\frac{3}{4\pi N_A}\right)^{1/3} \frac{1}{a_0}\left(\frac{A}{\rho}\right)^{1/3}, \qquad (1)$$

where A is the atomic weight, ρ [g/cm^3] is the plasma density, $a_0 = 5.292 \times 10^{-9}$ cm is the atomic length unit, and $N_A = 6.02 \times 10^{23}$ is Avogadro's number. Here and below, we use atomic units, in which we denote the temperature by Θ. The subsystems, numbered by j, differ from each other by the sets of occupation numbers of the bound (discrete) electronic states, $\{N_{nl}^j\}$, where n and l are the principal and orbital quantum numbers, respectively. Each subsystem also contains unbound (continuum) electrons. The states of subsystems are regarded as the states of plasma atoms and ions. Using

1063-780X/01/2712-1021$21.00

the density functional method [6] and approximately taking into account the exchange interaction, we arrive at the following equation for the bound electrons:

$$-\frac{1}{2}(R_{nl}^j)'' + \left[-V_j(r) + \frac{l(l+1)}{2r^2}\right]R_{nl}^j(r) = E_{nl}^j R_{nl}^j(r), \quad (2)$$

where the wave functions satisfy the normalization condition

$$\int_0^{r_0} [R_{nl}^j(r)]^2 dr = 1. \quad (3)$$

The boundary conditions required to determine the eigenfunctions $R_{nl}^j(r)$ and the eigenvalues E_{nl}^j of the energy can be imposed as follows:

$$R_{nl}^j(0) = 0, \quad R_{nl}^j(r_0) = 0. \quad (4)$$

The potential $V_j(r)$ has the form

$$V_j(r) = V_1^j(r) + V_2^j(r). \quad (5)$$

Here,

$$V_1^j(r) = \frac{Z}{r} - \frac{4\pi}{r}\int_0^r r_1^2 \rho_j(r_1)dr_1 - 4\pi\int_r^{r_0} r_1\rho_j(r_1), \quad (6)$$

$$V_2^j(r) = \frac{\pi\rho_j(r)}{\Theta}\left\{1 + 6\frac{\rho_j(r)}{\Theta^{3/2}} + \frac{\pi^4}{3}\left[\frac{\rho_j(r)}{\Theta^{3/2}}\right]^2\right\}^{-1/3}, \quad (7)$$

where $V_1^j(r)$ is the Coulomb interaction potential and $V_2^j(r)$ is the potential introduced artificially in order to approximately take into account the exchange interaction. The potential $V_2^j(r)$ can be described by different approximate formulas. For our analysis, we chose the approximate expression (7), which was proposed by Nikiforov and Uvarov [8].

The electron density has the form

$$\rho_j(r) = \rho_1^j(r) + \rho_2^j(r). \quad (8)$$

Here, the density of the bound electrons is equal to

$$\rho_1^j(r) = \frac{1}{4\pi r^2}\sum_{n,l} N_{nl}^j (R_{nl}^j(r))^2, \quad (9)$$

and the density of the unbound electrons is described in the quasiclassical approximation:

$$\rho_2^j(r) = \frac{\sqrt{2}\Theta^{3/2}}{\pi^2}\int_A \sqrt{y}\left\{1 + \exp\left[y - \frac{V_j(r)}{\Theta} - \frac{\mu}{\Theta}\right]\right\}^{-1} dy, \quad (10)$$

$$A: y > \frac{V_j(r)}{\Theta}.$$

The chemical potential μ can be deduced from the electroneutrality condition, $\sum_j W_j N_j = Z$, where $N_j = \sum_{nl} N_{nl}^j + 4\pi\int_0^{r_0} \rho_2^j(r) r^2 dr$ is the total number of electrons in the jth subsystem and W_j is the Gibbs distribution,

$$W_j = C g_j \exp\left(-\frac{E_j - \mu N_j}{\Theta}\right) \quad (11)$$

with E_j being the total energy and $g_j = \prod_{nl} C_{2(2l+1)}^{N_{nl}^j}$ being the statistical weight.

The set of equations (2)–(11) describes the state of the statistical ensemble of plasma ions. Obviously, the groups of equations describing the states of subsystems denoted by subscripts $j = 1, 2$, etc., are coupled through the electroneutrality condition. Such equations are impossible to solve for all plasma ions even with the most advanced computers. However, these equations can be solved for the subsystem of main (or "reference") ions, which have the highest densities W_j. Having solved Eqs. (2)–(11) for this ion subsystem, we can apply the perturbation theory to determine the quantum parameters of the remaining plasma ions with lower densities.

3. METHOD FOR INCORPORATING THE STARK BROADENING

In order to calculate the shape of the spectral line corresponding to the transition between the sublevels $\alpha = nlm$ and $\beta = n'l'm'$ of the levels $a = nl$ and $b = n'l'$, respectively, Golosnoĭ [3] proposed the following approximate formula, which is a linear combination of the dispersion formula and the Gauss distribution:

$$I_{\alpha\beta}(\omega) = f(\Gamma)\frac{\gamma_{\alpha\beta}}{2\pi}\frac{1}{(\omega-\omega_0)^2 + \left(\frac{1}{2}\gamma_{\alpha\beta}\right)^2} + [1 - f(\Gamma)]\frac{1}{\sqrt{\pi}\delta_{\alpha\beta}}\exp\left[-\left(\frac{\omega-\omega_0}{\delta_{\alpha\beta}}\right)^2\right], \quad (12)$$

where ω_0 is the transition rate, $\Gamma = \frac{1}{r_0\Theta}$, and $f(\Gamma) = \exp\left(-\frac{1}{3}Z_0 Z_A \Gamma\right)$. The charges Z_0 and Z_A will be defined below. As Γ increases, the function $f(\Gamma)$ tends to zero.

In calculations for a strongly nonlinear plasma, we set $f(\Gamma) = 0$ and described the spectral-line shape by

$$I_{\alpha\beta}(\omega) = \frac{1}{\sqrt{\pi}\delta_{\alpha\beta}} \exp\left[-\left(\frac{\omega - \omega_0}{\delta_{\alpha\beta}}\right)^2\right], \quad (13)$$

where

$$\delta_{\alpha\beta} = 2.5 C_{\alpha\beta}\zeta_{\max},$$

$$C_{\alpha\beta} = \sum_{n_1 l_1}{}' \left(\frac{|\langle n'l'm'|z|n_1 l_1 m\rangle|^2}{E_{n'l'} - E_{n_1 l_1}} - \frac{|\langle nlm|z|n_1 l_1 m\rangle|^2}{E_{nl} - E_{n_1 l_1}} \right). \quad (14)$$

Golosnoĭ [3] proposed to calculate the most probable value of the squared microfield $\zeta_{\max}$ from the formula

$$\zeta_{\max} = \frac{Z_A^2 \zeta_0}{\left[0.8\left(\frac{Z_A}{Z_B}\right)^4 + 4\frac{Z_A^4}{Z_B^5} Z_0 Z_C \Gamma + (Z_0 Z_A \Gamma)^2\right]^{1/2}}, \quad (15)$$

where $\zeta_0 = \frac{1}{r_0^4}$,

$$Z_A = \sum_k Z_k X_k, \quad Z_B = \left[\sum_k Z_k^{3/2} X_k\right]^{2/3}, \quad Z_C = \sum_k Z_k^2 X_k,$$

$X_k = \frac{N_k}{N}$, N_k is the density of the ions with charge Z_k, N [1/cm^3] is the nucleus density, and Z_0 is the charge of the emitting ion.

Of course, in our calculations, we took into account the effect of both the natural broadening and the Doppler broadening. This effect was found to be insignificant as compared to the Stark effect.

4. COMPARISON BETWEEN THE CALCULATED RESULTS AND EXPERIMENTAL DATA

In the figure, the experimentally measured spectral intensities of radiation from a xenon plasma are illustrated by the light curves, corresponding to the following experimental:

(*1*) $T = 32000$ K and $\rho = 6.26 \times 10^{-3}$ g/cm^3, the density of unbound electrons being $N_e = 4.1 \times 10^{19}$ cm^{-3};

(*2*) $T = 28500$ K and $\rho = 1.33 \times 10^{-3}$ g/cm^3, the density of unbound electrons being $N_e = 9.2 \times 10^{18}$ cm^{-3};

(*3*) $T = 27000$ K and $\rho = 6.86 \times 10^{-4}$g/cm^3, the density of unbound electrons being $N_e = 4.8 \times 10^{18}$ cm^{-3}; and

(*4*) flashlamp.

The heavy curves in the figure show the shapes of the $6s^4P$–$6p^4P^0$ 529.2-nm spectral line that were calculated for the temperatures T and densities ρ [g/cm^3] indicated in (*1*)–(*4*). Note that, in our calculations, the Hartree–Fock equation was solved by applying one of the most exact among the presently known methods [7]. However, even with this method, the position of the $6s^4P$–$6p^4P^0$ spectral line was found to deviate from the experimentally measured position by about 20%. Because of this, the calculated position was refined by using the experimental data. Note also that, in our calculations, we neglected the influence of the Stark effect on the populations of the electronic levels.

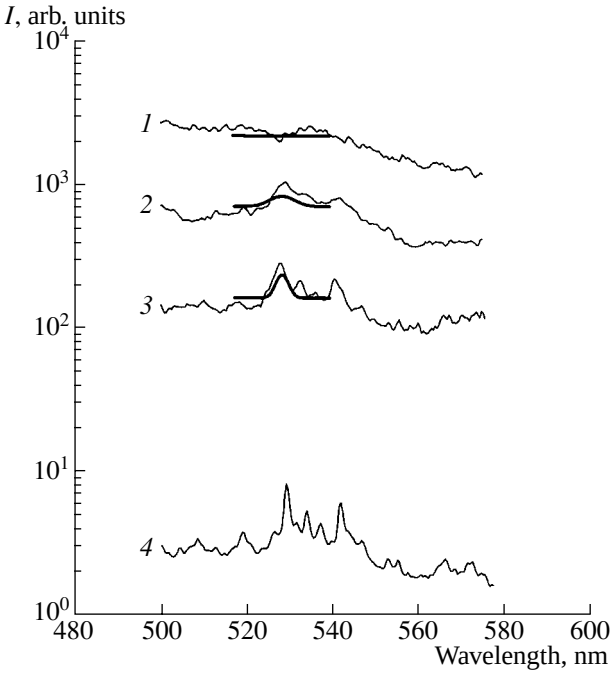

Experimentally measured spectral intensities of radiation from xenon plasmas with different temperatures and densities (light curves) and the shapes of the $6s^4P$–$6p^4P^0$ 529.2-nm spectral line (heavy curves) calculated for the same conditions.

5. CONCLUSION

A comparison between the calculated results described above and the experimental data obtained in [2] makes it possible to conclude that the mechanism for the disappearance of spectral lines in a strongly nonideal plasma can be attributed to the Stark broadening of the spectral lines. As was noted above, the method that was used to solve the Hartree–Fock equation [7] leads to a substantial deviation of the calculated position of the $6s^4P$–$6p^4P^0$ spectral line from that measured experimentally. This deviation is not associated with the values of the plasma temperature and density and seems to be a consequence of the correlation effects [7], which will be included in our model in a subsequent paper.

REFERENCES

1. V. E. Fortov and I. T. Iakubov, *Physics of Nonideal Plasma* (Hemisphere, New York, 1990).
2. M. Kulish, V. Gryaznov, A. Mezhipa, *et al.*, in *Proceedings of the International Conference on Physics of Strongly Coupled Plasmas, Binz, Germany, 1995*, p. 337.
3. I. O. Golosnoĭ, *Influence Calculation of Ion Microfields on Optical Properties of Matters* (Vses. Tsentr Matem. Model. Akad. Nauk SSSR, Moscow, 1991), No. 38.
4. N. Y. Orlov, Laser Part. Beams **15**, 627 (1997).
5. N. Y. Orlov and V. E. Fortov, in *Proceedings of the III International Conference on Intense Ion Beam Interaction with Matter, Moscow, 2000*, p. 268.
6. N. Yu. Orlov and V. E. Fortov, Fiz. Plazmy **27**, 45 (2001) [Plasma Phys. Rep. **27**, 44 (2001)].
7. C. Froese Fischer, T. Brage, and O. N. Jonsson, *Computational Atomic Structure: An MCHF Approach* (Institute of Physics Publ., Bristol, 1997).
8. A. F. Nikiforov and V. B. Uvarov, Chislennye Metody Mekh. Sploshnoĭ Sredy **4**, 114 (1973).

Translated by O. E. Khadin

Plasma Physics Reports, Vol. 27, No. 12, 2001, pp. 1025–1031. Translated from Fizika Plazmy, Vol. 27, No. 12, 2001, pp. 1085–1092.

NONIDEAL PLASMA

Phase Transition in Superdense Hydrogen and Deuterium

M. Bonitz*, I. A. Mulenko, E. N. Oleynikova**, V. S. Filinov***, V. E. Fortov***, and A. L. Khomkin****

**Faculty of Physics, University of Rostock, Germany*

***Associated Institute for High Temperatures, Russian Academy of Sciences, Izhorskaya ul. 13/19, Moscow, 127412 Russia*

****Institute for High Energy Densities, Associated Institute for High Temperatures, Russian Academy of Sciences, Izhorskaya ul. 13/19, Moscow, 127412 Russia*

Received May 11, 2001; in final form, June 25, 2001

Abstract—Results are presented from numerical simulations of the thermodynamic properties of superdense hydrogen and deuterium plasmas by the Monte Carlo method and from calculations by a multicomponent chemical model. The results obtained reveal the anomalous behavior of the thermodynamic functions and composition of molecular gas plasmas in the submegabar and megabar pressure ranges. Such behavior is interpreted as a dissociative phase transition. The results of calculations by the chemical model are compared with the experimental data on the equation of state and conductivity of hydrogen and deuterium plasmas. © *2001 MAIK "Nauka/Interperiodica".*

1. INTRODUCTION

Experiments on the thermodynamic and transport properties of dense hydrogen and deuterium plasmas [1–3] revealed the unusual behavior of the conductivity of hydrogen [1, 2] and the shock adiabat of deuterium [3] in the megabar pressure range. The results of [1, 2] show that, in the pressure range $P = 10^5$–2×10^6 atm, the conductivity of a hydrogen plasma increases rapidly (by nearly five orders of magnitude) as the pressure varies within relatively narrow (~40–50%) limits. The measurements were carried out in the temperature range $(4.5–10) \times 10^3$ K. From a theoretical standpoint, the behavior of the shock adiabat of deuterium measured in [3], which demonstrates a sharp change in the deuterium density in the megabar pressure range at densities of 0.5–1 g/cm^3, also seems unusual.

Such behavior of the thermodynamic and transport properties of a plasma indicates the possible existence of phase transitions of the first kind that are accompanied by a rapid or even abrupt change in the plasma composition and density. The occurrence of phase transitions in a low-temperature plasma was first hypothesized in [4]. Later, attempts were made to study the parameters of plasma phase transition, primary attention being focused on the Coulomb interaction [5–7].

In this paper, the behavior of the thermodynamic properties of hydrogen and deuterium plasmas in the above pressure and density ranges is studied comparatively by the Monte Carlo quantum method [8, 9] for hydrogen and by using the chemical model of a multicomponent nonideal plasma [10] for hydrogen and deuterium. It is shown that the experimentally observed behavior of the conductivity of dense hydrogen and the deuterium shock adiabat can be explained by the existence of a new phase transition occurring in dense hydrogen and deuterium. The critical transition temperature and the phase coexistence curve are found. The electric conductivity of hydrogen and the deuterium shock adiabat are calculated and compared with the experimental data.

2. NUMERICAL SIMULATIONS

For the numerical simulations of a hydrogen plasma, we use an original efficient modification of the Monte Carlo quantum method elaborated in [8, 9]. The modified method allows us to study dense degenerate plasmas over a wide range of densities and temperatures. We consider a system consisting of 50 electrons and 50 hydrogen ions in a cell with periodic boundary conditions.

Thermodynamic quantities are calculated as derivatives of the logarithm of the statistical sum [11]. The statistical sum of a quantum system is expressed through the density matrix. An exact expression for the density matrix of a quantum system at low temperatures is still unknown. To approximate this sum, we can represent it in the form of integrals over trajectories [11]. The spin variables are taken into account by the spin part of the density matrix, whereas the permutation operator acting on the spatial and spin coordinates of electrons allows for exchange effects. The sum is taken over all permutations with a given parity. For Fermi particles, this sum contains positive and negative terms, which poses the well-known "problem of signs."

1063-780X/01/2712-1025$21.00

In the developed approach [8, 9], the density matrix is described by the expression

$$\rho_s(q, [r], \beta) = C^s_{N_e} e^{-\beta U(q, [r], \beta)} \prod_{l=1}^{n} \prod_{p=1}^{N_e} \Phi^l_{pp} \det \left| \Psi^{n,l}_{ab} \right|_s. \quad (1)$$

The matrix does not contain the alternating-sign sum over permutations in the explicit form. The exchange effects are accounted for in the determinant of the exchange density matrix:

$$\left\| \Psi^{n,l}_{ab} \right\|_s \equiv \left\| \exp\left(-\frac{\pi}{\Delta\lambda_e^2} \left| (\mathbf{r}_a - \mathbf{r}_b) + \mathbf{y}^n_a \right|^2 \right) \right\|_s. \quad (2)$$

In formulas (1) and (2), we introduced the following notation: $U(q, [r], \beta)$ is the sum of Kelbg potentials, $\Phi^l_{pp} \equiv \exp[-\pi \left| \xi^{(l)}_p \right|^2]$, $\boldsymbol{\xi}^{[l]}_p$ are the dimensionless vectors connecting the nearest peaks of trajectories, $C^l_{pt} = \frac{(r^l_{pt} | y^l_{pt})}{2 |r^l_{pt}|}$, $\mathbf{y}^l_{pt} \equiv \mathbf{y}^l_p - \mathbf{y}^n_t$, $\mathbf{y}^n_a = \Delta\lambda_e \sum_{k=1}^{n} \boldsymbol{\xi}^{(k)}_a$, $r^l_{pt} \equiv r_{pt} + y^l_{pt}$, $\Delta\lambda_a^2 = \frac{2\pi\hbar^2 \Delta\beta}{m_a}$, $\Delta\beta$ is the increment of the modulus of the canonic distribution, the $(\ldots|\ldots)$ bracket denotes the scalar product, and m_a is the mass of particles of the a species.

The summation over spin variables results in a block structure of the exchange density matrix for electrons with the same spin projections. The important advantage of expression (2) is that the sum over permutations is written in the form of a determinant that can be easily calculated by the conventional methods of linear algebra.

Using the Monte Carlo quantum method, we calculated the isotherms of a hydrogen plasma at temperatures of 10, 20, and 50 kK. The most interesting is the 10-kK isotherm. On this isotherm, there is a plasma density range in which a stable solution is absent. The plasma density changes abruptly from 10^{23} to 2×10^{24} cm^{-3} in a narrow pressure range. A similar situation also occurs for the 20-kK isotherm, but in a narrower density range. On the 50-kK isotherm, the instability domain is absent and the dependence of the pressure on the density is smooth up to densities of 10^{26} cm^{-3}. It was found that the range of the hydrogen plasma density with such a peculiar behavior of the equation of state nearly corresponds to the density range in which a sharp increase in the hydrogen plasma conductivity is observed [1, 2]. Unfortunately, it is still impossible to numerically calculate the conductivity of a hydrogen plasma. The Monte Carlo method allows one to calculate the thermodynamic functions but not transport coefficients, such as the electric conductivity. To calculate these coefficients, the method of molecular dynamics should be applied. In addition, when simulating using the Monte Carlo quantum method, a system of electrons and nuclei is used. Some electrons and nuclei form bound states. This can be seen from the form of the pair distribution functions [8]. However, there is no significant difference between free and bound electrons, so that it is difficult to determine the composition exactly.

In some sense, the simulations of hydrogen plasma thermodynamics can be regarded as an additional experiment on determining the equation of state of dense hydrogen, which is all the more useful because, in experiments [1–3], the temperature was not measured.

3. CHEMICAL MODEL

In [10], a chemical model of a nonideal plasma with allowance for chemical reactions was proposed. A distinctive feature of this model is the exclusion of a classically inaccessible phase space volume from the ensemble of free particles when calculating the corrections for their interaction. This correction appears because some states of the particles under consideration are bound and form particles of other species. The corrections for the interactions involving neutral particles are represented in terms of a power series in the density with allowance for all types of pair and three-body charge–neutral and neutral–neutral interactions [10]. The corresponding second and third virial coefficients associated with the interaction of free particles of different species were calculated in [12] by using the Hill pseudopotentials [13]. The Hill pseudopotentials describing the charge–neutral and neutral–neutral interactions were calculated using the (12-4) and (12-6) Lennard–Jones potentials, respectively, as the initial ones. The classically inaccessible phase space volume was taken into account in [14] when calculating the corrections for the interaction in an ensemble of free charged particles. The derived corrections to the thermodynamic functions differ substantially from the conventionally used Debye corrections. The thermodynamic quantities for a multicomponent, chemically reacting plasma of an arbitrary composition are represented in terms of a series in different interaction types. It is taken into account that the particles of different species interact with each other through the Coulomb and van der Waals forces with the parameters of the initial interaction potentials characteristic of a given pair of particles; the electron component is assumed to be weakly degenerate. For hydrogen and deuterium plasmas, six components (namely, e^-, A, A^+, A^-, A_2, and A_2^+, where A is the element symbol) were taken into account.

The expression for the free energy of a multicomponent plasma with allowance for the above-listed interactions and chemical reactions has the form (see notation in [10, 14])

$$F = -TV\Bigg\{\sum_{i=1}^{M} n_i \ln\frac{eZ_i}{n_i} - \sum_{i=1}^{M} n_i^2 B_{ii} - 2\sum_{i=1}^{M}\sum_{j=i+1}^{M} n_i n_j B_{ij} - \frac{1}{2}\sum_{i=1}^{M} n_i^3 C_{iii} - \frac{3}{2}\sum_{i=1}^{M}\sum_{j=i+1}^{M} n_i n_j^2 C_{ijj} - 3\sum_{i=1}^{M}\sum_{j=i+1}^{M}\sum_{k=j+1}^{M} n_i n_j n_k C_{ijk} - \frac{n_e^2\lambda_e^3}{2^{7/2}} + \sum_k n_k z_k^2\Bigg[\ln(1 + z_k^2(\alpha/2 + \alpha^2/4 - f_1)) - \frac{\alpha/6 + \alpha^2/8 - f_1/2}{1 + z_k^2(\alpha/2 + \alpha^2/4 - f_1)}\Bigg]\Bigg\}. \quad (3)$$

The equation of state and the set of chemical balance equations are written in the form

$$P = T\Bigg\{\sum_{i=1}^{M} n_i - \sum_i \frac{(\alpha/6 + \alpha^2/8 - f_1/2) n_i z_i^2}{1 + z_i^2(\alpha/2 + \alpha^2/4 - f_1)} + \sum_{i=1}^{M} n_i^2 B_{ii} + 2\sum_{i=1}^{M}\sum_{j=i+1}^{M} n_i n_j B_{ij} + \sum_{i=1}^{M} n_i^3 C_{iii} + 3\sum_{i=1}^{M}\sum_{j=i+1}^{M} n_i n_j^2 C_{ijj} + 6\sum_{i=1}^{M}\sum_{j=i+1}^{M}\sum_{k=j+1}^{M} n_i n_j n_k C_{ijk} + \frac{n_e^2\lambda_e^3}{2^{7/2}}\Bigg\}, \quad (4)$$

$$\frac{n_k}{n_l n_p} = \frac{Z_k}{Z_l Z_p}\exp\Bigg\{-\Bigg[2\sum_{i=1}^{M} n_i(B_{ki} - B_{li} - B_{pi}) + \frac{3}{2}\sum_{i=1}^{M} n_i^2(C_{kii} - C_{lii} - C_{pii}) + 3\sum_{i=1}^{M-1}\sum_{j=i+1}^{M} n_i n_j(C_{kij} - C_{lij} - C_{pij})\Bigg] - \ln[1 + z_l^2(\alpha/2 + \alpha^2/4 - f_1)] - \ln[1 + z_p^2(\alpha/2 + \alpha^2/4 - f_1)] + \ln[1 + z_k^2(\alpha/2 + \alpha^2/4 - f_1)] + \frac{n_e\lambda_e^3}{2^{5/2}}(\delta_{le} + \delta_{pe} - \delta_{ke})\Bigg\}. \quad (5)$$

In Eqs. (3)–(5), we introduce the following notation: $f_1(\alpha) = \frac{\pi\sqrt{6}}{24}\alpha + \frac{\sqrt{2\pi}\times 3^{1/6}\Gamma\left(\frac{1}{6}\right)}{48}\alpha^{5/3}$; α is the plasma coupling parameter (it is calculated through the activities); Z_k, z_k, and n_k are the statistical sum, charge number, and density of the particles of k species, respectively; T and V are the plasma temperature and volume; B_{ij} and C_{ijk} are the second and third virial coefficients; M is the total number of plasma particle species; λ_e is the thermal wavelength of electrons; and δ is the Kronecker symbol.

It should be stressed that taking into account the second and third virial coefficients in the free energy and in the equation of state allows one, in principle, to determine the parameters of the vapor–liquid phase transition.

4. COMPARISON OF ANALYTICAL RESULTS WITH NUMERICAL AND PHYSICAL EXPERIMENTS. DISSOCIATIVE PHASE TRANSITION

The described approaches were used to calculate the equilibrium properties of hydrogen and deuterium plasmas over a wide region of the phase diagram. A comparison of the results of calculations for both described approaches shows their satisfactory agreement in the stability domain of both methods. At low densities, where the chemical model is certainly applicable, numerical simulations demonstrate the formation of atoms and molecules.

To study the possibility of a phase transition in the adopted version of the chemical plasma model, we extended the model to the parameter range in which the model is unstable, using the recommendations of [15]. The numerical algorithm is based on the Newton method. The convergence of the method is provided by the requirement that the densities of all the plasma components be positive during the iteration process. If the temperature and the density (the specific volume) are chosen as thermodynamic quantities, then the requirement for the densities to be positively defined is satisfied automatically for the entire P–V diagram.

The stability of the solution was examined along the isotherm by varying the pressure or the plasma density. To search for all of the existing solutions to the set of chemical balance equations, it is convenient to move along the phase diagram from the range of high temperatures. Performing numerical calculations along different isotherms with a sufficiently small step in density, we may notice that, starting from a certain temperature, a loop appears, which is characteristic of a gas–liquid phase transition (Fig. 1). To analyze the cause of the appearance of the phase transition, we calculated isotherms for a model system consisting of only atoms and molecules (Fig. 2, curve *1*). Calculations show that the

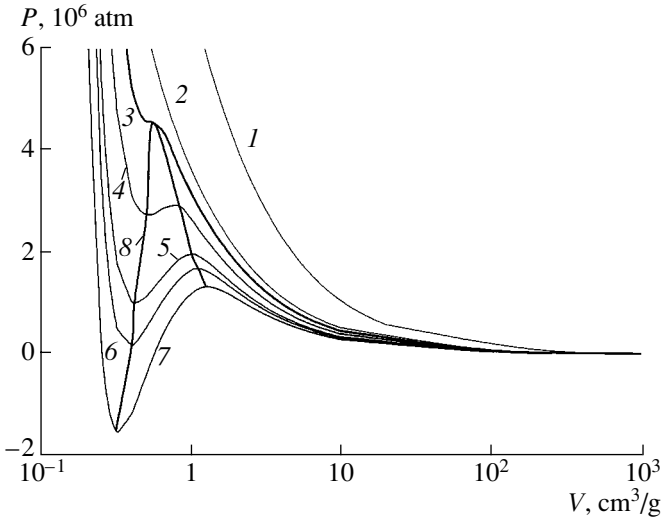

Fig. 1. Phase transition in a hydrogen plasma. Isotherms T = (*1*) 60, (*2*) 55, (*3*) 50, (*4*) 45, (*5*) 40, (*6*) 38, and (*7*) 35 kK are shown; the envelop *8* is the phase equilibrium curve (spinodal).

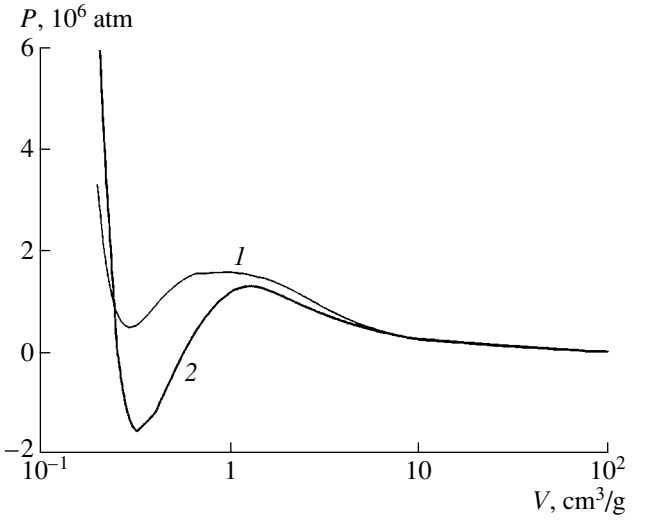

Fig. 2. Hydrogen isotherm for T = 35 kK in (*1*) the model system of atoms and molecules and (*2*) full-composition model.

main cause of the phase transition is the rapid increase in the magnitude of the total contribution from all of the second virial coefficients characterizing the pair interactions of heavy particles, which results in the intense dissociation of molecules. Taking into account all other types of particle interactions does not change the shape of the isotherm qualitatively (Fig. 2, curve *2*). In this case, the van der Waals loop becomes more pronounced. When the interaction between heavy particles is eliminated (on keeping the Coulomb interaction), the phase transition disappears. For $T < T_c$, the total second virial coefficient $B(T)$ is negative, whereas the third coefficient $C(T)$ is positive (Fig. 1, curves *4–7*). At temperatures above the critical temperature (Fig. 1, curve *3*) $B(T)$ changes its sign and the phase transition disappears (Fig. 1, curves *1*, *2*). At lower temperatures, such that $T < 1/3T_c$, the total third virial coefficient $C(T)$ is also negative. In this case, we failed to find a stable solution for the liquid phase. All the solutions lying on isotherms with $T \ll T_c$ to the left of the maximum have no physical meaning. The two-phase domain is bounded by curve *8*. The isotherm segments lying in this domain describe the states with a negative compressibility and also have no physical meaning. The value of the critical temperature for various materials is close to the dissociation energy of molecules or molecular ions.

The phase transition is accompanied by an abrupt change in the densities of all species (Fig. 3). The density jump occurs mainly due to the jump in the degree of dissociation, which allows us to call this transition the dissociative transition. It is interesting to note that the chemical model under consideration also describes an ordinary phase transition from a molecular gas into a molecular liquid at $T \sim 50$ K.

As was mentioned above, the abrupt change in the thermodynamic parameters of a hydrogen plasma was also observed in our numerical simulations using the Monte Carlo method. Figure 4 compares the analytical and simulation results. It can be seen that the model described in Section 3 not only predicts the phase transition qualitatively, but also gives a quite reasonable quantitative estimate for its position on the isotherm, which agrees with the results of numerical simulations. The obtained value of the critical temperature also agrees with the results of simulations (Fig. 4, curve *1*). The values of the internal plasma energy calculated by the chemical model and the Monte Carlo method are also in qualitative agreement (Fig. 5).

If the phase transition under consideration actually exists, then it must be accompanied by a sharp increase in the plasma conductivity, because, as is seen in Fig. 3, the density of free charge carriers in the transition point increases by three orders of magnitude. Such an increase in the electric conductivity was observed experimentally. In [1], a sharp decrease in the plasma resistivity at pressures of ~1 Mbar was recorded. A comparison of the results from calculations carried out using different models for the electron mobility shows (Fig. 6) that, at high pressures, the so-called hopping conductivity [16] shows the closest matching to the experiment:

$$\sigma_p = \frac{n_i e^2 D}{T}, \qquad (6)$$

where $D = r_p^2/\tau$ is the coefficient of the quantum diffusion of bound electrons from an atom to an ion along the applied field, $r_p = [3/4\pi(n_a + n_i)]^{1/3}$ is the average

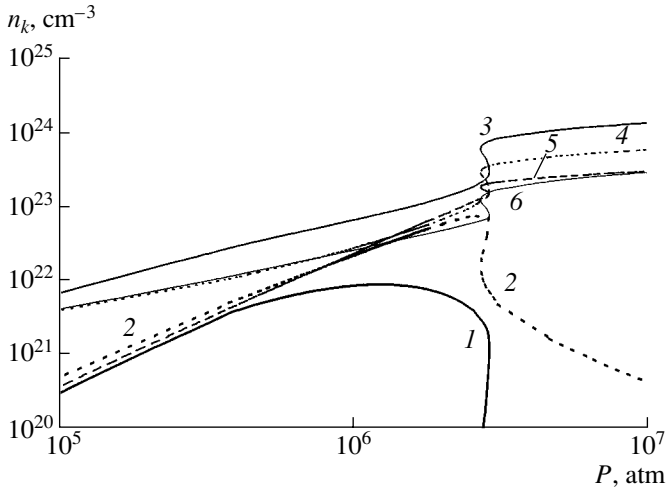

Fig. 3. Composition of a hydrogen plasma on the 45-kK isotherm: (*1*) H_2, (*2*) H_2^+, (*3*) H, (*4*) H^+, (*5*) H^-, and (*6*) e^-.

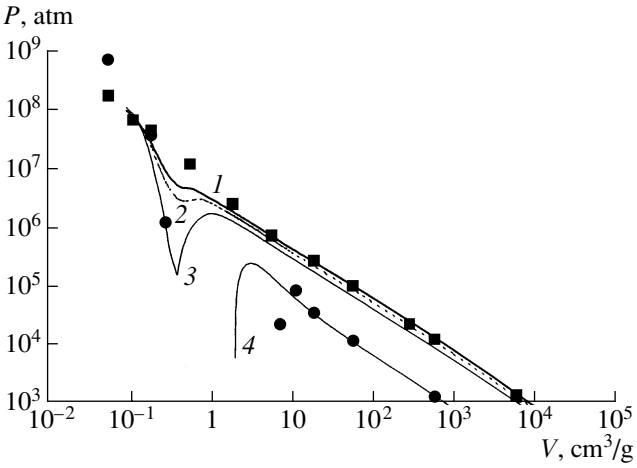

Fig. 4. Isotherms of a hydrogen plasma calculated by the chemical model for T = (*1*) 50, (*2*) 45, (*3*) 38, and (*4*) 10 kK and by the Monte Carlo method for T = 50 (squares) and 10 kK (circles).

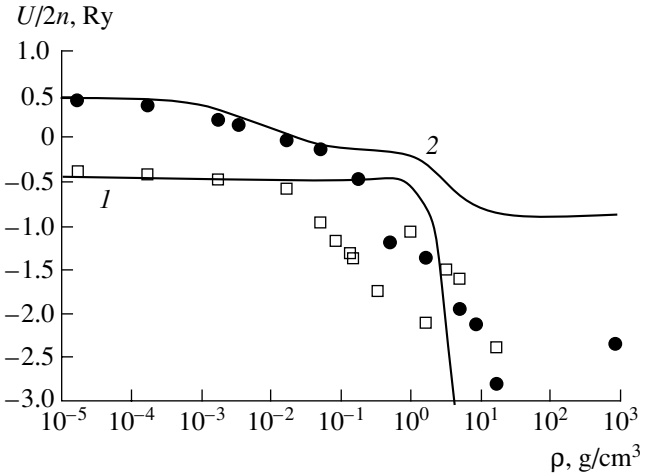

Fig. 5. Internal energy of a hydrogen plasma (U is the plasma energy per unit volume, and n is the total particle density of all species) calculated by the chemical model for T = (*1*) 10 and (*2*) 50 kK and by the Monte Carlo method for T = 10 (squares) and 50 kK (circles).

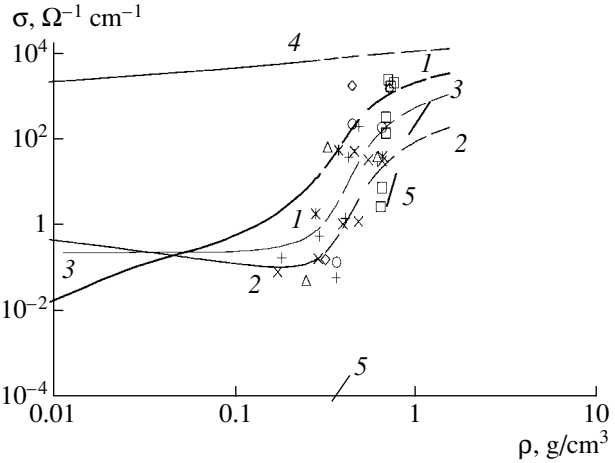

Fig. 6. Electric conductivity of a dense hydrogen plasma in the megabar pressure range along the isotherm T = 10 kK: (*1*) hopping conductivity, (*2*) gas-kinetic conductivity, (*3*) Drude formula, and (*4*) minimum metal conductivity. Curve (*5*) shows the hopping conductivity along the isotherm T = 4.5 kK, squares show the results of experiment [1], and the other symbols correspond to different experimental series of [2].

radius of the electron hopping, and $\tau = \hbar/\Delta E$ is the hopping time. According to this mechanism, the electron mobility depends on the density, because the quantity ΔE (the energy difference between the symmetric and antisymmetric terms in the A_2^+ molecule) is determined by the overlap integral for the electron wave functions [16]. Note that a sharp increase in the conductivity observed experimentally in [1] occurs at substantially (by a factor of 2.5) higher pressures than those predicted by the theory.

A large amount of experimental data is presented in [2], where a sharp increase in the electric conductivity of a hydrogen plasma was also pointed out in the density range 0.2–0.8 g/cm^3. In this case, the measured values of the plasma pressure range from 0.4 to 0.7 Mbar [2], which corresponds to the two-phase domain in Fig. 1. Consequently, the parameter range of the supposed phase transition found in our paper coincides with the range in which a rapid increase in the conductivity was observed in [2]. Although a rapid increase in the conductivity due to the abrupt change in the density and

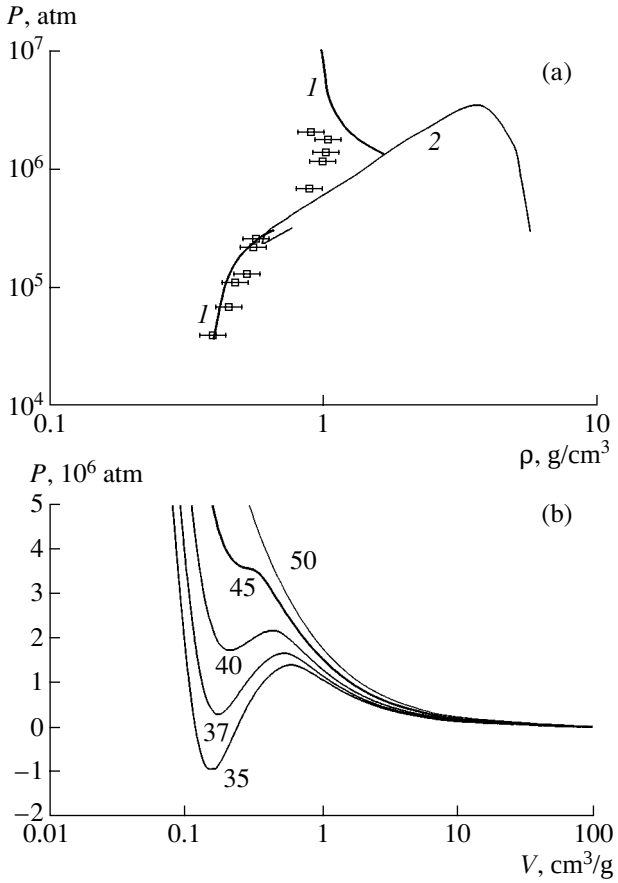

Fig. 7. Phase diagram of a deuterium plasma: (a) deuterium shock adiabat (curves *1* and *2* show the gas boundary of the two-phase domain, and squares show the results of experiment [3]) and (b) isotherms of a deuterium plasma (numerals by the curves show the temperature in kK).

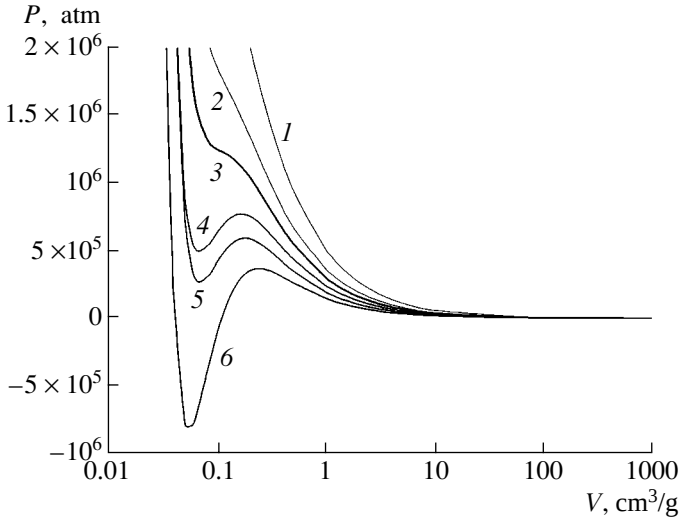

Fig. 8. Isotherms of an oxygen plasma for (*1*) 60, (*2*) 50, (*3*) 45, (*4*) 40, (*5*) 35, and (*6*) 30 kK.

composition takes place in all of the theoretical calculations, it is the hopping (ion) conduction that plays a dominant role in the dense phase (Fig. 6). The contribution from other (gas-kinetic) mechanisms is no more than 10% of the hopping conductivity. The minimum metal conductivity calculated assuming that, under the conditions of interest, all of the electrons become conduction electrons turns out to be overestimated (by nearly one order of magnitude). The bulk of the experimental data on the conductivity lies between curves *4* and *5* calculated along the 10- and 4.5-kK isotherms, respectively, which corresponds to the experimental temperature range. It should be noted, however, that all of the conductivity calculations for $\rho > 0.3$ g/cm^3 are evaluative in character, because the plasma composition in these states is calculated for unstable isotherm segments. Note also that calculations by the chemical model reliably describe only the gas–plasma branch of the isotherm. The calculations for the condensed phase are qualitative and only give estimates for the critical temperature, density, and pressure. The structure of the condensed phase (if it actually exists) can be deduced only from numerical simulations.

The anomalous behavior of thermodynamic quantities in a superdense deuterium plasma was also observed experimentally [3]. Figure 7a shows the calculated deuterium shock adiabat and the experimental results of [3]. The low-temperature branch of the shock adiabat ($T < 10$ kK) correctly describes the experimental data not only qualitatively, but also quantitatively. In addition, we observed a density jump in the adiabat near $\rho = 0.6$ g/cm^3. For $6 < T < 3.5$ kK, there is no solution to the Hugoniot adiabat equation in the gas phase. However, the calculated value of the density jump is significantly greater than the measured one. The high-temperature branch ($T > 30$ kK) of the calculated adiabat gives greatly overestimated values of the pressure at a given plasma density. This may be attributed to the scatter in the available data on the parameters of intermolecular interaction potentials for deuterium and to a significant error in the model itself near the phase transition. The proposed interpretation of the experimental data is original and nontraditional, because theoretical curves are usually continuous. The area under curve *2* in Fig. 7a determines the range of unstable solutions within the chemical model. The maximum of curve *2* (Fig. 7a) corresponds to the critical temperature $T =$ 4.5 kK (Fig. 7b).

A similar behavior of the thermodynamic quantities is also observed in superdense plasmas of other molecular gases. As an example, Fig. 8 shows the phase diagram of an oxygen plasma. The critical temperature is equal to ~45 kK (curve *3*), which is close to the dissociation energy of molecular oxygen O_2^+.

5.CONCLUSION

In this study, the equilibrium properties of superdense hydrogen and deuterium plasmas in the submegabar and megabar pressure ranges have been numerically simulated by the Monte Carlo method. The same pressure range has been studied by means of the previously elaborated chemical model [10, 12, 14]. An abrupt change in the thermodynamic plasma parameters has been revealed both analytically (by using the chemical model) and numerically (by the Monte Carlo method). The mentioned features of the phase diagram can be interpreted as a phase transition of the first kind. A stepwise change in the composition and density of the medium at pressures of ~1 Mbar is accompanied by a sharp increase in the electric conductivity, which was observed experimentally in [1, 2]. It is shown that, under these conditions, the dominant charge-transfer mechanism is the quantum diffusion of bound electrons (the hopping conduction).

We can assert that the available experimental data on the shock adiabat and the conductivity of hydrogen and deuterium plasmas, together with the results of numerical simulations by the Monte Carlo method and calculations by the chemical model, suggest the existence of a new type of phase transition in dense gases. A specific feature of this transition is that the component composition changes substantially on the phase boundary between a weakly dissociated molecular gas and an atomic liquid due to the intense dissociation of molecules at a high pressure. Further compression of the liquid can lead to metallization.

ACKNOWLEDGMENTS

We are grateful W. Ebeling, M. Schlanges, A.N. Starostin, Yu.G. Krasnikov, D. Kremp, and V.S. Vorob'ev for helpful discussions and valuable remarks. This work was supported in part by the grant "School of L.M. Biberman and V.S. Vorob'ev." The work of V.S. Filinov was also supported by the NIC Jülich and the Deutsche Forschungsgemeinschaft (Mercator-Programm).

REFERENCES

1. S. T. Weir, F. C. Mitchell, and W. J. Nellis, Phys. Rev. Lett. **76**, 1860 (1996).
2. V. E. Fortov, V. Ya. Ternovoĭ, S. V. Kvitov, *et al.*, Pis'ma Zh. Éksp. Teor. Fiz. **69**, 874 (1999) [JETP Lett. **69**, 926 (1999)].
3. W. J. Nellis, A. C. Mitchell, M. van Thiel, *et al.*, J. Chem. Phys. **79**, 1480 (1983); L. B. DaSilva, P. Celliers, G. W. Collins, *et al.*, Phys. Rev. Lett. **78**, 483 (1997).
4. G. É. Norman and A. N. Starostin, Teplofiz. Vys. Temp. **8**, 413 (1970).
5. W.-D. Kraeft, D. Kremp, W. Ebeling, and G. Röpke, *Quantum Statistics of Charged Particle Systems* (Plenum, New York, 1986; Mir, Moscow, 1988).
6. D. Saumon and G. Chabrier, Phys. Rev. A **46**, 2084 (1992).
7. M. Schlanges and M. Bonitz, Contrib. Plasma Phys. **35**, 109 (1995).
8. V. S. Filinov, M. Bonitz, and V. E. Fortov, Pis'ma Zh. Éksp. Teor. Fiz. **72**, 361 (2000) [JETP Lett. **72**, 245 (2000)].
9. V. S. Filinov, V. E. Fortov, M. Bonitz, and D. Kremp, Phys. Lett. A **274**, 228 (2000).
10. I. A. Mulenko, E. N. Oleĭnikova, V. B. Soloveĭ, and A. L. Khomkin, Teplofiz. Vys. Temp. **39**, 13 (2001).
11. R. P. Feynman and A. R. Hibbs, *Quantum Mechanics and Path Integrals* (McGraw-Hill, New York, 1965; Mir, Moscow, 1968).
12. I. A. Mulenko, V. B. Soloveĭ, A. L. Khomkin, and V. N. Tsurkin, Teplofiz. Vys. Temp. **37**, 518 (1999).
13. T. L. Hill, *Statistical Mechanics: Principles and Selected Applications* (McGraw-Hill, New York, 1956; Inostrannaya Literatura, Moscow, 1960).
14. A. L. Khomkin, V. S. Vorob'ev, I. A. Mulenko, and E. N. Oleĭnikova, Fiz. Plazmy **27**, 369 (2001) [Plasma Phys. Rep. **27**, 347 (2001)].
15. V. A. Dubovitskiĭ, Yu. G. Krasnikov, and G. A. Pavlov, Fiz. Plazmy **22**, 367 (1996) [Plasma Phys. Rep. **22**, 334 (1996)].
16. *Outlines of Physics and Chemistry of Low-Temperature Plasma*, Ed. by L. S. Polak (Nauka, Moscow, 1971).

Translated by N. F. Larionova

Plasma Physics Reports, Vol. 27, No. 12, 2001, pp. 1032–1038. Translated from Fizika Plazmy, Vol. 27, No. 12, 2001, pp. 1093–1100.

ELEMENTARY PROCESSES IN PLASMA

Relation between Electron Exchange and Nuclear Vibrations in the $H_2^+ + H_2^+ \longrightarrow H_3^+ + p$ Exothermic Ion–Molecular Reaction

V. A. Belyaev, M. M. Dubrovin, A. A. Terent'ev, A. E. Trenin, and G. V. Sholin

Russian Research Centre Kurchatov Institute, pl. Kurchatova 1, Moscow, 123182 Russia

Received July 17, 2001

Abstract—The effective cross section for the $H_2^+ + H_2^+ \longrightarrow H_3^+ + p$ reaction in the energy range 5.7–11.5 eV is measured by the split beam method. The maximum of the cross section at an energy of ~8 eV is related to the production of the H_4^{++} compound system. The reaction threshold $W_{thr} \approx 5$ eV provides evidence in favor of the classical model of the H_2^+ ion with the charge fixed on one of the nuclei throughout the collision event.

1. INTRODUCTION

Investigations of the energy levels of molecules consisting of multielectron atoms showed that *ab initio* calculations by the antisymmetrical molecular orbital (ASMO) method provide correct results only for the intermolecular interaction of atoms in a stable structure and fail when atoms and molecules interact at long distances typical of both the production of an intermediate compound in ion–molecular reactions and the formation of electronically excited or excimer molecules [1]. Using the example of an oxygen molecule, it was shown that, in calculating the atomic interaction at distances longer than the size of a stable molecule, the best results are obtained by taking into account not only atomic orbitals of an oxygen atom but also orbitals of O^- and O^+ ions. Here, exchange effects turn out to be of minor importance [2].

Based on the above approach, the diatomic molecular compound (DMC) method [3, 4] has been developed, in which the interatomic interaction of chemically defined structures is of primary importance, whereas electron exchange between identical atoms is of little significance. The method was successively used in studying not only multielectron atomic compounds but also simple structures, such as H_3, H_3^+, and H_3^{++} [5].

Strictly speaking, in studying electronically excited molecules and ion–molecular reactions, a chemical approach is taken in which orbitals that can occur as the distance between the nuclei constituting a molecule approaches infinity are assumed to be the basic ones. In other words, atomic constituents of a molecular structure should not change their properties drastically. In particular, in molecular ions (such as H_2^+ or H_3^+), only a successive transfer of an electron from one nucleus to another is possible, rather than a uniform distribution of the electron density among the nuclei. The uniform distribution of the electron density can only be a next order effect in terms of a small parameter equal to the ratio of the chemical bond energy to the ionization energy of the atomic structure.

In this paper, it is shown that studying the threshold behavior related to Coulomb repulsion in exothermic ion–molecular reactions makes it possible to verify the validity of the chemical approach and relate the electron exchange between nuclei to the excitation of molecular vibrations. As an example, we will consider an ion–molecular reaction that proceeds in pair collisions of H_2^+ ions.

According to modern theoretical views, among the four possible channels for the ion–molecular reaction,

$$H_2^+ + H_2^+ \longrightarrow \begin{cases} H_2^+ + H + p & -2.65\ \text{eV} \quad (1) \\ H + p + H + p & -5.30\ \text{eV} \quad (2) \\ H_2 + p + p & -0.82\ \text{eV} \quad (3) \\ H_3^+ + p & +3.18\ \text{eV} \quad (4) \end{cases}$$

the latter two must proceed via the formation of the intermediate H_4^{++} compound [3, 6], whereas channels (1) and (2) may be direct processes. Previous studies [7, 8] showed that channels (1) and (2) could not provide the observed probability of proton production at relative kinetic energies of $W \sim 7$ eV [9]. Therefore, at such energies, channel (4) should be of major importance because, during the decay of the intermediate compound, an exothermic channel prevails, all other factors being the same. Although channel (4) is exothermic, the need to overcome the Coulomb barrier makes it very sensitive to the mutual orientation of the colliding lin-

1063-780X/01/2712-1032$21.00 © 2001 MAIK "Nauka/Interperiodica"

ear molecular H_2^+ ions because, in order to form an intermediate compound, the ions must approach each other to the distance $R \sim 10^{-8}$ cm (comparable with the molecular size), at which atomic electron clouds can overlap.

The measured effective cross section for reaction (4) (on the order of $\sim 10^{-16}$ cm^2) indicates that the formation of an H_3^+ ion proceeds via an intermediate state, thus providing evidence in favor of Firsov's theoretical approach [10], proposed for the description of similar ion–molecular reactions. On the other hand, such a cross-section value points to the importance of this reaction for applications, because an appreciable number of H_3^+ ions in intense H_2^+ or proton beams extracted from a gas-discharge ion source increase the energy consumption and, therefore, decrease the efficiency of this source.

The paper is organized as follows. The concept of the experiment is described in Section 2, and the experimental setup and the method for recording the reaction under study are described in Section 3. The results of measurements are presented in Section 4 and discussed in Section 5 based on Firsov's theoretical concept with allowance for the DMC method, which has been developed in connection with studies of other ion–molecular reactions and excimer molecules. It is shown that the Coulomb threshold for reaction (4) depends on the molecular model used—the chemical model or the quantum mechanical one, in which the electron cloud is distributed uniformly between the two nuclei of an H_2^+ ion. Based on the probability of H_3^+ ion production measured at interaction energies of the colliding H_2^+ ions of several electronvolts, it is concluded that the chemical approach not only serves as a successful semiempirical calculation procedure but also adequately describes the processes occurring over time intervals much shorter than the period of nuclei vibrations, whereas the exchange of electron clouds between the nuclei correlates with these vibrations.

2. DESCRIPTION OF THE EXPERIMENT

The measurements were carried out by the split beam method (see [8] for details). To ensure collision events, a ribbon-shaped ion beam is split into two and then is focused so that the ion trajectories of the newly formed beams intersect in the focal region at a small angle φ. In the center-of-mass frame, the total kinetic energy of the colliding ions W (the interaction energy) is significantly less than their energy E in the laboratory frame. For equal ion masses, we have

$$W = \frac{1}{2}\varphi^2 E. \quad (5)$$

Therefore, it is possible to carry out measurements in an energy range of several electronvolts for particle beams with energies of several kiloelectronvolts, which greatly facilitates the experiment.

The probability of an inelastic process is determined from the production rate of the new particles (which will be referred to as "effect particles") in the beams after they have crossed each other. If $\varphi < 10°$, which is easily achieved, the effective cross section of the process is independent of φ (within an accuracy of 0.5%) and is equal to (see [8])

$$\sigma = n_{\text{eff}} V_0 h / I_1 I_2, \quad (6)$$

where n_{eff} is the production rate of the effect particles, V_0 is the velocity of the beam particles in the laboratory frame, I_1 and I_2 are the beam currents, and h is the beam height in the intersection region. The fact that the cross section of the process is almost independent of φ implies that, at small intersection angles, an uncertainty in the measured value of σ depends only slightly on the shape and horizontal dimensions of the beam intersection region (at a constant particle density in beams over the height h) and, according to formula (6), is only determined by the scatter in the particle energies in the beams:

$$\Delta\sigma/\sigma = \Delta E/2E = \Delta V_0/V_0. \quad (7)$$

The angular spread (together with the scatter in energies) affects, according to formula (5), only the scatter in the interaction energies

$$\Delta W/W = \Delta E/E + 2\Delta\varphi/\varphi. \quad (8)$$

In our experiments, the angle φ was equal to 4°.

To separate the ion–molecular reaction out of all the processes occurring in the focal region, the H_3^+ ions were recorded. It was taken into account that their energy was higher than that of H_2^+ ions by a factor of 1.5, because both the magnitude and direction of the ion velocity remained almost unchanged in the laboratory frame.

3. EXPERIMENTAL SETUP

The experiments were carried out in the DIVO facility [8]. The system for separating and recording the secondary particles was substantially modified. A schematic of the experimental setup is shown in Fig. 1.

Molecular hydrogen ions were produced in an RF ion source *S*. Then, they were extracted and an ion beam was formed by a lens system *L*. A magnet monochromator *M* separated H_2^+ ions out of the total ion flow, formed the beam, and directed it into a high-vacuum ($p \approx 10^{-7}$ torr) chamber HVC. At the entrance to the chamber, a diaphragm D_1 with two slits (2 mm in width and 8 mm in height) was installed, which split the primary ion beam into two beams (I_1 and I_2). To adjust the position of the focal region of the primary beam at diaphragm D_1, quadrupole lenses *QL* and vertical

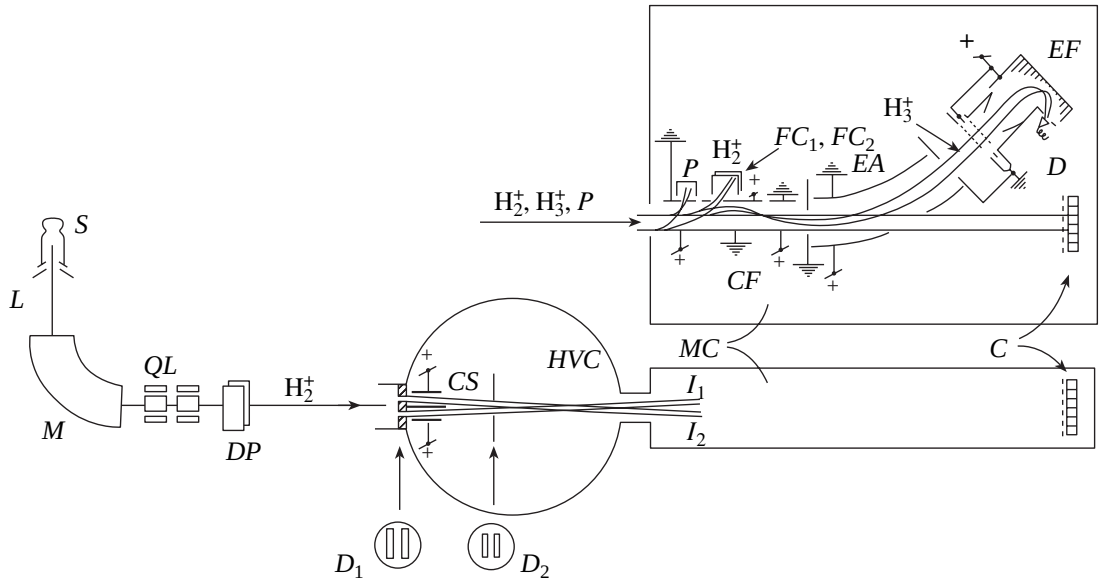

Fig. 1. Schematic of the DIVO facility: (*S*) ion source, (*L*) lens system, (*M*) magnet monochromator, (*QL*) quadrupole lenses, (*DP*) correcting deflector plates, (D_1, D_2) double-slit diaphragms, (*HVC*) high-vacuum chamber, (*CS*) beam convergence system, (*MC*) measurement chamber, (*C*) sectionalized collector, (*CF*) three-section capacitive filter, (FC_1, FC_2) Faraday cups, (*EA*) energy analyzer, (*EF*) electrostatic π funnel, and (*D*) detector.

deflector plates *DP* were used, which allowed us to attain approximately equal currents in the beams behind diaphragm D_1.

Slit diaphragm D_1 served as an entrance diaphragm of the beam convergence system *CS* consisting of horizontal deflector plates. The convergence system ensured the beam intersection at an angle of 4°, which was determined by the position and dimensions of the next diaphragm D_2 with two slits 1 mm in width and 5 mm in height. The beam positions, current ratio, and intersection angle were monitored by a sectionalized collector *C*.

A three-stage electrostatic system was used to separate the H_3^+ secondary (effect) ions out of the total flow consisting of H_2^+ primary ions, H_1^+ and H_3^+ secondary ions, and parasitic ions produced in the interaction of the beams with residual gas.

The first stage—a flat three-section capacitive filter *CF* with oppositely directed fields in the adjacent sections—separated protons and primary ions and directed the latter toward Faraday cups FC_1 and FC_2, which measured the beam currents.

The second stage—a cylindrical capacitive energy analyzer *EA*—separated H_3^+ effect ions, whose energy was higher than that of H_2^+ primary ions by a factor of 1.5, because, after mutual collisions between the beam particles with relative energies of no more than 15 eV, the particle velocities (which corresponded to an energy of several keV in the laboratory frame) remained almost unchanged.

The third stage—an "electrostatic π funnel" (*EF*), which decreased the cross section of the ion beam and rotated the beam by the angle π before recording—directed the effect ions separated out by the first and second stages toward a 9-mm-diameter entrance window of detector *D* (a secondary channel-type electron multiplier). The multiplier cathode intercepted all the ions that passed the π funnel through a window 40 mm in width and 30 mm in height. This was certainly the case for all of the effect ions. The rotation of the ion trajectories by the angle π before recording and the decrease in the entrance window area of the recording device ensured a deep reduction in the beam background noise (scattered ions, neutral particles, and X-ray photons produced in the interaction of the beam with the residual gas and the diaphragm surfaces).

The design of the three-stage electrostatic system for separating the effect ions ensured that, at equal potentials at all of the system electrodes, only ions of a definite energy arrived at detector *D*, which significantly facilitated the experiment and improved the stability of the device operation.

The RF ion source produced H_2^+ ions in various vibrationally excited states. The calculations of [11] showed that the typical lifetime of these ions is ~10^6 s. Since the probability of H_3^+ ion production may depend substantially on the vibrationally excited states of H_2^+ ions at the instant of collision, we decreased the number of vibrationally excited ions in the source by following a procedure used in [12]. A hydrogen–neon mixture (rather than pure hydrogen) with a volume ratio of 1 : 5

at a pressure of several units of 10^{-2} torr was supplied to the source. Under these conditions, collisions of vibrationally excited $H_2^+(v)$ ions with Ne atoms result in the $H_2^+(v \geq 2) + Ne \longrightarrow NeH^+ + H$ ion–molecular reaction, which proceeds at a high rate because, for $v \geq 2$, it is exothermic. For $v \leq 1$, the reaction is endothermic and proceeds at a much lower rate [13]. As a result, most of the ions that leave the source and form a beam are in the ground ($v = 0$) and first ($v = 1$) excited states with dissociation energies of 2.645 and 2.374 eV, respectively. Since the estimated reaction threshold for this reaction is 2.1–2.2 eV [14], a certain amount of H_2^+ ($v = 2$) ions with a dissociation energy of 2.118 eV may also be present.

4. MEASUREMENTS

The effective cross section $\sigma(W)$ for the ion–molecular reaction was determined from the measured number of H_3^+ ions arriving at the detector (which operated in a counting mode) in unit time (useful signal). The effective cross section and the corresponding energy were calculated by formulas (5) and (6), in which the numerical coefficients specifying the beam geometry in the intersection region were set at

$$W = 2.4 \times 10^{-3} E, \quad (5a)$$

$$\sigma = 1.26 \times 10^{-32} n_{\text{eff}} \sqrt{E} / I_1 I_2, \quad (6a)$$

where σ is in cm^2, W in eV, the intensity of the H_3^+ ion flux n_{eff} is in particle/s, the currents I_1 and I_2 are in A, and the energy of H_2^+ ions in the beams E is in eV.

For each energy value, the useful signal was derived from the results of four measurements with (I) both beams, (II) one beam, (III) the other beam, and (IV) no beams being in operation. In case I, the useful signal was recorded together with the background noise of both beams and instrumental noise: $N(\text{I}) = n_{\text{eff}} + n_1 + n_2 + n_{\text{in}}$. In cases II and III, there was no useful signal but the instrumental noise together with the background noise of one of the beams were recorded: $N(\text{II}) = n_1 + n_{\text{in}}$, $N(\text{III}) = n_2 + n_{\text{in}}$. In case IV, only the instrumental noise (which, under our conditions, was almost zero) was recorded: $N(\text{IV}) = n_{\text{in}}$. The useful signal was determined as $n_{\text{eff}} = N(\text{I}) - N(\text{II}) - N(\text{III}) + N(\text{IV})$.

To diminish the influence of the unstable operation of the ion source on the experimental results, each measurement was carried out for several seconds. The durations of each of the four measurements were the same and did not change throughout the entire time during which the required set of statistical data was accumulated. After every series of four measurements, the beam currents I_1 and I_2 were also measured.

To perform such measurements, the potentials at the electrodes of convergence system *CS* were consequently set at zero, so that the beams were not able to pass through diaphragm D_2 (Fig. 1).

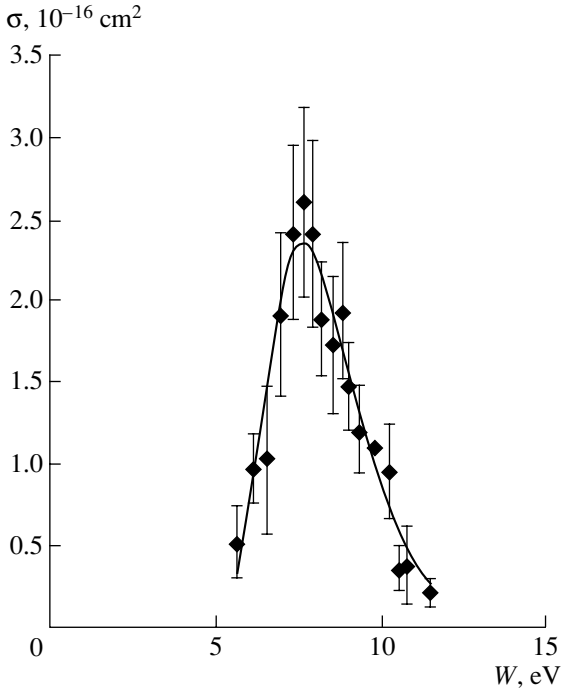

Fig. 2. Energy dependence of the effective cross section for the $H_2^+ + H_2^+ \longrightarrow H_3^+ + p$ ion–molecular reaction. The solid line fits the experimental results.

Average currents in the beams were $\sim 5 \times 10^{-8}$ A and grew as the ion energy E increased from 2 to 5 keV, which corresponded to the interaction energies between two ions from the different beams W = 5–12 eV. The useful signal amounted to 0.1–0.5 pulse/s, whereas the background noise of the beams was 10–20 pulse/s.

The results of measurements are shown in Fig. 2. In view of the small value of the useful signal and signal-to-noise ratio, the measurements lasted for many hours to attain the statistical error given in the figure. For this reason, the measurement of the effective cross section for a given energy W was preceded by the measurement for a certain (reference) W^* value in order to eliminate the possible change in the recording efficiency during such a long time. As a result, the relative dependence $\sigma(W)/\sigma(W^*)$ was determined [15]. It was assumed that, in measuring σ for the energy W, the statistical error was equal to $\Delta\sigma(W) + \Delta\sigma(W^*)$, whereas for the energy W^*, it was zero. The true $\sigma(W^*)$ value was obtained after averaging all the $\sigma(W^*)$ measurements and the absolute calibration of the systems for separating out and recording the effect ions.

For the purpose of absolute calibration, the H_3^+ ions extracted directly from the ion source were directed to detector D (Fig. 1); then, their current was reduced to a level corresponding to the number of the detector counts within the linear portion of its characteristics.

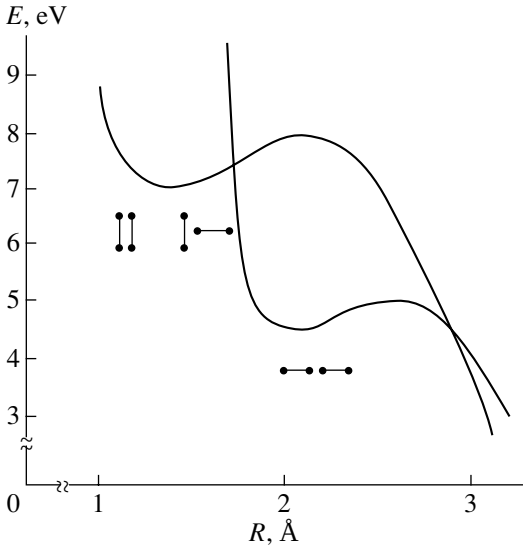

Fig. 3. Qualitative dependence of the singlet potential on the distance between H_2^+ ions for different mutual orientations of their axes. The curves for the T-type and collinear orientations coincide.

After that, a Faraday cup was installed in front of the π funnel (it is not shown in the figure), which intercepted all the H_3^+ ions, whose current was measured by an electrometer. The relation between this current and the number of detector counts per second determined the efficiency of H_3^+ ion recording, which turned out to be almost 100%. It was determined that $\sigma(W^* = 9.75\ \text{eV})$ was equal to $(1.10 \pm 0.14) \times 10^{-16}\ \text{cm}^2$.

5. DISCUSSION OF THE RESULTS

It is reasonable to interpret the obtained energy dependence of the effective cross section for H_3^+ ion production based on the statistical theory of ion–molecular reactions first used in [10] to analyze H_3^+ ion production in collisions between hydrogen molecules with H_2^+ ions. According to [10], reaction (4) proceeds via the formation of the H_4^{++} compound system. At the interaction energies of colliding molecules $W < 20$ eV, the energy of molecular electrons changes adiabatically, because the velocity at which the molecules approach each other, $V(H_2^+) \approx 3 \times 10^6$ cm/s, is much less than the electron velocity $V(e) \sim e^2/\hbar \approx 2 \times 10^8$ cm/s. Since the ion de Broglie wavelength is much less than the molecular size, the ion collisions can be described in the model of classical trajectories.

The total spin of a system consisting of two colliding H_2^+ molecular ions can be either 0 or 1, which allows one to speak about the singlet and triplet interaction potentials. When the distance between the ions approaches infinity, both potentials become the Coulomb potential. For the triplet interaction potential, an adiabatic collision between two H_2^+ molecules is not able to form an H_3^+ molecule, because this molecule, whose spin is equal to 1, is unstable and decomposes into an H atom and H_2^+ molecule. Hence, in the case of the triplet potentials, only channels (1)–(3) are feasible.

Characteristic of the singlet potential is that, as the ions approach each other, the Coulomb repulsion is replaced with van der Waals attraction, which results in a Coulomb barrier of finite height and a potential well of finite depth limited by the repulsion potential as the distance between the ions decreases further. A compound system forms when the ions occur in the potential well, i.e., when the distance between the H_2^+ ions becomes so small that the electron clouds of the ions start to overlap. This distance depends on both the mutual orientation of the H_2^+ molecular axes (linear, T-type, or collinear) and the position of the electron cloud in the molecule, which depends on the theoretical model of the H_2^+ molecule. In the chemical model, both the H atom and proton keep their individuality during the collision event and the molecule is regarded as a dumbbell with a charge concentrated on one of its ends; consequently, the gravity center of the molecule does not coincide with the center of charge. The quantum mechanical model implies that the electron cloud is distributed uniformly between the two nuclei; thus, each end of the dumbbell carries one-half of the positive proton charge and the center of the positive charge of the H_2^+ molecule resides exactly midway between the nuclei. As a result, within the quantum mechanical and classical models of the H_2^+ ion, the height of the Coulomb barrier and, therefore, the minimum interaction energy required to create a compound system turns out to be quite different because of the significant difference in the distances between the gravity center and the positive charge center.

For the singlet potential, the height of the Coulomb barrier can be easily determined assuming the Coulomb repulsion force to be equal to the van der Waals attraction force, because the repulsion characteristic of $R \longrightarrow 0$ does not yet come into play. If the mutual orientation of the molecules is linear, then the interaction energy required for the Coulomb barrier to be overcome during the formation of the H_4^{++} system is $W_q^{(4)} \approx 7.8$ eV in the quantum mechanical model, whereas in the chemical model, we have $W_{cl}^{(4)} \approx 5.1$ eV and the cross section is $\sigma \approx 0.3 \times 10^{-16}\ \text{cm}^2$. For the T-type mutual orientation of the axes, the chemical model predicts the threshold energy $W_{cl}^{(4)} \approx 8$ eV and a substantially higher cross section $\sigma^T \approx (1.5\text{–}2.0) \times 10^{-16}\ \text{cm}^2$. In the quantum model, the threshold for reaction (4) for the T-type configuration of the compound system is

$W_{q\perp}^{(4)} \approx 12$ eV. Finally, in collisions of molecules with parallel (collinear) axes, the classical and quantum mechanical models of an H_2^+ ion predict the thresholds $W_{cl\parallel}^{(4)} \approx 9$ eV and $W_{q\parallel}^{(4)} \approx 13$ eV, respectively. Figure 3 shows the qualitative dependences (calculated by the chemical model) of the singlet potential of the interaction between two H_2^+ ions on the distance between the ions for different mutual orientations of the ion axes.

Reaction (3), which is slightly endothermic, results in the production of two protons and also proceeds via the formation of an intermediate state. The threshold for reaction (3) is $W_{cl}^{(3)} \approx 5.8$ eV for the linear orientation of the molecules and $W_{cl\perp\parallel}^{(3)} \approx 9$ eV for the T-type and collinear orientations. In the quantum mechanical model, the corresponding thresholds for reaction (3) are $W_q^{(3)} \approx 8.6$ eV and $W_{q\perp\parallel}^{(3)} \approx 13$ eV.

The measured thresholds for reactions (2) [8] and (4) can be regarded as additional evidence in favor of the classical chemical approach to the description of the charge distribution in molecules during the collisions accompanied by ion–molecular reactions proceeding via the formation of intermediate states. A specific feature of the quantum mechanical model of an H_2^+ molecule is the averaging of the electron wave functions over the positions with respect to the nuclei. Here, a one-center wave function is actually used and the question as to how often the electron jumps from one center to another remains open. In the classical approach, a proton is attracted to an atom by the polarization force; as the proton moves deeper inside the electron cloud, this force decreases and Coulomb repulsion between the nuclei comes into play. Obviously, the equilibrium between nuclei in a molecule can only be dynamical; as the nuclei vibrate, the exchange of the electron cloud between them must correlate to the frequency of these vibrations. Since the duration of the collision event between H_2^+ ions in which the H_4^{++} compound system is produced is much shorter than the period of nuclei vibrations, the collision proceeds at a fixed instant distribution of the electron clouds rather than at an averaged quantum mechanical distribution. Interestingly, the ionization energy $I_{H_2^+} = 15.3$ eV of an H_2^+ molecular ion differs from the ionization energy of a hydrogen atom, $I_H = 13.6$ eV, by only about the potential energy of the vibrating nuclei, which is one-half of the dissociation energy $D = 2.7$ eV. According to [1, 2], these thermochemical estimates can be regarded as important evidence in favor of the classical model of the molecule structure. Moreover, for the two-center problem, the requirement that the classical electron orbits in a molecule be continuous unambiguously leads to the selection of the eight-shaped orbits correlating only to the oppositely directed angular moments about each center. This determines the choice of the electron wave function of the "binding orbital" type in an H_2^+ molecular ion. It is also important that, for the oppositely directed angular moments in an H_2 molecule, the currents in the region between the nuclei turn out to be parallel, which, according to the laws of electrodynamics, leads to the attraction between them. It is this attraction that seems to be the reason for the stability of the singlet states of diatomic molecules.

The obtained energy dependence of the effective cross section for H_3^+ production is resonant in character with a maximum at ~8 eV and a steep fall at $W \approx 10$–12 eV. Such a steep fall in the cross section for reaction (4) is related to the increasing role of direct reactions (1)–(3). Indeed, the dissociation of H_2^+ ions via these reactions can proceed by transferring the momentum directly to protons in molecules without the formation of H_4^{++} ions. Taking into account direct reaction (1) and especially reaction (2), whose thresholds, with allowance for Coulomb repulsion, lie just in the range 8–12 eV, the probability of producing the compound system is found to rapidly decrease. According to [6], this probability may even become zero when the interaction energy exceeds the threshold for reaction (4) by the so-called critical value.

The study of ion–molecular reactions with a Coulomb barrier may provide important information on the dynamics of electron clouds in molecules and crystals and their correlation with nuclear vibrations. The correlation between electron exchange and ion vibrations can be an important mechanism for nondissipative charge transfer in anisotropic media.

ACKNOWLEDGMENTS

We are grateful to N.N. Semashko, V.M. Kulygin, and Yu.M. Pustovoĭt for continuing interest and assistance in this work and to V.L. Stolyarov for providing the vacuum conditions of the experiments.

REFERENCES

1. W. Moffitt, Proc. R. Soc. London, Ser. A **210**, 245 (1951).
2. W. Moffitt, Proc. R. Soc. London, Ser. A **210**, 223 (1951).
3. J. Tilly and C. Truesdale, J. Chem. Phys. **65**, 1002 (1976).
4. E. E. Nikitin and S. Ya. Umanskiĭ, *Semiempirical Methods for Computing Atomic Interactions* (VINITI, Moscow, 1980); Itogi Nauki Tekh., Ser. Str. Mol. Khim. Svyaz' **7** (1980).
5. N. A. Bulavin, E. V. Bukharin, and V. G. Pevgov, Khim. Fiz., No. 12, 1718 (1982).
6. E. E. Nikitin, in *Theory of Elementary Atomic and Molecular Processes in Gases* (Khimiya, Moscow, 1970), p. 455.

7. V. A. Belyaev, M. M. Dubrovin, L. I. Men'shikov, and A. N. Khlopkin, Preprint No. 3762/12 (Institute of Atomic Energy, Moscow, 1983) [Preprint of INDC No. (CCP)-224/GA (IAEA, Vienna, 1984)].
8. V. A. Belyaev, M. M. Dubrovin, N. N. Semenov, and A. N. Khlopkin, Fiz. Plazmy **20**, 316 (1994) [Plasma Phys. Rep. **20**, 287 (1994)].
9. V. A. Belyaev, M. M. Dubrovin, and A. N. Khlopkin, Pis'ma Zh. Tekh. Fiz. **8**, 1399 (1982) [Sov. Tech. Phys. Lett. **8**, 601 (1982)].
10. O. B. Firsov, Zh. Éksp. Teor. Fiz. **42**, 1307 (1962) [Sov. Phys. JETP **15**, 906 (1962)].
11. D. R. Bates and G. Poots, Proc. Phys. Soc. London, Sect. A **66**, 784 (1953).
12. Amarjit Sen, J. W. McGowan, and J. B. A. Mitchell, J. Phys. B **20**, 1509 (1987).
13. W. A. Chupka and M. E. Russel, J. Chem. Phys. **49**, 5426 (1968).
14. Z. Herman and V. Pac'ak, Int. J. Mass Spectrom. Ion Phys. **24**, 355 (1977).
15. V. A. Belyaev, M. M. Dubrovin, A. A. Terent'ev, *et al.*, Fiz. Plazmy **27**, 955 (2001) [Plasma Phys. Rep. **27**, 901 (2001)].

Translated by N. N. Ustinovskiĭ

Plasma Physics Reports, Vol. 27, No. 12, 2001, pp. 1039–1047. Translated from Fizika Plazmy, Vol. 27, No. 12, 2001, pp. 1101–1110.

PLASMA DYNAMICS

Study of the Plasma in a Preformed Z-pinch Constriction

Yu. L. Bakshaev*, P. I. Blinov*, V. V. Vikhrev*, E. M. Gordeev*, S. A. Dan'ko*, V. D. Korolev*, S. F. Medovshchikov, S. L. Nedoseev**, E. A. Smirnova*, V. I. Tumanov*, A. S. Chernenko*, and A. Yu. Shashkov***

**Russian Research Centre Kurchatov Institute, pl. Kurchatova 1, Moscow, 123182 Russia*

***Troitsk Institute of Innovation and Fusion Research, Troitsk, Moscow oblast, 142092 Russia*

Received April 19, 2001

Abstract—The development of a preformed constriction in cylindrical agar-agar loads at currents of up to 3 MA is studied experimentally. The loads 3–5 mm in diameter have a mass density of 0.1 g/cm^3 and are filled with different materials. Due to the implosion of the constriction to a minimum size of 40–70 μm, a hot dense plasma (with the electron density $n_e = 10^{22}$ cm^{-3}, electron temperature T_e = 0.8–1.5 keV, and ion temperature T_i = 3–12 keV) is produced. It is found that the ion temperature substantially exceeds the electron temperature. The lifetime of the high-temperature plasma determined from the FWHM of a soft X radiation (SXR) pulse is shorter than 5 ns, the radiation power of photons with energies of ≥1 keV is higher than 0.5×10^{10} W, and their total energy attains 50 J. High-speed photography in the VUV, SXR, and optical spectral regions indicates the protracted generation of the high-temperature plasma. Calculations by the two-dimensional ideal MHD model of the Z-pinch show that the most important consequence of the protracted plasma generation in the constriction region is that the current is intercepted by a freshly produced plasma. In the course of plasma generation, the current near the axis inside the region of radius 50 μm is at most one-half of the total current. After the plasma generation comes to an end, almost the entire current is concentrated in this region for several nanoseconds; this process is accompanied by a sharp increase in the plasma temperature. © *2001 MAIK "Nauka/Interperiodica".*

1. INTRODUCTION

The first studies on Z-pinches revealed that regions emitting intense X radiation arise on the axis of the plasma column [1]. Experiments with deuterium showed that these regions also emit neutrons [2].

Investigations demonstrated that, in the emitting regions, the density and temperature of the plasma are substantially higher than those in the bulk pinch plasma. The high-temperature plasma is produced because of the MHD instability of the pinch and usually appears in the regions where constrictions are formed.

In connection with the observed increase in the plasma temperature in constrictions, it was proposed to use this effect to initiate a thermonuclear burning wave along the pinch [3, 4]. To ignite a thermonuclear fuel, it is necessary to produce one deep constriction with the plasma temperature and density as high as possible. In this case, the energy spent on creating the pinch will be compensated for by heat released during the propagation of the thermonuclear burning wave. Numerical calculations [5] show that, in order to ignite a thermonuclear burning wave along the Z-pinch, it is necessary to produce a plasma with a temperature of above 5 keV in a micron-sized pinch constriction.

At present, experiments are being conducted at the RRC Kurchatov Institute with the purpose of studying the possibility of producing a high-temperature plasma in a fast Z-pinch with the help of a preformed constriction. The first experiments on plasma compression carried out in the Module A 5-01 facility operating in the low-resistance mode [6] demonstrated the development of a deep constriction [7–9]. These experiments were conducted at currents of 0.8–1.5 MA with the use of profiled dielectric loads. Operation in the range of currents of 3–5 MA, attainable in modern facilities, offers the opportunity of further increasing such plasma parameters in the constriction as ρr (where ρ is the mass density and r is the radius) and the temperature T, which are important for ignition.

In this paper, we present the results from experimental studies of a plasma produced by the current flowing through profiled cylindrical agar-agar loads. Experiments were carried out in the S-300 facility at currents of 2–3 MA with a rise time of $\tau \approx 100$ ns [10].

2. DESCRIPTION OF THE EXPERIMENT

Experiments on the dynamics of a constriction in a high-density Z-pinch were carried out in the S-300 facility. The S-300 eight-module generator, which was created and put into operation at the RRC Kurchatov Institute in 1995, is intended for experimental research on inertial confinement fusion. This facility is capable of producing electric pulses with an energy of 300 kJ, a voltage of 1.3 MV, and a duration of 70 ns.

A high-voltage pulse produced by a forming system (*1*) is fed through an insulator 1 m in diameter (*2*)

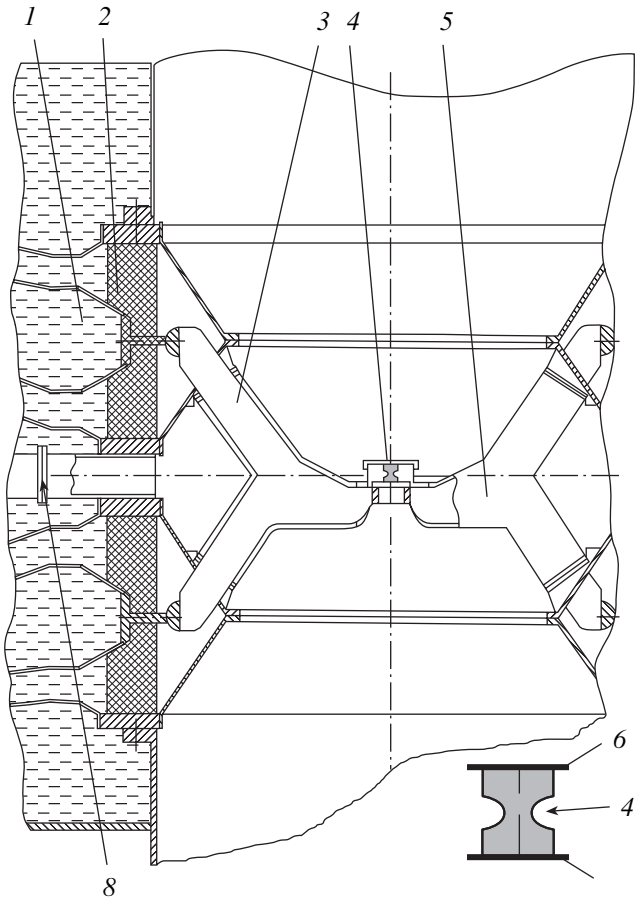

Fig. 1. Output unit of the S-300 facility: (*1*) water transmission lines, (*2*) insulator, (*3*, *5*) concentrator MITLs, (*4*) target unit with the load, (*6*) anode, (*7*) cathode, and (*8*) diagnostic tube.

to a vacuum energy concentrator (Fig. 1). The concentrator is built from vacuum magnetically insulated transmission lines (*3*, *5*) connected in parallel and joined in a target unit (*4*), in which the load (Z-pinch) is located. The interelectrode gap in the magnetically insulated lines of the concentrator is 1 cm, and the maximum electric field attains 500 kV/cm. The output inductance of the generator (the concentrator with the insulator and the target unit) is 14 nH. Under short-circuit conditions and at a voltage of 700 kV in the incident wave, a 4-MA current pulse with a 70-ns rise time was produced. The current through the physical load (liner) was higher than 3.5 MA, and the current through the Z-pinch attained 3.1 MA at a rise time of $\tau \approx 100$ ns.

As loads, we used profiled cylindrical agar-agar cylinders 5–10 mm in height and 3–5 mm in diameter with a preformed constriction 0.1–1 mm in diameter. Carbon-filled agar-agar loads, whose initial density could vary over a wide range from atmospheric-gas density to solid density (0.005–1 g/cm^3), were manufactured based on the technology elaborated at the Troitsk Institute of Innovation and Fusion Research [11]. In some experiments, we used deuterated polyethylene as a filling material. The use of agar-agar loads allowed us to model the dynamics of compression of condensed hydrogen at lower currents and, additionally, to efficiently transfer the energy from the generator to the load.

With the output resistance of the S-300 generator matched to the load, the inductance of the target unit was no higher than 6 nH. The loads were positioned along the axis of the target unit between two truncated stainless-steel cones with vertexes facing each other (Fig. 1). The cones were electrodes of the discharge gap; the distance between them could be varied from 6 to 10 mm. In some experiments, the filament material was doped with diagnostic additives of heavier elements (chlorine, copper, or potassium) in proportions of 1–10% of the number of atoms. To study the plasma compression in the Z-pinch constriction and to measure the plasma parameters, we used various X-ray diagnostics (Fig. 2).

The plasma temperature and density were deduced from the ratio between the intensities of hydrogen lines and helium-like ion lines (resonant and intercombination lines). The ion temperature was deduced from the Doppler broadening of spectral lines. The X-ray spectrum was measured with a spectrograph with a convex

cylindrical mica crystal [12]. Even for a small angular size of the source, the convex crystal of the X-ray spectrograph allowed observations over a wide spectral range from 2.5 to 13 Å, which usually included two to three orders of reflection of the lines. The width of an individual spectral line was determined by both its proper spectral width (predominantly, related to Doppler broadening) and the diameter of the radiation source. Depending on the order of reflection, the contribution to the line width from the spectral component increases, whereas the contribution from the geometric size of the source remains constant. This circumstance makes it possible to separate the geometric and spectral contributions to the line width [13]. The crystal generatrix was parallel to the Z-pinch axis. A horizontal slit 0.5 mm wide was positioned in front of the spectrograph so as to form the longitudinal image of the Z-pinch. The smaller scale of an individual point of the image was evaluated from the width of the image boundary (half-shadow). Beryllium and polypropylene foils of width 20 and 2 μm, respectively, were placed at the entrance to the spectrometer. The spectrum was recorded on a Kodak DEF film. The spectrograph was placed inside a protective lead case.

The dynamics of the plasma parameters was deduced from the discharge emission in the photon energy range 0.05–10 keV. VUV radiation and soft X radiation (SXR) were measured with vacuum photoemission detectors with aluminum photocathodes equipped with different filters. Structurally, the detectors were joined in vacuum units containing two or four detectors. The photoemission detectors were located in a diagnostic tube (*8*) (Fig. 1) at a distance of 0.9–3 m from the load axis.

The structure of the radiating plasma was determined with the help of time-integrated and frame photography. For time-integrated photography, we used pinhole cameras with apertures of 20, 50, and 100 μm; the magnification varied from 1.25 to 4. The highest resolution on the object was 40 μm for a magnification of 1.25 and a pinhole aperture of 20 μm.

For the frame photography of the plasma in the VUV and SXR spectral regions, we used a system of three X-ray image tubes. The spatial and time resolutions of the system were 100 μm and 3 ns, respectively. To study the character of the electric breakdown in the load and to trace the further behavior of the plasma in the visual spectral region, we used frame photography with image tubes (with a frame exposure of 5 ns) and high-speed streak-camera imaging. The time resolution of the streak camera was 1 ns, and its spatial resolution was 0.05 mm. In these experiments, the Z-pinch was traced in both the radial and axial directions.

Concurrently with the radiation pulses, we measured the electric parameters of the discharge gap: the voltage, current, and current time derivative at the entrance to the target unit.

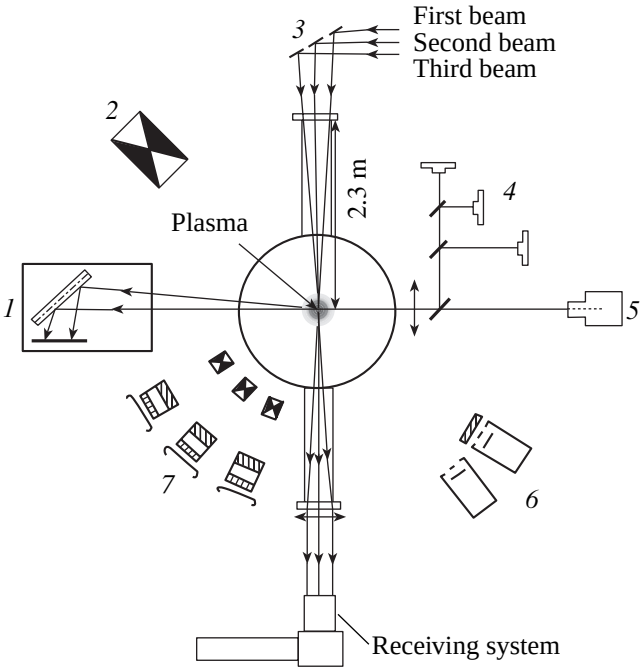

Fig. 2. Experimental arrangement: (*1*) crystal spectrograph, (*2*) pinhole camera, (*3*) laser, (*4*) three-frame electron-optical system, (*5*) high-speed streak camera, (*6*) VUV diodes, and (*7*) three-frame X-ray electron-optical system.

To study the evolution of the peripheral plasma, we used laser probing, which provided two-frame shadow or schlieren photographs of the object. The probing was performed at the second harmonic of a YAG : Nd laser at a wavelength of 532 nm with a 50-ns pause between the frames. The laser pulse duration was 10 ns, and the pulse energy was 20 mJ.

3. EXPERIMENTAL RESULTS

In experiments on the dynamics of plasma compression in the Z-pinch constriction, the energy of the incident wave fed to the concentrator was 100 kJ. The best matching between the generator and the agar-agar load with an initial diameter of 3–5 mm was achieved when the load height was 8–10 mm; in this case, the current attained 3 MA (Fig. 3). In these experiments, the mass density of loads varied from 0.05 to 1 g/cm^3. The initial diameter of the constriction was 0.5–1 mm. The mass per unit length in the constriction varied from 0.1 to 5 mg/cm. To provide high plasma parameters, which depend substantially on the current, it was necessary to achieve the matching between the plasma compression time and the current rise time. For loads with a density of 0.1 g/cm^3, the matching was achieved at initial constriction diameters less than 1 mm.

It was found that the process of plasma formation after the electric breakdown of carbon-filled agar-agar loads depended substantially on the initial density and radius of filaments. At initial densities lower than

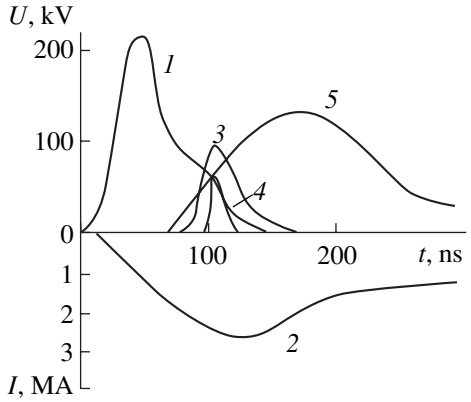

Fig. 3. Waveforms of (*1*) the voltage, (*2*) current, and SXR signals obtained with (*3*) 5-μm Dacron and (*4*) 10-μm Mylar filters and (*5*) without filters for an agar-agar load filled with carbon at a density of 0.1 g/cm^3 and an initial constriction diameter of <1 mm.

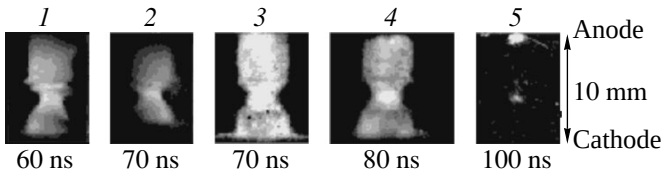

Fig. 4. Image-tube photographs of the agar-agar load in (*1*, *2*) the optical and (*3*, *4*, *5*) VUV–SXR spectral regions. Time is counted from the beginning of the current pulse.

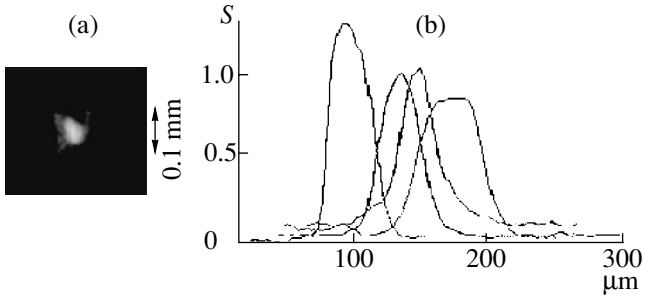

Fig. 5. (a) Pinhole photograph of the constriction region obtained with a 12-μm Mylar filter and (b) densitograms of the constriction produced by the compression of the agar-agar load filled with graphite at a density of 0.1 g/cm^3 and an initial constriction diameter of <1 mm.

5×10^{-2} g/cm^3 (which were close to those in experiments carried out in the Module A 5-01 facility) [14], a plasma corona with a diameter exceeding the load diameter was formed. The arising hot points were chaotically located in the volume occupied by a low-density plasma. In optical streak camera images obtained with axial tracing, it is seen that, at the beginning of the process, bright channels with diameters approximately equal to 1 mm arise. These channels exist for a long time during the discharge, the number of channels being no larger than 4–5. The transverse size of most of the bright channels changes slightly with time; only some of them expand in the axial direction with a velocity of 10^6 cm/s.

As the initial density increased to 0.1 g/cm^3, the integral pinhole photographs and the photographs obtained with X-ray image tubes showed the formation of a hot and dense plasma in the region of the preformed constriction (Figs. 4, 5), as was previously observed in experiments performed in the Module A 5-01 facility [7, 9]. The minimum constriction size was reached when the current was close to its maximum value. After the maximum compression, the plasma in the constriction began to expand.

In streak camera images obtained with axial tracing, it is seen that, against a rather intense radiation background, a bright region less than 1 mm in size arises and, then, 130 ns from the beginning of the current pulse, is split into two bright regions moving in the axial direction (Fig. 6a). The mean propagation velocity of the bright regions moving apart is 2×10^6 cm/s. In some experiments, the splitting and axial motion of bright regions were not observed. In streak camera images obtained with radial tracing, it is seen that the transverse size of the bright region is equal to 1 mm and does not vary for 100 ns. Then, the plasma begins to expand with a velocity of 2×10^6 cm/s in the radial direction (Fig. 6b). In streak camera images obtained with radial tracing, it is seen that the emission intensity sharply increases by the time when the current is close to its maximum value. The observed phase of intense emission lasts for 10–15 ns. Before the phase of the maximum emission intensity, while the current was increasing, we observed short bright bursts lasting for several nanoseconds.

This behavior of the plasma emission may be explained by the fact that the formation of a plasma from the solid phase of the agar-agar load takes a rather long time; the plasma also forms gradually and moves toward the axis over a rather long time close to the current rise time. In this case, the current is distributed in space between the axis and the pinch boundary. The character of the emission from the load constriction region observed in the frame photographs obtained with optical and X-ray image tubes also indicates the protracted plasma formation in the constriction (Fig. 4). In these photographs, it is seen that, up to 80 ns, the constriction size varies only slightly; 20 ns later, a bright point arises. A similar character of the formation of hot points was also observed in [7, 9].

The plasma compression is accompanied by the generation of SXR pulses. Figure 3 shows VUV signals behind a 12-μm Mylar filter (12 μm Dacron + 0.1 μm aluminum) and a 5-μm Dacron filter and also an unfiltered signal. The instant at which the hot plasma

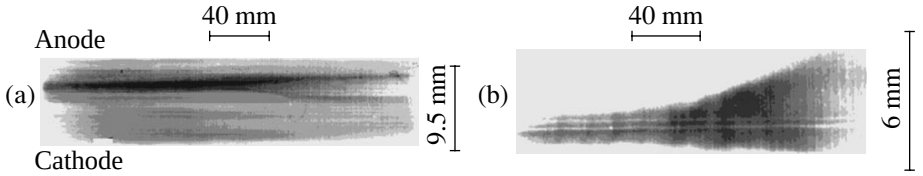

Fig. 6. Optical streak camera images obtained with (a) axial and (b) radial tracing.

appears is determined from the time when the SXR signal reaches its amplitude value (behind the 12-μm Mylar filter); this time corresponds to the maximum current. Note that the VUV diode with the 12-μm Mylar filter is most sensitive to photons with energies of 2 keV. The lifetime of the hot plasma determined from the FWHM of the SXR signal was shorter than 5 ns. The radiation power of photons with energies of 2 keV is higher than 5×10^9 W, and their total energy is 20–50 J.

In integral photographs obtained with the 12-μm Mylar filter (the corresponding cutoff energy at a level of 0.1 is 1.5 keV), it is seen that, a plasma with a minimum size of 40–70 μm is formed as a result of compression (Fig. 5). The measurements of the width of a half-shadow of the edge of the horizontal slit give a close value of the hot-plasma size: 60–70 μm.

The electron temperature and density in the constriction region were calculated by the collision-radiative model with allowance for the re-emission in lines [15]. Estimates by this model give the electron temperature T_e = (0.8–1.5) keV, ion temperature T_i = (1–12) keV, and electron density $n_e = (0.3–1) \times 10^{22}$ cm^{-3}. The characteristic emission spectrum from potassium and chlorine impurity ions is shown in Fig. 7. As is seen from the table, the ion temperature is substantially higher than the electron temperature.

Estimates for the relaxation times τ_{ee}, τ_{ii}, and τ_{ei} show that, for the measured plasma density, thermal equilibrium should be established both in the electron component and between the ions of different species. However, thermal equilibrium between the ions and electrons is not reached.

We note that the plasma parameters at the end of the compression depend substantially on the constriction profile. The highest plasma parameters are obtained with a constriction shaped like two truncated cones with the vertexes facing each other and the apex angle not exceeding 90°. For the load-material mass density close to the solid mass density, the formation of a hot plasma was observed in the region of the preformed constriction when the diameter of the constriction was less than 0.5 mm [14]. The compression was accompanied by a sharp increase in the voltage and the appearance of characteristic spikes in the filtered VUV signals. The typical size of the compressed plasma was on the order of 100 μm. For a load with a mass density of 1 g/cm^3, the plasma parameters (density and temperature) were substantially lower than those for loads with a mass density of 0.1 g/cm^3.

The dynamics of a relatively low-density peripheral plasma was studied with the help of two-frame shadow and schlieren photographs. The shadow photographs of the Z-pinch plasma are shown in Fig. 8a. Assuming that laser radiation is absorbed due to inverse bremsstrahlung, the electron density can be estimated as $n_e \geq 10^{19}$ cm^{-3}. The plasma velocity in the constriction region is at most 10^5 cm/s, and the velocity of the ejected plasma at the Z-pinch periphery is on the order of 4×10^6 cm/s. Schlieren photographs are presented in Fig. 8b. As a mask, we used a disk 1.5 mm in diameter positioned at the lens focus; this allowed us to measure the gradients in all directions lying in the plane perpendicular to the probing beam. The measured gradients lie within the range 4×10^{19} cm$^{-4} \leq |\text{grad} n_e| \leq 3 \times 10^{20}$ cm^{-4}. The velocity of the ejected plasma is close to that

Parameters of the high-temperature plasma

Experiment no.	Load composition	Z of the diagnostic additive	T_e, eV	T_i, eV	n_e, cm^{-3}	Plasma diameter, mm
1	Agar-agar(25%) + C(60%) + KCl(15%)	17	931	12014	3.72×10^{21}	0.34
1, another point	–	19	1330	3865	4.96×10^{21}	0.48
2	–	17	1172	8328	2.05×10^{21}	0.48
3	Agar-agar(35%) + C(60%) + $CuCl_2$(5%)	17	804	13614	1×10^{22}	0.3

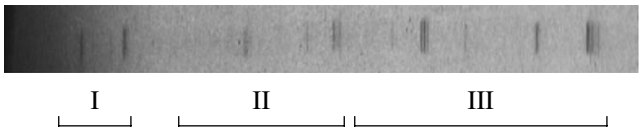

Fig. 7. X-ray spectrum of potassium and chlorine impurity ions for three orders of reflection.

obtained from the shadow photographs and is equal to $(4–5) \times 10^6$ cm/s.

4. MODELING OF THE PINCH DYNAMICS WITH ALLOWANCE FOR THE PLASMA FORMATION

An important feature of the compression of a Z-pinch produced using the filled agar-agar load is a gradual (rather than instantaneous) conversion of the load material into plasma. Therefore, when modeling the discharge, we should take into consideration not only the plasma dynamics, but also the dynamics of a neutral gas produced by the evaporation of the load material.

The problem of the gradual formation of the plasma shell of the pinch, including the entrainment of the neutral gas by the plasma shell, was analyzed in [16, 17] in the three-fluid model. These papers were devoted to discharges in hydrogen. It was shown that neutral (unionized) hydrogen is rather easily involved in motion due to charge exchange. As a result, the weakly ionized plasma shell moves to the axis of the system as a single entity.

A somewhat different situation occurs when the plasma is produced from agar-agar. The agar-agar load consists of chaotically placed solid filaments ~10 μm in diameter and a filling material (typically, carbon) between them. In the discharge, both the filament and the filling material gradually evaporate, rather than instantaneously convert into a plasma. The gas produced by evaporation is also gradually ionized and converted into a plasma. If the time needed for the material evaporation and plasma formation is comparable with the discharge current rise time, it is necessary to take into account the continuous generation of the plasma in the interelectrode space. For available pinch discharges, the time needed for the load material to be converted into a plasma is comparable to the current rise time (~100 μs). The most important consequence of the continuous plasma generation in the interelectrode gap is that the current is intercepted by a freshly generated plasma.

In [18], a different, simpler model was used to analyze the evolution of a wire liner. It was assumed that the wire liner is gradually converted into a gas and, then, into a plasma. The neutral gas of the evaporated liner material was assumed to be at rest until it was converted into a plasma. This approach simplifies the simulation, because it does not require a description of the motion of the neutral component. Here, we use a similar simplification.

Calculations were performed for the S-300 experimental conditions by the ideal two-dimensional Z-pinch model described in [17]. The discharge current in the circuit was taken from experiment (Fig. 3). The load configuration is shown in Fig. 9a. The initial constriction radius was 0.5 cm, and the initial material density was 0.1 g/cm^3.

The time evolution of the agar-agar load depends on both the incident radiation power and the heat transfer due the heat conduction to the evaporated material [19]. At present, simulations of plasma generation in the discharge encounter difficulties. To simplify calculations, it was assumed that the load material is converted into a plasma in a certain characteristic time τ_{ev}. The rate of the load evaporation and conversion into a plasma depends on the radiation power and the neutral (still unionized) load material. The radiation power is approximately proportional to the heat energy contained in the pinch plasma. Since the pinch heat energy is determined by the current squared and the pinch current grows linearly with time, the rate of the plasma for-

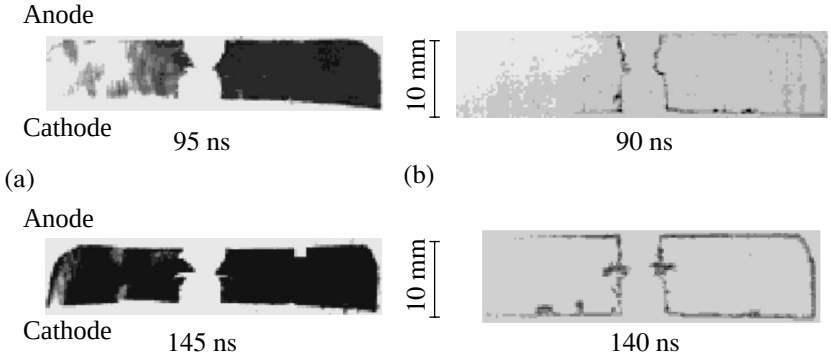

Fig. 8. (a) Shadow and (b) schlieren photographs. Time is counted from the beginning of the current pulse.

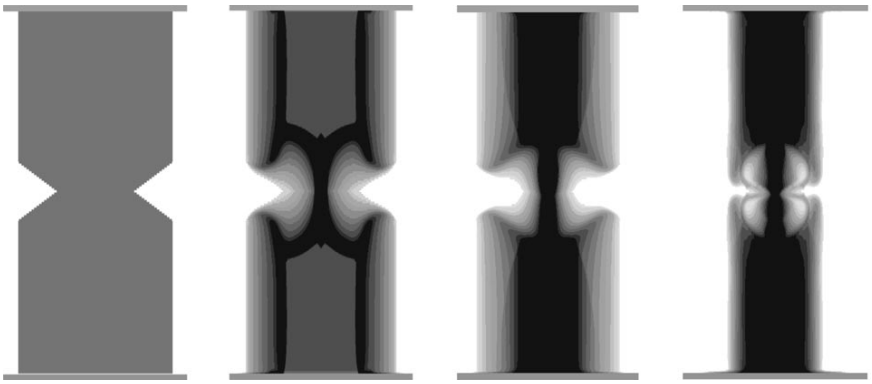

Fig. 9. (a) Configuration of the agar-agar load and (b)–(d) the electron density distribution at different times after the beginning of discharge.

mation in the space filled with the load material can be written in the form $d\rho/dt = 2\rho t^2/\tau_{ev}^3$, where ρ is the agar-agar mass density. The plasma density increases due to evaporation only in the regions containing the load material.

Calculations were performed with different characteristic times τ_{ev}. From a comparison of the calculated and experimental compression times, it was found that the load material in the constriction region has time to be converted during the current rise time. The best agreement between the experiment and simulations was achieved with the evaporation time τ_{ev} = 80 ns.

Figures 9b–9d show the electron density distributions at times 40, 60, 80, and 83 ns. Calculations show that the pinch is compressed and the current-carrying shell arrives at the pinch axis rather rapidly (by 36 ns). Then, the pinch compression stops. However, the pinch remains stable up to 80 ns and the development of the constriction does not lead to the pinch breaking. The stability of the pinch from 40 to 80 ns is explained by the fact that the gas surrounding the pinch flows into the pinch compression region and the number of particles in the cross section of the pinch near the constriction region does not decrease. After 80 ns, the process of plasma formation comes to an end and the pinch becomes unstable, so that, 3 ns later, a pronounced constriction is observed (Fig. 9d).

Figure 10 shows the radial profiles of the current density in the cross section of the constriction at t = 30 and 80 ns. At t = 30 ns, the current-carrying shell is seen to converge on the pinch axis. Besides a thin current layer pushing the plasma, we can see a small peak of the current density at a radius of 0.045 cm. This small current peak arises because it is necessary to accelerate a freshly generated plasma to the radial drift velocity $v = cE/B$, where $E(r)$ is the z-component of the electric field and $B(r)$ is the magnetic field in this region.

The current profile at t = 80 ns is typical of the main phase of the discharge from 36 to 80 ns. During this period of time, a fraction of the total current compresses the pinch plasma column near the axis (r < 0.15 mm). Another peak of the current density is located in the plasma-generation region (r = 0.25–0.5 mm). Characteristically, the current density increases toward the boundary of the plasma-generation region. This current peak exists while a plasma is being formed from the load material. The value of the current intercepted by the outer part of the plasma shell can be seen in the profiles of the current through the region of a given radius (Fig. 11). It is seen in Fig. 11 that from 10 to 50% of the total current is concentrated near the axis, and the remaining current is distributed in the plasma-generation region. After the process of plasma generation comes to an end, the current is rapidly redistributed and most of the current is concentrated in the constriction region (see the profile at 100 ns in Fig. 11).

Note that, in the region from 0.15 to 0.2 mm, the current is negative. In this region, a low-density plasma

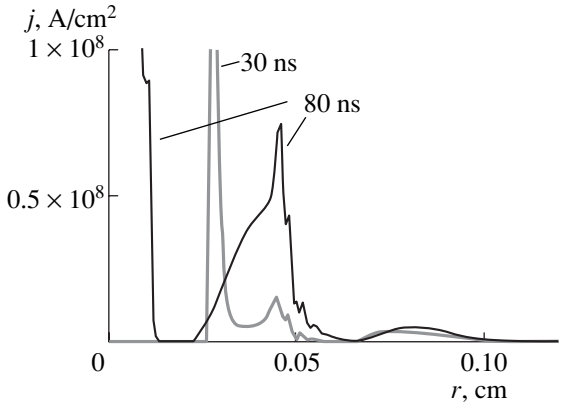

Fig. 10. Radial profiles of the current density in the constriction region at times of 30 and 80 ns.

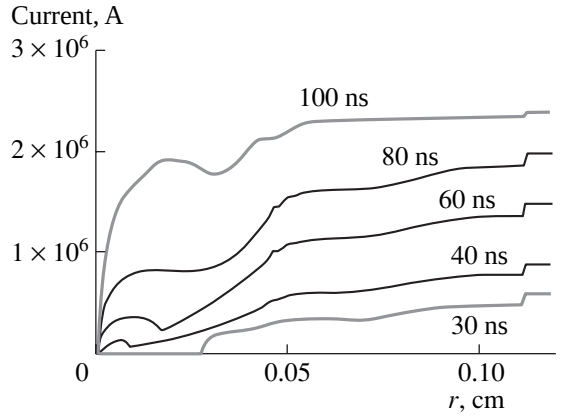

Fig. 11. Current through the pinch region of radius r in the cross section of the constriction, $I = Br/2c$, at different times.

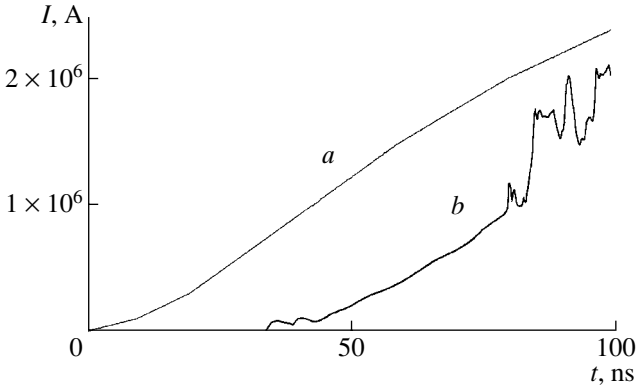

Fig. 12. Time evolution of (*a*) the discharge current and (*b*) the current through the region of radius 50 μm in the cross section of the constriction.

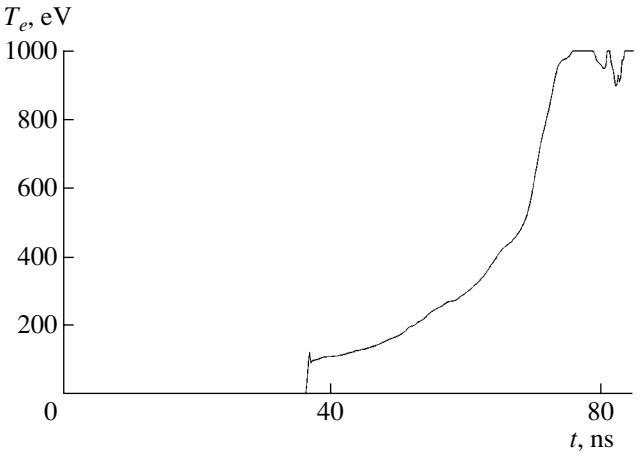

Fig. 13. Time behavior of the plasma temperature in the center of the constriction.

moving from the periphery enters the compressed pinch region and is slowed down because of both collisions with the slowly moving plasma in front of it and the compression of the frozen-in magnetic field of the current. The magnetic field pressure in this region pushes the plasma away from the axis, which is reflected in the negative electric current in this region.

The time variations in the total current and the current through the region of radius 100 μm are shown in Fig. 12. It is seen that the current at the axis arises when the plasma shell arrives there and then increases as the total current increases. However, the total current in this region is no higher than 50% of the total current during plasma generation. As soon as the plasma generation comes to an end, the current becomes almost totally concentrated inside the region of radius 100 μm (Fig. 12).

Figure 13 shows the time behavior of the plasma temperature in the central part of the load, where a high-temperature plasma emitting SXR is usually observed. It is seen that, when the plasma shell arrives at the axis (at t = 36 ns), the plasma temperature increases abruptly to ~100 eV. Then, the temperature slowly increases and the high temperature (above 1 keV) is reached only after the process of plasma generation comes to an end. During a relatively long period of time (from 36 to 80 ns), the plasma continuously flows into the constriction region in the radial direction and leaves this region through the ends. In this case, the number of particles in the constriction cross section varies only slightly, because it is governed by the balance between the plasma inflow in the radial direction and its outflow along the axis.

Thus, our investigations show that the process of gradual plasma generation stabilizes the Z-pinch against the formation of a constriction. This ensures the existence of a stable plasma pinch while the pinch current grows to its maximum level (~2.3 MA). After the plasma generation comes to an end, the pinch becomes unstable and the further development of the constriction occurs at the maximum pinch current.

5. CONCLUSION

Experiments performed in the S-300 facility have shown that, at a current of 3 MA (as well as in the previous experiments with a current of 1.5 MA [7]), a deep constriction develops in the region of the preformed neck. The compression of agar-agar loads leads to the formation of a high-temperature plasma region of size 40–70 μm. The time needed for the high-temperature plasma to be formed in the profiled load is comparable to the current rise time. The highest plasma parameters, $n_e = 10^{22}$ cm^{-3} and T_e = 1.5 keV, are obtained using the loads with initial mass densities of 0.1 g/cm^3. The lifetime of the high-temperature plasma is 5 ns. The power and total SXR energy in the photon energy range >1 keV are equal to 5×10^9 W and 20–50 J, respec-

tively. It is found that the ion temperature substantially exceeds the electron temperature; the ion temperature measured from the Doppler broadening of lines is in the range 3–13 keV. Laser probing shows that a peripheral plasma with a relatively low density ($n_e \le 10^{19}$ cm^{-3}) is slow-moving; its mass velocity during the current rise phase is no higher than 2×10^5 cm/s. The high-speed photography in the VUV, SXR, and visible spectral regions shows that the plasma generation is protracted. Shot-time plasma flows are carried away from the constriction region to the load axis over several nanoseconds.

The calculations show that, because of the material evaporation, a fraction of the current is intercepted by the peripheral plasma. The current flowing through the peripheral plasma reduces the magnetic field pressure at the pinch shell by a factor of 2.

The compression of the ionized plasma occurs at a rather early stage (40 ns). Then, during a relatively long period of time (from 40 to 80 ns), the number of particles in the constriction cross section varies only slightly and the pinch remains stable. After the plasma generation comes to an end, the pinch becomes unstable and further development of the constriction results in the appearance of a high-temperature plasma at the pinch axis. The process of gradual plasma formation stabilizes the Z-pinch against the formation of a constriction. This ensures the existence of a stable pinch while the pinch current grows to its maximum value.

ACKNOWLEDGMENTS

This work was supported in part by the Russian Foundation for Basic Research, project no. 99-02-16658.

REFERENCES

1. L. A. Artsimovich, M. A. Andrianov, O. A. Bazilevskaya, *et al.*, At. Énerg. **3**, 76 (1956).
2. S. V. Trussillo, B. Ya. Guzhovskiĭ, N. G. Makeev, and V. A. Tsukerman, Pis'ma Zh. Éksp. Teor. Fiz. **33**, 148 (1981) [JETP Lett. **33**, 140 (1981)].
3. V. V. Vikhrev and V. V. Ivanov, Dokl. Akad. Nauk SSSR **282**, 1106 (1985) [Sov. Phys. Dokl. **30**, 492 (1985)].
4. V. V. Yan'kov, Fiz. Plazmy **17**, 521 (1991) [Sov. J. Plasma Phys. **17**, 305 (1991)].
5. V. V. Vikhrev and G. A. Rozanova, Fiz. Plazmy **19**, 76 (1993) [Plasma Phys. Rep. **19**, 40 (1993)].
6. E. M. Gordeev, V. V. Zazhivikhin, V. D. Korolev, *et al.*, Fiz. Plazmy **19**, 1101 (1993) [Plasma Phys. Rep. **19**, 574 (1993)].
7. E. M. Gordeev, S. A. Dan'ko, Yu. G. Kalinin, *et al.*, in *Proceedings of the 4th International Conference on High-Power Particle Beams, San Diego, 1994*, Vol. 1, p. 167.
8. L. E. Aranchuk, S. A. Dan'ko, A. V. Kopchikov, *et al.*, Fiz. Plazmy **23**, 215 (1997) [Plasma Phys. Rep. **23**, 194 (1997)].
9. E. M. Gordeev, S. A. Dan'ko, Yu. G. Kalinin, *et al.*, Fiz. Plazmy **24**, 982 (1998) [Plasma Phys. Rep. **24**, 916 (1998)].
10. A. S. Chernenko, Yu. G. Gorbulin, Yu. G. Kalinin, *et al.*, in *Proceedings of the 11th International Conference on High-Power Particle Beams, Prague, 1996*, Vol. 1, p. 154.
11. S. L. Nedoseev, in *Proceedings of the International School of Plasma Physics, Varenna, Italy, 1989*, p. 575.
12. S. A. Dan'ko, in *Proceedings of the 12th International Conference on High-Power Particle Beams, Haifa, Israel, 1998*, Vol. 2, p. 459.
13. S. A. Dan'ko and A. A. Kvitchenko, Preprint No. 6154/7 (RRC Kurchatov Institute, Moscow, 1999).
14. Yu. L. Bakshaev, P. I. Blinov, A. S. Chernenko, *et al.*, in *Proceedings of the 18th Symposium on Plasma Physics and Technology, Prague, 1997*, p. 50.
15. S. A. Dan'ko and O. N. Yartseva, Preprint No. 4515/7 (Kurchatov Inst. of Atomic Energy, Moscow, 1987).
16. V. V. Vikhrev and S. I. Braginskii, in *Reviews of Plasma Physics*, Ed. by M. A. Leontovich (Atomizdat, Moscow, 1980; Consultants Bureau, New York, 1986), Vol. 10.
17. S. I. Ananin, V. V. Vikhrev, and N. V. Filippov, Fiz. Plazmy **4**, 315 (1978) [Sov. J. Plasma Phys. **4**, 175 (1978)].
18. V. V. Aleksandrov, A. V. Branitsky, G. S. Volkov, *et al.*, Fiz. Plazmy **27**, 99 (2001) [Plasma Phys. Rep. **27**, 89 (2001)].
19. A. É. Bugrov, I. N. Burdonskiĭ, V. V. Gavrilov, *et al.*, Zh. Éksp. Teor. Fiz. **111**, 903 (1997) [JETP **84**, 497 (1997)].

Translated by N. F. Larionova

Plasma Physics Reports, Vol. 27, No. 12, 2001, pp. 1048–1056. Translated from Fizika Plazmy, Vol. 27, No. 12, 2001, pp. 1111–1120.

PLASMA DYNAMICS

Acceleration of Dense Electron Bunches at the Front of a High-Power Electromagnetic Wave

A. S. Il'in*, V. V. Kulagin, and V. A. Cherepenin***

**Institute of Radio Engineering and Electronics, Russian Academy of Sciences, Mokhovaya ul. 18, Moscow, 103907 Russia*

***Sternberg Astronomical Institute, Moscow State University, Universitetskiĭ pr. 13, Moscow, 119899 Russia*

Received April 13, 2001; in final form, May 26, 2001

Abstract—The acceleration of dense electron bunches (e.g., those produced by the ionization of thin films) at the front of a high-power electromagnetic wave in vacuum is considered. It is shown that the reaction force of the intrinsic radiation of a bunch can play a significant role in the acceleration process because it gives rise to an additional accelerating force acting on the bunch and to forces that compress the bunch in the longitudinal direction. As a result, all of the bunch electrons can be synchronously accelerated during the first several half-periods of the external electromagnetic field. © *2001 MAIK "Nauka/Interperiodica".*

1. INTRODUCTION

In recent years, much attention has been devoted to the problem of electron acceleration by superintense laser pulses in vacuum [1–12]. Such problems are usually solved by investigating the propagation dynamics of an individual electron in the field of a high-power electromagnetic wave, in which case, in the equations of motion, the own radiation of the electrons and other collective effects are neglected.

The behavior of an individual electron in the field of a moderate-intensity electromagnetic wave (with the dimensionless amplitude $\alpha_0 = eE/mc\omega \le 1$, where e and m are the charge and mass of an electron, c is the speed of light, and E and ω are the amplitude and frequency of the electromagnetic field) is most often described by the ponderomotive potential model [1–7, 10], in which the electron motion is assumed to be a superposition of a relatively slow drift and rapid oscillations related to the fast changes in the wave phase at the instantaneous position of the electron. For superintense laser pulses achievable at the present time [13], we have $\alpha_0 \gg 1$, so that the ponderomotive potential model is inapplicable: the electron is already efficiently accelerated during the first half-period of the external field, while the field phase along the electron trajectory changes slowly.

Recently, new methods have been developed that make it possible to produce dense electron bunches by ionizing solid-state thin-film targets by ultrashort laser pulses [14], in which case the electron density in the bunches can be as high as the electron density in solids. In order to describe the acceleration of such electron bunches by a superintense ($\alpha_0 \gg 1$) laser field in vacuum, it is necessary to use new approaches, because, on the one hand, the ponderomotive potential model is inapplicable and, on the other hand, the self-action of the bunch via intrinsic radiation may be significant and, thus, should be taken into account in the analysis of the bunch motion.

In this paper, we study (both numerically and analytically) how a dense electron bunch produced by the ionization of a thin-film target is accelerated at the front of a superintense ($\alpha_0 \gg 1$) electromagnetic wave in vacuum. We take into account radiation effects and assume that the target ions are immobile.

The nonlinear electrodynamic effects in the interaction of high-power laser pulses with thin foils, such as harmonic generation and the change (sharpening) of the laser pulse shape, were considered, e.g., in [12, 15].

2. QUALITATIVE ESTIMATES

We start by considering some characteristic features of a model description of the collective radiative interaction between electrons. The idea of collective methods of charged particle acceleration was first originated in the mid-1950s by V.I. Veksler [16]. Let an electromagnetic pulse be incident on a dense electron bunch of volume V. For simplicity, we assume that the bunch dimensions in all directions are much smaller than the wavelength λ of the incident radiation. In order to estimate the role of collective effects, we begin by neglecting Coulomb repulsive forces between the bunch electrons. In other words, we assume that all electrons move along identical trajectories and the dipole moment d of the electron system has the form $d = Ner$, where N is the number of electrons in the bunch and r is the bunch coordinate. In this case, to the lowest order in v/c (where v is the velocity of an electron), the coordinate of the bunch moving in the field E of a plane wave satisfies the equation $\ddot{r} = eE/m$. As a result, the total intensity of dipole radiation is $I = 2N^2e^4E^2/3m^2c^3$ [17], and the effective scattering cross section σ, defined as the ratio of the total intensity of dipole radi-

ation to the intensity of the incident wave, is equal to $\sigma = 8\pi e^4 N^2/3m^2c^4$, which is N^2 times larger than the cross section for the Thomson scattering of radiation by one electron. Since the momentum lost by the incident wave is transferred to the electron bunch, the time-averaged force acting on the bunch is $f_{\sigma N} = 2e^4N^2E^2/3m^2c^4$. This means that the averaged force acting on an electron, $f_\sigma = f_{\sigma N}/N$, increases in proportion to the number of bunch electrons and, therefore, can be fairly strong for dense electron bunches, thereby indicating the presence of collective effects. Of course, for relativistic electron bunches, these estimates are incorrect, but they show that the radiative interaction force should be taken into account when the electron bunch density is sufficiently high.

As an example, let us compare the radiative interaction force with the conventional force (proportional to E) acting on an electron in the given field of a plane wave. Again, to the lowest order in v/c, we have $f_\sigma/eE = 2e^3NE/3m^2c^4$. Analyzing this ratio for one electron ($N = 1$), we can see that, even for the strongest laser fields achievable at the present time [13], the average radiation-reaction force f_σ is seven orders of magnitude smaller than eE. However, for bunches with a large number N of electrons, these forces can, in principle, be comparable. In fact, for an electron bunch with a density of 10^{22} cm^{-3} [14] and a volume of $V \approx \lambda^3$ and for an incident radiation with a wavelength of 1 μm, we obtain $N = 10^{10}$, so that the average radiation-reaction force is dominant.

An analogous conclusion can be drawn from a comparison of the average radiation-reaction force with the gradient ponderomotive force, which is usually regarded as the main driving force for electron acceleration by electromagnetic pulses in vacuum [1–7, 10]. For the gradient ponderomotive force, we have [4] $f_g = -e^2\nabla\overline{|E|^2}/2m\omega^2$. In this case, the force ratio is independent of the field strength and, for one electron, is equal to $f_\sigma/f_g = 4Ne^2\omega^2\Delta z/3mc^4$, where Δz is the characteristic scale length on which the field decreases. To be specific, we set Δz equal to 100 wavelengths, in which case the force ratio f_σ/f_g for a bunch consisting of one electron is on the order of 10^{-4}. This indicates that, for low-density electron bunches, the radiation-reaction force can be neglected. However, for dense bunches containing about $N \approx 10^{10}$ electrons, the average radiation-reaction force f_σ is much stronger than the gradient ponderomotive force f_g for $\Delta z = \lambda/2$ and, thus, should be incorporated into the equations of motion.

We emphasize that taking into account the radiation-reaction force is only important in problems of the acceleration of dense electron bunches. Even for high-current electron beams with a typical density of about 10^{12} cm^{-3}, there is at most one electron in a volume of $V \approx \lambda^3$; hence, for such beams, the radiation-reaction force can nearly always be neglected.

The above qualitative considerations show that the acceleration of dense electron bunches should be described with allowance for collective effects. Generally, efforts to exactly incorporate the radiation-reaction forces in a system with many relativistic electrons run into significant difficulties [17]. Numerical modeling implies the simultaneous solution of Maxwell's equations and the relativistic equations of motion for many electrons. However, this way is fairly complicated and the physical interpretation of the final numerical results is far more difficult. An alternative is to use a model that sometimes makes it possible to derive analytic expressions for the radiation-reaction force in the case of many electrons, e.g., the so-called 1D3V model, in which the electron motion is described in terms of one spatial coordinate and three velocity components. It is clear that this model provides an adequate description of the main processes occurring during the ionization of thin films by high-power laser pulses. Here, we apply a combined (numerical and analytical) version of the 1D3V model; i.e., we reduce the problem to the solution of equations of motion (which are ordinary delayed differential equations).

3. MODEL AND BASIC EQUATIONS

We consider a medium that is homogeneous in the plane perpendicular to the z-axis; i.e., we assume that the charge and current densities ($\rho(z, t)$ and $\mathbf{j}(z, t)$) depend only on the coordinate z and time t. Let us first represent the charge and current densities as $\rho(z, t) = \sigma\delta[z - Z(t)]$ and $\mathbf{j}(z, t) = \sigma\mathbf{v}(t)\delta[z - Z(t)]$, where σ is the surface charge density. Physically, these representations describe a thin plane charged sheet that is infinite in the x and y directions and is composed of electrons that all move in the same manner (the longitudinal coordinate and velocity of the electrons are $Z(t)$ and $\mathbf{v}(t)$, respectively). In this case, formal solutions to Maxwell's equations can be obtained using a Green's function approach [18–20]:

$$E_{ze}(z, t) = 2\pi\sigma\,\mathrm{sgn}[z - Z(t')], \quad (1)$$

$$\mathbf{E}_{\perp e}(z, t) = -\frac{2\pi\sigma\boldsymbol{\beta}_\perp(t')}{1 - \beta_z(t')\,\mathrm{sgn}[z - Z(t')]}, \quad (2)$$

$$\mathbf{H}_e(z, t) = \frac{2\pi\sigma\boldsymbol{\beta}_\perp(t') \times \mathbf{e}_z}{1 - \beta_z(t')\,\mathrm{sgn}(z - Z(t'))}\,\mathrm{sgn}[z - Z(t')], \quad (3)$$

where $\mathbf{E}_{\perp e} = E_{xe}\mathbf{e}_x + E_{ye}\mathbf{e}_y$, $\mathbf{v}_\perp = v_x\mathbf{e}_x + v_y\mathbf{e}_y$, $\boldsymbol{\beta} = \mathbf{v}/c$, and the delay time t' is determined from the equation $c(t - t') = |z - Z(t')|$.

Expressions (1)–(3) are one-dimensional (or, more precisely, 3+1-dimensional) analogues of the classical Lienard–Wiechert solutions [17] and describe the field of an infinite charged (electron) sheet, in which case the field components E_{ze} and $\mathbf{E}_{\perp e}$ can be interpreted as the near field and radiation field of the sheet, respectively.

Now, we consider a medium whose initial charge density is arbitrarily distributed along the z-axis, on which the medium is assumed to occupy region Ω. We divide this region into thin electron sheets of width dz_0 by the planes perpendicular to the z-axis and describe the state of each sheet by Lagrangian variables. Specifically, let $Z(z_0, t)$ be the longitudinal coordinate of the sheet with the initial coordinate $z_0 \in \Omega$, and let $\beta_z(z_0, t) = \partial Z(z_0, t)/c\partial t$ and $\beta_\perp = \beta_\perp(z_0, t)$ be the dimensionless longitudinal and transverse velocities of the sheet. In other words, we number the sheets by their initial coordinates z_0. In accordance with expressions (1)–(3), the total radiation field of the charged medium is the sum of the radiation fields of the elementary sheets:

$$E_{zs}(z, t) = 2\pi\int_\Omega \rho(z_0)\,\mathrm{sgn}[z - Z(z_0, t)]\,dz_0, \tag{4}$$

$$\mathbf{E}_{\perp s}(z, t) = -2\pi\int_\Omega \rho(z_0)\frac{\boldsymbol{\beta}_\perp(z_0, t'(z, z_0, t))}{1 - \mathrm{sgn}[z - Z(z_0, t)]\beta_z(z_0, t'(z, z_0, t))}dz_0, \tag{5}$$

$$\mathbf{H}_s(z, t) = 2\pi \times \int_\Omega \rho(z_0)\frac{\boldsymbol{\beta}_\perp(z_0, t'(z, z_0, t)) \times \mathbf{e}_z\,\mathrm{sgn}(z - Z(z_0, t))}{1 - \mathrm{sgn}(z - Z(z_0, t))\beta_z(z_0, t'(z, z_0, t))}dz_0, \tag{6}$$

where the delay time $t'(z, z_0, t)$ for each sheet is determined from expressions (1)–(3).

The interaction of electrons with the self-consistent radiation field gives rise to the effective "viscous" force $\mathbf{F}_s = e\mathbf{E}_s + e\boldsymbol{\beta} \times \mathbf{H}_s$, which acts on each electron in the sheet [17, 18]:

$$\frac{d\mathbf{p}}{dt} = e\mathbf{E} + e\boldsymbol{\beta} \times \mathbf{H} + \mathbf{F}_s, \tag{7}$$

where $\mathbf{p}$ is the relativistic electron momentum and $\mathbf{E}$ and $\mathbf{H}$ are the strengths of the external electromagnetic field (the field strengths $\mathbf{E}$ and $\mathbf{H}$ are assumed to be consistent with the model of a medium that is homogeneous in the x and y directions; i.e., the medium is assumed to remain homogeneous throughout the evolution of the system). Note that the radiation-reaction force $\mathbf{F}_s$ has both transverse and longitudinal components, the latter component being highly nonlinear. Thus, for an infinitely thin electron sheet, the transverse and longitudinal force components are equal to [see expressions (1)–(3) and Eq. (7)]

$$\mathbf{F}_{s\perp} = -2\pi\sigma e\boldsymbol{\beta}_\perp, \quad F_{sz} = -2\pi\sigma e|\boldsymbol{\beta}_\perp|^2\beta_z/(1 - \beta_z^2). \tag{8}$$

First, we consider the nonrelativistic limit, in which $v_z \ll v_y \ll c$. We estimate the average force exerted by a normally incident, monochromatic, electromagnetic wave with frequency ω and amplitude E_0 on an infinitely thin electron sheet.

That the average pressure force exerted by the wave on the electron sheet does exist is clear from the following physical considerations. Without allowance for the intrinsic radiation of the sheet and the related radiative loss, the charges move along closed trajectories (in the frame of reference in which the charges are, on average, at rest). Such motion of the charges is a superposition of transverse oscillations at the frequency of the incident wave and longitudinal oscillations at the doubled frequency [17], in which case the period-averaged pressure force exerted by the wave on the electron sheet vanishes. If we now take into account the intrinsic radiation of the electron sheet, we can see that the charge trajectories do not close upon themselves, which indicates that the incident wave is scattered (the reflection coefficient of the sheet for the wave is nonzero) and, hence, loses its momentum. It is this momentum loss that gives rise to the average pressure force with which the wave acts on the electron sheet [18]. In turn, this force is governed by the collective effects and becomes stronger as the electron density increases. The pressure force exerted by a wave on an individual electron was investigated in [7–9].

Mathematically, the average pressure force is associated with the Lorentz force acting on the electrons in an external wave. In fact, let us simplify matters by setting $v_z = 0$. In this case, expressions (7) and (8) for the complex velocity amplitude $\tilde{v}_y = \tilde{v}_0\exp(i\omega t)$ yield $\tilde{v}_0 = -ie\tilde{E}/[m\omega(1 - i\alpha)]$, where the dimensionless parameter $\alpha = 2\pi\sigma e/mc\omega$ characterizes the relative influence of the collective (radiation) effects on the motion of an electron bunch and $\tilde{E}$ is the complex amplitude of the electric field of the wave. Consequently, in Eq. (7) for the transverse electron momentum [see also expressions (8)], the reaction force $\mathbf{F}_{s\perp}$ of the intrinsic radiation of the electrons gives rise to an additional change in the phase of the momentum $\mathbf{p}_\perp$ with respect to the wave phase. As a result, in the equation for p_z, the Lorentz force not only has the purely oscillatory component, which describes electron oscillations in the prescribed field of the external wave, but also has the nonzero, slowly varying component, which governs the average pressure force. For $v_z = 0$, the averaged (over the period $T = 2\pi/\omega$) Lorentz force $\mathbf{F} = e\boldsymbol{\beta} \times \mathbf{H}$ acting on an individual electron in the longitudinal direction has the form

$$\langle F_z\rangle = \frac{\alpha}{1 + \alpha^2}\frac{e^2|E_0|^2}{2mc\omega}. \tag{9}$$

Force (9) is maximum at $\alpha = 1$. Physically, the existence of the maximum stems from the fact that, as $\alpha \longrightarrow 0$, the average pressure force acting on an individual electron vanishes (the collective effects play an unimportant role), whereas, as $\alpha \longrightarrow \infty$, the effective viscous

force increases, so that the electrons become practically immobile and, accordingly, the Lorentz force vanishes.

The pressure force per unit area of the electron sheet is related to the pressure force (9) acting on an individual electron by $F = \langle F_z \rangle n$, where $n = \sigma/e$ is the surface electron density. As a result, we have $F = [\alpha^2/(1 + \alpha^2)][E_0^2/4\pi]$. Consequently, the pressure force per unit area is maximum for $\alpha \longrightarrow \infty$ and is described by the conventional expression following from the familiar expression for the Maxwell stress tensor [17] (in the limit $\alpha \longrightarrow \infty$, the electron sheet is completely reflecting [18]).

Figure 1 shows the time evolution of this force in the case of acceleration of a plane electron sheet in a prescribed field ($\alpha = 0$, Fig. 1a) and with allowance for radiative losses ($\alpha = 0.1$, Fig. 1b). For clarity, the field amplitude is chosen to be moderate, $\alpha_0 = 2$, and the Coulomb interaction between the electrons in the sheet is neglected. From Fig. 1b, one can see that the average pressure force is nonzero: the amount by which the plot of the instantaneous pressure force deviates from a zero value upward is larger than downward. In addition, the fact that the period of the force increases with time indicates an increase in the longitudinal velocity of the electron sheet, in which case, during each next half-period of the external field, the effective time of the interaction of the electron sheet with the external field is longer and, because of the Doppler transformation, the pressure force amplitude is smaller. In a prescribed field (Fig. 1a), the period and amplitude of the pressure force both remain constant, so that the electron sheet is not accelerated.

Now, we proceed to an analysis of the relativistic equations of motion that follow from expression (7).

4. INTERACTION OF AN INFINITELY THIN ELECTRON SHEET WITH A PLANE WAVE

We begin by considering the interaction between an external wave and an idealized system consisting of a single, infinitely thin electron sheet with a constant surface charge density σ. Let the electromagnetic field of the wave have the components $E_y = -H_x = E_0 \sin(\omega t - kz + \varphi_0)$, where φ_0 is the initial wave phase and $k = \omega/c$ is the wave vector along the z-axis. For the electron sheet, we introduce the normalized time $\tau = \omega t$, normalized longitudinal coordinate $Z = kz$, and normalized relativistic momentum $\mathbf{P} = \mathbf{p}/mc = \boldsymbol{\beta}/\sqrt{1-\beta^2}$. We also denote by θ the wave phase with respect to the electron sheet, $\theta = \tau - Z + \varphi_0$. Then, from expression (7), we obtain the relativistic equations of motion

$$\frac{dP_y}{d\theta} = \alpha_0 \sin\theta - \frac{\alpha\beta_y}{1-\beta_z}, \tag{10}$$

$$\frac{dP_z}{d\theta} = \frac{\alpha_0}{1-\beta_z}\beta_y \sin\theta - \frac{\alpha\beta_z\beta_y^2}{(1-\beta_z)^2(1+\beta_z)}. \tag{11}$$

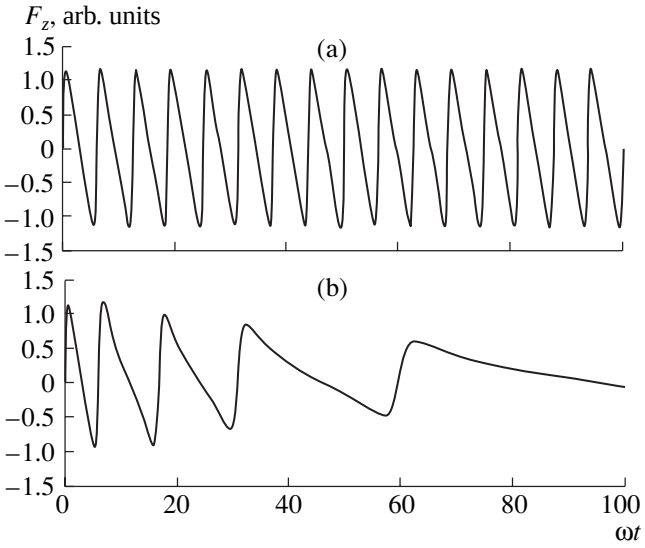

Fig. 1. Time evolutions of the longitudinal force acting on a plane electron sheet accelerated (a) in a prescribed field ($\alpha = 0$) and (b) with allowance for radiative losses ($\alpha = 0.1$) for the case $\alpha_0 = 2$.

Let us investigate the asymptotic behavior of the solution to Eqs. (10) and (11) on sufficiently long time scales on which the longitudinal electron velocity β_z becomes close to unity. In this case, the inertial term $dP_y/d\theta$ in Eq. (10) can be neglected and we arrive at the following equation for the longitudinal momentum:

$$P_z \approx \frac{\alpha_0^2}{4\alpha}\left(\theta - \frac{1}{2}\sin 2\theta\right). \tag{12}$$

On long time scales, P_y is a small quantity proportional to P_z^{-1}. As a result, the relativistic factor becomes $\gamma = (1 + P_y^2 + P_z^2)^{1/2} \approx P_z$. In accordance with Eq. (12), this factor, on average, increases linearly with the phase θ and essentially coincides with the so-called longitudinal relativistic factor $\gamma_\parallel = (1 - \beta_z^2)^{-1/2}$. In this case, the longitudinal velocity obeys the asymptotic expression

$$\beta_z = \frac{P_z}{\sqrt{1 + P_y^2 + P_z^2}} \approx 1 - 8\left(\frac{\alpha}{\alpha_0^2}\right)^2 \theta^{-2}. \tag{13}$$

The asymptotic behavior of the relativistic factor $\langle\gamma\rangle$, which is averaged over oscillations of the phase θ and is expressed in terms of the normalized time τ, can be obtained from Eq. (12) and expression (13):

$$\langle\gamma\rangle \approx \langle\gamma_\parallel\rangle \approx \frac{3^{1/3}}{2}\left(\frac{\alpha_0^2}{\alpha}\right)^{1/3}\tau^{1/3}. \tag{14}$$

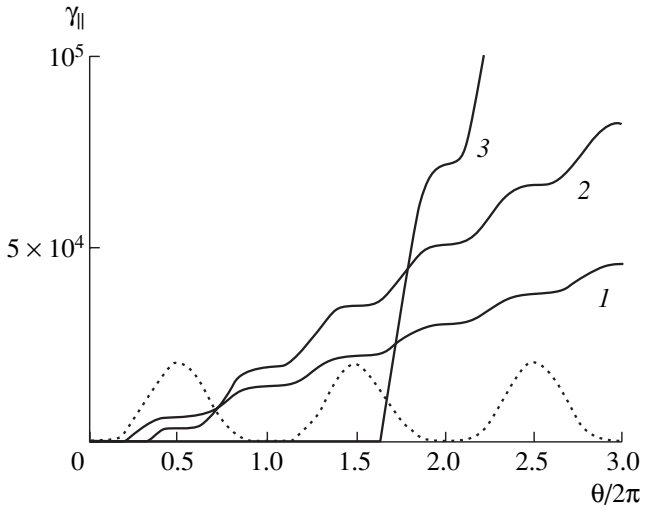

Fig. 2. Longitudinal relativistic factor $\gamma_\parallel$ calculated as a function of the phase θ for $\alpha_0 = 100$ and different values of α (solid curves): α = (*1*) 1, (*2*) 0.5, and (*3*) 0.1. The dashed curve shows the relativistic factor γ calculated for $\alpha = 0$.

Figure 2 shows the longitudinal relativistic factor $\gamma_\parallel$ calculated as a function of the phase θ for $\alpha_0 = 100$ and different values of α (solid curves). Profiles *1–3* are obtained by numerically solving Eqs. (10) and (11) with zero initial values of the coordinate and velocity of the sheet. The larger the parameter α, the earlier the results obtained start to agree well with the asymptotic solution to Eq. (12). Thus, for $\alpha = 1$ (curve *1*), good agreement is achieved already at $\theta/2\pi \approx 0.2$. For lower surface charge densities, the time required for the regime of efficient acceleration of the sheet to be established is longer (see curve *2* for $\alpha = 0.5$ and curve *3* for $\alpha = 0.1$). For comparison, we also plot the total relativistic factor γ (dashed curve) calculated for $\alpha = 0$ (i.e., without allowance for the collective radiation effects). It should be noted that, in contrast to the case $\alpha = 0$, in which the velocity vector continuously oscillates, the character of electron motion at $\alpha > 0$ is radically different: after the asymptotic acceleration regime corresponding to expression (12) is achieved, the transverse electron velocity becomes negligible and the total energy of the electrons is mainly governed by their longitudinal motion.

As was expected, when the intrinsic radiation of the electron sheet is systematically taken into account, the energy of the electrons that are accelerated even by a plane wave, on average, increases without bound in proportion to the phase θ. The dependence of the electron energy on time is much weaker: the electron energy increases in proportion to the cube root of time. Also, an important point here is that the radiation-reaction force always accelerates the sheet, unlike the gradient ponderomotive force f_g, which can both accelerate and decelerate the electrons.

5. INTERACTION OF A GAUSSIAN LASER BEAM WITH A THIN ELECTRON SHEET

Above, we have considered acceleration by plane waves. However, it is of great interest to investigate the acceleration of electron bunches by realistic laser fields that can be generated in present-day experiments. The laser field is usually well-described by the lowest Gaussian mode; i.e., it decreases with distance from the axis and from the focal plane of the beam [1, 4]. Consequently, there is an effective interaction region: the electrons that escape from this region essentially cease to be accelerated. Let the transverse dimensions of an electron sheet be much smaller than the radius ω_0 (in units of $\lambda/2\pi$) of a Gaussian beam at the waist. In this case, we can neglect the dependence of the beam amplitude and phase on transverse coordinates and assume that they are unchanged over the electron sheet. In addition, let the initial longitudinal momentum of the sheet be sufficiently high (such that $\gamma_{\parallel 0} \gg 1$). Under these assumptions, the dimensionless amplitude α_0 and the wave phase both depend on the coordinate Z of the sheet. Then, Eqs. (10) and (11) yield the following expression for the relativistic factor:

$$\gamma_\parallel^3 - \gamma_{\parallel 0}^3 = \frac{3}{4\alpha}\int_{-\infty}^{+\infty} \alpha_0^2(Z)\sin^2[\theta + \varphi(Z)]\,dZ, \qquad (15)$$

where $\alpha_0(Z) = \alpha_0(1 + (2Z/\omega_0^2)^2)^{-1/2}$ and $\varphi(Z) = \arctan(\omega_0^2/2Z)$. In this case, for $\gamma_{\parallel 0} \gg 1$ and moderate values of ω_0, the phase $\theta(Z)$ is essentially constant over the interaction region ($\theta(Z) \approx \theta(0) = \varphi_0$), so that we can take the integral in expression (15) approximately and obtain

$$\gamma_\parallel^3 - \gamma_{\parallel 0}^3 \approx \frac{3\pi\alpha_0^2\omega_0^2}{16\alpha}. \qquad (16)$$

Note that the main contribution to the integral in expression (15) comes from distances Z_{int} from the focal plane that are about several $\omega_0^2/2$. Thus, at the distance $Z_{\text{int}} = 5\omega_0^2/2$ from the focal plane, the relativistic factor is smaller than its maximum value by only 20%. The change in the relativistic factor depends only on the laser beam power $I \propto \alpha_0^2\omega_0^2$ and, at a fixed laser power, is independent of the beam radius at the waist. The sharper the focusing of the laser beam, the shorter is the region of efficient acceleration. In this sense, we may say that the electron sheet is accelerated as if the Gaussian beam hits the sheet, thereby increasing its translational energy over a very short time.

After a sequence of Q hits by high-power laser pulses, the longitudinal relativistic factor of the sheet becomes

$$\gamma_{\|Q}^3 - \gamma_{\|0}^3 = \frac{3\pi\alpha_0^2\omega_0^2}{16\alpha}Q. \quad (17)$$

We can see that, for a large number Q of laser pulses, the longitudinal relativistic factor can be fairly high.

Hence, because of the collective radiation effects, it is, in principle, possible to accelerate an electron sheet to arbitrarily high energies not only by a plane electromagnetic wave but also by a sequence of high-power laser pulses. Of course, this conclusion is valid only under the assumptions of the above idealized model, which was developed to describe the interaction of an electromagnetic wave with an infinitely thin electron sheet without allowance for Coulomb repulsive forces between the accelerated electrons. However, in a sense, this idealized model gives an upper estimate for the possible values of the relativistic factor γ that can be achieved in the acceleration of finite-thickness electron bunches by a high-power electromagnetic wave. This acceleration process is the subject of the next section.

6. INTERACTION OF A PLANE WAVE WITH A FINITE-THICKNESS ELECTRON BUNCH

We consider a plane electron bunch with the initial coordinate z_0, the normal to the bunch being aligned with the z-axis. Let a linearly polarized plane electromagnetic wave with the wave vector $\mathbf{k}$ be incident on the bunch along the z-axis. We assume that the bunch thickness l is finite and is much smaller than the wavelength $\lambda = 2\pi/k$ of the electromagnetic wave (an electron bunch with a thickness equal to several λ is compressed by the incident wave to a thickness $l \ll \lambda$ [21]). As was shown above, the reaction force of the intrinsic radiation of the bunch gives rise to a nonzero average pressure force exerted by the external field on the electron bunch. The fundamental difference between the case of a finite-thickness electron bunch and the case of acceleration in a prescribed field is in the presence of forces that compress the bunch along the z-axis.

First, we estimate the forces acting in the external field $\mathbf{E}$ on the left and right boundaries of the electron bunch without allowance for Coulomb interaction between the electrons in the bunch. In this case, all of the electrons in the wave field move along essentially the same trajectories and the field of the own radiation of the bunch is described by expressions (1)–(3). According to these expressions and Eq. (7), the left and right boundaries of the bunch experience the forces $F_{zL} = 2\pi\sigma e(1+\beta_z)^{-1}\beta_y^2$ and $F_{zR} = -2\pi\sigma e(1-\beta_z)^{-1}\beta_y^2$, respectively. The mean of these forces is the effective radiative friction force F_{sz}, which acts on the entire bunch in the z direction [see expression (8)]. Consequently, different electron sheets inside a finite-thickness bunch experience different radiative friction forces because, inside the bunch, the field of the intrinsic radiation changes along the z-axis [18]. Note that the radiative friction forces acting on the left and right boundaries of an electron bunch have opposite signs, thereby indicating the compression of the bunch; moreover, the higher the longitudinal velocity β_z of the bunch, the larger the extent to which the bunch is compressed. These forces can partially prevent the spreading of the bunch (an increase in the bunch thickness) due to Coulomb repulsive forces between the electrons and thus are, in a sense, analogous to magnetic attractive forces between the parallel currents of moving charges.

Figure 3 shows the time evolutions (in the laboratory frame) of the longitudinal momenta of several electron sheets in a bunch accelerated by a high-power electromagnetic pulse in vacuum. The time evolutions were calculated for $l = \lambda/100$ with allowance for Coulomb interaction between the sheets. In Fig. 3a, the evolutions of p_z were calculated without allowance for the compressing reaction force of the intrinsic radiation of a bunch, in which case Coulomb forces repulse the sheets. In Fig. 3b, the evolutions were calculated with allowance for both Coulomb forces and the forces compressing the bunch in the longitudinal direction. A comparison between Figs. 3a and 3b shows that, during the first half-period of a high-power electromagnetic pulse, Coulomb forces are in large measure counterbalanced. As a result, in the initial acceleration phase, all of the bunch electrons can, in principle, move along identical trajectories and emit radiation coherently. We can thus conclude that collective effects play an important role in the acceleration dynamics of a dense electron bunch.

In the 1D3V model, the interaction of an electromagnetic pulse with a dense plasma slab can be described correctly only with allowance for both Coulomb interaction among the electron sheets and Coulomb interaction between the electron sheets and the ion background of the target. In fact, this model is applicable if the distance between the electron and ion bunches is much smaller than the transverse dimensions of the bunches (this makes it possible to consider the bunches to be plane rather than point charges). In addition, the possibility of neutralizing the ion background on short time scales of about several tens of field periods seems to be problematic because of an extremely large charge of the background. As a result, in numerical modeling, the ion background is regarded as being immobile and the interaction between the ion background and the electron bunch is assumed to be purely Coulombic. Note that the condition for the incident wave front to remain planar, $r^2/(b\lambda) \gg 1$ (where r is the radius of the laser beam and b is the distance from the focal plane), turns out to be far less stringent than the assumptions of the model; consequently, in what follows, we restrict ourselves to considering a plane wave.

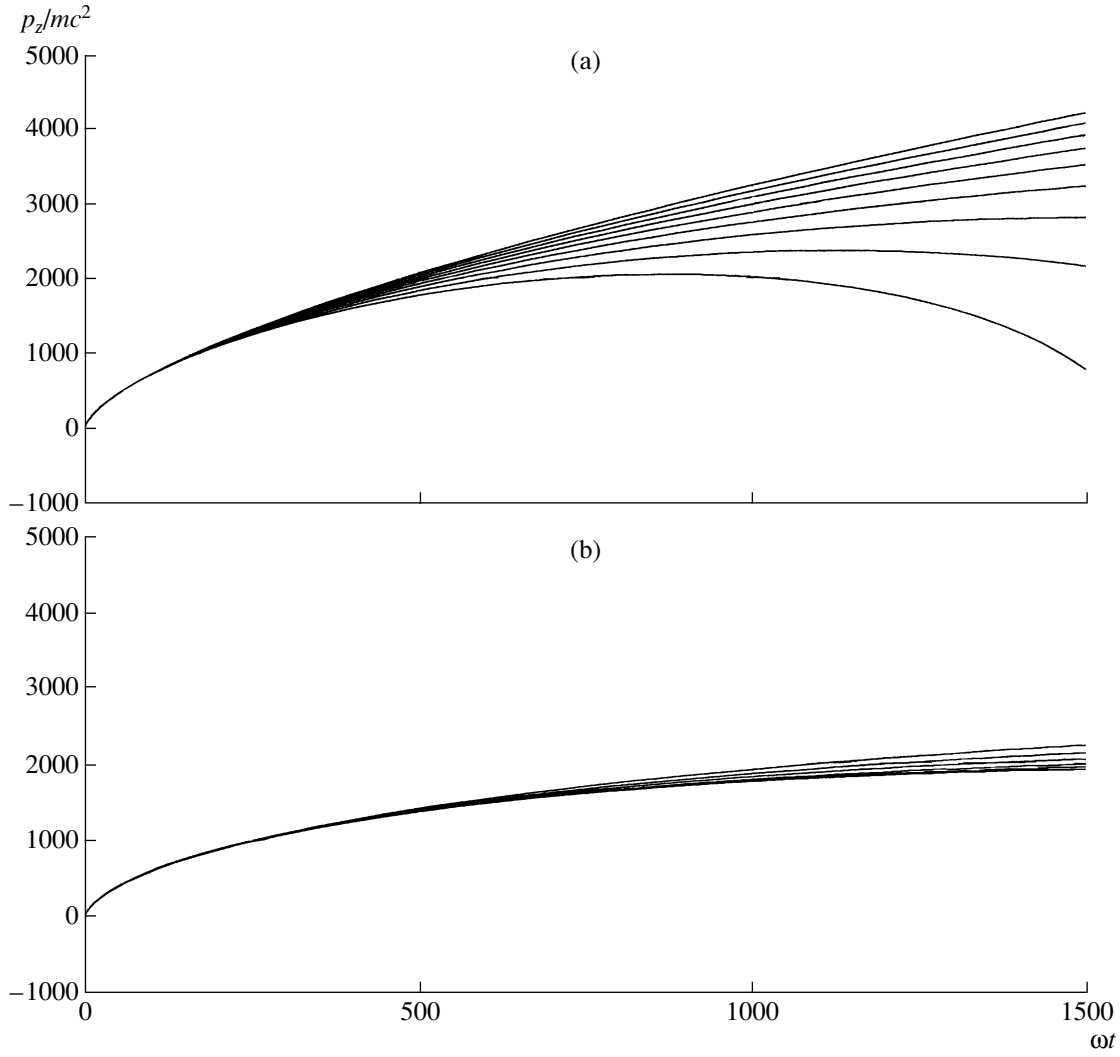

Fig. 3. Time evolutions of the longitudinal momentum p_z calculated for several electron sheets accelerated at the front of a high-power ($\alpha_0 = 100$, $\alpha = 1$) electromagnetic wave (a) without and (b) with allowance for radiation forces.

The results of numerical simulations of the acceleration of an electron bunch with the thickness $l = \lambda/100$ are illustrated in Fig. 4, which shows the time evolutions of the transverse and longitudinal momenta, p_y and p_z, calculated for $\alpha_0 = 100$ and different values of the parameter α. This value of the dimensionless amplitude α_0 corresponds to an ultrarelativistic electromagnetic pulse, in which the electrons are already accelerated to relativistic energies over a time interval much shorter than the period of the external wave. As soon as an electron is accelerated to a relativistic velocity, the amplitude of the Lorentz force decreases significantly in accordance with the Doppler transformation, so that the accelerating forces subsequently have essentially no impact on the motion of the electron, which thus experiences only Coulomb forces and the forces that compress the electron bunch. The Coulomb attractive forces exerted by the target ions on the electrons act to reduce the longitudinal electron momentum p_z. Then, the external field reverses polarity and the process repeats itself. Note that, during the next half-periods of the external field, the compressing forces become weaker, so that the Coulomb forces break the bunch up into parts: the Coulomb repulsive forces between the electron sheets reverse the direction of motion of the sheets closest to the ion background and continue to accelerate the farthest sheets; as a result, the bunch is actually destroyed. Such electron motion is characteristic of all situations in which plane electron bunches are accelerated by external waves to ultrarelativistic energies. On the other hand, for small values of α (Fig. 4b), the electron sheets move synchronously on longer time scales (up to several periods of the external wave; in the laboratory frame, this corresponds to fractions of a picosecond) as compared with the case in which the values of α are large (Fig. 4a). In addition, for large val-

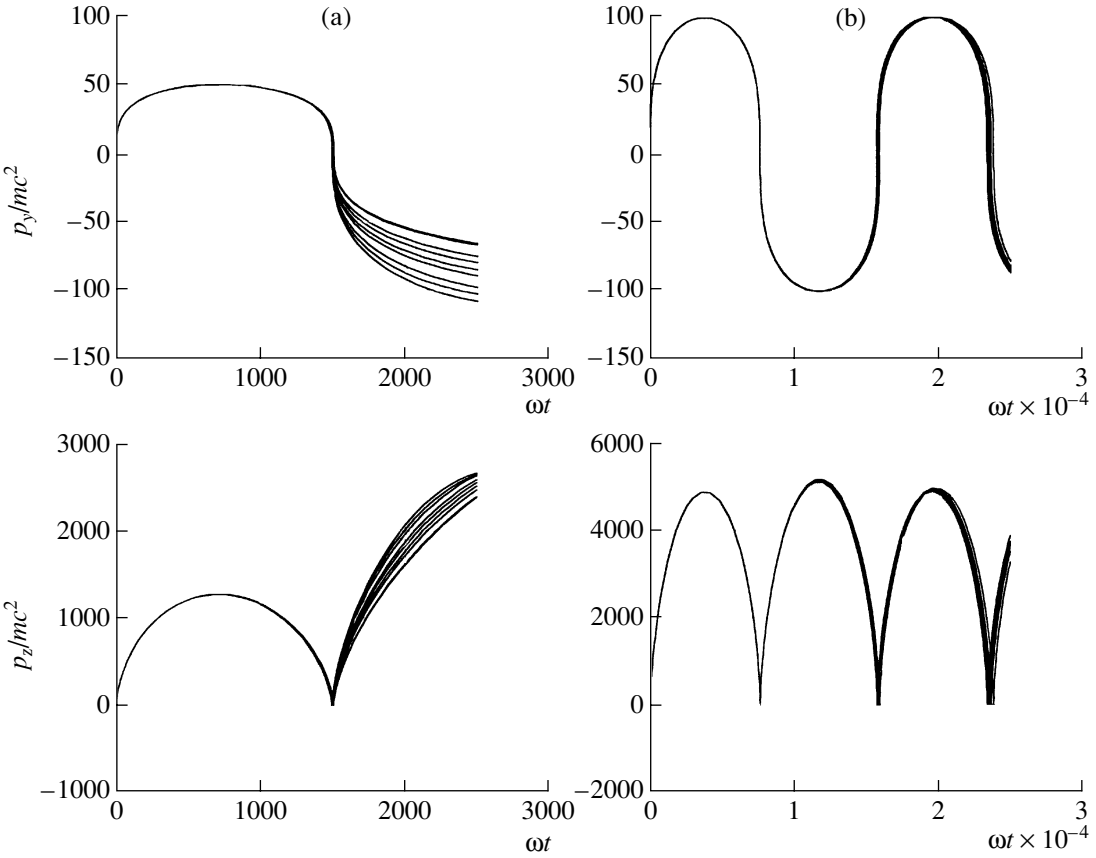

Fig. 4. Time evolutions of the transverse and longitudinal momenta, p_y and p_z, calculated for several electron sheets accelerated at the front of a high-power ($\alpha_0 = 100$) electromagnetic wave in vacuum for $\alpha =$ (a) 1 and (b) 0.001. In both cases, the bunch thickness in the z direction during acceleration remains much smaller than λ.

ues of α, the maximum longitudinal momentum p_z acquired by the electron sheets is smaller because of the greater strength of the viscous force resulting from the reaction force of the intrinsic radiation of a bunch [see expression (8)]. Note, however, that the larger the parameter α, the higher is the charge of the accelerated bunch; this effect may play a governing role in some practical applications.

Hence, depending on the values of the parameters α_0 and α, the stage of the synchronous acceleration of all the sheets comprising an electron bunch in a moving frame of reference associated with the electron bunch may last from one-half of the period of an external wave to several periods; in the laboratory frame, this corresponds to time intervals of thousands of femtoseconds. We emphasize that, even with the acceleration parameters that are achievable at the present time ($\alpha_0 = 30$), dense electron bunches can be accelerated to ultrarelativistic energies; moreover, during acceleration, the time evolutions of the transverse and longitudinal momenta, p_y and p_z, correspond to those in Fig. 4, but the stage of synchronous acceleration is shorter and the amplitudes of the momenta p_y and p_z are smaller.

The momentum acquired by the electrons during acceleration may be on the order of α_0^2, which corresponds to the maximum longitudinal momentum of an electron in a prescribed field. Note that, under these acceleration conditions, the average pressure force of the external wave does not have enough time to manifest itself in full measure because of the short duration of the phase of synchronous acceleration: a real bunch is destroyed before the acceleration process reaches the asymptotic regime described by Eq. (12).

7. DISCUSSION OF THE RESULTS

Let us estimate the values of the parameters α and α_0 that can be achieved at the present time. The surface charge density σ is determined by the volume electron density N_v within the bunch and the bunch thickness l. For $l = \lambda$ and for a wavelength of about $\sim 10^{-4}$ cm, the first of these parameters is approximately equal to $\alpha \approx 25$ at $N_v = 10^{22}$ cm^{-3}. For a thinner bunch or a lower electron density N_v, the parameter α is smaller. Thus, for $l = 10$ nm, we obtain $\alpha \approx 0.25$.

For an incident wave with an intensity of 1.38×10^{18} W/cm^2 and with the wavelength $\lambda = 10^{-4}$ cm, we have $\alpha_0 = 1$. For present-day devices capable of generating pulses with a power of about 100 TW [13], the parameter α_0 is approximately equal to 30. On the other hand, there are projects aimed at producing petawatt laser pulses, which will ensure larger values of α_0, up to 100–200. We stress that, since the electron bunch is actually accelerated by the first half-wave of the external field, the pulse envelope should be as close as possible to a rectangular shape (optimally, the duration of the pulse should be from one to two periods of oscillations).

The above process of acceleration of a dense electron bunch by an external electromagnetic wave in vacuum differs significantly from the traditional process of electron acceleration. In fact, the accelerated bunch turns out to be inside the region occupied by the wave (rather than outside this region, as is the case in conventional accelerators). Moreover, such dense electron bunches exist only for a short time (fractions of a picosecond for the values of the dimensionless amplitude α_0 that are achievable at the present time); then, the bunches are destroyed by Coulomb repulsive forces. The destruction of the bunch restricts the maximum possible values of the relativistic factor γ. On the other hand, when the space charge in the electron bunch is partially neutralized (e.g., by positive ions or positrons), the bunch can be stabilized over a longer time so that the acceleration process may reach the asymptotic regime described by Eq. (12).

Note that essentially all of the energy of the accelerated electron bunch is governed by its longitudinal motion, because the transverse velocity of the bunch is much lower than unity. The size of the corresponding experimental device is determined primarily by the size of the system generating ultrashort laser pulses, because, in reality, the plasma bunches are accelerated over distances of about fractions of a millimeter at a rate of about tens of TeV/m. The acceleration method that we have considered here may find applications in studying the interaction of relativistic electrons with matter, the generation of ultrashort X-ray and γ-ray pulses, etc.

In conclusion, note that the above acceleration model can also be useful for investigating the interaction of high-power subpicosecond laser pulses with thick (semi-infinite) targets.

REFERENCES

1. F. V. Hartemann, S. N. Fochs, G. P. Le Sage, *et al.*, Phys. Rev. E **51**, 4833 (1995).
2. E. Esarey, P. Sprangle, and J. Krall, Phys. Rev. E **52**, 5443 (1995).
3. G. Malka, E. Lefebvre, and J. L. Miquel, Phys. Rev. Lett. **78**, 3314 (1997).
4. B. Quesnel and P. Mora, Phys. Rev. E **58**, 3719 (1998).
5. L. J. Zhu, Y. K. Ho, J. X. Wang, *et al.*, Phys. Lett. A **248**, 319 (1998).
6. J. X. Wang, Y. K. Ho, Q. Kong, *et al.*, Phys. Rev. E **58**, 6575 (1998).
7. A. L. Troha, J. R. van Meter, E. C. Landahl, *et al.*, Phys. Rev. E **60**, 926 (1999).
8. F. V. Hartemann and A. K. Kerman, Phys. Rev. Lett. **76**, 624 (1996).
9. J. E. Moore, Phys. Rev. E **59**, 2281 (1999).
10. Wei Yu, M. Y. Yu, J. X. Ma, *et al.*, Phys. Rev. E **61**, R2220 (2000).
11. J. X. Wang, W. Scheid, M. Hoelss, and Y. K. Ho, Phys. Lett. A **275**, 323 (2000).
12. S. V. Bulanov, V. A. Vshivkov, G. I. Dudnikova, *et al.*, Fiz. Plazmy **23**, 284 (1997) [Plasma Phys. Rep. **23**, 259 (1997)].
13. G. A. Mourou, C. P. J. Barty, and M. D. Perry, Phys. Today **51** (1), 22 (1998).
14. R. V. Volkov, V. M. Gordienko, M. S. Dzhidzhoev, *et al.*, Kvantovaya Élektron. (Moscow) **24**, 1114 (1997).
15. V. A. Vshivkov, N. M. Naumova, F. Pegoraro, and S. V. Bulanov, Phys. Plasmas **5**, 2727 (1998).
16. V. I. Veksler, At. Énerg. **2**, 427 (1957).
17. L. D. Landau and E. M. Lifshitz, *The Classical Theory of Fields* (Nauka, Moscow, 1988; Pergamon, Oxford, 1975).
18. A. S. Il'in, V. V. Kulagin, and V. A. Cherepenin, Radiotekh. Élektron. (Moscow) **44**, 389 (1999) [J. Communicat. Techn. Electron. **44**, 385 (1999)].
19. V. L. Bratman and C. V. Samsonov, Phys. Lett. A **206**, 377 (1995).
20. S. L. Ziglin, A. S. Il'in, V. V. Kulagin, and V. A. Cherepenin, Radiotekh. Élektron. (Moscow) **45**, 1253 (2000) [J. Communicat. Techn. Electron. **45**, 1247 (2000)].
21. B. Rau, T. Tajima, and H. Hojo, Phys. Rev. Lett. **78**, 3310 (1997).

Translated by G. V. Shepekina

Plasma Physics Reports, Vol. 27, No. 12, 2001, pp. 1057–1078. Translated from Fizika Plazmy, Vol. 27, No. 12, 2001, pp. 1121–1142.

LOW-TEMPERATURE PLASMA

Streamer Breakdown of Long Gas Gaps

N. L. Aleksandrov* and E. M. Bazelyan**

**Moscow Institute of Physics and Technology, Institutskiĭ proezd 9, Dolgoprudnyĭ, Moscow oblast, 141700 Russia*

***Krzhizhanovskiĭ Power Engineering Institute, Leninskiĭ pr. 19, Moscow, 117927 Russia*

Received July 19, 2001

Abstract—Results obtained from numerical simulations of the streamer breakdown of long (longer than 10 cm) gas gaps at atmospheric pressure are reviewed. Most attention is focused on air under normal conditions and at elevated temperatures characteristic of the rebreakdown in the postspark channel that is cooled after the primary spark discharge has come to an end. The main stages of the evolution of a streamer discharge into an arc are considered, and the features of this phenomenon are analyzed as functions of the initial conditions. The main macroscopic processes that govern the composition and dynamics of the streamer plasma in different discharge stages are revealed. The experimental data and the results of computer simulations provide evidence for a nonthermal mechanism for streamer breakdown in noble gases. © *2001 MAIK "Nauka/Interperiodica".*

1. INTRODUCTION

In gas-discharge physics, the term "electric breakdown" usually means the process of plasma production in an external electric field. In contrast, by "breakdown" here we mean the creation of a highly conducting plasma channel with a descending current–voltage (*I–V*) characteristic, in which case the electric circuit is short-circuited, the voltage across the gap drops, and the discharge current is mainly determined by the internal resistance of the high-voltage source. It is precisely this phenomenon—a complete distortion of the insulation properties of the gas medium—that is regarded as breakdown in high-voltage engineering. If the generator continues to power the electric circuit, then, in the gap, an arc channel appears that can be maintained by a very weak electric field (with a strength of about 10–100 V/cm). The transformation of a spark channel into an arc can be regarded as the final stage of pulsed breakdown.

The refinement of the term "breakdown" should not be regarded as merely a terminology problem. This is a matter of great concern in solving numerous applied problems. As an example, let us imagine that a short nanosecond overvoltage pulse is imposed on a far lower long-term operating voltage in an electric circuit. We assume that the overvoltage pulse is strong enough to give rise to a streamer that develops across the entire insulation gap so rapidly that the streamer plasma's conductivity remains essentially unchanged and ensures a high current in the discharge circuit (below, we will show that this process is possible). If the time scale on which the process occurs is insufficiently long for the gas to be heated, then, after the overvoltage pulse is completely damped, the discharge cannot be maintained by the low operating voltage and comes to an end. A rapid recovery of the breakdown strength makes it possible to avoid emergency situations. Although the current is high, we cannot speak of a complete breakdown of the insulation gap if the *I–V* characteristic of the created discharge channel is nondescending.

The best-studied spark breakdown is the breakdown in air, which is an insulating medium that is widely used in present-day high-voltage engineering. In order to achieve a descending *I–V* characteristic of a spark channel in air, it is necessary to heat the air to temperatures higher than 5000 K (which are intrinsic to arc discharges). The lowest voltages for breakdown of long gaps with a highly nonuniform electric field are ensured by the leader mechanism. The leader channel is heated already in the development stage. The energy required for this heating is provided by the accompanying simultaneous growth of numerous streamers that continuously originate from the head of the leader channel. Although each of the streamers remains cold, their total energy is high enough to heat the leader channel to temperatures of 5000–6000 K [1–3].

Because of its two-stage nature, the leader process is fairly inertial. Under laboratory conditions, the leaders propagate with velocities on the order of 10^6 cm/s on micro- and millisecond time scales, while the propagation velocity of the leader in lightning on the kilometer scale is higher by a factor of 10–100.

It was shown theoretically and confirmed experimentally that a solitary streamer cannot be heated as it propagates in the interelectrode gap [3]. The reason for this is that the energy deposited in the streamer channel is severely limited: $W \sim U^2$, where U is the voltage across the gap. The specific energy deposition W_s into the streamer plasma cannot be increased by raising the voltage, because, due to the ionization expansion, the radius of the channel increases in proportion to $\sim U$ and its cross-sectional area, in proportion to U^2, so that we have $W_s \approx$ const [4]. In reality, the gas is heated after the

1063-780X/01/2712-1057$21.00

streamer bridges the discharge gap. Nevertheless, in many situations, the streamer discharge is the most rapid process in the breakdown of long gaps with a highly nonuniform electric field and is thus attractive for use in many technical applications (such as high-speed spark switches, protecting dischargers, and spark connectors for power equipment). Among the drawbacks of the streamer breakdown phenomenon, we can mention the destruction of gas insulation by ultrashort voltage pulses.

In most of the experimental [5–8] and theoretical [9–14] papers on streamer breakdown, a study was made of streamer discharges on centimeter scales. It was established that streamer breakdown proceeds through three stages: in the first stage, the streamer bridges the gap; in the second stage, the ionization waves propagate through the channel formed in the first stage; and, in the third stage, the gas in the channel is heated uniformly, giving rise to an arc. The transition to an arc is thought to occur by two alternative mechanisms. One mechanism is associated with the thermal expansion of the channel: during such expansion, the density N of neutral particles in the channel decreases isobarically and the reduced electric field E/N increases, thereby intensifying the electron impact ionization of gas molecules [9–11]. The second mechanism is associated with the generation of active particles (atoms and excited molecules) in the gap, in which case new ionization mechanisms involving these particles come into play [12–14]. Generally, both of these mechanisms can operate simultaneously, so that which one of them will dominate the transition to an arc depends on particular circumstances.

The data on the streamer breakdown of gas gaps with lengths of several tens of centimeters is much less extensive, although this phenomenon is of interest not only from the physical point of view but also from the standpoint of practical applications. There have been practically no experiments in this field, and theoretical investigations (primarily, by computer simulations) began only in recent years. It may be expected that all the stages of the development of streamer breakdown in a long gap will differ significantly from those in a short gap. Since a long streamer develops on a long time scale, the decay of the plasma in the streamer channel plays an important role and thus affects the plasma parameters at the time when the streamer bridges the gap. For centimeter-scale gaps, the ionization waves in the second stage play an insignificant role. However, it was asserted [15] that they may become more important for long discharges. We may even draw an explicit analogy with the main stage of lightning, during which the return stroke increases the current in the channel and its conductivity by several orders of magnitude. The return wave mechanisms in the streamer and in the leader channel of lightning are in fact very similar, but the characteristic scales of the phenomenon (in particular, the energy scales) are radically different. For long gaps, the relative importance of different mechanisms for the transition to an arc in the third stage should also differ strongly from that for short gaps. In order for a long streamer to develop, it is necessary to apply a higher voltage; as a result, the electric potential of the growing channel rises and, accordingly, the channel radius increases substantially because of the radial ionization expansion. As the channel radius increases, the time of the hydrodynamic expansion of the channel becomes longer; consequently, the intensification of impact ionization as the reduced electric field E/N grows plays a lesser role.

Our purpose here is to review the papers aimed at the numerical simulations of the streamer breakdown of long gaps. Main attention is focused on the microscopic analysis of the mechanisms for maintaining a gas-discharge plasma. We start with a brief description of the computer model that was used to obtain the main results on breakdown in cold and heated air. In Section 3, we consider a streamer breakdown in air under normal conditions and determine the conditions under which this process comes to an end. We also present new results concerning both the choice of the radius of the streamer channel under streamer breakdown conditions and the breakdown of a gap under the combined action of a short-term overvoltage pulse and a small-amplitude long-term voltage pulse. Section 4 is devoted to hot air that was either preheated in a special way or kept its high temperature in the channel that remains after the primary breakdown during a short-term switching-off of the voltage. The conditions for breakdown of heated air are far less restrictive. Finally, in Section 5, we consider the breakdown in noble gases and demonstrate that a spark channel with a descending I–V characteristic forms by a nonthermal mechanism.

2. COMPUTATIONAL MODEL

The streamer breakdown is simulated by using a one-and-a-half-dimensional (1.5D) model that identifies the channel with a cylinder of constant radius. Here, this model, which was described in detail in [16–18], is described only briefly. The set of equations for the processes in air includes Poisson's equation and the balance equations for electrons, positive and negative ions, excited molecules, atoms, and new chemical compounds produced in the course of breakdown. The electric field is determined under the assumption that only the side surface of the channel is charged. If, in the course of breakdown, the electron density, electric field, and discharge current evolve to essentially uniform distributions, then the further evolution of the system is traced by using a zero-dimensional model.

In order to calculate the energy parameters, the set of equations also includes the balance equations for the translational energy of neutral particles and the vibrational energy ε_V of nitrogen molecules. Although nitrogen molecules are not of crucial importance in describing the development of the streamer, they play a key role in the final breakdown stage, when the streamer

evolves into an arc. The energy balance equations have the form

$$c_v N\frac{\partial T}{\partial t} = (\lambda_T + \lambda_R + \delta\lambda_E)jE + j_{\text{ion}}E + Q_{VT},$$
$$\frac{\partial \varepsilon_v}{\partial t} = \lambda_V jE - Q_{VT}, \quad (1)$$

where $Q_{VT} = \dfrac{\varepsilon_v - \varepsilon(T)}{\tau_{VT}(T)}$. The rest of the notation is as follows: c_v is the heat capacity (per particle) of the gas at a constant volume; T is the temperature of neutral particles; j and j_{ion} are the densities of the electric current carried by the electrons and ions, respectively; λ_T, λ_R, λ_V, and λ_E are the fractions of the electron energy that are transferred to the translational, rotational, vibrational, and electronic degrees of freedom of neutral particles, respectively; and τ_{VT} is the vibrational–translational (V–T) relaxation time of N_2 molecules. In Eqs. (1), it is assumed that the entire rotational energy of molecules and a fraction of the energy of electronic degrees of freedom transform instantaneously into heat. In most of the calculations, the fraction of energy transformed from electronic states of molecules into heat was set to be $\delta = 0.3$.

In the model, the hydrodynamic expansion of the streamer channel is not considered, because streamer breakdown develops on a short time scale. In most cases, the heating of a gas in the channel, which is accompanied by an increase in the pressure, lasts for 10^{-7} s or less. The characteristic time of hydrodynamic expansion is markedly longer. Hydrodynamic effects may be important to include only when estimating the breakdown voltages under the action of voltage pulses having relatively long rise times (longer than 100–200 ns), in which case the breakdown process is extended over time. However, hydrodynamic effects can be neglected when estimating the threshold for streamer breakdown of cold air, in which case the rise time of the voltage pulses should be much shorter. If necessary, the upper estimate of the role of hydrodynamic effects was obtained by comparing the results of numerical simulations carried out without allowance for the channel expansion (at increasing pressure) with the results from the simulations of the isobaric expansion, when the initial pressure remains unchanged throughout the entire expansion process because of the increase in the channel radius.

After the streamer bridges the gap, the current through the cathode surface is governed by electrode effects. In our model, the cathode sheath and emission processes at the cathode surface are ignored, because, in calculations, the cathode voltage drop was negligible in comparison with the voltage across a long gap (under normal conditions in air, this voltage was usually higher than 100 kV).

The kinetic scheme of our model takes into account the main processes of the production of electrons and their losses in air with a gas temperature from 300 to 7000 K in an external electric field E/N up to 1000 Td (1 Td = 10^{-17} V cm^2). For weak reduced electric fields E/N and high temperatures, the model gives a thermodynamically equilibrium plasma composition. For T = 300 K, the model reduces to a traditional model describing discharges in air under normal conditions [19]. The rate constants for electron processes and the electron energy balance in an electric field are determined by numerically solving the Boltzmann equation for electrons in the familiar two-term approximation. Under the assumptions of our model, the electron parameters are functions of the reduced electric field E/N; the gas temperature T; the gas composition; and the vibrational temperature T_v of N_2 molecules, which can be substantially higher than T.

3. AIR BREAKDOWN UNDER NORMAL CONDITIONS

In [20], the model described above was used to numerically investigate the streamer breakdown of long air gaps under normal conditions. Let us discuss the results obtained in [20] in more detail.

3.1. Streamer Propagation in the Discharge Gap

The initial breakdown stage (the propagation of a streamer until it bridges the gap) was modeled numerically using, as an example, a cathode-directed (positive) streamer in the gap between the sphere and the plane for different degrees of nonuniformity of the electric field and different rise times of the voltage pulse.

3.1.1. Highly nonuniform field. Starting from the anode, the streamer accelerates. The larger the anode radius r_a, the longer the path of acceleration. If the voltage is fixed, the maximum streamer velocity $v_{s\max}$ decreases with increasing r_a. As the voltage drop across the extending channel and the electric charge on the channel surface increase, the field near the streamer head gradually decreases and the streamer propagation slows down. Together with the streamer velocity v_s, the electron density n_e in the produced streamer plasma varies in the same proportion, because, to sufficient accuracy, $n_e \propto v_s$ [3, 16, 17]. At the instant when the streamer bridges the gap, the electron density profile $n_e(x)$ along the channel is determined, on the one hand, by a decrease in the ionization rate at the wave front of the extending streamer and, on the other hand, by a fairly fast loss of electrons in "old" segments of the channel.

The electron loss is dominated by the dissociative recombination of cluster ions with electrons, whose rate may be higher than 10^{24} cm^{-3} s^{-1} because of the fairly high initial electron density. The rate of the dissociative attachment of electrons to molecules is several

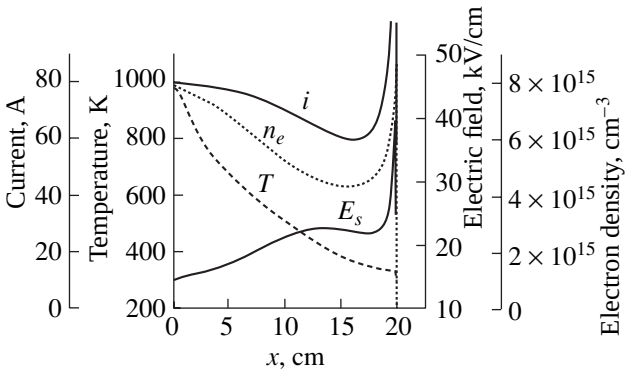

Fig. 1. Profiles of the conduction current, electron density, electric field, and gas temperature along a streamer channel of radius 0.05 cm at the instant at which the streamer bridges a 20-cm-long air gap between the sphere and the plane. The calculations were carried out for a 500-kV rectangular voltage pulse and the anode radius r_a = 2 cm.

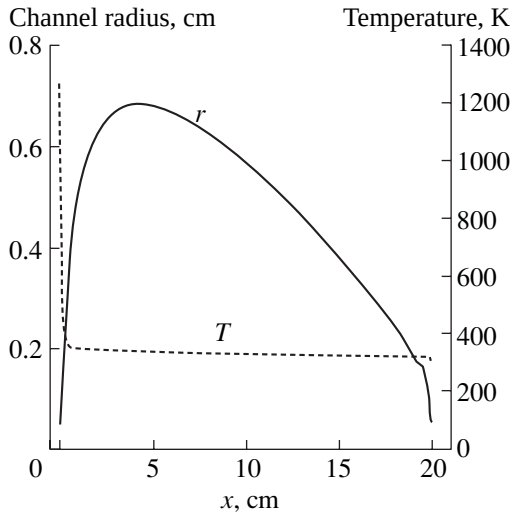

Fig. 2. Variation in the streamer radius and profile of the gas temperature along the gap with allowance for the ionization expansion of the channel. The initial streamer radius and the remaining parameters are the same as in Fig. 1.

times smaller, and the three-body attachment rate is tens of times smaller. The destruction of negative ions is of minor importance, because, even in the oldest segments of the channel, their density is small compared to the electron density.

The higher the voltage across the gap, the more pronounced is the change in the plasma velocity and density along the streamer. This effect is quite natural, because, as the voltage increases, the time required for the streamer to bridge the gap decreases, so that the effect of the plasma decay in the old segments of the channel becomes progressively less important. Figure 1 shows the electron density profile along the streamer channel of radius 0.05 cm at the instant when the streamer bridges a gap of length 20 cm. The streamer formed in a discharge driven by a 500-kV rectangular voltage pulse, which is intense enough for streamer breakdown. We can see that the electron density variations along the channel are not too large: the ratio of the maximum value of n_e to its minimum value is close to two. The longitudinal electric field $E_s(x)$ in the channel behaves in essentially the same manner: it increases fairly gradually from the anode toward the cathode, except in the immediate vicinity of the streamer head, where the field E_s increases sharply from tens to hundreds of kilovolts per centimeter at a distance comparable to the channel radius (Fig. 1). The conduction current along the channel, $i \sim \mu_e(E_s)E_s(x)n_e(x)$ (where μ_e is the electron mobility), varies to an even lesser extent: it decreases from the anode to the cathode by an amount of 35% or less. By the time when the streamer comes into contact with the cathode surface, the gas temperature in the old segments of the streamer (near the anode) is the highest (it can become as high as 1000 K), while the gas near the cathode remains practically unheated (Fig. 1).

Recall that, in the 1.5D model, the streamer radius serves as an input parameter and many results are very sensitive to its value. Consequently, to obtain more or less realistic numerical results requires a "correct" choice of the streamer radius. In order to make the model free of this obvious drawback, it is expedient to take into account the ionization expansion of the channel. In our earlier papers [18, 21], we showed that the final results are weakly sensitive to the *a priori* specified initial radius, because the channel that has already been formed experiences a very rapid ionization expansion (over a time scale of fractions of a nanosecond) in the radial electric field of the surface charge of the streamer. The higher the voltage across the gap, the more important are the consequences of such expansion. Figure 2 shows how the streamer radius changes along the streamer axis at the time when the streamer bridges a 20-cm-long air gap at an applied voltage of 500 kV. Except in the short anode and cathode regions where there is no radial electric field, the channel radius has enough time to increase by approximately one order of magnitude—up to 0.5–0.8 cm. It is this radius that should be incorporated into the 1.5D model in order to analyze the conditions for streamer breakdown. The channel with such a large radius does not have enough time to be heated. By the time at which the streamer bridges the gap, the gas is heated to several tens of degrees above its initial temperature (Fig. 2). The only exception is a very short region near the anode, where the channel experiences no expansion and the gas is heated to a temperature higher than 1000 K. The calculated current in the channel increases appreciably with radius. From Fig. 3, one can see that, at r = 0.5 cm, the current over most of the channel volume varies between 500 and 800 A, in which case, however, the calculated mean current density does

not increase but instead decreases markedly (from 8–10 kA/cm^2 at r = 0.05 cm to 0.65–1 kA/cm^2 at r = 0.5 cm) as the radius increases; i.e., the mean current density is roughly inversely proportional to the channel radius. This predictable result stems from the fact that the calculated electron density in a streamer plasma is inversely proportional to the radius r. In a channel with a large radius, the electron density also varies insignificantly along the streamer (Fig. 3).

3.1.2. Characteristic features of the development of a streamer in a gap with a uniform field. A gap of length d with a uniform distribution of the electric field can be regarded as a limiting case of a system in which the anode radius is large. However, it should be kept in mind that, if the electric field is below the threshold E_i (which is about 30 kV/cm under normal conditions in air), then, in order to drive the streamer, it is necessary to enhance the field in a certain small region. In a gap shorter than d < 50 cm, the streamer is continuously accelerated until it bridges the gap [18]. For the same voltage and length d, the velocity of a streamer in a uniform field becomes equal to that of a streamer in a nonuniform field only just before the streamer reaches the cathode. Such "equalization" of velocities is ensured by the continuous acceleration of the streamer in a uniform field and its slowing down in a nonuniform field. As a result, the average streamer velocity in a uniform field turns out to be lower and, accordingly, the time required for it to cross the gap increases.

The characteristic behavior of the velocity variation is qualitatively reflected in the electron density distribution along the streamer channel. In a uniform electric field, the electron density n_e increases from the anode toward the cathode; moreover, for the same voltage, the density values $n_e(x)$ over the entire channel in a uniform field are markedly lower than those in a highly nonuniform field, except in the immediate vicinity of the cathode (Figs. 1, 4). A lower streamer velocity results in a lower current in the discharge gap. The current profile along the channel is seen to be highly nonuniform (Fig. 4). The energy is scattered in the channel and is thus lower than that in a highly nonuniform field, and the gas is heated to a substantially lower temperature. The calculated results illustrated in Fig. 4 show that the gas temperature in the hottest channel region near the anode is lower than 450 K, while the gas temperature at the same radius (0.05 cm) and voltage (500 kV) in a streamer in a highly nonuniform field is higher by a factor of two.

3.1.3. Effect of the rise time of the voltage pulse. As the rise time of the voltage pulse increases, the electric field in the anode region, where the streamer accelerates, weakens. As a result, the maximum streamer velocity, the electron density in the streamer plasma, the current in the channel, and the highest possible gas temperature all become lower [20]. A delayed growth of the voltage to its peak value (i.e., a longer rise time of the pulse voltage) does not remedy the situation

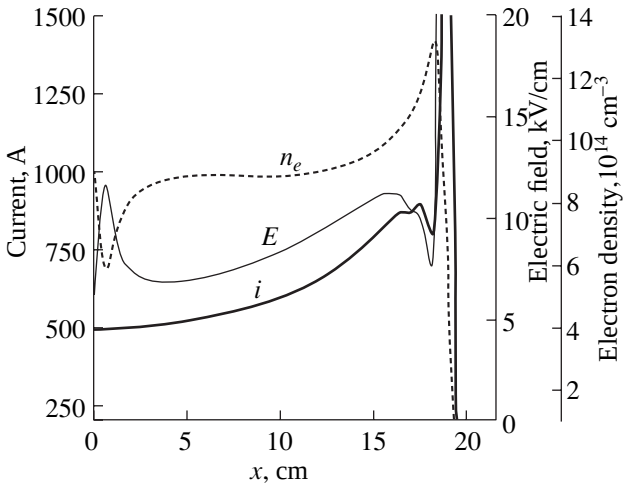

Fig. 3. Profiles of the conduction current, electron density, and electric field along a streamer channel of radius 0.5 cm. The remaining parameters are the same as in Fig. 1.

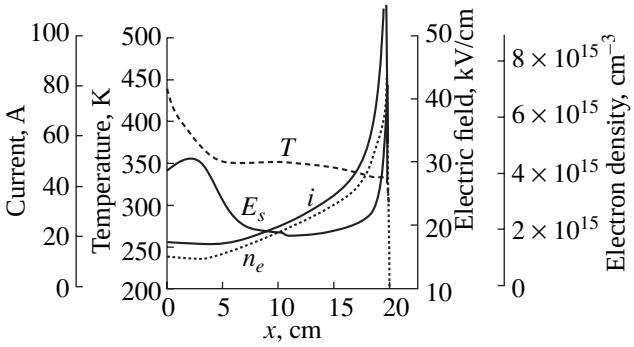

Fig. 4. Profiles of the conduction current, electron density, electric field, and gas temperature along a streamer channel with a uniform electric field. The remaining parameters are the same as in Fig. 1.

completely, because nanosecond times are insufficient to charge the channel segments (with finite capacitance) far from the anode due to the relatively low conductivity of the channel, which has already been formed. This situation is especially true for the streamer head; therefore, its charge and the field ahead of the ionization wave forming the streamer do not strictly follow the growth of the voltage to its maximum value. The longer the streamer, the larger the time delay.

The numerical results illustrated in Fig. 5 characterize a streamer that develops in the gap between the sphere and the plane under the action of a voltage pulse such that the voltage increases to its peak value (500 kV) according to a linear law $U(t) = A_U t$. When the rate at which the voltage increases is $A_U = 2 \times 10^4$ kV/μs, the rise time of the voltage pulse is equal to 25 ns, which is long enough for the streamer to bridge the gap. For calculations, the radius of the streamer

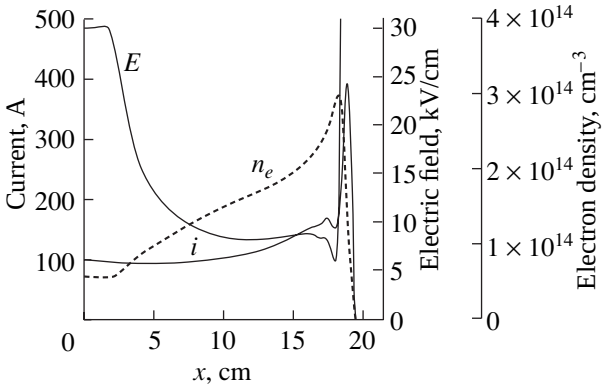

Fig. 5. Profiles of the conduction current, electron density, and electric field along a streamer channel of radius 0.5 cm in the case of a voltage pulse growing according to a linear law $U(t) = A_U t$ to a peak amplitude of 500 kV at the rate $A_U = 2 \times 10^4$ kV/μs. The remaining parameters are the same as in Fig. 1.

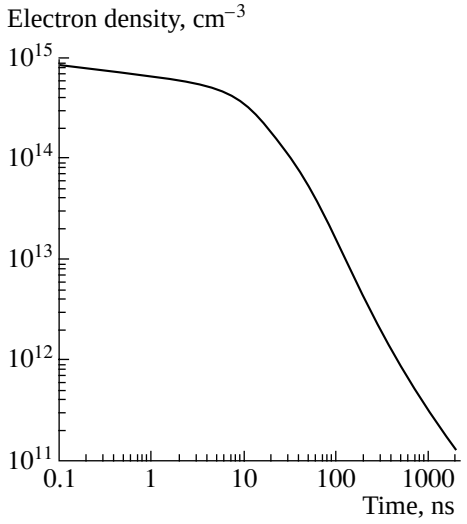

Fig. 6. Time evolution of the electron density in a streamer channel in the middle of the gap in the case when the overvoltage applied to the gap is instantaneously switched off and the mean electric field in the gap falls from 25 to 12.5 kV/cm at the time when the streamer bridges the gap. The zero-dimensional calculations were carried out under conditions analogous to those of Fig. 3.

channel was set equal to $r = 0.5$ cm, which made it possible to compare the results obtained with the results that are presented in Fig. 3 and refer to a rectangular pulse with the same maximum voltage. Although the voltage increases to approximately its maximum value ($U = 450$ kV) by the time when the streamer bridges the gap, the current and mean electron density in the streamer are both lower by a factor of approximately five than those calculated for a rectangular voltage pulse. We can see that, near the anode, there is a region in which the electric field is elevated up to 30 kV/cm. This region should be regarded as a secondary ionization wave that has just originated and is characteristic of streamer processes at a rapidly growing voltage [22]. The time interval over which the voltage is applied is too short for this wave to manifest itself more or less clearly. Since the energy release is small, the gas in the hottest part of the channel is heated at most by 10°.

The revealed tendencies in the behavior of the parameter of a streamer plasma are retained for voltage pulses with longer rise times. It is natural to presume that streamer breakdown is more likely to occur under the action of pulses having short rise times to peak voltages (a few nanoseconds or less). The longer the gap, the more restrictive are the requirements for the rise time of the voltage pulse.

It is important to note that the plasma parameters in the streamer channel that has already bridged the gap should differ strongly between the particular experiments carried out for the same parameters of the voltage pulse. The reason for this lies in the statistical time delay of the discharge: the streamer may start from the anode at different times and, accordingly, may develop at different instantaneous values of the voltages and different instantaneous rates at which the voltage increases. This circumstance should be kept in mind in trying to reconstruct particular experimental data by computer simulations.

Nevertheless, even when the conditions for breakdown are most favorable, the plasma in the channel remains practically unheated at the instant when the streamer bridges the gap. Although the streamer plasma can be fairly dense and can carry currents up to hundreds of amperes, the channel still does not possess a descending *I–V* characteristic. Even if the electric field is reduced at least by one-half after the gap is bridged by the streamer, the streamer plasma will decay very rapidly and the current across the gap will terminate. In Fig. 6, the results of simulations demonstrate the dynamics of this process in the case of a streamer plasma with the initial density $n_{e0} = 9 \times 10^{14}$ cm^{-3} (this value was used to calculate the results shown in Fig. 3); it was assumed that, after the applied voltage was instantaneously switched off, the mean electric field in the gap fell from 25 to 12.5 kV/cm. Over a time interval of 200 ns after the switching-off of the voltage pulse, the electron density decreases by two orders of magnitude, and, over a time interval of about 1 μs, the current across the gap decreases from the maximum value (780 A) to only 0.3 A. As the plasma decays, the gas temperature in the channel remains essentially the same as (or only slightly higher than) the temperature of the surrounding gas. This process does not resemble short-circuiting of the insulation gap.

3.2. Dynamics of the Streamer Channel after Bridging the Gap

3.2.1. Waves of the elevated electric field. As the streamer crosses the discharge gap, the electric field in

the streamer channel is determined by the current, which charges the newly produced segments of the channel to the potential φ_t of the streamer head and corrects for the charge of the already produced segments in accordance with the varying voltage across the gap, in which case the streamer conductivity does not directly affect the current magnitude. The electric field $E_s(x)$ in the channel cross section with the coordinate x (the origin of the coordinates is chosen to lie at the anode surface) is established so as to ensure the electric current $i(x)$ required for the propagation of the streamer.

As the streamer comes into contact with the cathode, the streamer head acquires a zero potential and the voltage U_0 totally drops across the channel. The electric potential profile along the channel changes, thereby changing the charge of the side surface of the channel. The process manifests itself as the propagation of the waves of the current and electric field from the cathode toward the anode along the channel (the so-called return waves). In short gaps (about a fraction of a centimeter), the ionization process at the return wave front is considered to be of crucial importance. It is this factor that is thought to be responsible for a substantial increase in the streamer plasma density and, accordingly, for the subsequent evolution of the streamer channel into an arc [23]. That is why, before proceeding with a numerical analysis of secondary waves in long streamers, it is expedient to consider a short streamer that bridges the gap with a length of about 1 cm. In Fig. 7, the results of numerical simulations illustrate the evolution of a streamer channel after the streamer bridges a 1-cm-long gap between the sphere and the plane. The diameter of the spherical anode is set equal to 0.2 cm, and the streamer diameter is 0.03 cm. The streamer is driven by a 28-kV rectangular voltage pulse, which is intense enough for the gap breakdown. Starting from the cathode, the return wave of the strong field is damped very rapidly (Fig. 7a). The peak electric field, which is close to 200 kV/cm, falls off below 30 kV/cm over a time interval as short as 0.3 ns. As a result, the electron density increases extremely slowly, if at all. One nanosecond after bridging the gap (when the return wave is damped almost completely and the electric field has become uniform over most of the gap), the plasma density in the main part of the channel remains practically unchanged (Fig. 7b). The streamer plasma density n_e is seen to vary (by a factor of two to three) only in the anode and cathode regions. By the time when the return wave is damped completely, the gas temperature changes by an even smaller amount: in the most heated cross section of the channel, it increases by less than 50°. As for the difference in the currents measured at the cathode and anode, it is also captured well by the numerical model. In the situation at hand, the maximum current through the cathode surface during the return wave stage amounts to 50 A, while the maximum current at the anode is as low as 1.2 A (Fig. 7c). We stress that, in real experiments, the

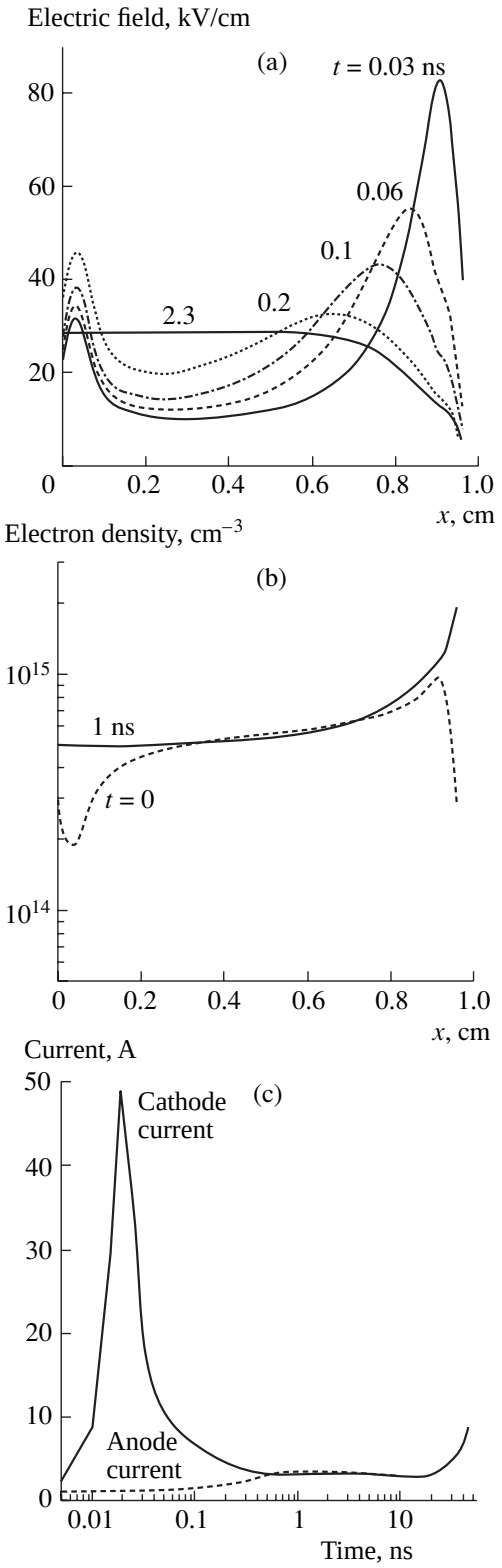

Fig. 7. Time evolutions of (a) the electric field and (b) electron density along a streamer channel of radius 0.03 cm and (c) the electric current at the electrodes after a 1-cm-long gap between the sphere and the plane is bridged by the streamer. The calculations were carried out for a 28-kV rectangular voltage pulse and with an anode radius r_a = 0.2 cm.

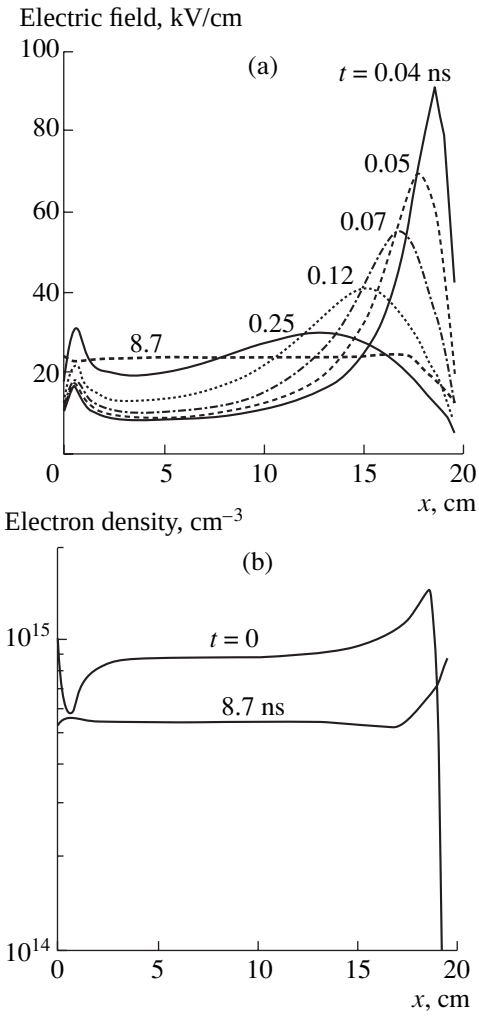

Fig. 8. Time evolutions of (a) the electric field and (b) electron density along a streamer channel of radius 0.5 cm after a 20-cm-long gap between the sphere and the plane is bridged by the streamer. The calculations were carried out for a 500-kV rectangular voltage pulse and the anode radius r_a = 2 cm.

current driven by the return wave was difficult to measure exactly, because its calculated full width at half-maximum was shorter than 10^{-10} s.

Analyzing the results of a numerical simulation of short streamers naturally yields the conclusion that the return ionization wave plays a negligible role in the evolution of the channel after the streamer bridges the gap (the same conclusion was drawn as early as 1984 by Sigmond [15]). The only effect of the return wave is that the electric field becomes uniform over the main part of the streamer channel. This effect is particularly favorable for the numerical modeling of streamer breakdown, even though it does not profoundly influence the breakdown mechanism.

Having convinced ourselves that the role of the return wave in short gaps is grossly exaggerated, we can hardly expect that it will have a more or less significant effect on the evolution of long streamers. In fact, in long gaps, the consequences of the propagation of the return ionization wave along the streamer channel are even less important. In cold air, the wave is most pronounced only at high overvoltage ratios, when the plasma conductivity in the channel remains relatively high after the streamer has bridged the gap.

The parameters of the propagating return wave can be inferred from the numerical results that are shown in Fig. 8 and were computed for a 500-kV rectangular voltage pulse applied to a 20-cm-long gap between the sphere and the plane. As will be shown below, this voltage is sufficiently high for breakdown. The return wave is seen to be rapidly slowed down and damped. Like in the short channel, the peak electric field at the wave front also falls to about 30 kV/cm over the time interval equal to 0.3 ns; during this time, the wave propagates only one-fourth of the gap (starting from the cathode) (Fig. 8a). The electric field and electron density equalize along the channel not only because of the ionization process but also (and to an even greater extent) because of the more rapid electron loss in electron–ion recombination reactions in the parts of the channel where the streamer plasma was originally denser (Fig. 8b). As a result, over a time interval shorter than 10 ns, the electron density in the main part of the channel is nearly equalized. The same is true of the electric field, which approaches its value averaged over the gap, $E_c = U/d$. By the end of this time interval, the electric field in the channel is established at a much higher level, causing the current to increase by a factor of approximately 1.5 at a decreased electron density n_e. As the return wave propagates in the streamer channel and the electric field is redistributed, the gas temperature of the streamer plasma changes insignificantly (by at most 100°).

As is expected, the parameters of the return wave are sensitive to the streamer radius, which serves as an input parameter for the numerical model. However, the final results obtained for different values of the streamer radius differ only quantitatively (and by no means fundamentally). This was confirmed by a series of test calculations carried out in [20] for a streamer channel of radius 0.05 cm (Fig. 9). Such a thin solitary streamer at a voltage of 500 kV is nothing more than a model abstraction, because, in reality, the radial electric field at its side surface would be greater than 1000–1500 kV/cm and would excite an extremely strong radial ionization wave, which, in turn, would force the channel to expand to the "relevant" radius. Nonetheless, these numerical estimates are of interest, because they provide insight into the most extreme case of this type.

The results of these simulations confirm the features of breakdown described above: the ionization wave is, as before, damped over a time scale of fractions of a nanosecond and, over a time interval of about 10 ns after the streamer bridges the gap, the electric field in the channel becomes essentially uniform (Fig. 9a);

moreover, its equalization is again governed by the loss of a number of electrons in regions where the electron density is excessive (Fig. 9b). The test simulations also demonstrate all of the effects of the return wave propagating in a long streamer: the strong field region propagates toward the anode, the current through the cathode surface is much higher (at most, by one order of magnitude) than that through the anode surface, and, as the return wave is damped, the cathode current rapidly (for about 0.04 ns) decreases by one-half and gradually approaches the anode current. Although a thin streamer channel is heated to a somewhat higher temperature, the heating again remains insignificant: the gas temperature increases by 400 K near the cathode and by at most 200 K near the anode. The process of streamer breakdown in a gap with a uniform electric field also differs from that analyzed above only in a few details, which are associated with the fact that the plasma conductivity in the streamer channel is lower; this, in turn, leads to a slower propagation of the return wave and its stronger damping [20].

Hence, the mechanisms governing the evolution of a streamer into an arc channel come into play after the return wave is completely damped, i.e., when the electron density, electric field, and current are equalized along the channel.

3.2.2. Evolution of a quasi-uniform streamer channel. After the equalization of the plasma parameters along the streamer channel, the evolution of the channel can be modeled by applying a zero-dimensional model. The related calculations show that the channel radius determines the initial electron density and, to some extent, the initial gas temperature, thereby determining the time of heating (Fig. 10) but not its consequences, which almost completely depend on the electric field in the channel. A series of test calculations carried out for $r = 0.5$ cm yielded the following times t_h of heating the gas in the channel to a temperature of 6000 K, at which the streamer plasma acquires essentially all of the properties of an arc plasma (see table).

E, kV/cm	20.0	22.5	25.0	27.5	30.0
t_h, ns	1600	430	130	55	29.5

Since the leader process in a weaker external field may develop on a time scale of about 1 μs, we should actually speak of the streamer breakdown when the electric field E is close to 25 kV/cm and the heating time becomes as short as several tenths of a microsecond.

By the time at which the process of the transformation of the streamer channel has come to an end, the current density j_s increases to tens of kiloamperes per square centimeter. It should be noted that this value of the current density is not too sensitive to the channel radius adopted for simulations (Fig. 10). The change in the heating time, Δt_h, is also not very significant: as the channel radius r increases from 0.05 to 0.5 cm, the quantity Δt_h changes by no more than a factor of two.

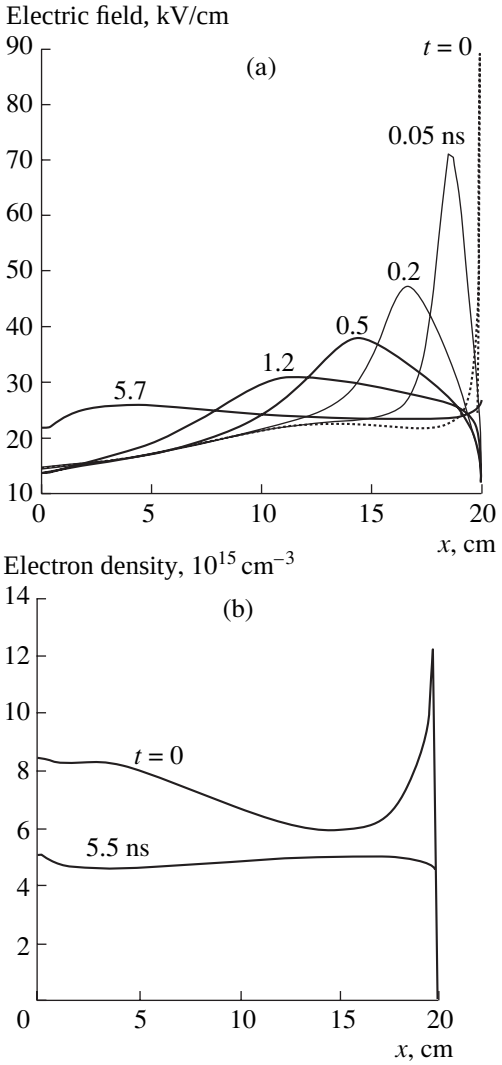

Fig. 9. Time evolutions of (a) the electric field and (b) electron density along a streamer channel of radius 0.05 cm after the gap is bridged by the streamer. The voltage pulse and gap parameters are the same as in Fig. 8.

This justifies the use of a 1.5D model with a constant channel radius. During heating, the electron density in the channel increases by two orders of magnitude and, finally, becomes higher than 10^{16} cm^{-3} (Fig. 11).

We emphasize that, after the streamer bridges the gap, the energy deposited in the channel is high. In the case at hand (r = 0.5 cm), the calculated current increases to $I_{max} \sim$ 10–15 kA. Over a time interval of about $\Delta t_h \sim 100$ ns, the charge carried away from a high-voltage pulse generator (HPG) is equal to $Q \sim 1$ mC. In this case, in order for the output voltage of the generator not to drop too markedly, its internal resistance $R \ll U_{max}/I_{max}$ should be on the order of 10–1 Ω. There are few traditional nanosecond generators that satisfy such requirements, the more so because the output capacitance of the generator, $C \gg Q/U_{max}$, should be suffi-

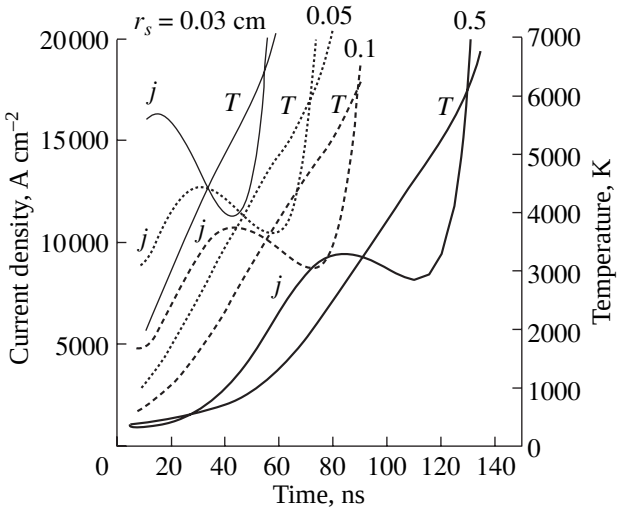

Fig. 10. Time evolutions of the current density and gas temperature in channels of radii 0.03, 0.05, 0.1, and 0.5 cm after a 20-cm-long gap between the sphere and the plane is bridged by the streamer. The evolutions were calculated at a distance of 10 cm from the anode for a 500-kV rectangular voltage pulse and the anode radius r_a = 2 cm.

ciently high (about 10 nF) in order for the generator to be capable of maintaining the output voltage during the discharging of this capacitance as the streamer channel is heated. Accordingly, an attempt to experimentally investigate the evolution of a long streamer channel into an arc will encounter significant difficulties.

Under real conditions, a nanosecond voltage pulse may turn out to be insufficiently long for the breakdown process to come to an end. The pulse may be damped when the instantaneous gas temperature T is still far below the temperature characteristic of an arc. Nevertheless, even such a pulse changes the state of the gas medium, so that a weaker electric field is required in order for the breakdown process to come to an end. The problem formulated with allowance for the above considerations is oriented toward practical applications, because it allows one to reconstruct how the air insulation is affected by the combined action of a nanosecond overvoltage and a long-term applied operating voltage, which ensures the residual electric field E_{oper} in the discharge channel. The character of the process when the overvoltage applied to the gap is switched off is reconstructed in Fig. 12. In a channel of radius 0.5 cm, the electric field that was established after the gap was bridged by the streamer is equal to 25 kV/cm. At 94.5 ns, by which time the gas was heated to 3500 K, the field very rapidly falls off to E_{oper} = 6.45 kV/cm. Then, the electric field remains unchanged. A jumplike decrease in the field is accompanied by a decrease in the current (by a factor of 2.8, i.e., in proportion to the electron drift velocity $v_e \sim E^{0.73}$ in the energy range under consideration). A further decrease in the current over a time interval of about 60 ns is a consequence of the decay of a streamer plasma in a depressed electric field. Over this time interval, the electron density decreases by nearly one order of magnitude (Fig. 13). The channel conductivity starts growing when the gas is heated to a temperature of about 4000 K, at which the associative ionization reaction

$$N + O \longrightarrow e + NO^+ \qquad (2)$$

becomes important.

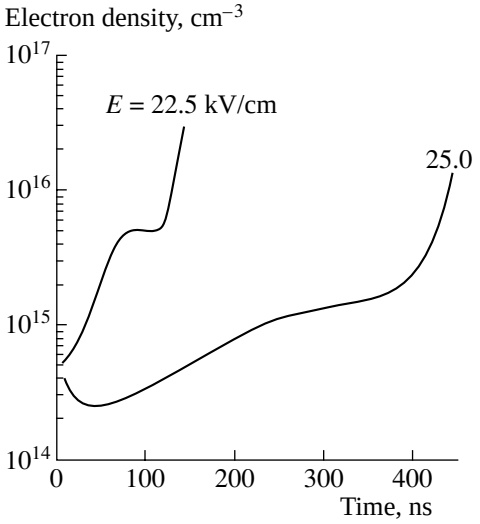

Fig. 11. Time evolutions of the electron density in a channel of radius 0.5 cm after the electric field in the channel relaxes to two different uniform levels. The calculations were carried out for a 20-cm-long gap between the sphere and the plane.

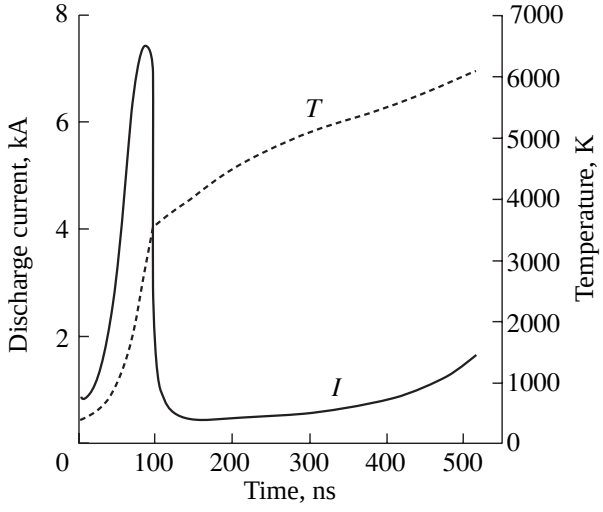

Fig. 12. Time evolutions of the discharge current and gas temperature in a channel of radius 0.5 cm in the case when the mean electric field decreases instantaneously from 25 to 6.45 kV/cm at the time t = 100 ns, when the gas is heated to a temperature of 3500 K.

Taking into account the fact that the streamer breakdown may compete with the leader breakdown (provided that the streamer develops on a time scale of a few tenths of a microsecond), we determined the residual electric field E_{oper} ensuring that the channel is heated to a temperature of 6000 K over a time of 0.5 μs. This temperature value was conditionally accepted to be the critical temperature characteristic of an arc: before the overvoltage applied to the gap is switched off, the electric field in a channel of radius 0.5 cm was equal to 25 kV/cm. In Fig. 14, the results of computer simulations show that the residual field E_{oper} starts decreasing rapidly after the channel is heated to 2000 K. However, only at a temperature of 3600 K, the field just at the end of breakdown falls below the level 5 kV/cm, which characterizes the breakdown strength of air under the action of a long-term operating voltage. In other words, under normal conditions, an air gap cannot be affected by a highly nonuniform electric field with a peak strength of more than 5 kV/cm because of the inevitable leader breakdown. For the same reason, the breakdown strength of the gap bridged by a streamer actually decreases only when the applied nanosecond voltage pulse is strong enough to heat the gas in the channel to a temperature of about 4000 K.

The calculated nonmonotonic evolution of the current in the streamer after the return wave was damped and the electric field was equalized (Fig. 10) provides evidence for a fairly complicated kinetic scheme of the breakdown process: as the breakdown develops, different reactions of the production of electrons and their losses vary in importance. Not all of these reactions have been exhaustively investigated, and the rate constants of many reactions are known only approximately. Based on the relevant existing database, we can assume that, in the initial breakdown stage, the electrons are produced mainly in the reactions of step electron-impact ionization and associative ionization of electronically excited nitrogen molecules [20], among which $N_2(A^3\Sigma_u^+)$ molecules have the highest density. The reactions involving these molecules dominate electron production and ensure an increase in the electron density in an as yet cold channel at a relatively weak electric field of 25 kV/cm (Fig. 15). A temporary decrease in the current j is attributed to the reduction in the density of the electronically excited N_2 molecules because of the production of active particles that collide with the excited molecules and rapidly quench them. As the gas is heated to temperatures $T > 4000$ K, the electron density n_e and current j again start increasing in a stable fashion because the electrons are now produced in reaction (2), which is essentially completely insensitive to the electric field. In such a hot gas, the electric field also has no impact on the generation of N and O atoms, because they are produced via thermal dissociation. In this situation, the rate of reaction (2) decreases only slightly even in a zero electric field. As for the electrons, they are lost only in dissociative recombination with simple molecular ions (mainly NO^+), while electron attachment to neutral particles is of negligible importance.

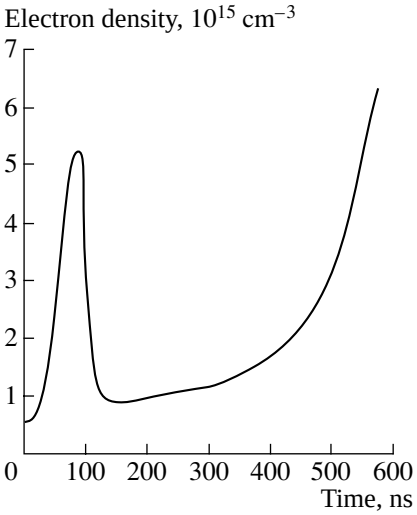

Fig. 13. Time evolution of the electron density in the channel. The conditions are the same as in Fig. 12.

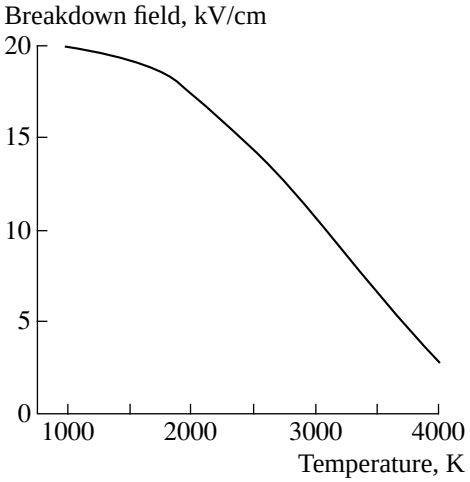

Fig. 14. Dependence of the "operating" breakdown electric field on the gas temperature at which the field decreases sharply. The remaining parameters are the same as in Fig. 12.

It should be kept in mind that the numerical model developed here is evaluative in character not only from the standpoint of incorporating the kinetic reaction but also for describing the energy balance in the channel. This primarily concerns fast heating processes, whose rates are governed by the fraction of energy that is transferred from the electronically excited states of molecules. Calculations carried out with allowance for the essential variations in the parameters of the related processes [20] showed that they markedly affect the time scale on which a breakdown develops and rela-

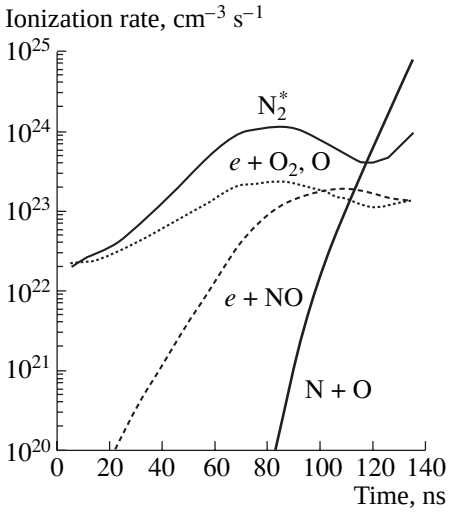

Fig. 15. Time evolutions of the rate constants for ionization in the channel at an applied electron field of 25 kV/cm. The calculations were carried out for the processes involving the electronically excited N_2 molecules, electron impact ionization of O_2 molecules and O ions, electron impact ionization of NO molecules, and associative ionization in collisions between N and O atoms.

tively weakly (to within 10%) influence the breakdown threshold. The same is true of the degree to which the initial electric field is nonuniform, as well as of the streamer channel radius, which serves as an input parameter for simulating the streamer propagation.

4. REBREAKDOWN OF LONG GAPS

For the breakdown of a long air gap to occur under normal conditions, it is necessary to apply extremely strong and short voltage pulses. However, the conditions for breakdown in gaps in which the gas is preheated are not so restrictive. Such conditions are typical of, e.g., spark rebreakdown. The rebreakdown of a slowly cooled gas channel that remains after an electric arc has come to an end plays an important role in the operation of current switches and is even more important for exploiting high-voltage electric power transmission lines (in the case of automatic reclosing of the line immediately after short-circuiting). It is well known that the parameters of the rebreakdown differ appreciably from those of a primary breakdown in an unperturbed gas. In air, the threshold for rebreakdown can be much lower than that for primary breakdown [24, 25]; the same is true of SF_6 [26].

The rebreakdown of the channel that is cooled after an arc discharge has come to an end was numerically modeled in our paper [27] for a long air-filled gap between the sphere and the plane. In that study, we used a 1.5D model with uniform radial profiles of all of the air parameters. We neglected the hydrodynamic expansion of the channel and assumed that the ionization wave covers the entire cross section of the heated channel. (The cooling of the channel was not modeled; instead, the initial temperature and initial composition of the air in the channel at the time when high voltage was applied for a second time were used as the input parameters.) These fairly rough, approximate assumptions allowed us to study the main characteristic features of the development of the rebreakdown, which had not been clarified previously even at a qualitative level. In particular, we showed that, in contrast to the primary breakdown, which usually proceeds through the leader process [1–3], the rebreakdown is, in essence, a version of the streamer breakdown. Let us analyze the results obtained for the rebreakdown in more detail.

4.1. State of the Gas Medium in the Cooling Channel

When the current is not too high, the air temperature in an arc channel ranges from 6000 to 10000 K. After the current is switched off, the heated channel cools at a slow rate. Consequently, we can assume that the air composition in the channel is in a local thermodynamic equilibrium and correspondingly changes as the air temperature T decreases. The auxiliary numerical calculations carried out in [27] in order to simulate the relaxation of the composition of the heated air as its temperature T decreases very rapidly showed that the assumption of the equilibrium character of the composition is valid for electrons and O and N atoms but it may fail to hold for NO molecules. The equilibrium density of NO molecules is maximum at $T_{max} \approx 3000$–3500 K at atmospheric pressure. As the air cools, the NO density rapidly relaxes for $T > T_{max}$; in contrast, for $T < T_{max}$, the NO molecules are decomposed at a far lower rate, so that the NO density does not have enough time to follow the decrease in the temperature. In fact, in this case, NO molecules are lost in the reactions

$$NO + N \longrightarrow O + N_2, \quad (3)$$

$$NO + O \longrightarrow N + O_2, \quad (4)$$

whose rate is fast at high temperatures T and decreases exponentially at $T < T_{max}$, because the density of N atoms is too low and the energy threshold for reaction (4) is high (about 1.7 eV). In the cooling channel, the density N_{NO} of NO molecules decreases mainly because of the diffusion on the same time scales on which the channel cools by heat conduction. For this reason, the relationship between N_{NO} and T in the cooling channel at low temperatures can be written in an approximate form:

$$N_{NO}(T) = N_{NO}(T_{max})T/T_{max}. \quad (5)$$

In computations carried out in [27], the initial air composition was assumed to be thermodynamically equilibrium everywhere, except for NO molecules, which were described by relationship (5) if the initial temperature was in the range $T < T_{max}$.

4.2. Ionization Wave in the Cooling Channel

After the primary breakdown, the dielectric properties of the air start reconstructing as the channel cools in the temperature range $T < 3000$ K. In this situation, the rebreakdown in a gap with a nonuniform electric field begins from the formation of an ionization wave near the electrode having a small radius (in the case at hand, this is an anode) and its further propagation along the channel. Qualitatively, this wave is analogous to a streamer propagating in unperturbed air. However, its quantitative parameters are highly sensitive to the initial air temperature T and the residual conductivity of the channel.

In order to investigate the effect of the residual electron density n_{e0} on the propagation of the ionization wave, the initial stage of the rebreakdown in the gap between the sphere and the plane was modeled in [27] for the gap length $d = 30$ cm and for different densities n_{e0}. The radii of the anode and the plasma channel were chosen to be 2 and 0.5 cm, respectively. Figure 16 shows the time evolutions of the longitudinal electric field in the channel at atmospheric pressure and at $T(t = 0) = 3000$ K and $n_{e0} = 10^9$ and 10^{11} cm^{-3}. (The latter density value corresponds to the thermodynamically equilibrium density at $T = 3000$ K.) The figure also shows the axial profiles of the electron density at the time by which the ionization wave propagates a distance of 25.5 cm. Calculations show that the higher the residual electron density n_{e0}, the more hampered is the wave propagation in the channel that remains after the primary breakdown has come to an end. This conclusion stems from the fact that the residual electrons drifting in the external electric field induce a space charge along the entire primary channel (in particular, in the region ahead of the ionization front), thereby smoothing out the longitudinal field nonuniformity and causing the ionization wave to damp. Consequently, at a sufficiently high residual density n_{e0}, the electron density profile along the channel that remains behind the ionization front is highly nonuniform.

That the electron density in the channel behind the ionization wave is lower than that in a streamer plasma in air under normal conditions is also attributed to the lower air density N. In fact, according to [3, 17], the electron density behind the ionization wave is about $n_e \sim \nu_i/\mu_e$, where ν_i and μ_e are the ionization rate and the electron mobility at the ionization front. For a fixed ratio E/N, we have $\nu_i \sim N$ and $\mu_e \approx N^{-1}$, which yield $n_e \sim N^2$, indicating that the electron density decreases significantly as the air is heated at a constant pressure.

As is the case with a streamer in cold air, the ionization wave in the cooling channel drives the return wave of the elevated electric field when it reaches the opposite electrode. The results of simulation of this return wave are illustrated in Fig. 17. At a low applied voltage, the electric field at the return wave front is weak, the ionization rate is slow, and the ionization process

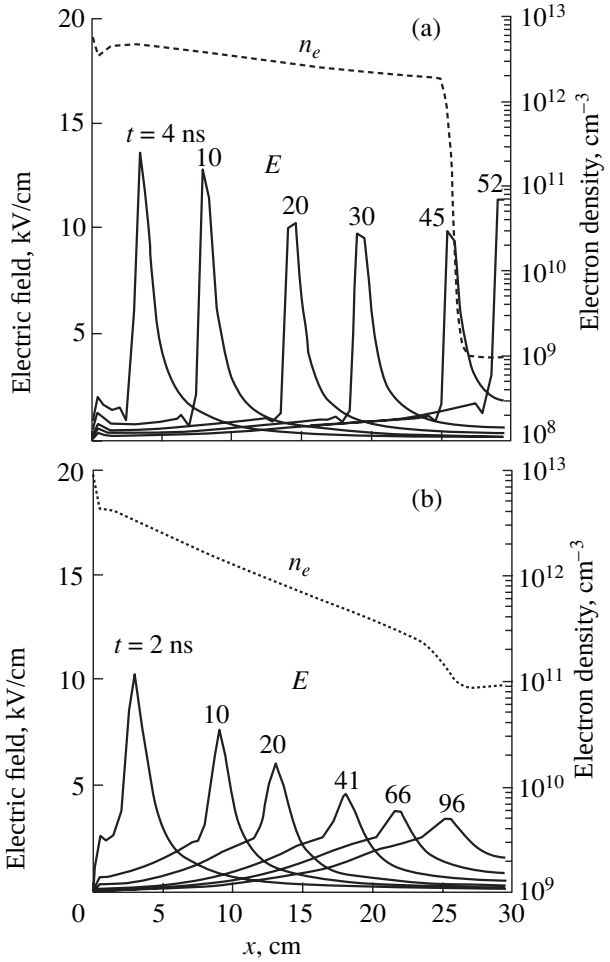

Fig. 16. Time evolutions of the electric field in the channel and longitudinal profiles of the electron density at the time by which the ionization wave propagates a distance of 25.5 cm for $T(t = 0) = 3000$ K and n_{e0} = (a) 10^9 and (b) 10^{11} cm^{-3}, the applied voltage being $U = 30$ kV.

affects the propagation of the field along the channel only slightly. The electric field is primarily, if at all, redistributed via the electron–ion recombination, which acts to enhance electron losses in the regions in which the electron density n_e is elevated and to hinder them in the regions of depressed electron density. As a result, the axial profiles of n_e and E are equalized. The calculations carried out in [27] show that the electron density relaxes to a longitudinally uniform profile at the level n_e^*, which usually lies between 10^{10} and 10^{12} cm^{-3}, on a time scale of about 1–10 μs. Since the current at such a low electron density is weak, the channel temperature on this time scale increases only slightly. As a result, as is the case with the primary streamer breakdown, the channel will evolve into a highly conducting hot arc only in the next stage, in which it will be heated uniformly over its entire length.

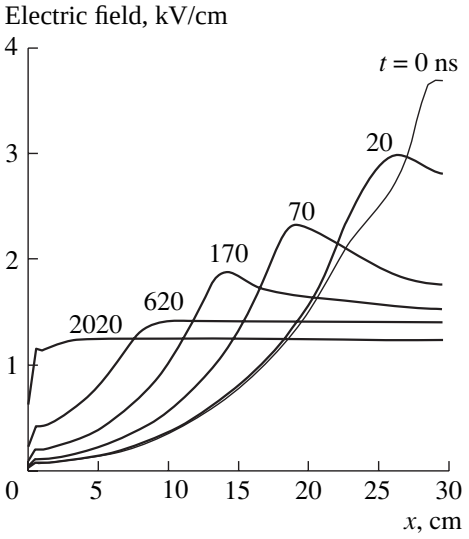

Fig. 17. Time evolutions of the electric field in the channel during the propagation of the return wave at $T(t = 0) = 3000$ K, $U = 40$ kV, and $n_{e0} = 10^{11}$ cm^{-3}. The initial time corresponds to the instant when the primary ionization wave bridges the gap.

4.3. Evolution of a Quasi-Uniform Plasma Channel

The evolution of a quasi-uniform plasma channel, which is the key stage of the development of the rebreakdown in the cooling channel, is characterized by uniform longitudinal profiles of the electric field and the plasma parameters and, therefore, can be studied by means of a zero-dimensional modeling. In order to illustrate the mechanism by which the electron density increases in the external electric field applied for a second time, Fig. 18 shows the time evolutions of the mean rate constant k_i of the electron impact ionization, the rate constant k_r of the electron–ion recombination, the gas temperature T, and the vibrational temperature T_V of N_2 molecules. The corresponding calculations were carried out for $T(t = 0) = 2000$ K. The calculated results show that the initial increase in n_e (for $t > 1.5$ ms) is associated with an increase in T_V, which increases the number of high-energy electrons and enhances the ionization by superelastic collisions of electrons with the vibrationally excited N_2 molecules. Parenthetically, the observed peak in the time evolution $T_V(t)$ reflects the production of O atoms, which efficiently quench the excited molecules, thereby lowering the vibrational temperature T_V over the time interval $0.7 < t < 1.5$ ms, over which the electron density is low. The evolution of the rate constant k_r is weakly sensitive to the air heating to a temperature of 3000 K.

Figure 19 shows the electric field strength E and the reduced electric field E/N, both corresponding to the threshold for the rebreakdown and calculated in [27] as functions of $T(t = 0)$ at $n_e^* = 10^{12}$ cm^{-3}. In the range 600–3000 K, the field E decreases from 7.5 to 0.2 kV/cm. It is important to note that, in this range, the reduced electric field E/N is not constant, but decreases from 60 to 8 Td. This circumstance contradicts standard approaches for determining the threshold for the rebreakdown under an explicit or implicit assumption that the reduced field is constant [24, 28].

At $T(t = 0) = 3000$ K, the calculated threshold electric field for the rebreakdown is of the same order of magnitude as the intrinsic fields in arc channels. Consequently, we can conclude that, for $T(t = 0) > 3000$ K, the air in the cooling channel has not yet started to reconstruct its dielectric properties.

As the air cools to temperatures of $T(t = 0) < 3000$ K, the associative ionization reaction (2) terminates,

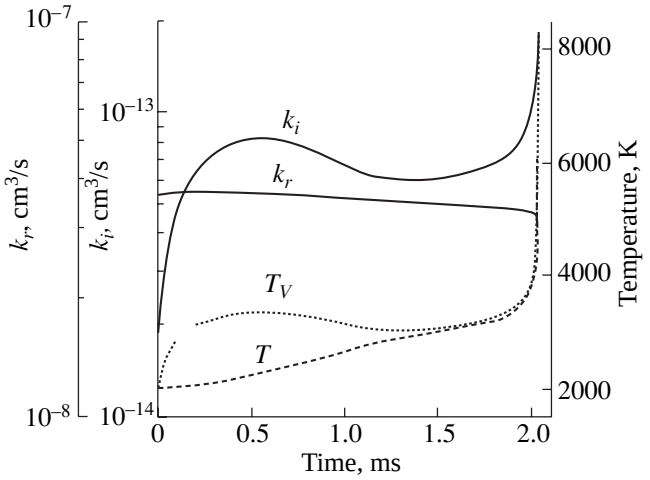

Fig. 18. Time evolutions of the parameters k_i, k_r, T, and T_V at $T(t = 0) = 2000$ K, $E = 1$ kV/cm, and $n_e^* = 10^{12}$ cm^{-3}.

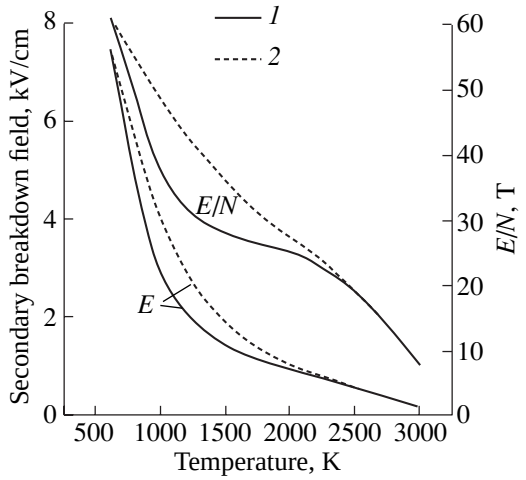

Fig. 19. Threshold values of E and E/N calculated as functions of the initial gas temperature in the cases of (*1*) cooling and (*2*) heating of the air in the channel.

resulting in a rapid enhancement of the threshold reduced field E/N and, accordingly, in a high rate of electron impact ionization of neutral particles. Recall that, at $T(t = 0) > 1000$ K, this ionization process primarily involves NO molecules, whose ionization energy (9.27 eV) is relatively low.

From Fig. 19, we can see that, in the range $T(t = 0) < 1000$ K, the reduced electric field E/N experiences another sharp increase, which is attributed to the appearance of negative ions. At such low temperatures, electron attachment to O_2 molecules is no longer counterbalanced by the reverse processes; as a result, the electron losses are substantially enhanced and the threshold for the rebreakdown increases. In turn, in such strong electric fields, the ionization process is dominated by collisions of electrons with O_2 molecules, while the role of NO molecules becomes insignificant.

Figure 20 displays the time evolutions of the rates of different ionization processes under the conditions prevailing in the rebreakdown in the cooling channel. One can see that, as the air cools, electron impact ionization gives way to associative ionization, whose rate is determined by the air temperature and is independent of the electric field. Consequently, a rapid decrease in the field will not cause a rapid decrease in the plasma conductivity, and we may say that the process of the rebreakdown has come to an end.

There is reason to believe that the threshold for the rebreakdown depends weakly on the channel radius r_c. In fact, the main processes that govern the threshold develop in a uniform electric field $E = U/d$ (where U is the applied voltage and d is the interelectrode distance), which is independent of r_c. Analogously, the specific energy release during the rebreakdown is also independent of r_c. These considerations justify the use of a zero-dimensional model.

The electric field E shown in Fig. 19 has the meaning of the threshold field for the rebreakdown only when it is below the threshold for breakdown of cold air. In long air channels with a nonuniform electric field, the breakdown of cold air usually occurs via the leader mechanism. The mean threshold fields for leader breakdown in air-filled gaps of lengths 1–5 m were measured to be 4–5 kV/cm [29]. Consequently, according to Fig. 19, the air in the cooling channel stops reconstructing its dielectric properties when it cools to temperatures 700–800 K. At lower temperatures T, the breakdown can develop along a channel other than the cooling channel.

Above, we analyzed the breakdown of air in a cooling channel in which the density of NO molecules no longer changes in the range $T < T_{max}$, because it is this range in which the reactions involving NO molecules slow down very rapidly. It is also of interest to consider the breakdown of slowly heated air, in which case the density of NO molecules is thermodynamically uniform and, in the range $T < T_{max}$, is appreciably lower than the density typical of the cooling channel. This situation was investigated numerically in our paper [30]. The related numerical results are also shown in Fig. 19. We can see that, in the range $T(t = 0) = 800$–2000 K, the threshold for breakdown of heated air is far above that of cooled air because of the lower density of NO molecules. The difference in the thresholds is maximum (35%) at $T = 1200$ K. The pronounced hysteresis effect manifests itself in the fact that the threshold for breakdown of air at a fixed temperature depends on the way in which this state of air was achieved (heating or cooling).

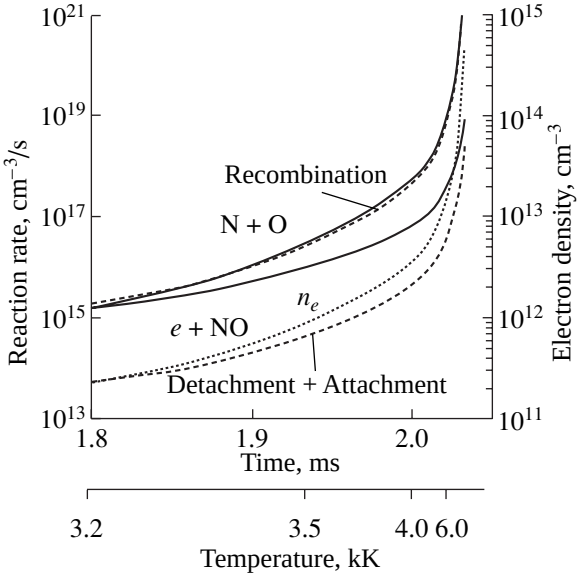

Fig. 20. Time evolutions of both the electron density and the rate constants that govern the electron density in the final stage of the rebreakdown. The conditions are the same as in Fig. 18.

5. NONTHERMAL MECHANISM FOR BREAKDOWN IN NOBLE GASES

There is reason to believe that the streamer breakdown is much easier to initiate in noble gases. In this case, the conductivity of the streamer channel is significantly higher and decreases more slowly with time (because electrons are not attached to neutral particles), and the electron–ion recombination rate is slower. Additionally, a large fraction of the deposited energy can be immediately converted into heat because of the absence of the vibrational degrees of freedom, which accumulate significant energy during the development of a spark in air, thereby hindering the onset of breakdown. That this was in fact true was confirmed by the experiments carried out in [31, 32]. It was found that a streamer breakdown in gaps with lengths of tens of centimeters develops over time intervals of several microseconds and that the mean electric field during the

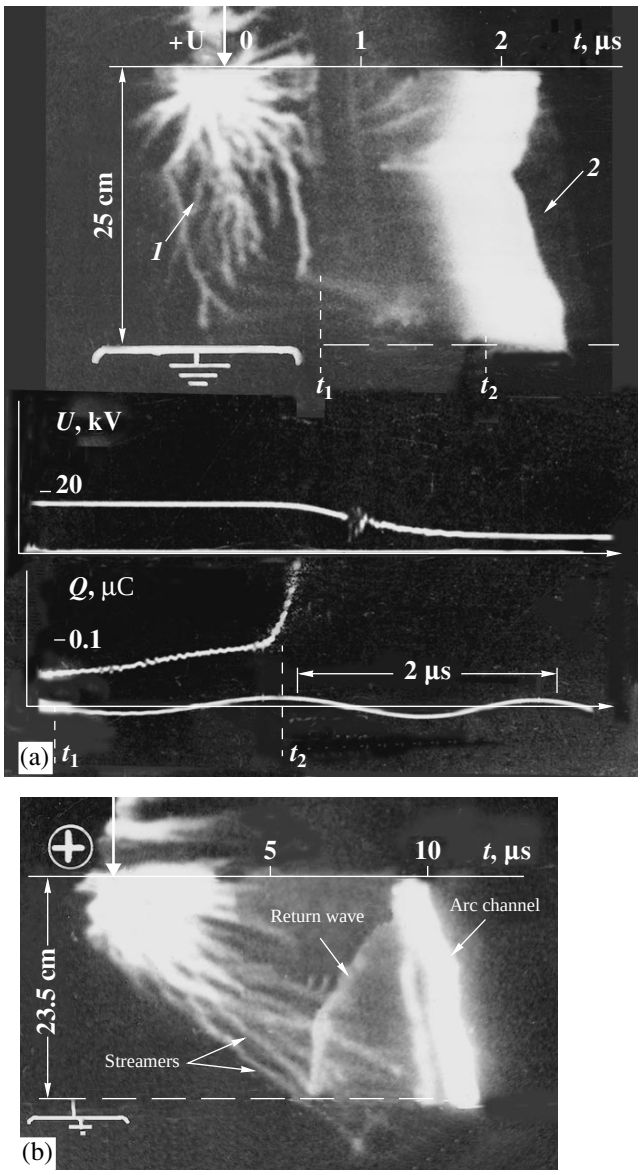

Fig. 21. Evolution of the streamer channel into an arc in Ar in a 25-cm-long gap: (a) streak photograph of the discharge and waveforms of the voltage and the charge carried along the channel after bridging the gap; and (b) visualization of the return wave with the help of a plane cathode equipped with a 3-cm-long needle. The primary streamer (*1*) evolves into an arc (*2*).

breakdown in Ar is about 650 V/cm, which is weaker than that for air by a factor of 30 to 40. It is surprising that, in contrast to the breakdown in air, the energy deposited in the discharge turns out to be too low to attribute the observed increase in the electric current during the breakdown in Ar to the gas heating. Hence, it was clear that the streamer breakdown in noble gases is nonthermal in nature. The nonthermal breakdown mechanism was explained in [32].

5.1. Experimental Results

The measurements were carried out in a transparent cylindrical chamber filled with Ar at the temperature $T = 293$ K at atmospheric pressure. A study was made of rod–plane gaps, the length of the gap being up to 40 cm. In most of the experiments, the length of the gap was 25 cm. A positive voltage from 10 to 60 kV was applied to the rod electrode. The experiments were aimed at measuring both the electric current through the streamer channel after bridging the gap and the voltage drop across the gap; the streak photographs of discharges were taken by an image converter.

The experiments showed that the streamers in Ar and air differ in their properties. Thus, the mean electric field required to initiate the breakdown of Ar in a long gap was measured to be 400 V/cm, which is lower than that for air by a factor of 12. Above, we have shown that, under normal conditions, a streamer that slowly (over a time interval of several microseconds) bridges a long gap cannot drive the breakdown because the streamer channel has already decayed when the streamer propagates across the gap. Breakdowns in Ar are free of this drawback, so that the phenomenon of streamer breakdown driven by a slowly propagating streamer is easy to observe in noble gases.

Figure 21a shows the streak photograph of the developing breakdown and the corresponding waveforms of the voltage across the gap and the charge carried along the channel of the streamer that has bridged the gap. The discharge was recorded by opening the electronic shutter at the instant when the voltage was applied to the gap and the scanning of the discharge began after a time delay, at the instant when the streamer closely approached the cathode. As a result, both the static image of the discharge and the streak photograph of its final phase were displayed. We can see that the state of the plasma channel did not change radically after the streamer bridged the gap. Only 2 μs after the bridging, the current in one of the streamer channels between the electrodes started growing without any evident cause (this channel can be readily distinguished by its peculiar bending) and the channel itself became very bright. Figure 21b shows the streak photograph of the breakdown process in the experiment in which the cathode was equipped with a 3-cm-long needle. With such a cathode, it was possible to clearly visualize the return ionization wave. Starting from the tip of the needle when the streamer bridged the gap, the return wave approached the anode over a time interval of 2.5–4.5 μs (under the breakdown voltage), without causing any significant change in the conduction current. The current was observed to increase very rapidly only after the return wave had reached the anode. Simultaneously, the voltage drop across the gap was observed to decrease sharply, indicating that the channel had acquired a descending *I–V* characteristic and, consequently, that the gap is bridged.

The total energy deposition W was determined from the measured charge Q carried along the streamer channel and the measured voltage across the gap. At the breakdown voltage U_{br}, the total energy deposited before the rapid avalanche-type growth of the current was equal to $W = QU_{br} = (6–8) \times 10^{-4}$ J. In a 25-cm-long channel with a radius of 0.1 cm, the gas temperature increased (at the expense of this energy deposition) by no more than 2 K. It is precisely the insignificant role of the thermal effects that makes the streamer breakdown in Ar different from the spark breakdown in air, which is always thermal in nature [1, 3].

5.2. Results of Numerical Modeling

In [32], the streamer breakdown in Ar was simulated under the experimental conditions described in the previous section. The simulations were carried out based on the above 1.5D model, in which the kinetic scheme was adjusted for Ar. Specifically, the electron energy distribution function and the ionization mechanisms in Ar were calculated with allowance for Coulomb collisions, elastic electron–atom collisions, the dissociation of argon dimers, the excitation and ionization of atoms in the ground and electronically excited states, and the corresponding reverse processes. The rate constants of the electron processes were calculated as functions of the reduced electric field E/N, the degree to which Ar atoms are excited, and the degree of ionization $\alpha = n_e/N$.

The computations were carried out for a 25-cm-long Ar-filled gap between the sphere and the plane under normal conditions. The radius of the spherical anode was set equal to 0.5 cm, and the streamer radius was varied from 0.1 to 0.25 cm.

Because of the absence of electron attachment to argon atoms and the lower rate of dissociative recombination of positive ions with electrons (the dominant ions being Ar_3^+ ions), the plasma in the streamer channel in Ar decays at a much slower rate in comparison with that in air. As a result, all of the streamer parameters in argon and air are correspondingly different. In particular, in argon, the electron density and electric field evolve to nearly uniform profiles along the channel, except for a region near the streamer head (Fig. 22).

According to calculations, the gap is bridged at a mean electric field of 500 V/cm, which agrees qualitatively with the measured result (400 V/cm). Calculations show that, as is the case in air, the streamer reaches the cathode and excites the return wave of a strong electric field (Fig. 23). In this case, the drift motion of the electrons produced by the streamer substantially reduces the electric field amplitude in the return wave already at distances of several centimeters from the cathode. That is why, in experiments, the return wave was usually observed only in a small cathode region, and it was observed over the entire gap volume only when the cathode was equipped with a needle (Fig. 21b).

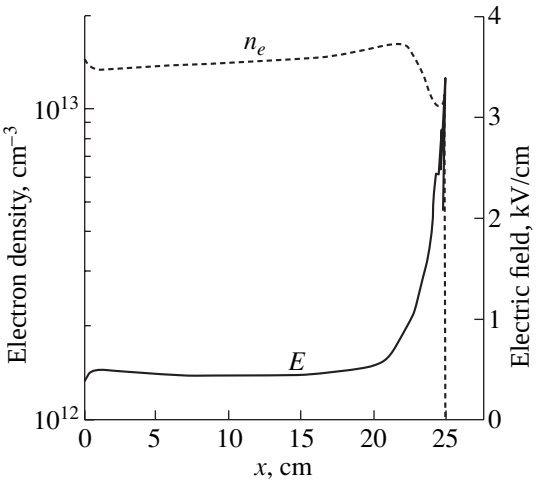

Fig. 22. Longitudinal profiles of the electron density and electric field in the channel at U = 22 kV in Ar at the instant when the gap is bridged.

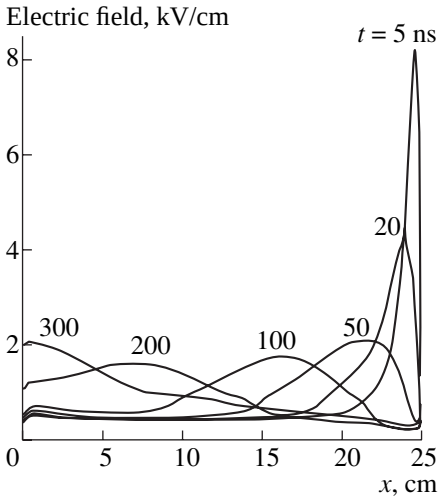

Fig. 23. Time evolutions of the electric field in the channel during the propagation of the return wave. The conditions are the same as in Fig. 22.

The propagating return wave smoothes the axial profile of the electric field in the channel. The rate of this process becomes markedly higher when the applied voltage is sufficiently high to ensure additional ionization of the gas at the front of the return wave over the entire length of the channel. The numerical model used in simulations is capable of capturing not only the return wave, which propagates from the cathode toward the anode, but also the reflected return wave, which propagates from the anode toward the cathode. The longitudinal profile of the electric field in this reflected wave at the time 300 ns is shown in Fig. 23. Note that the return wave may experience many reflections. From

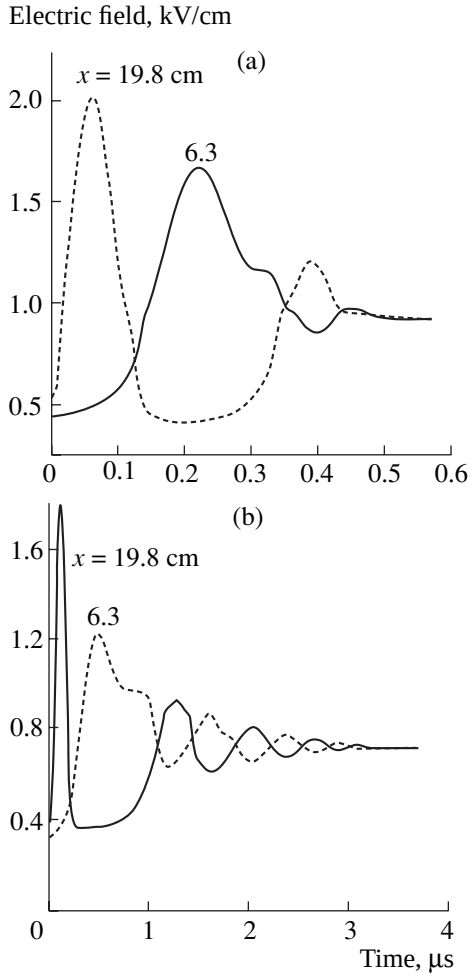

Fig. 24. Time evolutions of the electric field in the channel at two different distances from the anode at U = (a) 22 and (b) 17 kV.

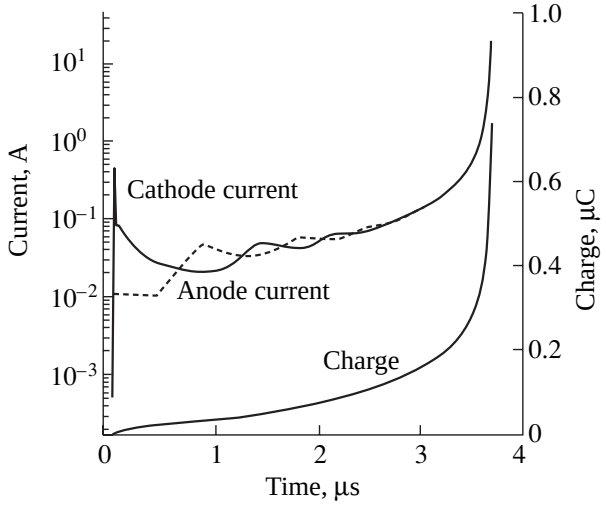

Fig. 25. Time evolutions of the charge carried toward the cathode and the anode and cathode currents. The conditions are the same as in Fig. 24b.

the calculated results illustrated in Fig. 24a (which shows the time evolutions of the electric field at different cross sections of the channel), we can see that, at the voltage U = 22 kV, the streamer breakdown evolves into a stable regime over a time shorter than 0.5 μs, after the return wave has already crossed the gap twice. As the voltage is decreased to the breakdown threshold (17 kV), the electric field is equalized over a longer time interval (about several microseconds) and the return wave crosses the gap many times before the breakdown evolves into a stable regime (in Fig. 24b, this effect is manifested by peculiar oscillations of the calculated time evolution $E(t)$). The current in the channel oscillates to a lesser extent (Fig. 25), because the electron drift velocity in Ar is weakly sensitive to the electric field variations in the range under consideration. Figure 25 also implies that the integral of the current (or, equivalently, the charge carried along the channel) is already a monotonic function of time. This conclusion agrees with the results of the experiment that is illustrated in Fig. 21a and in which the charge carried along the channel increased over a time interval of several microseconds after bridging the gap.

By the time when the current starts growing in an avalanche fashion (for $t > 3$ μs in Fig. 25), the electric field and electron density are equalized almost completely along the entire channel (Fig. 26), so that the further evolution of the streamer plasma is strictly synchronous. This is confirmed by the accompanying increase in the channel brightness in the streak photographs shown in Fig. 21. The calculated breakdown voltage (17 kV) also agrees with that measured experimentally (16 kV). The energy deposited in this prebreakdown stage is extremely low. Calculations show that, at the breakdown threshold, the deposited energy is lower than 2–3 mJ (the measured energy deposition was found to be approximately the same). In this case, the gas temperature in the channel actually increases by no more than several degrees, so that thermal effects are insignificant. On the other hand, the calculation and experiment both provide evidence for the very rapid increase in the current, which may be restricted only by the internal resistance of the high-voltage source.

An analysis of the numerical results shows that the observed increase in the current is associated not with the gas heating, which could enhance the reduced electric field E/N or give rise to thermal ionization, but rather with the intensification of stepwise ionization through the excitation of electronic states of Ar atoms,

$$e + \mathrm{Ar} \longrightarrow e + \mathrm{Ar}^*; \quad e + \mathrm{Ar}^* \longrightarrow 2e + \mathrm{Ar}^+,$$

in a nearly constant reduced electric field. When the electric field is not too strong, the electron-impact excitation rate in Ar is usually much higher than that in molecular gases, because, in atomic gases, there are no vibrational and rotational degrees of freedom of neutral particles, so the mean electron energy is higher.

Figure 27 shows the time evolutions of the electric field and stepwise ionization rate in the channel during

the final breakdown stage. At a low electron density n_e, the stepwise ionization rate in the channel synchronously follows the field evolution. However, 0.4 μm later, when the density n_e becomes higher than (3–4) × 10^{13} cm^{-3}, the decrease in the electric field can no longer counterbalance the continuing increase in the stepwise ionization rate because the latter depends nonlinearity on n_e. It is also important to note that, in the final stage of breakdown in Ar, the rate constant of the excitation of atoms also increases with n_e because of the effect of electron–electron collisions, which leads to a partial Maxwellianization of the electron energy distribution. In turn, under the combined action of stepwise ionization and Coulomb collisions, the *I–V* characteristic of the plasma channel becomes descending, indicating the onset of breakdown.

In air, the above effects of stepwise processes and Coulomb collisions on the ionization rate are, as a rule, insignificant. In fact, stepwise ionization is usually almost insensitive to the metastable states of O_2 molecules because the excitation energy of these states is low (1–2 eV). The stepwise ionization through the excitation of the electronic states of N_2 molecules also plays a minor role, because these states are efficiently quenched in collisions with O_2 molecules. In addition, electron–electron collisions have a pronounced influence on the electron energy distribution only when the electron–electron collision frequency is comparable with the electron energy relaxation rate. Since the electron energy relaxation rate in air is much higher than that in Ar, the effect of Coulomb collisions in air is negligible during the development of breakdown and becomes important only in the final phase, when the local thermodynamic equilibrium is reached. As for the breakdown threshold, it is governed by the processes occurring in the earlier stage.

The calculated time delay of the breakdown (the interval between the times at which the streamer bridges the gap and the current starts growing rapidly) increases from 10^{-7} to 10^{-6} s as the applied voltage is decreased and becomes as long as several microseconds at the threshold voltage. The experiments yielded approximately the same results.

Model simulations show that, when the electron density and current increase by a factor of 10^3, the gas temperature in the channel is lower than 350 K. This indicates that the breakdown mechanism is nonthermal in character. Of course, due to the Joule heating at a high current, the gas temperature in the channel will inevitably increase to typical arc temperatures. However, this temperature level will in fact be reached after the initiation of the arc discharge.

5.3. Effect of Small O_2 Admixtures

In [31, 33], it was shown experimentally that, in long gaps, even a small (1%) admixture of O_2 to Ar results in the evolution of the streamer breakdown into a leader breakdown. It is natural to presume that such a high sensitivity of the mechanism for arc breakdown in Ar to small O_2 admixtures is associated with electron attachment to oxygen molecules. However, elementary estimates show that the time scales on which the breakdown develops in argon with a small oxygen admixture are short in comparison with those on which the electrons are attached to O_2 molecules. This effect was explained in [33] based on the results of numerical simulations of the streamer properties in Ar : O_2 mixtures.

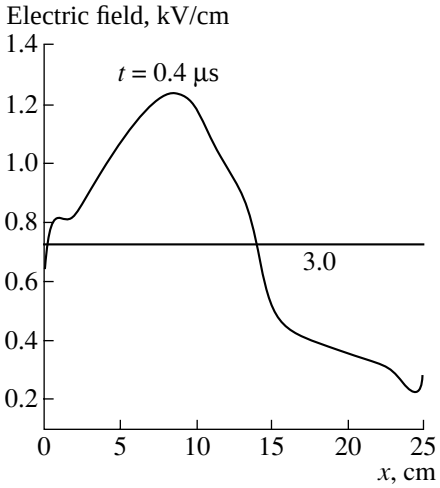

Fig. 26. Time evolution of the electric field profile along the channel after bridging the gap.

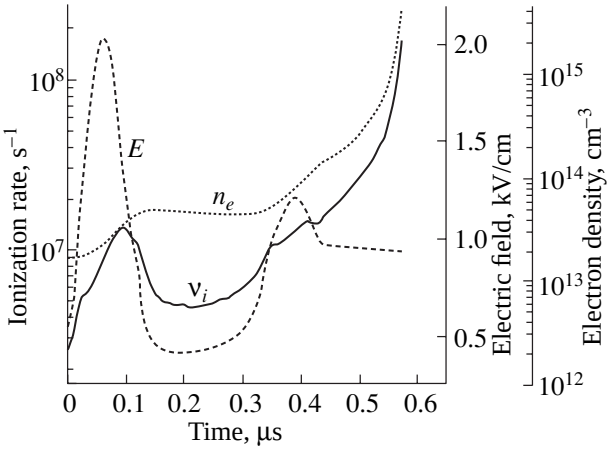

Fig. 27. Time evolutions of the electric field, gas temperature, and stepwise ionization rate after bridging the gap. The evolutions were calculated at a distance of 19.8 cm from the anode for U = 22 kV.

Figure 28 presents the streak photograph of a spark discharge in Ar with a 1% admixture of O_2. The discharge was photographed under the same conditions as those in Fig. 21, which refers to pure Ar. The only exception is the applied voltage, which was increased

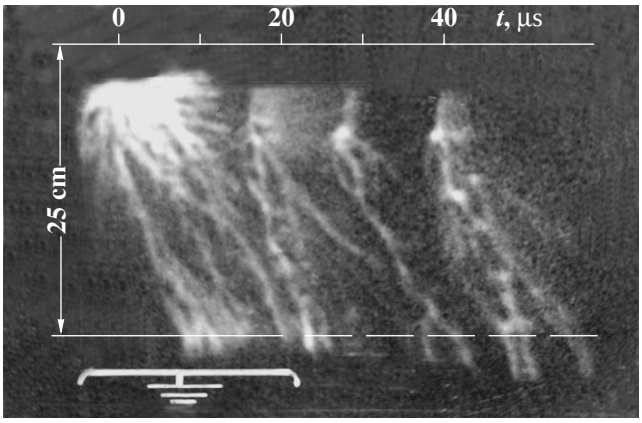

Fig. 28. Streak photograph of a streamer discharge in an Ar : O_2 = 99 : 1 mixture at U = 24 kV.

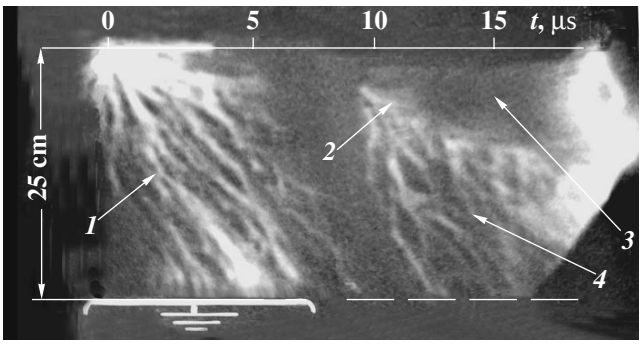

Fig. 29. Streak photograph of the streamer and leader phases of a discharge in an Ar : O_2 = 99 : 1 mixture at U = 30 kV: (*1*) initial streamer phase, (*2*) leader head, (*3*) leader channel, and (*4*) streamer zone of the leader.

to 24 kV in an Ar : O_2 mixture. Nevertheless, the streamer breakdown was not observed, although the threshold voltage for breakdown in pure Ar is lower by a factor of approximately 1.5. The waveforms of the charge carried along the channel of a streamer after the bridging of the gap showed that small O_2 admixtures sharply decreased the lifetime of the streamer plasma: the plasma lifetime in Ar : O_2 mixtures was as short as 1 μs or less, while the plasma lifetime in pure Ar was several tens of microseconds. Accordingly, the charge carried along the channel is lower: in an Ar : O_2 = 99 : 1 mixture, it is $Q \approx$ 1–2 nC, while, in pure argon, it is $Q \approx$ 10–15 nC. In addition, the larger the amount of O_2, the stronger the mean electric field E_{av} required to bridge the gap. In mixtures containing from 0 to 5% of O_2, the mean field E_{av} increases almost linearly from 400 to 1800 V/cm.

In Ar : O_2 mixtures, the decay of the streamer after it bridges the gap is not accompanied by an increase in the current, provided that the voltage U is not too high. An increase in the applied voltage gives rise to a leader. The streak photograph in Fig. 29 clearly demonstrates all of the pronounced structural elements of the leader, in particular, the leader head, which is much brighter than both the leader channel and the streamers that start from the head. Since the leader channel emits mainly red and infrared lights, it is seen to be very dark, because the sensitivity of the photocathode of the image converter used in the experiments is maximum in the blue part of the visible spectrum. From Fig. 29, we can distinctly see that the breakdown occurs just after the leader comes into contact with the cathode. Qualitatively, this process is analogous to that in long air-filled gaps [3]. As the streamer breakdown evolves into the leader breakdown, the breakdown voltage U_{br} doubles. For the leader mechanism in an Ar : O_2 = 99 : 1 mixture, we have U_{br} = 30 kV, whereas the breakdown voltage for the streamer mechanism in a 25-cm-long gap filled with pure Ar is 16 kV.

The influence of small O_2 admixtures on the parameters of a long streamer in Ar was modeled in [33]. The kinetic scheme applied in [33] was developed by properly adjusting the scheme used in [32] for Ar to incorporate the following processes involving O_2 molecules: first, the reactions that are responsible for the formation of the electron energy distribution; second, the reactions of dissociation, excitation, and electron impact ionization of O_2 molecules and electron attachment to them; and, finally, the corresponding reverse reactions.

Numerical calculations with the model based on the kinetic scheme adjusted in such a way made it possible to reconstruct the main experimentally observed features of the evolution of the parameters of a long streamer in Ar with small O_2 admixtures. Thus, the mean electric field at the instant at which the streamer bridges the gap was found to be stronger by a factor of 1.6 for a 1% admixture of O_2 and by a factor of 2.2 for a 2% oxygen admixture, the corresponding experimental findings being 1.5 and 2.33, respectively. The same agreement was achieved in reconstructing the effect of O_2 admixtures on both the lifetime of the streamer plasma and the charge carried along the streamer channel.

A fairly high degree of confidence in the calculated results made it possible to use the model to refine the role of particular reactions associated with the production and loss of electrons in the gas mixture with the aim of establishing the primary cause of such significant changes in the properties of streamers in Ar with small O_2 admixtures. The results of the corresponding computations showed that O_2 molecules manifest themselves primarily in the efficient quenching of the excited Ar atoms, thereby slowing down the stepwise ionization processes in the streamer channel. Under the

conditions in question, a small oxygen admixture resulted in the decay of the channel and thus prevented the streamer breakdown. As a result, the threshold for the streamer breakdown became very high (higher than the threshold for the leader breakdown).

6. CONCLUSION

Although streamer breakdown in long gas gaps with a highly nonuniform electric field is very important for practical applications, it has been studied very poorly and still remains one of the most unclear phenomena in the physics of spark discharges. Streamer breakdown has been observed more or less systematically only in experiments with noble gases (for air under normal conditions, only some fragmentary results have been obtained). Until recently, there has been essentially no study of the mechanism for streamer breakdown. Here, we have reviewed recent papers in which better insight into the details of streamer breakdown was provided by comparing the results of numerical modeling with the exceedingly little experimental data. We have analyzed the development of breakdown at the microscopic level and described the main kinetic processes that are responsible not only for the streamer propagation but also for the evolution of the streamer channel into an arc channel after the streamer bridges the gap.

We have shown that return ionization waves play an insignificant role in the streamer evolution. The conclusion about the possible analogy between the return stroke in the main stage of a lightning discharge and the return waves in the streamer channel has not been confirmed. Regardless of the length of the gap, the streamer acquires a descending *I–V* characteristic only after the damping of the wave processes that equalize the electric field along the streamer channel. The gas heating to the threshold temperatures for associative ionization reactions (which are not affected directly by the electric field) is not the only cause of the evolution of the streamer channel into a state with a descending *I–V* characteristic. In noble gases, we have revealed the phenomenon of nonthermal streamer breakdown, which is associated with the onset of the ionization instability driven by electron–electron collisions and stepwise ionization.

To drive streamer breakdown in cold air requires strong (about 20–30 kV/cm) electric fields and voltage pulses having nanosecond rise times. Such stringent requirements become far less restrictive when the air is heated to temperatures of about 1000 K or higher. When analyzing the streamer breakdown in hot air, we predicted a possible hysteresis effect. The results of numerical modeling show that the threshold voltage for the streamer breakdown is lower if the air temperature $T < 3000$ K before applying the high-voltage pulse to the gap is achieved by cooling (rather than heating) the air. This effect is associated with different amounts of NO molecules in the cooling and heating air.

We can also anticipate that processes analogous to the streamer breakdown take place during the propagation of the so-called dart leader in multistroke lightning flashes [4, 34]. The dart leader is an ionization wave that is initiated when a new charged center (convective cell) in a thundercloud comes into play and propagates along the cooling plasma channel formed by the preceding return stroke of the subsequent components of lightning. Although all of the scales characteristic of lightning flashes and discharges under laboratory conditions are very different, the phenomenon of the dart leader is thought to have properties in common with the rebreakdown along the channel that remains after an arc discharge. The question about this analogy is very interesting not only from a theoretical point of view but also from the standpoint of practical applications and is worthy of further investigation.

ACKNOWLEDGMENTS

This work was supported in part by the Russian Foundation for Basic Research, project no. 00-02-17399.

REFERENCES

1. J. M. Meek and J. D. Craggs, *Electrical Breakdown of Gases* (Wiley, New York, 1978).
2. Yu. P. Raizer, *Gas Discharge Physics* (Nauka, Moscow, 1992; Springer-Verlag, Berlin, 1991).
3. E. M. Bazelyan and Yu. P. Raizer, *Spark Discharge* (Mosk. Fiz. Tekh. Inst., Moscow, 1997; CRC, Boca Raton, 1997).
4. E. M. Bazelyan and Yu. P. Raizer, *Physics of Lightning and Lightning Protection* (Fizmatlit, Moscow, 2001; IOP, Bristol, 2000).
5. E. Marode, J. Appl. Phys. **46**, 2005 (1975).
6. A. Gibert, J. Dupuy, M. Bayle, and P. Bayle, J. Phys. D **16**, 1463 (1983).
7. M. Cernak, E. M. van Veldhuizen, I. Morva, and W. R. Rutgers, J. Phys. D **28**, 1126 (1995).
8. A. Larsson, J. Phys. D **31**, 1100 (1998).
9. E. Marode, F. Bastien, and M. Bakker, J. Appl. Phys. **50**, 140 (1979).
10. F. Bastien and E. Marode, J. Phys. D **18**, 377 (1985).
11. P. Bayle, M. Bayle, and G. Forn, J. Phys. D **18**, 2395 (1985).
12. A. E. Rodriguez, W. L. Morgan, K. E. Touryan, *et al.*, J. Appl. Phys. **70**, 2015 (1991).
13. S. Ganesh, A. Rayabooshanam, and S. K. Dhali, J. Appl. Phys. **72**, 3957 (1992).
14. G. V. Naidis, J. Phys. D **32**, 2649 (1999).
15. R. S. Sigmond, J. Appl. Phys. **56**, 1355 (1984).
16. A. E. Bazelyan and E. M. Bazelyan, Teplofiz. Vys. Temp. **31**, 867 (1993).
17. N. L. Aleskandrov, A. E. Bazelyan, E. M. Bazelyan, and I. V. Kochetov, Fiz. Plazmy **21**, 60 (1995) [Plasma Phys. Rep. **21**, 57 (1995)].

18. N. L. Aleksandrov and E. M. Bazelyan, J. Phys. D **29**, 740 (1996).
19. I. A. Kossyi, A. Yu. Kostinsky, A. A. Matveyev, *et al.*, Plasma Sources Sci. Technol. **1**, 207 (1992).
20. N. L. Aleskandrov, E. M. Bazelyan, N. A. Dyatko, and I. V. Kochetov, Fiz. Plazmy **24**, 587 (1998) [Plasma Phys. Rep. **24**, 541 (1998)].
21. N. L. Aleskandrov and E. M. Bazelyan, Fiz. Plazmy **22**, 458 (1996) [Plasma Phys. Rep. **22**, 417 (1996)].
22. N. L. Aleskandrov and E. M. Bazelyan, Zh. Éksp. Teor. Fiz. **118**, 835 (2000) [JETP **91**, 724 (2000)].
23. L. B. Loeb, *Electrical Coronas* (Univ. of California Press, Berkley, 1965).
24. G. V. Butkevich, *Processes in Arcs during Electric Circuit Switching* (Énergiya, Moscow, 1973).
25. K. Tsuruta, I. Takahashi, Y. Kanzaki, *et al.*, IEEE Trans. Plasma Sci. **17**, 560 (1989).
26. E. Schade and K. Ragaller, IEEE Trans. Plasma Sci. **10**, 141 (1982).
27. N. L. Aleksandrov and E. M. Bazelyan, J. Phys. D **31**, 1343 (1998).
28. K. Tsuruta and H. Ebara, IEEE Trans. Electr. Insul. **27**, 451 (1992).
29. T. Udo, IEEE Trans. Power Appar. Syst. **64**, 471 (1964).
30. N. L. Aleksandrov and E. M. Bazelyan, IEEE Trans. Plasma Sci. **27**, 1454 (1999).
31. E. M. Bazelyan, V. A. Goncharov, and A. Yu. Goryunov, Izv. Akad. Nauk SSSR, Énerg. Transp., No. 2, 154 (1985).
32. N. L. Aleksandrov, E. M. Bazelyan, A. Yu. Gorunov, and I. V. Kochetov, J. Phys. D **32**, 2636 (1999).
33. N. L. Aleksandrov, E. M. Bazelyan, and G. A. Novitskii, J. Phys. D **34**, 1374 (2001).
34. E. M. Bazelyan, Fiz. Plazmy **21**, 497 (1995) [Plasma Phys. Rep. **21**, 470 (1995)].

Translated by G. V. Shepekina

Plasma Physics Reports, Vol. 27, No. 12, 2001, pp. 1079–1088. Translated from Fizika Plazmy, Vol. 27, No. 12, 2001, pp. 1143–1152.

LOW-TEMPERATURE PLASMA

Electron Temperature in a Decaying Molecular Nitrogen Plasma in the Presence of Weak Electric Fields

N. A. Gorbunov, N. B. Kolokolov, and F. E. Latyshev

Institute of Physics, St. Petersburg State University, Ulyanovskaya ul. 1, St. Petersburg, 198504 Russia

e-mail: gorbunov@pobox.spbu.ru

Received May 29, 2001; in final form, July 17, 2001

Abstract—The electron energy distribution function in an afterglow molecular nitrogen plasma is studied both experimentally and theoretically under the conditions of weak electric fields such that the electron gas is heated by superelastic collisions of electrons with vibrationally excited molecules. Based on the mean electron energy balance, it is established that, depending on the degree of plasma ionization and the vibrational temperature of nitrogen molecules, an afterglow plasma may evolve into two states, differing in electron temperature. This kind of bistability is found to stem from the difference in the main mechanisms for electron energy losses in the two stable states. The prediction that the shape of the electron energy distribution function should change in a jumplike manner when a weak electric field is imposed has been confirmed experimentally. © *2001 MAIK "Nauka/Interperiodica".*

1. INTRODUCTION

A distinctive feature of molecular plasma is the close relation between the distribution of free plasma electrons and the distribution over the vibrational levels of molecules in the ground state [1]. This relation is especially pronounced in the presence of weak (or zero) electric fields in which the plasma electrons are heated mainly by collisions with vibrationally excited molecules in the ground or electronically excited states. Such a plasma is produced by a charged particle beam or occurs in the afterglow of an electric discharge.

The electron energy distribution function (EEDF) was calculated for the first time in [2–4] together with the distribution over the vibrational levels of nitrogen molecules in the ground state $X^1\Sigma_g^+$ and electronically excited metastable state $A^3\Sigma_u^+$. It was found that, in an afterglow plasma, the EEDF is nonmonotonic in shape, because the cross sections for the excitation of the vibrational levels of the ground state of nitrogen molecules have a series of maxima in a narrow energy range $\varepsilon_1 \le \varepsilon \le \varepsilon_2$, where $\varepsilon_1 \approx 1.6$ eV and $\varepsilon_2 \approx 3.7$ eV. This resonant dependence on energy is attributed to the fact that the vibrational excitation proceeds through the formation of an unstable negative ion. It was shown that, over a wide range of conditions, the electron temperature T_e defined as $T_e = 2\langle\varepsilon\rangle/3$ (where $\langle\varepsilon\rangle$ is the mean electron energy) is close to the vibrational temperature T_v corresponding to the distribution of nitrogen molecules over vibrational levels.

However, the EEDF measured in the first experiments on an afterglow discharge plasma in nitrogen [5] was found to differ greatly in shape from the previously calculated EEDFs. Thus, for $\varepsilon \le \varepsilon_1$, the majority of electrons obeyed a Maxwellian distribution with $T_e \approx 1000$ K. This value of T_e was three times lower than the expected temperature T_v corresponding to the vibrational distribution of nitrogen molecules in the ground state. It was established that the amount by which the EEDF decreases can be characterized by the temperature $T^* \approx 3000$ K, which corresponds to the vibrational temperature T_v only in the range $\varepsilon_1 \le \varepsilon \le \varepsilon_2$ of the efficient excitation and deexcitation of the vibrational levels of nitrogen molecules. The shape of the high-energy part of the EEDF was found to be governed by superelastic collisions of thermal electrons with nitrogen molecules in the electronically excited states $A^3\Sigma_u^+$, $B^3\Pi_g$, etc.

Additional measurements carried out at different times after the discharge-current pulse ended ($t \le 500$ μs) showed that, at the pressure $P = 0.3$ torr, the shape of the EEDF remains essentially unchanged during different phases of the discharge afterglow [6]. A model proposed in [6] was intended to approximately calculate the EEDF under the basic assumption that it is bi-Maxwellian. The Maxwellian shape of the EEDFs in the thermal energy range was explained as being due to the dominant role of electron–electron collisions. The electron temperature was specified as the parameter extracted from the measurement results. It was assumed that, in the energy range $\varepsilon_1 \le \varepsilon \le \varepsilon_2$, a decrease in the EEDF is determined by the vibrational temperature $T^* = T_v$. The high-energy part of the EEDF was calculated with allowance for superelastic collisions of electrons with nitrogen molecules in the electronically excited states, whose population served as a computa-

1063-780X/01/2712-1079$21.00

tion parameter. The results obtained in [7, 8] in solving the Boltzmann equation with allowance for electron–electron collisions agree well with the experimental results of [6].

Further experiments showed that, as the discharge current grows and the pressure rises to 0.5 torr, the electron temperature T_e increases and reaches a value of about $T_e \sim T_v$ [9]. An interesting behavior of T_e in nitrogen with a small (about 1%) argon admixture at the pressure $P = 1$ torr was observed experimentally in [10, 11]. In the initial phase of the afterglow, the electron temperature T_e was close to T_v. Then, the temperature T_e was observed to experience a jumplike decrease at a practically constant T_v. The time at which the electron temperature T_e started to deviate in a jumplike manner from T_v depended on the discharge-pulse current, which governed the initial electron density and initial vibrational temperature. Numerical integration of the Boltzmann equation [11] showed that, when the electron density n_e is high, the electron temperature T_e is close to T_v. This circumstance was explained as being due to electron–electron collisions. For certain values of n_e and T_v, the Boltzmann equation has two different solutions with two different electron temperatures T_e. It is this bistability that causes the experimentally observed jumplike changes of the electron temperature T_e in time. Calculations of the EEDF showed that, in certain ranges of n_e and T_v values, such bistability can also manifest itself in pure nitrogen [12].

Up to now, the effect of weak electric fields on the EEDF in electric discharges in nitrogen has been studied very little. Weak electric fields were taken into account by Dyatko *et al.* [7], who calculated the EEDF for discharges in nitrogen at $T_v = 3000$ K. On the one hand, the effect of reduced electric fields with the same strengths as those used in [7] (about $E/N \sim 1$ Td) can be estimated from the mean energy balance equation for a purely Maxwellian electron distribution. In this way, the electron temperature T_e can be expected to change by ~10%. On the other hand, the calculations of the EEDF from the kinetic equation showed that the mean electron energy changes by several times. However, in [7], this circumstance was not discussed in detail.

Numerical solution of the Boltzmann equation makes it possible to determine either T_e for a nonequilibrium EEDF in terms of the mean electron energy or the characteristic amount by which the EEDF decreases in a certain energy range. In this way, however, it is difficult to examine the influence of various parameters on the value of T_e. In contrast, it is well known that a useful way of describing the afterglow plasma in atomic gases is by theoretically analyzing the Maxwellian part of the EEDF on the basis of the mean electron energy balance equation [13–15]. This approach provides a simple analysis of the processes that affect the temperature of the thermal electrons over a wide range of parameters. The electron temperature T_e obtained in this way agrees with the results of numerical calculations of the EEDF to an accuracy with which the actual cross sections for various elementary processes can be determined experimentally.

Our purpose here is to develop a method that is aimed at determining the electron temperature T_e in an afterglow plasma in a molecular gas and that is based on an analysis of the electron energy balance equation. We use this method to qualitatively examine the conditions for the formation of bistable states of the EEDF in molecular nitrogen. We also analyze the effect of weak electric fields on the discharge afterglow and compare the theoretical results with the data of our experiments.

2. BOLTZMANN EQUATION

We study the formation of the EEDF in a nitrogen plasma on the basis of the time-independent Boltzmann equation in the local approximation, which is valid when the electron energy relaxation length is $\lambda_\varepsilon \ll \Lambda$, where Λ is the characteristic diffusion length [16]. The corresponding criterion for molecular gases was discussed in detail in [17]. The criterion for the formation of the local EEDF in nitrogen plasma is approximately satisfied in the range $PR \geq 0.1$ torr cm, where P is the neutral gas pressure and R is the radius of the gas-discharge tube. The experiments described here were carried out under the conditions of the formation of a local EEDF. Further analysis also refers to these conditions.

In the local approximation, the terms with spatial gradients in the kinetic equation can be neglected. As a result, the kinetic equation for the isotropic part of the EEDF has the form

$$\frac{d}{d\varepsilon}\left[D(\varepsilon)\frac{df(\varepsilon)}{d\varepsilon} + V(\varepsilon)f(\varepsilon)\right] = C(\varepsilon), \quad (1)$$

$$\int_0^\infty f(\varepsilon)\sqrt{\varepsilon}d\varepsilon = 1. \quad (2)$$

Here, the diffusion coefficient $D(\varepsilon) = D_{eE} + D_{\rm el} + D_{\rm rot} + D_{ee}$ in energy space accounts for the effect of the electric field (D_{eE}), elastic electron–molecule collisions ($D_{\rm el}$), electron-impact excitation and deexcitation of the rotational levels of nitrogen molecules ($D_{\rm rot}$), and electron–electron collisions (D_{ee}); the dynamic friction rate $V(\varepsilon) = V_{\rm el} + V_{\rm rot} + V_{ee}$ in energy space is governed by the processes just mentioned; and $C(\varepsilon)$ is the integral of inelastic collisions. For a molecular nitrogen plasma, the expressions for $D(\varepsilon)$, $V(\varepsilon)$, and $C(\varepsilon)$ are presented, e.g., in [6].

In our calculations, the cross sections for elastic collisions of electrons with nitrogen molecules and those for the excitation of the rotational levels were taken from [18] and [19], respectively. The electron–electron collisions were described by the analytic expressions taken from [20]. These expressions approximate the

electron–electron collision integral with an accuracy of 20%, which is comparable to the accuracy with which the cross sections for electron–molecule collisions are measured.

It is well known [21] that, in a discharge plasma in molecular nitrogen, the electron energy loss is associated mainly with the excitation of the vibrational levels of molecules in the ground state $X^1\Sigma_g^+$. In self-sustained discharges, the excitation of the higher-lying electronic states $A^3\Sigma_u^+$, $B^3\Pi_g$, etc., may influence the energy balance only when the reduced electric field is sufficiently strong, $E/N > 40$ Td [22, 23]. An analysis of these conditions goes beyond the scope of our study, because electron heating in such a strong electric field is far more intense than in collisions with the excited molecules [1].

The electron gas can be heated by collisions with both the molecules $X^1\Sigma_g^+(v)$, $v \geq 1$, which are vibrationally excited from the ground state, and the molecules in the electronically excited states $A^3\Sigma_u^+$, $B^3\Pi_g$, etc. In an electric discharge, the most populated excited state is the metastable state $A^3\Sigma_u^+$. The threshold energy for exciting this state from the ground molecular state $X^1\Sigma_g^+(v = 0)$ is $\varepsilon_0 = 6.2$ eV. The density of the metastable molecules can be as high as about 10^{11} cm^{-3} [24]. However, this density is much lower than the density of molecules vibrationally excited from the ground state. Consequently, when the temperature corresponding to the vibrational distribution of the ground state lies in the range $T_v \geq 1000$ K, the heating of the majority of electrons by collisions with molecules in the $A^3\Sigma_u^+$ state can be neglected in comparison with that associated with the deexcitation of the vibrational levels $X^1\Sigma_g^+(v)$ of the ground state. This temperature range is characteristic of an electric discharge or an afterglow plasma.

The above considerations show that, for a wide range of conditions in a non-self-sustained discharge and an afterglow plasma, the governing role in the formation of the EEDF is played by such inelastic processes as the excitation and deexcitation of the vibrational levels of the ground state of nitrogen molecules. The problem at hand can be further simplified by representing the integral for inelastic collisions of electrons with molecules in the Fokker–Planck (divergence) form. This approach was used by Lyagushchenko and Tendler [25] to construct an analytic solution for the EEDF in a discharge plasma in molecular nitrogen. The form of the solution that they obtained corresponds qualitatively to the results of previous calculations. More recently, this approach was applied to analyze the nonlocal properties of the EEDF in a nitrogen plasma [17] and an afterglow plasma in nitrogen [6] and to examine the conditions under which the differential conductivity in gas mixtures becomes negative [26]. The use of the divergent form of the inelastic collision integral to describe the excitation of the vibrational levels is justified by the fact that the most probable inelastic processes are those in which the vibrational quantum number v changes insignificantly. The cross sections $\sigma_{0v}(\varepsilon)$ for the excitation of the vibrational levels from the ground state decrease sharply with v [27]. As a result, over the range $\varepsilon_1 \leq \varepsilon \leq \varepsilon_2$ of the efficient excitation and deexcitation of the vibrational levels, the change in the electron energy E_{0v} due to inelastic collisions is much smaller than the energy itself. An analogous assertion is valid for transitions between the vibrational levels of the excited molecules. An analysis of the corresponding cross sections showed that they are also resonant in character [28, 29]. The cross sections are observed to be maximum for transitions in which the amount $E_{kv} = E_{0v} - E_{0k}$ by which the energy changes is on the order of the vibrational quantum energy $E_v = 0.29$ eV of a nitrogen molecule. In terms of the small parameter $E_{kv}/\varepsilon \ll 1$, which characterizes the processes of vibrational excitation and deexcitation, $X^1\Sigma_g^+(k) + e \longleftrightarrow X^1\Sigma_g^+(v) + e$, the inelastic collision integral $C_{\text{vibr}}(\varepsilon)$ can be written as

$$C_{\text{vibr}}(\varepsilon) = \frac{d}{d\varepsilon}\left[D_{\text{vibr}}(\varepsilon)\frac{df(\varepsilon)}{d\varepsilon} + V_{\text{vibr}}(\varepsilon) f(\varepsilon)\right], \quad (3)$$

where

$$V_{\text{vibr}}(\varepsilon) = \varepsilon^{3/2}\sum_{v=1}^{8}\sum_{k=0}^{v}\frac{E_{kv}}{\varepsilon}\nu_{kv}(\varepsilon),$$
$$D_{\text{vibr}}(\varepsilon) = T_v V_{\text{vibr}}(\varepsilon). \quad (4)$$

Here, $\nu_{kv}(\varepsilon) = \sqrt{2e/m}\sqrt{\varepsilon}\,\sigma_{kv}(\varepsilon)n_k$ is the excitation rate of the vibrational level with the number ν from the lower lying level with the vibrational quantum number k and density n_k, and e and m are the charge and mass of an electron. The matrix of the cross sections $\sigma_{kv}(\varepsilon)$ used in our calculations was taken from [29]. The matrix elements $\sigma_{01}(\varepsilon)$, $\sigma_{02}(\varepsilon)$, and $\sigma_{03}(\varepsilon)$ in the near-threshold energy range were determined from the experimental data of [30]. The energies E_{kv} of the vibrational levels corresponded to the data from [31].

We substitute expressions (3) and (4) into Eq. (1) and integrate the resulting equation twice to obtain the following expression for the EEDF:

$$f(\varepsilon) = C_n \exp\left(-\int_0^{\varepsilon}\frac{d\varepsilon}{T(\varepsilon)}\right). \quad (5)$$

Here, the normalizing constant C_n is determined by formula (2) and the characteristic amount $T(\varepsilon)$, by which the EEDF decreases, has the form

$$T(\varepsilon) = \frac{\dfrac{2e^2E^2}{3m\nu_{\rm el}(\varepsilon)} + T_g[\delta_e\nu_{\rm el}(\varepsilon) + \delta_{\rm rot}\nu_{\rm rot}(\varepsilon)] + T_e\nu_{ee}(\varepsilon)A_0 + T_v\sum_{v=1}^{8}\sum_{k=0}^{v}\frac{E_{kv}}{\varepsilon}\nu_{kv}(\varepsilon)}{\delta_{\rm el}\nu_{\rm el}(\varepsilon) + \delta_{\rm rot}\nu_{\rm rot}(\varepsilon) + \nu_{ee}(\varepsilon)A_0 + \sum_{v=1}^{8}\sum_{k=0}^{v}\frac{E_{kv}}{\varepsilon}\nu_{kv}(\varepsilon)}, \quad (6)$$

where E is the electric field strength, $\nu_{\rm el}(\varepsilon)$ is the frequency of elastic collisions between electrons and nitrogen molecules, $\delta_{\rm el} = 2m/M$ is the energy transfer coefficient in elastic collisions, M is the mass of an N_2 molecule, T_g is the gas temperature, $\delta_{\rm rot} = 8B/\varepsilon$ is the energy exchange rate constant for the excitation of the rotational levels, B is the rotational constant of an N_2 molecule, $\nu_{\rm rot}(\varepsilon)$ is the excitation rate of the rotational levels, $\nu_{ee}(\varepsilon)$ is the electron–electron collision frequency, $A_0(\varepsilon/T_e) = 0.385\varepsilon/T_e$ for $\varepsilon/T_e \le 2.6$, and $A_0(\varepsilon/T_e) = 1$ for $\varepsilon/T_e \ge 2.6$.

Expression (6) implies that $T(\varepsilon)$ differs strongly between different energy ranges. In an afterglow plasma ($E = 0$) with the degree of ionization $\xi = n_e/[N_2] > 10^{-6}$, the thermal energy range $\varepsilon < \varepsilon_1$ is dominated by electron–electron collisions, so that we have $T(\varepsilon) \approx T_e$. In the energy range $\varepsilon_1 \le \varepsilon \le \varepsilon_2$ of the efficient excitation of vibrational levels, we have $T(\varepsilon) \approx T_v$, provided that $\xi < 10^{-3}$. Consequently, in an afterglow plasma in nitrogen, the EEDF in the range $10^{-6} \le \xi \le 10^{-3}$ can be bi-Maxwellian in character. This conclusion is supported by both the experimental data [5, 6, 9] and the numerical results [7, 8]. In an afterglow plasma with a higher degree of ionization ($\xi > 10^{-3}$), the entire energy range under consideration is dominated by electron–electron collisions, so that the EEDF decreases exponentially. This is confirmed by the corresponding numerical computations [23]. In order to calculate the EEDF from formulas (5) and (6), it is necessary to determine the electron temperature, because the EEDF at hand satisfies kinetic equation (1) regardless of the value of T_e [32]. In turn, the electron temperature should be found from the mean electron energy balance equation.

3. MEAN ELECTRON ENERGY BALANCE EQUATION

Under the assumptions of our model, the balance equation for the mean electron energy $\langle\varepsilon\rangle$ can be written in the form

$$\frac{\partial\langle\varepsilon\rangle}{\partial t} = H_{eE} + H_{\rm el} + H_{\rm rot} + H_{\rm vibr}^{-} + H_{\rm vibr}^{+}, \quad (7)$$

where the change in the mean electron energy is governed by the effect of the electric field (H_{eE}), elastic electron–molecule collisions ($H_{\rm el}$), quasi-elastic processes of the excitation and deexcitation of the rotational levels ($H_{\rm rot}$), energy loss in the excitation of the vibrational levels of nitrogen molecules ($H_{\rm vibr}^{-}$), and energy gain in superelastic collisions with vibrationally excited molecules ($H_{\rm vibr}^{+}$).

We consider the case in which the EEDF forms in a quasisteady fashion as the electron density n_e and vibrational temperature T_v change. This process starts several microseconds after the electric discharge has come to an end [3, 4, 23]. In the case at hand, the electron temperature T_e is determined under the assumption that the right-hand side of Eq. (7), $H(T_e) = H_{eE} + H_{\rm el} + H_{\rm rot} + H_{\rm vibr}^{-} + H_{\rm vibr}^{+}$, is equal to zero; i.e., $H(\bar{T}_e) = 0$. The solution to the latter equation can have one or several roots. By analyzing the behavior of the function $H(T_e)$ near the resulting solutions $\bar{T}_e$, it is possible to examine their stability properties in terms of the discharge parameters [33]. In our model, these are T_g, T_v, n_e, and E. For $\partial H(\bar{T}_e)/\partial T_e < 0$, the root in question is stable. In the opposite case $\partial H(\bar{T}_e)/\partial T_e > 0$, the root is unstable. A small perturbation $\Delta\bar{T}_e$ grows with time until the system evolves into another stable state.

4. NUMERICAL RESULTS

The results of the calculation of $H(T_e)$ at $E = 0$ for different vibrational temperatures and electron densities are illustrated in Fig. 1. In calculations, the nitrogen density was taken to be the same as in experiments, $[N_2] = 10^{16}$ cm^{-3}. For $T_v = 0.23$ eV (Fig. 1a) and low electron densities ($n_e < 10^{11}$ cm^{-3}), the function $H(T_e)$ has a single root at $\bar{T}_{e1} \approx 0.075$ eV. Since $\partial H(\bar{T}_{e1})/\partial T_e < 0$, this root is stable. The EEDF at $T_e = \bar{T}_{e1}$ and $n_e = 2 \times 10^{10}$ cm^{-3} is represented by curve *1* in Fig. 2. We can see that the EEDF is characteristically bi-Maxwellian. The majority of electrons, which are in the thermal energy range $\varepsilon < \varepsilon_1$, obey a Maxwellian distribution with temperature T_e. The electrons that are in the range $\varepsilon_1 \le \varepsilon \le \varepsilon_2$ obey a distribution characterized not only by the electron temperature but also by the vibrational temperature T_v. A comparison between the terms in the energy balance equation shows that the primary mechanism by which the electrons are cooled is associated with the energy loss in the excitation of the rotational levels. The electron heating is governed by the deexcitation of the most populated lower vibrational levels with $v = 1, 2$ (Fig. 1d). The primary heating mechanism is governed

by the nonresonant parts (at $\varepsilon < 1$ eV) of the deexcitation cross sections $\sigma_{10}(\varepsilon)$ and $\sigma_{20}(\varepsilon)$, because it is these parts that are responsible for heating the majority of electrons.

As the electron density increases, electron–electron collisions become more frequent, leading to an increase in the effective energy transferred from high-energy ($\varepsilon > \varepsilon_1$) electrons to thermal electrons [13]. The higher the electron temperature T_e, the more important is the role of superelastic collisions with nitrogen molecules that are vibrationally excited to the levels v = 3–5 (Fig. 1d). This effect is associated with the large cross sections for the resonance deexcitation of these levels at energies of about $\varepsilon \approx 0.8$–1.5 eV. The electron temperature T_e stops increasing when the electron energy begins to be lost primarily in the excitation of the vibrational levels.

The qualitative picture of the processes occurring in an afterglow plasma is illustrated by the dependence $H(T_e)$ at $n_e = 10^{11}$ cm^{-3} (Fig. 1a, curve *3*). We can see that, at a higher electron density n_e, the solution to the energy balance equation has additional roots. The solution at hand has three roots. The first root is almost the same as that at lower densities. The second root at $\bar{T}_{e2} = 0.16$ eV is unstable because it satisfies the condition $\partial H(\bar{T}_{e1})/\partial T_e > 0$. The third root at $\bar{T}_{e3} = 0.19$ eV is again stable. For the second stable state, the EEDF is represented by curve *2* in Fig. 2. The characteristic feature of this EEDF is that, over the energy range of the efficient excitation and deexcitation of the vibrational levels, the electron density increases sharply (by more than three orders of magnitude).

At a higher vibrational temperature ($T_v = 0.26$ eV), the states of an afterglow plasma can also be bistable at low electron densities (Fig. 1b). The value of the first root in the range of low T_e values depends only slightly on n_e and is equal to $\bar{T}_{e1} = 0.085$ eV. For this state, we have $H_{\mathrm{rot}}(\bar{T}_{e1}) > H^{-}_{\mathrm{vibr}}(\bar{T}_{e1})$. The second root is unstable. The value of the third root depends strongly on n_e. At high electron densities ($n_e \geq 10^{11}$ cm^{-3}), the temperature $\bar{T}_{e3} = 0.255$ eV practically coincides with T_v. For an EEDF with this value of T_e, the dominant mechanism for electron energy losses is the excitation of the vibrational levels, so that we have $H^{-}_{\mathrm{vibr}}(\bar{T}_{e3}) > H_{\mathrm{rot}}(\bar{T}_{e3})$. As may be seen, a transition to another stable state indicates that a different mechanism for energy losses has come into play.

The lower the electron density n_e, the stronger is the effect of the processes of the excitation of the rotational levels on the shape of the EEDF in the thermal energy range $\varepsilon \leq \varepsilon_1$. These processes act to form an EEDF with its own characteristic temperature T_g. However, the principle of energy balance, which is governed by the

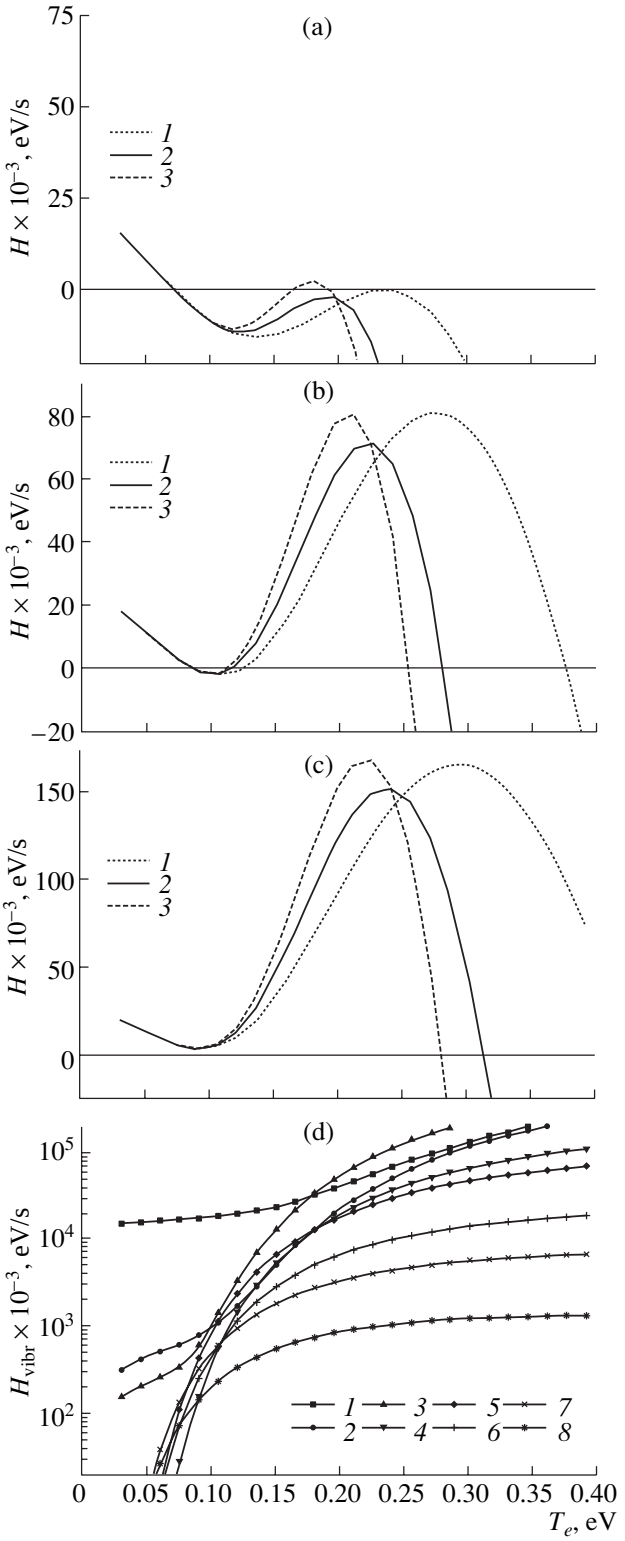

Fig. 1. Mean electron energy calculated from the balance equation as a function of the electron temperature T_e at different vibrational temperatures T_v = (a) 0.23, (b) 0.26, and (c) 0.28 eV and different electron densities n_e = (*1*) 5×10^9, (*2*) 2×10^{10}, and (*3*) 10^{11} cm^{-3} and (d) the rate of electron heating associated with the excitation of the eight lowest lying vibrational levels as a function of the electron temperature T_e at $T_v = 0.23$ eV and $n_e = 2 \times 10^{10}$ cm^{-3}.

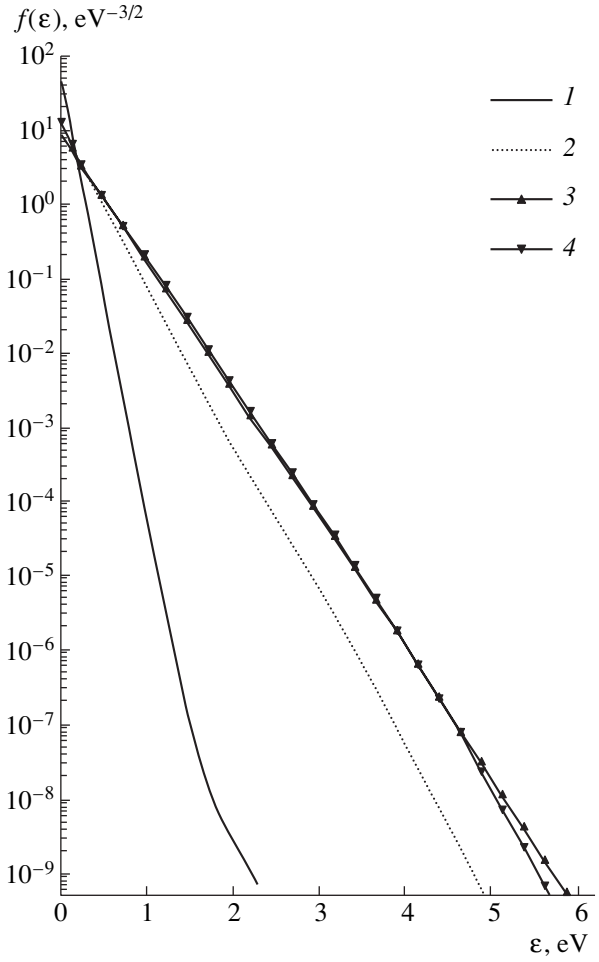

Fig. 2. EEDF in the discharge afterglow in nitrogen at (*1*) T_v = 0.23 eV, $n_e = 2 \times 10^{10}$ cm^{-3}, and T_e = 0.075 eV; (*2*) T_v = 0.23 eV, $n_e = 10^{11}$ cm^{-3}, and T_e = 0.195 eV; (*3*) T_v = 0.26 eV, $n_e = 10^{11}$ cm^{-3}, and T_e = 0.255 eV; and (*4*) T_v = 0.26 eV, $n_e = 5 \times 10^9$ cm^{-3}, and T_e = 0.375 eV.

processes of the excitation and deexcitation of the vibrational levels, implies that the EEDF should be close to a Maxwellian function with the temperature $T(\varepsilon) \approx T_v$. Consequently, as can be seen from curves *2* and *3* in Fig. 1b, a decrease in the electron density leads to a displacement of the quantity $\bar{T}_{e3}$ toward the high energy range. As a result, an increase in T_e compensates for the progressively smaller effect of the electron–electron collision rate on the shape of the EEDF in the thermal energy range $\varepsilon \le \varepsilon_1$. Hence, over the entire energy range $\varepsilon \le \varepsilon_3$, the EEDF is essentially an exponential function with $T(\varepsilon) \approx T_v$ (Fig. 2, curves *3*, *4*).

At higher vibrational temperatures (up to T_v = 0.28 eV), there remains the only stable state in which the EEDF in the electron density range under consideration is characterized by the temperature $\bar{T}_e \ge T_v$. In this case, over the entire energy range, the EEDF is close to Maxwellian in shape with $T(\varepsilon) \approx T_v$. In the low energy range $\bar{T}_e < 0.1$ eV, there is no longer a root, because, for $T_v \ge 0.27$ eV, the energy loss in the excitation of the rotational levels cannot compensate for electron heating by collisions with vibrationally excited molecules.

Let us analyze how the electric field affects the energy balance at T_v = 0.23 eV and $n_e = 2 \times 10^{10}$ cm^{-3}. Recall that, for E = 0, there exists a single stable solution corresponding to the root at $\bar{T}_{ea}$ = 0.075 eV (Fig. 3a, curve *1*), in which case the EEDF is bi-Maxwellian in character (Fig. 2, curve *1*). The energy balance is dominated by the losses associated with the excitation of the rotational levels (Fig. 3b). We can see that even a slight additional electron heating could lead to the appearance of the second stable solution in the range of high electron temperatures T_e.

Imposing a weak electric field (E/N = 0.4 Td) is sufficient for the solution to Eq. (7) to have a root in the range of high electron temperatures, specifically, at $\bar{T}_{eb}$ = 0.21 eV (Fig. 3a, curve *2*). This solution is seen to be unique. It is of interest to note that, in the energy balance equation, the field term $H_{eE}(\bar{T}_{eb})$ is small in comparison with the term $H^+_{\text{vibr}}(\bar{T}_{eb})$ and makes a contribution of about 10% (Fig. 3b). Hence, the applied weak electric field plays the role of a peculiar trigger mechanism that gives rise to an avalanche-like electron heating associated with the deexcitation of the vibrationally excited molecules (Fig. 3b) and forces the EEDF to evolve into another steady state with the temperature $T_e \approx T_v$.

As the electric field is increased up to E/N = 1.7 Td, the electron temperature continues to grow and, in the energy balance equation, the above two terms again satisfy the condition $H^+_{\text{vibr}}(\bar{T}_{ec}) > H_{eE}(\bar{T}_{ec})$ (Fig. 3b). In this case, however, the value $\bar{T}_{ec}$ = 0.27 eV is larger than T_v. In the thermal energy range $\varepsilon \le \varepsilon_1$, the field term $D_{eE}(\varepsilon)$ contributes insignificantly to expression (6) in comparison with the term $D_{ee}(\varepsilon)$. In this energy range, a decrease in the EEDF is determined by the electron temperature $T(\varepsilon) = \bar{T}_{ec}$.

In our study, we compared the EEDFs calculated for T_v = 0.26 eV and $n_e = 2 \times 10^{10}$ cm^{-3} from the analytic model proposed here with the EEDFs obtained in [34] by integrating the Boltzmann equation numerically. When determining the EEDF, we calculated the cross sections of the processes involving vibrationally excited molecules in the same way as was done in [34] for set II of the cross sections. The results of the comparison are illustrated in Fig. 4. In the absence of the electric field, the two calculation methods give nearly the same values of T_e in the thermal energy range $\varepsilon \le \varepsilon_1$, in which the majority of electrons are concentrated. The

EEDFs are seen to differ in shape only in the transitional energy range ($\varepsilon \approx 1$ eV), in which the electron–electron collision rate is comparable to the rate of the excitation of the vibrational levels of nitrogen molecules. We attribute this discrepancy to the error introduced into our model by the Fokker–Planck representation of the integral for inelastic collisions of electrons with molecules. Because of the inelastic nature of electron–molecule collisions, the EEDF spreads out into the lower energy range by an amount equal to the vibrational quantum energy. Of course, this effect is captured by numerical simulations but it cannot be described by the analytic model used here. The EEDFs calculated numerically and analytically for E/N = 1.7 Td are almost the same. Imposing the electric field results in a sharp increase in the electron temperature. In the energy range $\varepsilon_1 \le \varepsilon \le \varepsilon_2$, the decrease in the EEDF is, as before, determined by the vibrational temperature T_v.

Hence, even a weak electric field in which the electron temperature T_e grows in avalanche fashion may be responsible for a severalfold enhancement of the ambipolar diffusion in the plasma and a severalfold reduction of the recombination rate for charged particles. In such a field, the number of electrons in the range $\varepsilon_1 \le \varepsilon \le \varepsilon_2$ increases sharply, resulting in a jumplike increase in the rate at which the electrons excite the vibrational levels of nitrogen molecules. Since the shape of the EEDF changes, the rate of the excitation of the electronic terms of nitrogen molecules from the higher lying vibrational levels of the ground state can increase by several orders of magnitude [35]. The factors just mentioned may have a strong influence on the entire sequence of plasmochemical reactions occurring in an afterglow plasma in nitrogen.

5. EXPERIMENTAL OBSERVATIONS OF THE EEDF

Our calculations revealed several scenarios for the relaxation of the EEDFs in the discharge afterglow. Which of the scenarios will occur depends on the initial conditions, which are governed by the values of n_e and T_v at the end of the discharge current pulse.

For $T_v \approx 0.23$ eV and a sufficiently high electron density in the discharge plasma ($n_e > 10^{11}$ cm^{-3}), the electron temperature T_e in an afterglow plasma rapidly relaxes to the value $T_e \approx T_v$ and then remains unchanged until the electron density decreases to $n_e \sim 5 \times 10^{10}$ cm^{-3} due to diffusion and/or recombination processes. In this case, the EEDF with this value of the electron temperature T_e becomes unstable. As a result, the electron temperature T_e decreases in a jumplike manner to T_e = 0.08 eV and the shape of the EEDF changes. An analogous behavior of T_e was experimentally observed in [10, 11].

If the initial electron density in the discharge plasma is $n_e < 5 \times 10^{10}$ cm^{-3} and the vibrational temperature is about $T_v \approx 0.23$ eV, then the electron temperature T_e rapidly relaxes to a small value ($T_e < 0.1$ eV) after the discharge current pulse has come to an end. Since the value of the first stable root depends only slightly on n_e,

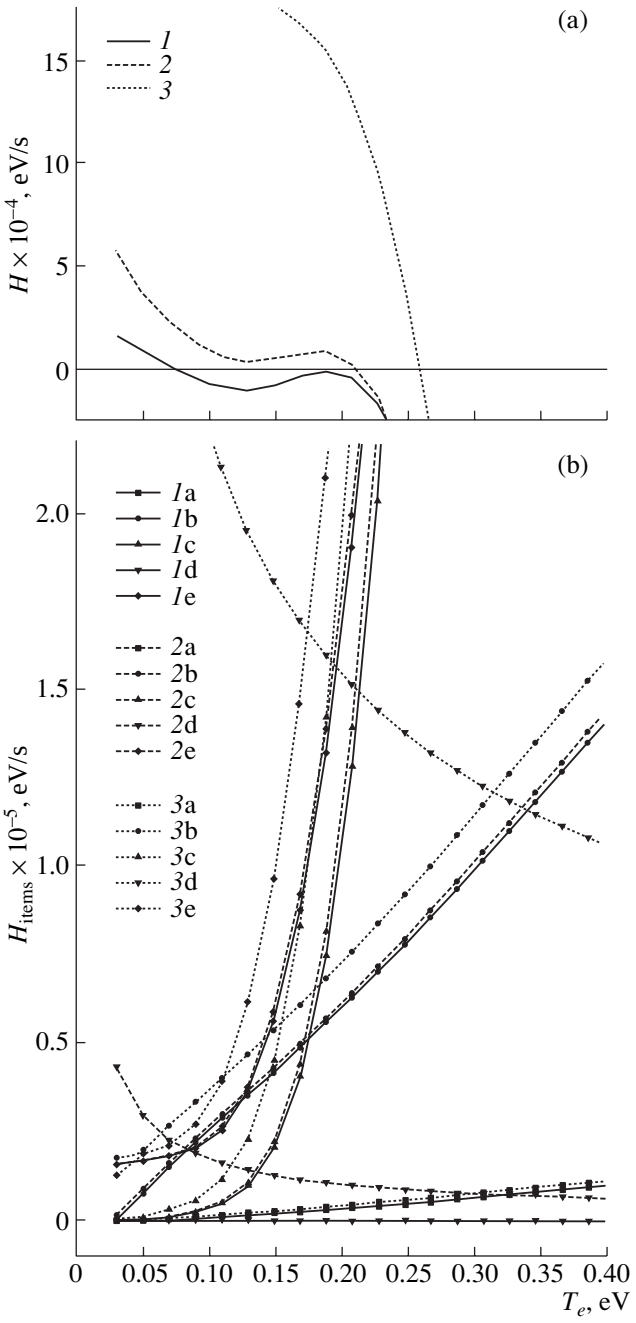

Fig. 3. (a) Mean electron energy balance and (b) distribution of the energy that is lost and gained by the electrons at T_v = 0.23 eV and $n_e = 2 \times 10^{10}$ cm^{-3} for different electric field strengths E/N = (*1*) 0, (*2*) 0.4, and (*3*) 1.7 Td. In Fig. 3b, the letters in the curve legends refer to the terms in the mean electron energy balance equation: (a) $|H_{\text{el}}|$, (b) $|H_{\text{rot}}|$, (c) $\left|H^{-}_{\text{vibr}}\right|$, (d) $|H_{eE}|$, and (e) $\left|H^{+}_{\text{vibr}}\right|$.

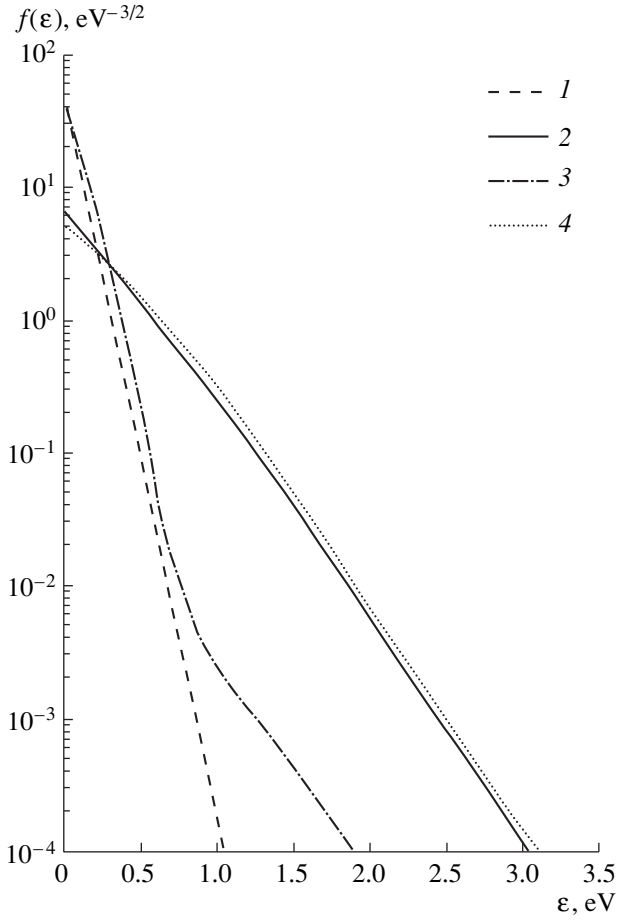

Fig. 4. EEDFs calculated from our model (curves *1*, *2*) and obtained in [34] (curves *3*, *4*) at $T_v = 0.26$ eV and $n_e = 2 \times 10^{10}$ cm^{-3} for different electric field strengths E/N = (*1*, *3*) 0 and (*2*, *4*) 1.7 Td.

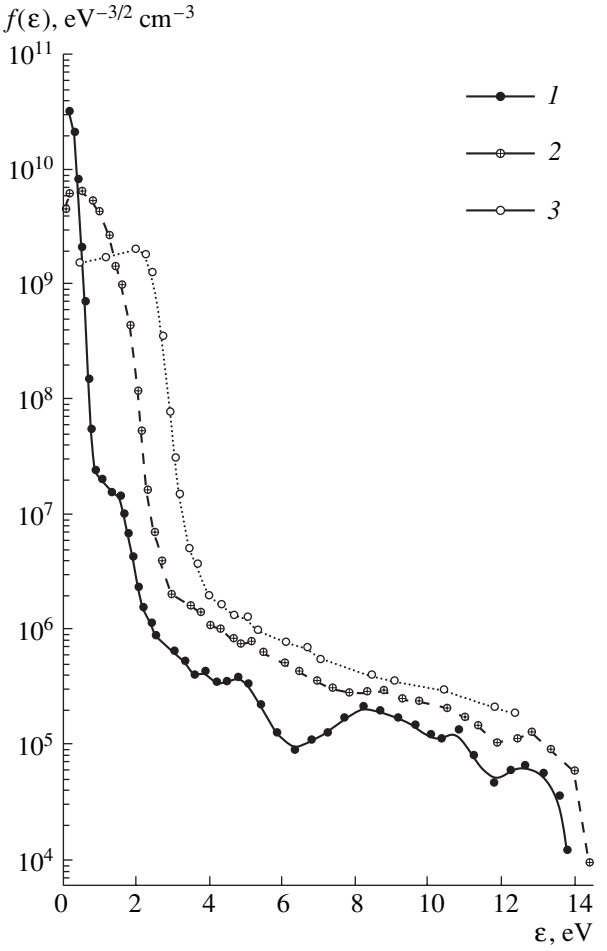

Fig. 5. EEDFs measured at different electric field strengths E/N = (*1*) 0, (*2*) 0.4, and (*3*) 1.7 Td.

the temperature T_e remains unchanged throughout the entire afterglow stage. This behavior of the electron temperature in an afterglow plasma was experimentally observed in discharges in nitrogen at the pressure P = 0.3 torr [6]. In the experiments of [6], the electron temperature was found to be unchanged ($T_e = 0.09$ eV) over a time interval of 100–500 μs.

At higher vibrational temperatures ($T_v \approx 0.26$ eV), the electron temperature rapidly relaxes to the value $T_e \approx T_v$ and then remains unchanged until T_v decreases to $T_v \approx 0.23$ eV. If the electron density at this time is $n_e < 5 \times 10^{10}$ cm^{-3}, the electron temperature T_e will decrease in a jumplike fashion.

Here, we describe the first experimental measurement of the EEDF in a nitrogen plasma in the presence of a weak electric field. The measurements were carried out during the discharge afterglow in pure nitrogen at the pressure P = 0.3 torr in a discharge tube with the radius R = 1.7 cm. The experimental device and the technique for measuring the EEDF were described in detail in [5, 6]. The current pulse duration was τ = 7 μs, the repetition rate of the pulses was f = 1.25 kHz, and the discharge current was I_d = 250 mA. The duration of the additional current pulse that governed the electric field strength in the afterglow was 30 μs. The EEDF was measured 80 μs after the electric discharge came to an end, i.e., 20 μs after the beginning of the heating pulse. The electric field strength was measured from the potential difference between two probes.

The measured EEDFs (normalized to the electron density) are shown in Fig. 5, in which curve *1* reflects the EEDF measured in the absence of the field. The majority of electrons are seen to obey a Maxwellian distribution with the temperature $T_e = 0.09 \pm 0.01$ eV. In the energy range of the efficient excitation and deexcitation of the vibrational levels, the decrease in the EEDF is determined by the effective temperature $T(\varepsilon) = 0.25 \pm 0.05$ eV. The high-energy part of the EEDF is governed by the deexcitation of the electronically excited states of nitrogen molecules by thermal electrons. The electron density measured from the plasma conductivity when an electric current flowed through

the plasma was $n_e = 2 \times 10^{10}$ cm^{-3}. According to our calculations of the EEDF, the experimentally measured value of the electron temperature T_e corresponds to the range $T_v \le 0.25$ eV.

Imposing an electric field with the strength E/N = 0.4 Td radically changes the shape of the EEDF (curve *2* in Fig. 5). In this case, the results from the probe measurements of the EEDF in the low-energy range $\varepsilon \le \varepsilon_1$ are distorted by instrumental effects. The distortions are introduced by the smoothing influence of the electric field along the probe (in the case at hand, over a distance of 15 mm), and, in the energy range $0 \le \varepsilon \le 3T_e$, they are caused by the drain of electrons to the probe. As a result, we failed to determine the electron temperature T_e in the energy range $\varepsilon \le \varepsilon_1$ by probe measurements. However, in the energy range $\varepsilon_1 \le \varepsilon \le \varepsilon_2$, the EEDF in the presence of the electric field is seen to increase by more than two orders of magnitude over that in the absence of the field ($E = 0$).

Increasing the electric field up to E/N = 1.7 Td leads to a further increase in the EEDF in the energy range $\varepsilon_1 \le \varepsilon \le \varepsilon_2$. The amount by which the EEDF decreases over this energy range remains the same as that in the absence of the field and, accordingly, is again determined by the temperature T_v. On the whole, the results of the calculation of the EEDF (Fig. 4) are in good qualitative agreement with the experimental data.

6. CONCLUSION

We have carried out experimental measurements and theoretical analysis of the relaxation of the electron temperature during the discharge afterglow in molecular nitrogen under the conditions of weak electric fields. The EEDF is calculated with allowance for the electric field, electron–electron collisions, elastic electron–molecule collisions, and the processes of the excitation and deexcitation of the rotational and vibrational levels of the ground state of nitrogen molecules. The shape of the EEDFs is calculated analytically by using the Fokker–Planck representation of the integral for inelastic collisions in which the vibrational levels are excited. The electron temperature is determined from the mean electron energy balance equation. This approach makes it possible to qualitatively analyze the effect of both the temperature corresponding to the vibrational distribution of nitrogen molecules and the degree of plasma ionization on the electron temperature T_e. We have established that, depending on the values of n_e and T_v, an afterglow plasma may evolve into two states differing in the electron temperature T_e. When the electron temperature is low, $T_e < 0.1$ eV, the main cooling mechanism for electrons is associated with the energy loss in the excitation of the rotational levels, whereas electron heating is governed by the deexcitation of the most populated lower vibrational levels with $v = 1, 2$. The second stable solution, for which $T_e \approx T_v$, is established in the range $T_v \ge 0.25$ eV. In this case, the electron energy balance is governed by the processes of the excitation and deexcitation of the vibrational levels. Hence, we have shown that the existence of bistable states stems from the fact that the primary mechanism for electron energy losses changes with increasing the electron temperature. This change is associated with the resonant nature of the cross sections for the excitation of the vibrational levels of nitrogen molecules in the ground state. A comparison between the results of our analytic model for calculating the EEDF with the available numerical results shows that the model correctly describes the evolution of the electron temperature T_e.

The transition from one stable state to another (with a lower value of T_e) can manifest itself as a jumplike change in time of the electron temperature in a decaying nitrogen plasma. This jump may be associated with a decrease in n_e and/or T_v during the relaxation process. As a result, the rate at which the thermal electrons are heated by collisions with vibrationally excited molecules decreases.

Our analysis shows that weak electric fields can change the electron temperature T_e at the expense of a jumplike transition from one stable state to another. However, the electric field has a minor direct effect on electron heating in comparison with the deexcitation of the vibrationally excited molecules. Hence, the electric field plays the role of a peculiar trigger mechanism that forces the EEDF to evolve into another steady state. Our experimental investigations confirmed the prediction that the imposition of a weak electric field causes the EEDF to change in a jumplike manner.

ACKNOWLEDGMENTS

We are grateful to N.A. Dyatko for discussing the results obtained. This work was supported in part by the Russian Foundation for Basic Research, project no. 00-02-17662.

REFERENCES

1. *Nonequilibrium Oscillatory Kinetics*, Ed. by M. Capitelli (Springer-Verlag, New York, 1986; Mir, Moscow, 1989).
2. C. Gorse, M. Capitelli, and A. J. Ricard, J. Chem. Phys. **82**, 1900 (1985).
3. F. Paniccia, C. Gorse, J. Bretagne, and M. Capitelli, J. Appl. Phys. **59**, 4004 (1986).
4. C. Gorse, M. Cacciatore, M. Capitelli, *et al.*, Chem. Phys. **119**, 63 (1988).
5. N. A. Gorbunov, N. B. Kolokolov, and A. A. Kudryavtsev, Zh. Tekh. Fiz. **58**, 1817 (1988) [Sov. Phys. Tech. Phys. **33**, 1104 (1988)].
6. N. A. Gorbunov, N. B. Kolokolov, and A. A. Kudryavtsev, Zh. Tekh. Fiz. **61** (6), 52 (1991) [Sov. Phys. Tech. Phys. **36**, 616 (1991)].

7. N. A. Dyatko, I. V. Kochetov, and A. P. Napartovich, Fiz. Plazmy **18**, 888 (1992) [Sov. J. Plasma Phys. **18**, 462 (1992)].
8. G. Colonna, C. Gorse, M. Capitelli, *et al.*, Chem. Phys. Lett. **213**, 5 (1993).
9. A. A. Kudryavtsev and A. I. Ledyankin, Phys. Scr. **53**, 597 (1996).
10. Yu. Z. Ionikh, N. B. Kolokolov, A. V. Meshchanov, and N. V. Chernysheva, Opt. Spektrosk. **88**, 560 (2000) [Opt. Spectrosc. **88**, 502 (2000)].
11. N. A. Dyatko, Yu. Z. Ionikh, N. B. Kolokolov, *et al.*, J. Phys. D **33**, 2010 (2000).
12. N. A. Dyatko and A. P. Napartovich, in *Contributed Papers of the 20th Summer School and International Symposium on Physics of Ionized Gases, Zlatibor, 2000*, p. 115.
13. A. B. Blagoev, Yu. M. Kagan, N. B. Kolokolov, and R. I. Lyagushchenko, Zh. Tekh. Fiz. **44**, 339 (1974) [Sov. Phys. Tech. Phys. **19**, 215 (1974)].
14. N. B. Kolokolov, A. A. Kudryavtsev, and A. B. Blagoev, Phys. Scr. **50**, 371 (1994).
15. N. A. Gorbunov, N. B. Kolokolov, and F. E. Latyshev, Zh. Tekh. Fiz. **71** (4), 28 (2001) [Tech. Phys. **46**, 391 (2001)].
16. L. D. Tsendin, Plasma Sources Sci. Technol. **4**, 200 (1995).
17. N. A. Gorbunov, K. O. Iminov, and A. A. Kudryavtsev, Zh. Tekh. Fiz. **58**, 2301 (1988) [Sov. Phys. Tech. Phys. **33**, 1403 (1988)].
18. L. G. H. Huxley and R. W. Crompton, *The Diffusion and Drift of Electrons in Gases* (Wiley, New York, 1974; Mir, Moscow, 1977).
19. M. A. Morrison and N. F. Lane, Phys. Rev. A **16**, 975 (1977).
20. Yu. B. Golubovskiĭ, Yu. M. Kagan, and R. I. Lyagushchenko, Zh. Éksp. Teor. Fiz. **57**, 2222 (1969) [Sov. Phys. JETP **30**, 1204 (1969)].
21. L. M. Biberman, V. S. Vorob'ev, and I. T. Yakubov, *Kinetics of Nonequilibrium Low-Temperature Plasmas* (Nauka, Moscow, 1982; Consultants Bureau, New York, 1987).
22. N. L. Aleksandrov, A. M. Konchakov, and É. E. Son, Fiz. Plazmy **4**, 1182 (1978) [Sov. J. Plasma Phys. **4**, 663 (1978)].
23. A. G. Ponomarenko, V. N. Tishchenko, and V. A. Shweigert, Teplofiz. Vys. Temp. **25**, 787 (1987).
24. D. I. Slovetskiĭ, *Mechanisms of Chemical Reactions in Nonequilibrium Plasma* (Nauka, Moscow, 1980).
25. R. I. Lyagushchenko and M. B. Tendler, Fiz. Plazmy **1**, 836 (1975) [Sov. J. Plasma Phys. **1**, 458 (1975)].
26. R. V. Chiflikyan, Fiz. Plazmy **22**, 71 (1996) [Plasma Phys. Rep. **22**, 66 (1996)].
27. A. K. Kazanskiĭ and I. I. Fabrikant, Usp. Fiz. Nauk **143**, 601 (1984) [Sov. Phys. Usp. **27**, 607 (1984)].
28. A. A. Mikhajlov and V. A. Pivovar, Zh. Tekh. Fiz. **45**, 1063 (1975) [Sov. Phys. Tech. Phys. **20**, 668 (1975)].
29. A. A. Mihajlov, V. D. Stojanovic, and Z. Lj. Petrovic, J. Phys. D **32**, 2620 (1999).
30. M. Allan, J. Phys. B **18**, 4511 (1985).
31. K. P. Huber and G. Herzberg, *Molecular Spectra and Molecular Structure*, Vol. 4: *Constants of Diatomic Molecules* (Van Nostrand, New York, 1979).
32. V. E. Golant, A. P. Zhilinskii, and I. E. Sakharov, *Fundamentals of Plasma Physics* (Atomizdat, Moscow, 1977; Wiley, New York, 1980).
33. A. A. Andronov, A. A. Vitt, and S. E. Khaikin, *Theory of Oscillators* (Fizmatgiz, Moscow, 1959; Pergamon Press, Oxford, 1966).
34. N. A. Dyatko, I. V. Kochetov, and A. P. Napartovich, J. Phys. D **26**, 418 (1993).
35. N. L. Aleksandrov, I. V. Kochetov, and A. P. Napartovich, Teplofiz. Vys. Temp. **23**, 849 (1985).

Translated by O. E. Khadin